Ollscoil Chathair Bhaile Átha Cliath
Dublin City University

Stabilised and Targeted Copper(II) Polypyridyl Oxidative Chemical Nucleases

Nicolò Zuin Fantoni M.Sc.

Ph. D. Thesis

Assoc. Prof. Andrew Kellett
School of Chemical Sciences
Faculty of Science and Health
Dublin City University
Ireland

January 2020

Declaration

I hereby certify that this material, which I now submit for assessment on the programme of study leading to the award of Doctor of Philosophy is entirely my own work, and that I have exercised reasonable care to ensure that the work is original, and does not to the best of my knowledge breach any law of copyright, and has not been taken from the work of others save and to the extent that such work has been cited and acknowledged within the text of my work.

Signed: _____ ID No.: 15211014 Date: _____

Dedicated to my family

'Imagine the unimaginable'
Nobel Laureate Bernard Lucas Feringa

Publications

- Fantoni N., Lauria T., Kellett A. 'Genome Engineering with Synthetic Copper Nucleases'. *Synlett.*, **2015**, 26 (19), 2623-2626.
- Zuin Fantoni N., Molphy Z., Slator C., Menounou G., Toniolo G., Mitrikas G., McKee V., Kellett A. 'Polypyridyl-Based Copper Phenanthrene Complexes: A New Type of Stabilized Artificial Chemical Nuclease'. *Chem. Eur. J.*, **2018**, 25(1), 221-237
- Toniolo G., Louka M., Menounou G., Fantoni, N. Z., Mitrikas G., Efthimiadou E. K., Masi A., Bortolotti M., Polito L., Bolognesi A., Kellett A., Ferreri C., Chatgilialoglu C. '[Cu(TPMA)(Phen)](ClO4)2 : Metallodrug Nanocontainer Delivery and Membrane Lipidomics of a Neuroblastoma Cell Line Coupled with a Liposome Biomimetic Model Focusing on Fatty Acid Reactivity'. *ACS Omega*, **2018**, 15952-15965
- Brustolin L., Nardon C., Pettenuzzo N., Fantoni N. Z., Quarta S., Chiara F., Gambalunga A., Trevisan A., Marchiò L., Pontisso P., Fregona D. 'Synthesis, chemical characterization and cancer cell growth-inhibitory activities of Cu(II) and Ru(III) aliphatic and aromatic dithiocarbamato complexes'. *Dalton Trans.*, **2018**, 15477-15486.

Poster and scientific talks

Poster title

- Fantoni, N., Lauria, T., Avella, G., Barron, N., Kellett, A. *'ClickGene: Click Chemistry for Future Gene Therapies to Benefit Citizens, Researchers and Industry'.* 68th Irish Universities Chemistry Research Colloquium, University College Cork, Ireland, 23rd-24th June 2016.
- Fantoni, N., Lauria, T., Avella, G., Barron, N., Kellett, A. *'ClickGene: Click Chemistry for Future Gene Therapies to Benefit Citizens, Researchers and Industry'.* 1st Medicinal Chemistry Ireland Conference, Trinity College Dublin, Ireland, 1st July 2016.
- Fantoni, N.; Molphy, Z.; McKee, V.; Kellett, A. *'Artificial Metallo-Nucleases for Gene Editing'.* XVII Symposium on Chemistry of Nucleic Acid Components (SCNAC), Český Krumlov, Czech Republic, 4-9th June 2017.
- Fantoni, N.; Molphy, Z.; McKee, V.; Kellett, A. *'Caged Copper (II) Oxidative Chemical Nucleases'.* Inorganic Dublin 2017, Trinity College Dublin, Ireland, 13th December 2017.
- Fantoni, N.; Molphy, Z.; McKee, V.; Kellett, A. *'Caged Copper (II) Oxidative Chemical Nucleases'.* 3rd School of Chemical Sciences Chemistry Day, Dublin City University, Ireland, 4th May 2018.
- Zuin Fantoni, N.; Molphy, Z.; Slator, C.; Menounou, G.; McKee, V.; Kellett, A. *'Stabilized Copper(II) Oxidative Chemical Nucleases'.* European School of Medicinal Chemistry (ESMEC), Urbino, Italy, 1st-5th July 2018.

Scientific talks

- Fantoni, N.; McKee, V.; Barron, N.; Kellett, A. *'Molecular Scissors as Synthetic DNA Cutters'.* COST Action CM1201: Biomimetic Radical Chemistry & ClickGene Meeting, Grenoble, France, 25-27th March 2016.
- Fantoni, N.; Molphy, Z.; McKee, V.; Kellett, A. *'Gene Editing with Copper(II)-TPMA Oxidative Chemical Nucleases'.* 2nd School of Chemical Sciences Chemistry Day, Dublin City University, Dublin, Ireland, 12th May 2017.

- Fantoni, N.; Molphy, Z.; McKee, V.; Kellett, A. *'Gene-editing with Nucleic Acid Click Chemistry'*. 3rd School of Chemical Sciences Chemistry Day, Dublin City University, Dublin, Ireland, 4th May 2018.
- Fantoni, N.; Molphy, Z.; Slator, C.; Menounou, G.; McKee, V.; Kellett, A. *'Polypyridyl-based Copper Phenanthrene Complexes: A New Class of Stabilized Artificial Chemical Nuclease'*. 70th Irish Universities Chemistry Research Colloquium, Queen's University, Belfast, United Kingdom, 21st-22nd June 2018.
- Zuin Fantoni, N.; Molphy, Z.; Slator, C.; Menounou, G.; McKee, V.; Kellett, A. *'Polypyridyl-based Copper Phenanthrene Complexes: A New Class of Stabilized Artificial Chemical Nuclease'*. European School of Medicinal Chemistry (ESMEC), Urbino, Italy, 1st-5th July 2018.

Awards

- Fluorochem poster prize at the 3rd School of Chemical Sciences Chemistry Day. Poster title: Gene-editing with Nucleic Acid Click Chemistry.

Table of Contents

Table of figures

Tables of tables

Abbreviations

A	Adenine
AB	Abasic site
ACN	Acetonitrile
AMN	Artificial metallo-nucleases
AP	Apurine/apyrimidine
ATR	Attenuated total reflection
5′-BCN	5′-endo-Bicyclo[6.1.0]non-4-yn-9-ylmethyl(2-(2-hydroxyethoxy)ethyl)carbamate
Bipy	2,2-Bipyridine
BSA	Bovine serum albumin
C	Cytosine
cccDNA	Covalently closed circular DNA
CCDC	Cambridge crystallographic data centre
^{13}C-NMR	Carbon-13 nuclear magnetic resonance
COSY	Correlation spectroscopy
CRISPR	Clustered regularly interspaced palindromic repeats
ctDNA	Calf thymus DNA
CuAAC	Copper promoted alkyne-azide cycloaddition
$Cu(ClO_4)_2$	Copper perchlorate
Cw-EPR	Continuous wave electron paramagnetic resonance
dG	Deoxyguanine
dI	Deoxyinosine
DIPEA	*N,N*′-Diisopropylethylamine
dU	Deoxyuracil
DMSO	Dimethylsulfoxide
DMF	Dimethylformamide
DMPO	5,5′-Dimethyl-1-pyrroline *N*-oxide
DMTU	*N*,*N*′-Dimethylthiourea
DNA	Deoxyribose nucleic acid
dsDNA	Double-stranded DNA
DPA	*Di*-(2-pyridylmethyl)amine
DPPN	Benzo[*i*]dipyrido[3,2-a:2′,3′-c]phenazine
DPPZ	Dipyrido[3,2-a:2′,3′-c]phenazine
DPQ	Dipyrido[3,2-f:2′,3′-h]quinoxaline
EDTA	Ethylenediaminetetraacetate
ENDOR	Electron nuclear double resonance
ESE	Electron spin echo
ESI-MS	Electrospray ionization mass spectrometry
EtBr	Ethidium bromide
FID	Free induction decay
Fpg	Formamidopyrimidine [fapy]-DNA glycosylase
FT	Fourier transform
G	Guanine
GFP	Green fluorescent protein
hAAG	Human alkyladenine DNA glycosylase

HDR	Homologous directed repair
HEPES	(4-(2-Hydroxyethyl)-1-piperazineethanesulfonic acid)
HMG	High mobility group
HJ	Holliday junction
^{1}H-NMR	Proton nuclear magnetic resonance
HPLC	High performance liquid chromatography
HSQC	Heteronuclear single quantum correlation
HYSCORE	Hyperfine sublevel correlation
IR	Infrared spectroscopy
K_{app}	Apparent binding constant
KP1019	[trans-$RuCl_4(Ind)_2$]$^-$
L-DNA	Linear DNA
Me-Tar-U	Methyltartronylurea
MG	Methyl greenl
Na-*L*-Asc	Sodium-*L*-ascorbate
NAMI-A	[ImH][*trans*-$RuCl_4$(DMSO-S)(Im)]
$4N_3$-BenzylDPA	*N*-4-azidobenzyl-*N*-*di*-(2-picolyl)amine
NHEJ	Non-homologous end joining
NH_4OAc	Ammonium acetate
NQR	Nuclear quadrupole resonance
$5N_3$-TPMA	*N*-5-(azidomethyl)pyridine-*N*-*di*-(2-picolyl)amine
$6N_3$-TPMA	*N*-6-(azidomethyl)pyridine-*N*-*di*-(2-picolyl)amine
OC	Open circular
ON	Oligonucleotides
PACT	Photoactivated chemotherapy
PCT	Photochemotherapy
PD	1,10-Phenanthroline-5,6-dione
PDT	Photodynamic therapy
pdU	5-(1-propargylamino)-2′-deoxyuridine
Ph	Phthalate
Phen	1,10-Phenanthroline
PNA	Peptide nucleic acids
PPA	Polypycolylamines
PPC	Polynuclear platinum complexes
Pu	Purine
Py	Pyrimidine
ROS	Reactive oxygen species
SC	Supercoiled DNA
SPAAC	Strain promoted alkyne-azide cycloaddition
ssDNA	Single-stranded DNA
T	Thymine
TALEN	Transcription activator-like effector nucleases
TBE	Tris/Borate/EDTA

TBP	Trigonal bipyramidal
TBTA	Tris[(1-benzyl-1H-1,2,3-triazol-4-yl)methyl]amine
TEAA	Triethylammonium acetate
TFO	Triplex forming oligonucleotide
Th	Terephthalate
THF	Tetrahydrofuran
TLD1433	*rac*-[Ru(dmb)$_2$(IP-3T)]Cl$_2$
T_M	Thermal melting
TO	Thiazole orange
TPMA	*Tris*-(2-pyridylmethyl)amine
U	Uracil
WC	Watson-Crick
ZFN	Zinc finger nuclease

Units of Measurement

Å	Angstrom
Abs	Absorbance
cm	Centimeter
cm^{-1}	Reciprocal wavelength
cP	Centipoise
C_{50}	Concentration required to reduce 50% fluorescence
°C	Degrees Celcius
δ	NMR chemical shift
ΔT_M	Difference in thermal melting
ε_{max}	molar absorption coefficient
g	Gram
h	Hour
Hz	Hertz
K_{app}	Apparent binding constant on DNA
K_{cat}	Apparent catalytic rate constant
L	Litre
M	Molar
mg	Milligram
MHz	Megahertz
min	Minute
ml	Millilitre
mmol	Millimoles
mM	Millimolar
mol	Mole
Mp	Melting point
ng	Nanogram
nM	Nanomolar
nm	Nanometres
pH	$-\log_{10}[H^+]$
ppm	Parts per million
Q	Fluorescence quenching
r	[drug]/[DNA] ratio
s	Seconds
T_M	Thermal Melting
V	Volt
v/v	Volume per volume
U	Enzyme units
µL	Microliter
µM	Micromolar

Abstract

Nicolò Zuin Fantoni M. Sc.

Stabilised and Targeted Copper(II) Polypyridyl Oxidative Chemical Nucleases

Gene editing has emerged as an important tool for altering the genomes of living cells with unprecedented ease. By targeting underlying genes of interest, this field has the potential to transform the treatment of human disease. Enzymatic nucleases—in particular CRISPR-Cas9—epitomize the current state of art in gene editing technology but are often limited by large size and complex design. The development of small molecule bio-mimetics of enzymatic nucleases has recently sparked efforts for potential applications in cancer therapy, DNA footprinting and protein engineering. One such example is represented by the artificial metallo-nuclease (AMN) $[Cu(1,10\text{-phenanthroline})_2]^+$ (Cu-Phen) which, in the reduced Cu(I) form, semi-intercalates duplex DNA, promoting reactive oxygen species (ROS) production and DNA oxidative cleavage. Cu-Phen type systems, however, exhibit limitations including: (i) speciation, (ii) promiscuous binding and *off*-target damage leading to general toxicity. The first part of this thesis reports a new family of stabilized Cu(II)-AMNs where a caging polypyridyl ligand scaffold (*tris*-(2-pyridylmethyl)amine, TPMA) was combined with Cu(II)-phenathrene chemical-nuclease cores (with phenanthrene being either 2,2'-bipyridine or phenazines such as Phen, 1,10-phenanthroline-5,6-dione (PD), dipyridoquinoxaline (DPQ) and dipyridophenazine (DPPZ)). EPR studies identified these complexes to have high solution stability with phenazine intercalators enhancing DNA recognition and binding compared to Cu-TPMA alone. Nuclease analysis then identified a distinctive oxidative profile compared to classical Sigman and Fenton-type reagents.

Although the TPMA ligand afforded increased solution stability, its steric hindrance prevented the high DNA binding observed for $[Cu(Phen)(Phenazine)]^{2+}$-type complexes. A new series of Cu(II)-DPA derivatives (where DPA is *di*-(2-pyridylmethyl)amine) was therefore developed. By removing one pyridine from the TPMA scaffold we sought to enhance intercalation while maintaining suitable solution stability. Furthermore, penta-coordination around the Cu(II) center exposed a free coordination site for the inner-sphere production of ROS.

Finally, caged Cu(II)-AMNs were coupled with triplex forming oligonucleotides (TFOs) for GFP-gene targeted knockdown. To achieve this, azide-alkyne cycloaddition

was employed to ‘click’ azide-modified AMN scaffolds to various alkyne-TFO derivatives. Gene-directing properties were then studied using a variety of techniques including UV melting, polyacrylamide and agarose gel electrophoresis and quantitative polymerase chain reaction (qPCR). The results of the AMN-TFO hybrids were compared to state-of-the-art nucleases such as CRISPR-Cpf1 and type II restriction endonucleases.

Chapter I

DNA-drug interactions and targeted nucleases

I. 1. Nucleic acid structure

I. 1.1. A-, B- and Z-DNA

From a biological point of view, life can be interpreted as the safe storage and transfer of biological information. In eukaryotic cells biological information is stored as a double stranded deoxyribonucleic acid (dsDNA) sequence within the nuclei and DNA plays a critical role in protein expression and in promotion of many cellular functions.[1,2] The structure of DNA was first resolved in 1953 by Watson, Crick and Franklin representing a major milestone that sparked new research in chemistry, chemical biology and genome engineering.[3–5] Nucleic acids are polymers composed by multiple repeating nucleobases linked together by a phospho(deoxy)ribose backbone (Figure I-1A). In duplex DNA two of these polynucleotide strands coil around each other in an antiparallel fashion exploiting the definite recognition between nucleobases and yielding the double helical structure. Rigidity of the double helix is provided by the inter-chain hydrogen bond formation and π-π stacking interactions between nucleobases. Coupling between DNA bases follows the Chargaff's rules whereby purines and pyrimidines pair in a 1:1 ratio (adenine:thymine and guanine:cytosine).[6]

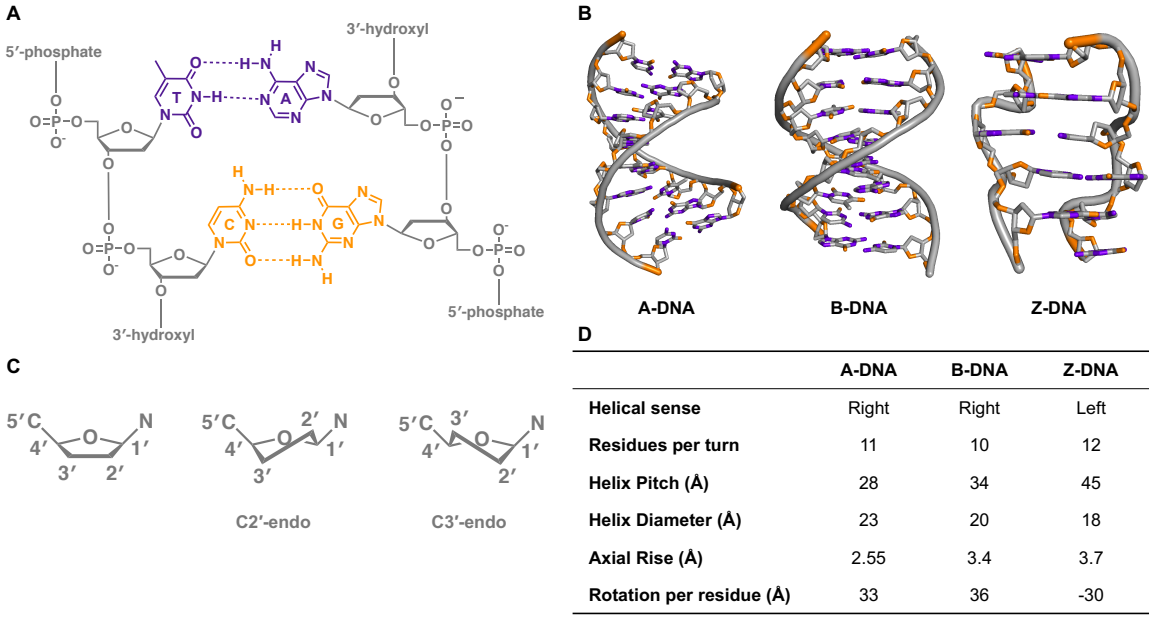

D

	A-DNA	B-DNA	Z-DNA
Helical sense	Right	Right	Left
Residues per turn	11	10	12
Helix Pitch (Å)	28	34	45
Helix Diameter (Å)	23	20	18
Axial Rise (Å)	2.55	3.4	3.7
Rotation per residue (Å)	33	36	-30

Figure I-1. A Base-pair interaction of the four nucleobases within the phosphate backbone; **B** main three forms of double DNA helix: A-DNA (PDB: 1VJ4), B-DNA (PDB: 1BNA) and Z-DNA (PDB: 2DCG); **C** conformational geometries of the 2′-deoxyribose ring in the DNA duplexes; **D** Structural differences among the three duplex conformations.

In cells, DNA exist primarily as three biologically-active double-helical structures: the right handed A- and B-DNA and the left handed Z-DNA (Figure I-1B). Among these three

forms, B-DNA is the most commonly found in physiological environments. Here, the 2′-deoxyribose ring is locked in the C2′-endo configuration (Figure I-1C) and the π-π stacking interactions between nucleobases orient them perpendicular to the axis of the double helix.[7] The glycosidic bond is locked in the *anti*-configuration and its asymmetrical edges cause unequal grooves in the DNA duplex called major and minor groove. The major groove is marked by the hydrophobic environment of the exposed nucleobases and it is wider (10.5 Å) than the minor groove (4.8 Å) where the hydrophilic phosphate chains reside. Between the base pairs of B-DNA there is an axial rise of 3.4 Å (0.34 nm) and a 34.5° twist angle associated with every residue rotation while the width of the helix diameter is 20 Å (Figure I-1D).[8,9] The A- form of the double helix is common for DNA duplexes in anhydrous environments, in some protein-DNA complexes and for RNA-based double helices (due to the steric restrictions imposed by the 2′-hydroxyl group on the ribose). Compared to B-DNA, its structure is shorter and more compacted along the helical axis but with a wider diameter. In A-DNA the ribose ring is puckered in the C3′ endo conformation resulting in a reduced distance between nucleobases (axial rise of 2.25 Å) and a slight unwinding of the helical structure (11 base pairs per turn versus the 10.5 of B-DNA).[2] In contrast to A- and B-DNA conformations, Z-DNA has a left-handed double helical structure and a single narrow groove similar to the minor groove of B-DNA. This, together with the alternating sugar pucker (C2′-endo for pyrimidines and C3′ endo for purines) and glycosidic bond (*anti* for pyrimidines and *syn* for purines) provides a zig-zag arrangement of the phosphate backbone within the helical structure, hence the name Z-DNA. Transition from B- to Z-DNA is promoted *in vivo* by the torsional strains generated when DNA is underwound by processive enzymes such as polymerases and helicases.[10,11] *In vitro* a similar flip between the two forms is achieved at high salt concentrations or treating B-DNA with *di*-nuclear complexes that interact electrostatically with the nitrogen (N7′) of guanines in poly[d(G-C)$_2$] sequences causing transition to the Z-form.[12]

In cells, DNA length can extend up to 10^8-10^9 nm and it is mostly packed in a compact underwound (negative)—or only transiently overwound (positive)—structure called supercoiled DNA. DNA supercoiling is essential not only in that it compacts DNA in a small volume but also because it governs accessibility to information and hence transcriptional regulation. Winding of the supercoil is defined by two terms: the twist (T_w) and the writhe (W_r). The twist is defined as the number of times a strand wrap around the other along the helical axis and right-handed duplexes have positive T_w values whereas left-

handed DNA is associated to negative T_w. The writhe instead is the result of covalently closed circular DNA (cccDNA). Here DNA ends are covalently joined to form a constrained structure where any change in T_w results in supercoiling or writhing of the double-helix. This close relationship between T_w and W_r is defined by the linking number ($L_k = T_w + W_r$) which in cccDNA is constant and changes only when one of the strands is nicked to release the overall topological tension.[2] Topoisomerases are enzymes that can bind DNA increasing (*e.g.* girase) or decreasing (*e.g.* topoisomerase I) the amount of negative supercoiling.[13] Similarly, winding is affected also during cellular replication and transcription processes and DNA is usually overwound downstream DNA/RNA polymerase enzymes and underwound upstream.

I. 1.2. Tertiary DNA structures: G-Quadruplex, I-motifs, the Holliday junction, DNA triplexes.

In addition to the three canonical DNA duplexes (A-, B- and Z-DNA), nucleic acids can arrange to form a variety of structures with biological relevance such as: G-quadruplexes, I-motifs, the Holliday junction and triple helical structures (also known as H-DNA; Figure I-2).[14]

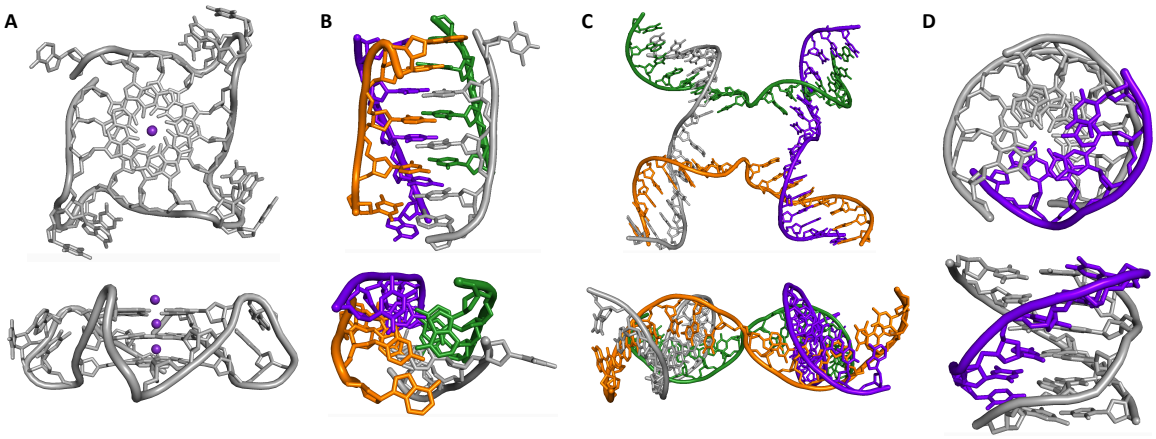

Figure I-2. Higher order DNA structures **A** G-Quadruplex (PDB: 1KF1); **B** I-motif (PDB: 1BQJ); **C** the Holliday junction (PDB: 467D); **D** triple helix (PDB: 1BWG).

I. 1.2.1. G-quadruplex

G-quadruplexes are four-stranded structures formed by guanine-rich sequences where the Watson-Crick edge of each G-nucleobase is paired with the Hoogsteen edge of the adjacent guanine. These structures can exist in different topologies caused by the association of one to four G-rich strands stabilized in their interaction by the presence of a central divalent cation (*i.e.* magnesium; Figure I-2A).[15] G-quadruplexes are very common in telomeric

DNA repeats suggesting a regulatory role in the telomeric control of cell replication. The length of telomeres is usually shortened during cell replication until the Hayflick limit is reached and cell apoptosis is initiated.[16] Misregulation of this process and of telomerase activity can cause cell immortality and tumorigenesis.[17] Developing compounds that can specifically target these structures has particular relevance for understanding the involvement of G-quadruplexes in cellular pathways and for therapeutic purposes.

I. 1.2.2. I-motif

I-motifs are four stranded, intercalated structures formed by C-rich sequences extruded from G-rich regions. These motifs are formed by the stacked intercalation of hemiprotonated C^+•C base pairs and are usually less stable at physiological pH than their G-quadruplex counterparts due to requirement for slightly acidic environments (Figure I-2B).[18] C-rich sequences are common within the human genome and i-motifs have been associated to telomeric, centromeric and promoter regions of proto-oncogenes suggesting possible regulatory functions in replication and transcription of DNA. Recently the presence of i-motifs and their regulatory roles were identified in the nuclei of human cells *in vivo*.[19]

I. 1.2.3. The Holliday junction

Holliday junctions (HJ) are cross-shaped, branched nucleic acid structures characterized by four annealed dsDNA sequences (Figure I-2C). This crossover arrangement forms during homologous recombination (HR) at sequences containing NCC trinucleotide cores (provided the nucleobase is not a thymine).[20] Holliday junctions are interesting as possible targets for combination anticancer therapies that selectively inhibit homologous recombination and increase PARP1 (poly(ADP-ribose) polymerase) sensitivity. In addition Holliday junctions might have a role as alternative mechanisms for the extension of telomeres in that HR is involved in the process. The development of HJ-specific probes has therefore diagnostic potential in uncovering the role of Holliday junctions as an alternative mechanism for the lengthening of telomeres in immortalized cells lacking telomerases.[21]

I. 1.2.4. DNA triplexes

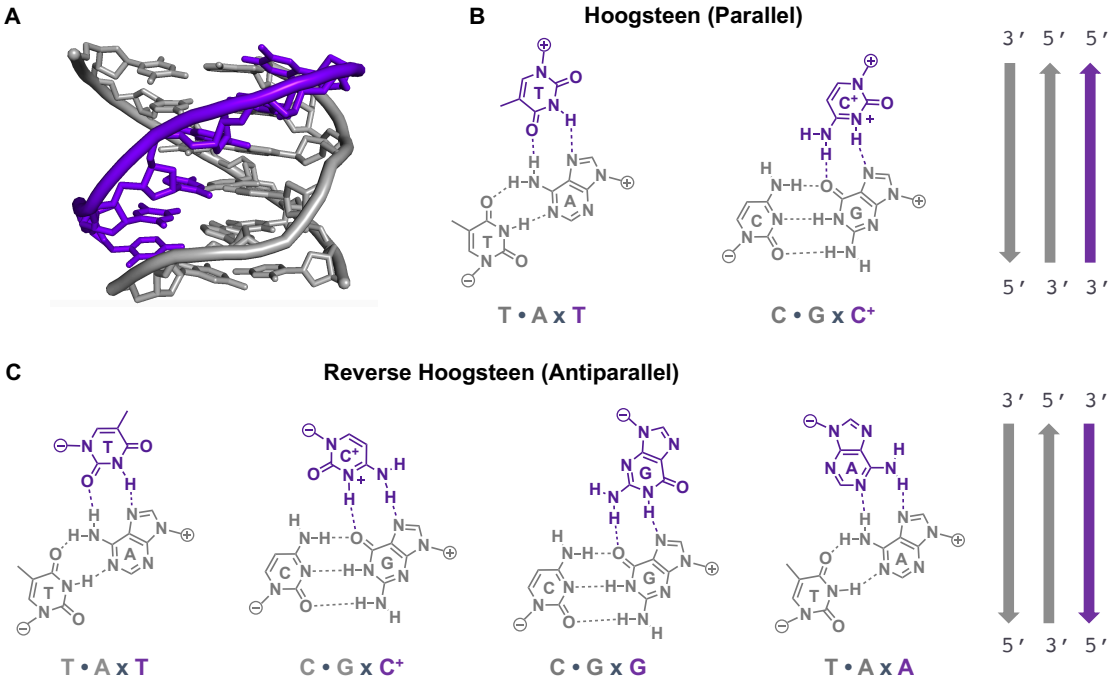

Figure I-3. A Triplex solution structure obtained by NMR studies (PDB: 1BWG); **B** Hoogsteen (parallel) base paired triplet schemes along with cartoon representation of the TFO strand orientation; **C** Reverse Hoogsteen (antiparallel) base triplet along with cartoon representation of the TFO strand orientation. (Hoogsteen and Watson-Crick bonding are represented by "x" and "•", respectively).

H-DNA is a triple helical arrangement where a third nucleic acid strand, called triplex forming oligonucleotide (TFO), recognises and binds a specific dsDNA sequence by hydrogen bond formation at the Hoogsteen face (major groove; Figure I-3A). TFO binding is ruled by a specific code where presence of a polypurinic target represents an essential requirement to form concerted hydrogen-bonds among the three nucleobases.[22] Only purines can establish an extra pair of hydrogen bonds required for recognition by the third nucleobase on the TFO. The nucleotide content of the TFO defines orientation to the purinic target and pyrimidine-rich sequences prefer parallel (Hoogsteen; Figure I-3B) binding, whereas polypurinic strands favour antiparallel base pairing (reverse Hoogsteen; Figure I-3C). Parallel triplexes are more stable than antiparallel due to the isomorphism of T•AT and C^+•GC triplets, which resent of minor backbone tension compared to the reverse Hoogsteen base pairs. However, parallel TFOs require acidic environments in order to ensure formation of stable hydrogen bonds by complete cytosine protonation in the C^+•GC triplet.[23] In past years, considerable indirect evidence of triplex formation and function *in vivo* was found by immunofluorescence using triplex-specific monoclonal antibodies. Further studies are however required to delineate if these structures arise *in vivo* from DNA

triplexes or from RNA recognition of dsDNA sequences (*cf.* ref. 24).[24] The high abundancy of triplex target sites upstream of eukaryotic genes suggests a possible role of these structures in transcriptional regulation and led to the design of various TFOs with modified backbones and stabilizing moieties aimed to induce triplex-mediated gene-silencing.[25–27] The unique base-base recognition properties of TFOs have also been extensively exploited in combination strategies to develop small molecule-oligonucleotide hybrids with directed mutagenesis and cleavage.[28]

I. 2. An introduction to non-covalent and covalent small molecule-DNA interaction

The amphipatic nature and polymorphism of nucleic acids make DNA an exceptional substrate for the development of small molecules and biomaterials capable of interacting and reacting at specific loci on the genomic code.[29] Interaction of small chemotypes with DNA usually falls within two classes: non-covalent and covalent (Figure I-4). Non-covalent interactions are reversible and can be further divided into external electrostatic binding, groove binding and intercalation (including threading intercalation).[30,31]

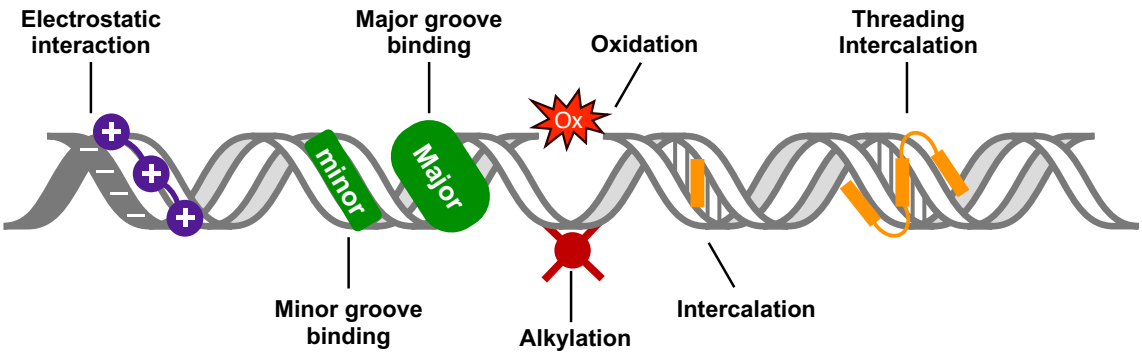

Figure I-4. Different modes of drug-DNA binding, from left to right: electrostatic interaction, minor and major groove binding, covalent modification (*i.e.* alkylation or oxidation), intercalation and threading intercalation.

The external electrostatic interaction is a non-covalent type of binding that occurs between small, positively charged molecules and the negative charge on the phosphate backbone of DNA. Cationic species such as metal ions, polyamines or charged opioid scaffolds diffuse along DNA interacting non-specifically with the phosphate groups on the minor groove.[32] The electrostatic interaction is followed by insignificant perturbation of the DNA structure and it usually represents a pre-association step in binding of metal complexes to nucleic acids.[33] Small molecules capable of electrostatic interaction have

found applications as DNA condensation agents or stabilizer of tertiary nucleic acid structures such as triple helices.[34,35]

Groove binders interact either with the minor (i.e. netropsin, polyamides) or major (i.e. majority of DNA-binding proteins, methyl green) groove of DNA mainly through hydrogen bonding. This interaction together with other van der Waals and specific electrostatic contacts provides sequence selective binding and a series of small molecules such as DAPI, Hoechst 33258, netropsin and distamycin show sequence bias to the minor groove of AT-rich regions of DNA.[30] Specificity by this chemotype arises from the gap for interaction provided in the minor groove by poly[d(A-T)$_2$] regions and is different from to GC-rich sequences where geometry is affected by the bulky amino groups of guanine residues.[36,37] On these bases the defined recognition of groove binders was used also in combination with various gene editors to direct nucleobase modification.[38,39]

Intercalation is a type of binding characteristic of planar aromatic molecules. These chemotypes insert in between adjacent base pairs interacting with the nucleobases through hydrophobic and π-π stacking interactions.[33,40,41] As a consequence, single intercalators are usually less sequence-selective than groove binders, but specific binding was recently shown for aromatic rings with particular modifications or multinuclear intercalative species.[31,42] The intercalative interaction causes elongation of the DNA structure which is followed by an increase in the helix pitch and helical unwinding.[43] DNA affinity and perturbation properties of intercalators have been widely used to develop various stabilizing agents for DNA tertiary structure [44], probes[21,45,46], mutagens and potential anticancer agents[31,47,48]. Threading intercalation is an alternative type of intercalation observed for flat aromatic systems flanked by bulky substituents. This type of binding has slower association and dissociation constants compared to canonical intercalators in that for binding to occur one of the bulky groups has to 'thread' through the stacked nucleobases.[49,50]

Covalent interactions are non-reversible and are often preceded by a non-covalent preassociation step. Here, binding involves a chemical reaction with DNA which generates a permanent modification on the genome altering its structure and function. Various covalent modifications can be introduced at the nucleic acid interface and they are usually divided in nucleotide alkylation, platination, 'metallation' and oxidation. Alkylating agents are among the oldest anticancer drugs and they include nitrogen and sulphur mustards, nitrosoureas, triazenes and ethyleneimines. These chemotypes react with the nucleophilic

moieties of biological materials—for example the N7- or N1- atoms on guanine or adenine nucleobases, respectively—causing the formation of covalent adducts that inhibit DNA replication and RNA transcription.[51,52] Similarly, metal complexes can undergo ligand substitution and form non-reversible metal-nucleobase adducts. Among these, cisplatin (and derivatives) are best known for interacting with DNA in this manner, but complexes of other metal ions such as Ni(II) and Ru(II) can also directly bind to DNA.[53,54] In particular, some Pt(IV) and Ru(II) chemotypes were designed to undergo DNA metallation upon photoactivation of the complex, introducing an interesting cytotoxic mechanism that aims to overcome the general toxicity usually associated to DNA alkylators.[55–58]

In the case of DNA oxidation, a covalent modification is caused by interaction of reactive oxygen species (ROS) or metal-oxo species. ROS production is usually catalysed by a redox active metal that activates an oxygen molecule through reduction. This process generates reactive intermediates such as superoxide ($O_2^{\bullet-}$) and hydrogen peroxide (H_2O_2) which can further react producing hydroxyl radicals ($^{\bullet}OH$) and other metal-oxo species.[59] Reactivity of ROS at the nucleobase moiety usually generates a variety of mutagenic modifications dependent on the nature of the radical and of the nucleobase. Conversely, interaction with the sugar ring usually results in hydrogen abstraction and in a cascade of radical reactions that end in strand excision.[60]

Overall, a wide variety of metal complexes has been designed and tested for their binding and reactivity at the DNA interface. The structural and DNA-recognition properties of the organic ligands have been combined with the wide range of coordination environments, accessible redox potentials, thermodynamic and kinetic properties of the metal centre.[61–64] This synergy facilitates inorganic compounds to target nucleic acids for applications in the fields of anticancer therapy, DNA footprinting probes, gene-editing and protein engineering.[63,65,66]

I. 3. Clinical metal complexes interacting with DNA

I. 3.1. Platinum derivatives

In the past years, a wide range of metal-based compounds has been developed for anticancer purposes, but cisplatin and its derivatives still represent the leading chemotherapeutics. Cisplatin (*cis*-Pt, [$Pt(NH_3)_2Cl_2$]) was first synthesized in 1844 by Michele Peyrone and its *cis*-geometry was assigned by Alfred Werner in 1863 distinguishing it from the *trans*-isomer.[67,68] However, it was only in 1965 when interaction

of the complex with DNA and its antiproliferative effects were discovered during electrode studies on *E. coli*.[5,69] The discovery of cell growth inhibition by cisplatin quickly led to its application in anticancer therapy and nowadays it is administered intravenously in saline buffer for the treatment of various forms of cancer (*i.e.* testicular, melanoma, bladder, non-small-cell-lung carcinomas, and in combination therapy, against ovarian cancer).[70,71] Once in the circulatory system, cisplatin is carried to cells where permeation into the cytosol occurs either through passive diffusion—due to its neutral charge—or active transport by copper transporter (hCTR) proteins.[72] The low chloride concentration within the cell (~3-20 mM) causes hydrolysis of the Cl^- substituents and activates the drug first to *cis*-$[Pt(NH_3)_2Cl(H_2O)]^+$ and then to the aqua complex *cis*-$[Pt(NH_3)_2(H_2O)_2]^{2+}$.[73] In this form, cisplatin is highly reactive towards various intracellular biomaterials and with respect to DNA it reacts with the nitrogen (N7) on purine bases yielding 1,2-intrastrand cross-links (47-50% 1,2-GG and 23-28 % 1,2-AG). Formation of the *cis*-Pt/DNA adducts causes a kink in the helical structure which inhibits polymerase binding, prevents DNA replication and transcription and ultimately leads to cell death.[74–76] Despite also transplatin (*trans*-Pt) coordinates DNA nucleobases, it lacks any chemotherapeutic potential further emphasizing the primary role of the 1,2-intrastrand cross-link geometry in the antitumoral action of cisplatin. Inspired by *cis*-Pt, an extensive range of platinum derivatives were designed on the *cis*-geometry but only carboplatin (1989) and oxaliplatin (2002) received worldwide FDA approval for clinical use (Figure I-5A) while nedaplatin, lobaplatin and heptaplatin (Figure I-5B) are currently employed only in Japan, China and South Korea, respectively.[64] Nonetheless, the therapeutic potency of *cis*-platin derivatives is overshadowed by intrinsic or acquired cancer cell resistance, bioaccumulation and dose-limiting toxicity (i.e. nausea, ototoxicity, neurotoxicity, myelosuppression and nephrotoxicity).[77]

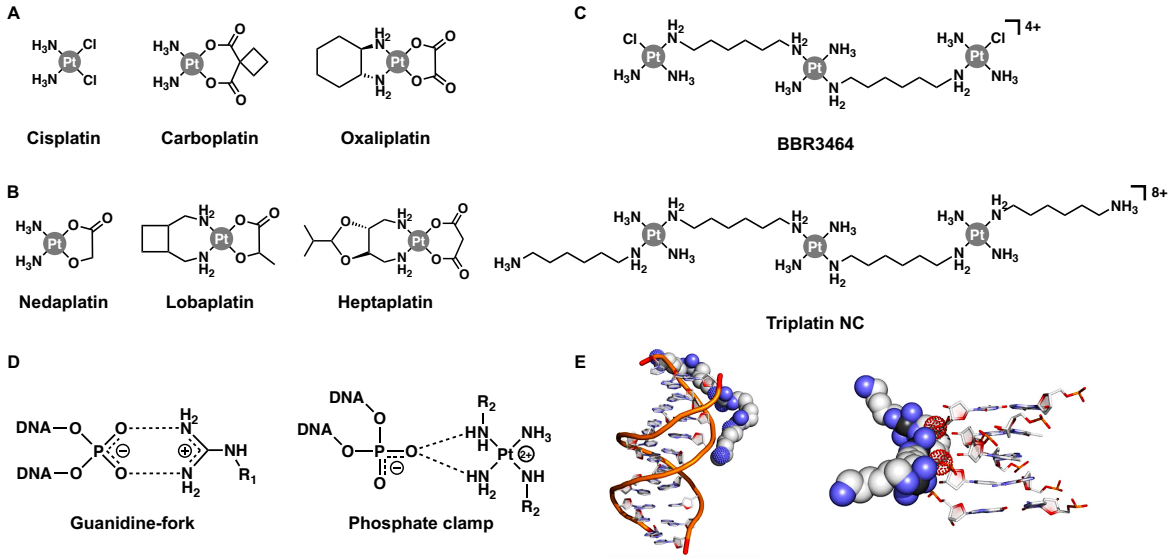

Figure I-5. Molecular structure of cisplatin derivatives **A** FDA approved (cisplatin, carboplatin, oxaliplatin) or **B** employed in single markets (nedaplatin, lobaplatin, heptaplatin); **C** Transplatin polynuclear derivatives with cytotoxic activity [{*trans*-$PtCl(NH_3)_2$}$_2$-μ-{*trans*-$Pt(NH_3)_2(NH_2(CH_2)_6NH_2)_2$}]$^{4+}$ (BBR3464), and [{*trans*-$Pt(NH_3)_2(NH_2(CH_2)_6NH_3)$}$_2$-μ-{*trans*-$Pt(NH_3)_2(NH_2(CH_2)_6NH_2)_2$}]$^{6+}$ (TriplatinNC); **D** Comparison in binding interaction of a guanidino-fork clamping by arginine residues (left) and the phosphate clamp of TriplatinNC chemotypes (right); E) Interaction modes of TriplatinNC with DNA: backbone tracking (left) and groove spanning (right).

With the aim of introducing molecular interactions not accessible to monomeric complexes, a series of polynuclear platinum complexes (PPCs) with structural similarities to *trans*-Pt was designed and synthesised in the Farrell group (Figure I-5C).[78] These platinum complexes are characterised by *di*- or tri-nuclear transplatin cores connected through alkanediamine linkers of various length. In contrast to the 1,3-intrastrand and 1,2-intrastrand cross-links caused by transplatin and cisplatin on neighbouring nucleobases, these chemotypes promote 1,2-, 1,3-, 1,4- and 1,6- interstrand crosslinks (IXLs) where platination sites on opposite strands are separated by up to five base pairs.[79,80] The interstrand adducts induce very small conformational distortions in the DNA structure with 10° bending of the helix axis and 9° unwinding of the duplex for the 1,3- and 1,4-crosslinks.[81] For these reasons, the antitumoral activity by polynuclear platinum complexes might arise from the obstruction that interstrand adduct formation imposes on DNA and RNA polymerase machineries. This suggests a pharmacological mechanism that differs from cisplatin where the kink in the double helix promotes Pt-adduct recognition by HMG protein protecting the 'alkylated' site from excision repair mechanisms.[78] Similar to *cis*-Pt, also here DNA-crosslinking proceeds via hydrolysis of the chloride groups and is preceded by pre-association with the phosphate backbone. In the case of BBR3464—only

trinuclear complex entering phase II clinical trials—the presence of a charged central moiety aids pre-association allowing the formation of directional isomers depending on the nature of the crosslink (1,2-IXL forms in the 3′-3′ direction; 1,6-IXL forms in the 5′-5′ direction while 1,4-IXL show no preferentiality).[82]

In order to examine the pre-association mechanism further, a series of non-covalent high-affinity Pt-complexes was prepared by substitution of chlorides with NH_3 or 'dangling amines'. The presence of substitution-inert moieties introduces a distinctive type of 'non-covalent' DNA-binding compared to the covalent interaction by canonical *cis*- and *trans*-Pt derivatives.[79] Here, the protonated amine groups bind to the oxygens of the phosphate backbone (OP) establishing N-O-N motifs which resembles, to a certain extent, the OP-clamping of guanidine groups on arginine residues (Figure I-5D).[83,84] This type of binding induces either groove spanning or backbone tracking (Figure I-5E) depending on the presence of poly[d(A-T)$_2$] or poly[d(G-C)$_2$] sequences, respectively. Both types of interaction are followed by a perturbation of the DNA structure in that: *i*) a greater axial bend and axial path length shortening ratio are induced, *ii*) DNA is slightly bent in the major groove and *iii*) the minor groove width profile is modestly impacted.[85] Despite the non-covalent nature of binding, the distortion induced in the double helix resembles the structural perturbation caused by covalent bifunctional 1,2-intrastrand adducts with cisplatin. In addition, among these chemotypes TriplatinNC showed antitumoral activity on various cell lines within the low micromolar range further emphasizing that covalent interaction is not a prerequisite for the cytotoxicity by the complexes.[83,85]

I. 3.2. Clinically validated non-platinum chemotherapeutics

Systematic toxicity of cisplatin derivatives sparked new research to discover complexes with different pharmacokinetic and pharmacodynamic profiles. Among these, ruthenium complexes attracted considerable interest in that their therapeutic activity (including anticancer activity) was first recognised by Dwyer in 1950 but largely forgotten until the discovery of cisplatin.[86,87] In the last three decades however a wide range of ruthenium complexes have been synthesized and investigated as potential chemotherapeutics with some showing activity against cisplatin-resistant tumours and with three chemotypes entering clinical trials.[88–90] NAMI-A—a Ru(III) coordination compound of formula [ImH][*trans*-$RuCl_4$(DMSO-S)(Im)] (where Im = imidazole)—was the first ruthenium drug undergoing human testing. Phase I trials showed several side effects including—but not

limited to—mild hematologic toxicity, quite disabling nausea, vomiting, and diarrhoea. Due to these results, new Phase I/II clinical trials were performed in combination therapy with gemcitabine, a nucleoside derivative with chemotherapeutic efficacy on non-small cell lung cancer. However, lack of efficacy results and the toxicity profile caused suspension of NAMI-A from clinical trials.[91] KP1019/KP1339—the $IndH^+$ and Na^+ salts, respectively, of an octahedral Ru(III) species with general formula [*trans*-$RuCl_4(Ind)_2]^-$ (where Ind = indazole)—was the second Ru(III) complex entering Phase I trials. This drug showed promising results including disease stabilization for 8-10 weeks on patients with solid tumours and only mild toxicities.[92] Both NAMI-A and KP1019 mechanism of action is supposed to start from activation by reduction to the Ru(II) derivative *in vivo*. While DNA has been proposed as one of the biological targets for KP1019, the antimetastatic activity of NAMI-A is however associated to combined effects on angiogenesis control and antiinvasive properties towards tumour cells and blood vessels.[89,93]

Recently, the photochemical properties of some Ru(II) complexes—and also Pt(IV)[56,70], Rh(III)[94], Os(II)[95] and Ir(III)[96] chemotypes—has increased interest in their application in photodynamic therapy (PDT), photochemotherapy (PCT) and photoactivated chemotherapy (PACT).[54,90,97,98] In these cases, cytotoxicity is activated upon irradiation of the soft tissue with a penetrating red light. This pharmacodynamic profile has particular relevance because it allows restriction of the therapeutic effect to the diseased tissue preventing onset of side toxicities. One such example is the racemic mixture *rac*-[$Ru(dmb)_2$(IP-3T)]Cl_2 (TLD1433, where IP-3T = imidazo[4,5-f][1,10]-phenanthroline (IP) ligand appended to an α-terthienyl (3T) as the organic chromophore and dmb = 4,4′-dimethyl-2,2′-bipyridine), which was the first Ru(II)-based photosensitizer to enter human clinical trials (ClinicalTrials.gov, identifier NCT03053635). This complex has long-lived triplet ^{3}IL and ^{3}ILCT states which allow $^1O_2$ sensitization and electron-transfer, respectively, producing extremely potent photocytotoxic effects. In addition, the bright luminescence given by the ^{3}MLCT states provides this photosensitizer with theragnostic capacity.[90] DNA damage studies by this complex highlighted that upon irradiation single strand cleavage is triggered at 500 nM loading with onset of double strand cleavage at higher concentrations.[99] Interestingly, damage was enhanced in the presence of glutathione (GSH), a reductant known to play an essential role in platinum chemotherapeutic detoxification.[100] Promoted double strand cleavage by TLD1433 in the

presence of GSH and other important antioxidants gives prominence to a unique cytotoxic mechanism which can overcome the limitations by usual platinum therapeutics.

I. 3.3. Bleomycin

Another clinically established type of metallo-chemotherapeutic is represented by bleomycins—a family of anticancer antibiotics elaborated by *Streptomyces Verticillus*—where cytotoxicity is induced through a redox active metal capable of promoting oxidative DNA damage.[101] These molecules are characterized by a common glycopeptide core, but they differ in the pendant sugar and positively charged tail modifications (Figure I-6). Bleomycins bind DNA sequences specifically by interaction between the N3- and N4-atoms of their pyrimidine moiety with the N3- and N2- atoms of guanine nucleobases.[102,103] DNA binding is aided by cooperative interaction of the bithiazole tail through nucleobase intercalation or minor groove recognition. Finally, the pendant positively charged tail interact electrostatically with DNA enhancing the overall binding affinity.[104,105,102] Despite the sugar modification not contributing in DNA binding and recognition, it was proposed to affect solubility and cell permeability.[106,107]

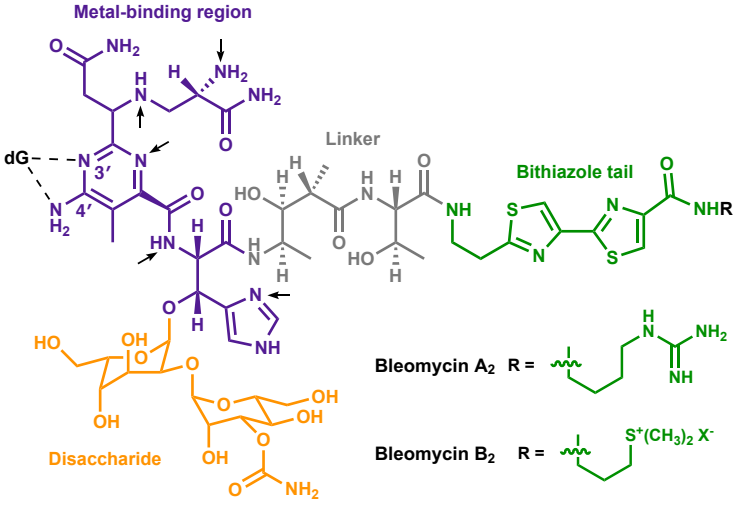

Figure I-6. Molecular structure of bleomycin. The metal binding region (purple) has five nitrogen atoms (indicated by arrows) available to coordinate a metal ion. The linker region (grey) and bithiazole tail (green) aids DNA recognition and binding while the disaccharide moiety (orange) is supposed to enhance solubility and cellular uptake.

DNA cleavage by bleomycin is promoted by the metal-binding domain which comprises a β-aminoalanine-pyrimidine-β-hydroxyhistidine moiety. Here a redox active metal ion (primarily Fe^{2+}, but also Cu^{2+}, Mn^{2+} or Co^{3+}) is coordinated by five nitrogen ions leaving the sixth coordination site open for interaction with an oxygen molecule.[108] In the presence of reductant, the metal bound domain promotes production of reactive oxygen

species (ROS) and abstraction of the C4′ hydrogen from the deoxyribose ring of DNA. Depending on O_2 availability the 4′-radical intermediate further reacts with H_2O or O_2 leading to a cascade of reactions that result either in formation of 4′-oxidized abasic site or strand excision, respectively.[109–111] Nowadays, bleomycins are used clinically as a mixture of different congeners (60% bleomycin A_2 and 30% bleomycin B_2, denoted as Blenoxane, Figure I-6) or in combination with other therapeutics for the treatment of several types of tumors, notably squamous cell carcinomas and malignant lymphomas. Their therapeutic efficacy is associated with low myelosuppression and immunosuppression levels but is limited by dose-dependent pneumonitis.[101]

I. 4. Artificial metallo-nucleases

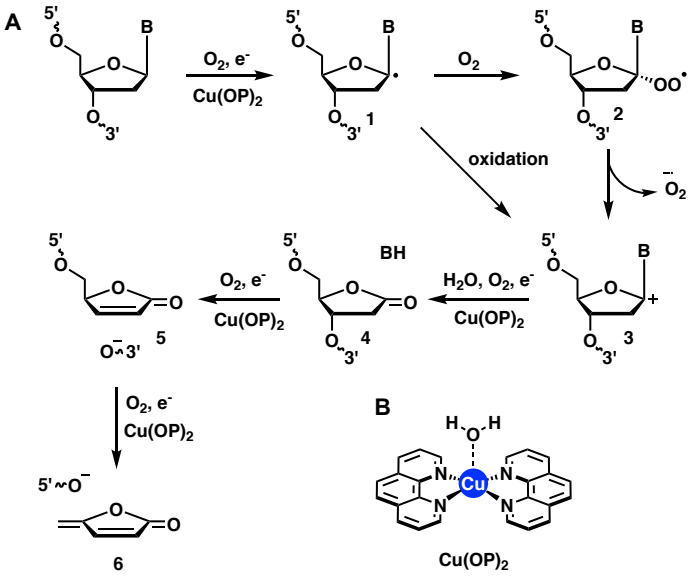

Figure I-7. A Radical oxidation mechanism by CuPhen resulting in direct strand cleavage; **B** Molecular structure of the $[Cu(1,10\text{-phenantroline})_2(H_2O)]^{2+}$.

I. 4.1. Cleavage mechanism by $[Cu(1,10\text{-phenantroline})_2]^{2+}$

In parallel to natural compounds such as bleomycins, other transition metal complexes have been developed and studied for their DNA binding properties and artificial metallo nuclease (AMNs) activity. Complexes of various redox active metals (such as Cu, Fe, Mn, Ni, Co, Ru and Rh) can promote oxidative DNA damage at nucleobase and/or deoxyribose moiety and among these, Cu-AMNs have been extensively investigated due to their accessible redox states, variety of coordination geometries and endogenous nature of the metal.[63,112,113] DNA binding and oxidation by AMN has therefore been exploited for the development of potential antibacterial, antifungal and anticancer drugs, for DNA footprinting, gene silencing and protein engineering. $[Cu(1,10\text{-phenantroline})_2]^{2+}$ (CuPhen,

Figure I-7B) is the most studied AMN representative both for its cleavage mechanism and biological applications.[114–117] In the presence of exogenous reductant and oxidant CuPhen induces direct single or double strand cleavage along the minor groove of poly[d(A-T)$_2$] sequences.[118] In the reduced form CuPhen semi-intercalates the nucleobases of DNA promoting production of ROS which cause abstraction primarily of the C1′ hydrogen (C5′ and C4′ at a lower extent) from the deoxyribose ring.[119,120] Seminal work by Greenberg *et al*. on the oxidative mechanism by CuPhen identified that after hydrogen abstraction direct strand breakage proceeds through formation of a peroxyl radical intermediate.[115,121] Here, expulsion of superoxide generates an oxidized C1′ cation intermediate that in presence of other two CuPhen undergoes β-elimination and conversion from 3′-furanone to the free 5-methylene furanone (Figure I-7A). The interaction of CuPhen with deoxyguanosine was further studied by our group and shown to generate 8-oxo-7,8-dihydro-2′-deoxyguanosine (8-oxo-dG) lesions within superhelical plasmid DNA using an enzyme-linked immunosorbent assay (ELISA).[122,123]

I. 4.2. CuPhen-modified chemotypes

Inspired by CuPhen, various structural modifications were introduced in the complex scaffold aimed to improve its stability, DNA recognition and reactivity (Figure I-8).[123,124] Carboxylate ligands were introduced by our group affording a series of mononuclear and bridged dinuclear complexes with higher anticancer activities (low μM range) than cisplatin against various cell lines (MCF-7, DU145, SK-OV-3, HT29). Interestingly copper(II) bis-phen complexes with pendant phthalate showed nuclease activity also in absence of exogenous oxidant or reductant and were the first 'self-activating' complexes reported in the literature (Figure I-8A).[59,125] A dinuclear complex of this series—Cu-Oda, [{Cu(Phen)$_2$}$_2$(μ-Oda)]$^{2+}$—showed discrimination of AT/AT from TA/TA steps of dodecamer palindromic sequences through induction of B- to Z-like DNA change or by intercalative binding.[42] In order to introduce stronger DNA interactions and sequence recognition, one phenanthroline ligand was substituted with phenazine intercalators of extended aromaticity to yield a class of heteroleptic complexes with general formula Cu-Phen-*N,N*′ (where *N,N*′ = dipyridoquinoxaline, DPQ; dipyridophenazine, DPPZ and benzo[i]dipyridophenazine, DPPN; Figure I-8B). These complexes showed binding constants for calf thymus DNA (ctDNA) within ~10^7 M (bp)$^{-1}$ and are currently the best binders among the CuPhen derivatives reported in the literature.[123,124]

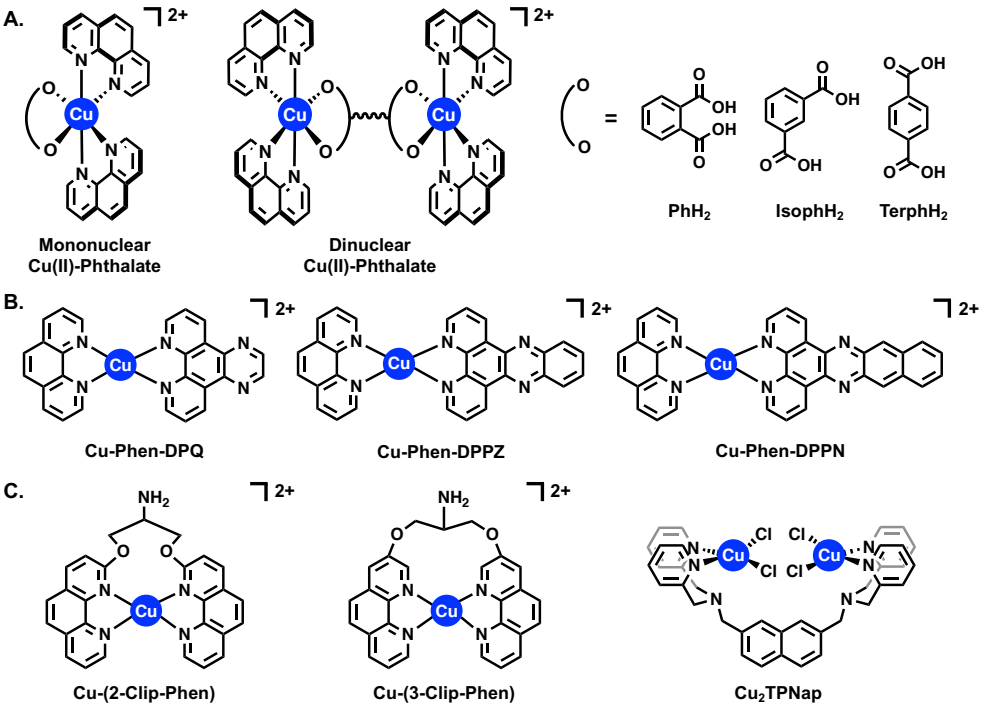

Figure I-8. Molecular structures of **A** mononuclear and dinuclear 'self-activating' Cu(II) phthalate complexes; **B** mononuclear heteroleptic Cu-Phen-Phenazine complexes; **C** 'stabilized' Cu-Clip-Phen and Cu-polypyridyl derivatives.

I. 4.3. Stabilized artificial metallo-nucleases

Despite their prominent binding profile, Cu(II) bis-phenanthrene systems tend to form new species in solution and the second coordinated ligand dissociates yielding the inactive monocoordinated complex.[126,127] In order to tackle this stability issue various strategies have been employed and covalent bridging linkers were used to tether two phenanthrene ligands together or polypyridyl scaffolds were coordinated to form 'metal-caged' complexes. In the first strategy serinol bridges were introduced between either the C2 or C3 (2-Clip-Phen and 3-Clip-Phen, respectively) carbon of Phen in order to favor the 2:1 Phen:Cu ratio (Figure I-8C).[128] Here, position and nature of the linker significantly influenced the activity of the compounds and 3-Clip-Phen was 60-fold more efficient as AMN than CuPhen whereas 2-Clip-Phen was only twice more effective in DNA cleavage. The high activity of 3-Clip-Phen was attributed by DFT calculations to low structural rearrangement energy barriers between Cu(II)/Cu(I) oxidation states which allows the complex to retain a certain planarity ideal for intercalation and minor groove binding.[129] In the second approach, polypyridyl ligands have been extensively used to afford stable complexes where the metal is 'caged' within an environment that mimics the histidine-rich active site of copper proteins. Hence, these complexes have been used to gain an insight in the mechanism of oxygen binding and activation of several Cu-enzymes such as

hemocyanin, tyrosinase and multicopper oxidase.[130–132] More recently however these chemotypes were studied also for their capability in promoting oxidation of bio-organic substrates and for their application as artificial metallo-nucleases.[133] DNA recognition and oxygen activation are strongly dependent on complex nuclearity and the coordination environment around copper.[134] While mononuclear Cu-AMNs are considered promiscuous in their DNA binding and cleavage, *di*- and tri-nuclear complexes were found to recognize distinct structural features of nucleic acids. Two Cu-polypyridyl compounds, $[Cu_2(D^1)(H_2O)_2]^{4+}$ and $[Cu_3(TP1)(H_2O)_3(NO_3)_2]^{4+}$ (where D^1 = dinucleating ligand with two tris-(2-pyridylmethyl)-amine units covalently linked in their 5-pyridyl positions by a -CH_2CH_2- bridge and TP1 = 2,2′,2″-*tris*(*di*-picolylamino)triethylamine) bind and cleave junctions between single and double stranded DNA in a sequence specific fashion. Here site-specific cleavage is afforded by the coordination of at least one copper to G-rich strands.[135,136] Guanine has in fact the highest coordination affinity to transition metal and is the most easily oxidized nucleobase followed by adenine, thymine, and cytosine.[136,137] The same group also showed that modification of the linker spacer between copper cores can switch oxidation selectivity from the usually targeted deoxyribose ring to guanine nucleobases of frayed DNA sequences.[138] Similarly, [Cu_2(*tetra*-(2-pyridyl)-NMe-naphthalene)Cl_4] (Cu_2TPNap) was shown to target the major groove of dsDNA and to induce single strand breaks in the absence of added reductant.[139] The coordination environment and nuclearity are known to control also the type of Cu_nO_2 coordination geometry, hence the oxygen activation mechanism and type of radical produced which ultimately results in a wide variety of DNA oxidation products.[140] In this context Cu-AMNs provide not only an alternative pharmacological mechanism to state-of-the-art chemotherapeutics but are also invaluable tools to probe DNA structural conformations, protein binding and to chemically modify genetic structure and information.

I. 5. DNA footprinting

Developed in 1978 by Galas and Schmitz, DNA footprinting is a technique used for studying sequence selectivity of DNA binding compounds, and it exploits the protection from cleavage provided by a ligand bound to its genomic site. It is based on a co-joining of the Maxam-Gilbert DNA sequencing method with the DNAse-protected fragment isolation technique.[141] Footprinting templates are radiolabelled strands of 50-200 base pairs that are cleaved both in the presence and absence of a binding agent. The region bound to the ligand is protected from cleavage and creates a gap or "footprint" in the ladder of digested products when these are resolved through polyacrylamide gel electrophoresis (PAGE). The nuclease agent should therefore cleave DNA in an aspecific fashion in order to provide an even distribution of cleaved fragments. DNase I is the most common nuclease used in footprinting experiments but it generates an erratic ladder of cleavage products, as its efficiency is affected by global and local DNA structure.[142,143] In this context mononuclear chemical nucleases can provide an exceptional alternative tool to enzymatic nucleases due to their aspecific cleavage. Various complexes such as methidiumpropyl-EDTA Fe(II) (MPE), uranyl photocleavers, and copper phenanthroline have therefore been employed in DNA footprinting.[144] Using these tools, footprinting allowed to elucidation of the sequence-specific binding of various small molecules, proteins and triplex-forming oligonucleotides.

I. 6. Protein Engineering

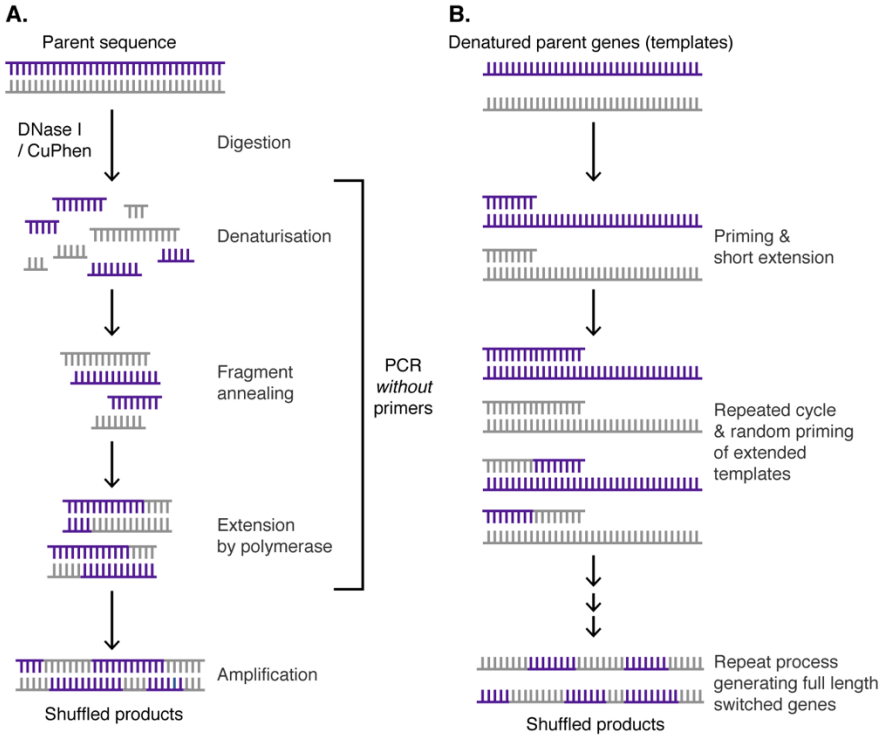

Figure I-9. A DNA shuffling through primerless PCR; **B** staggered extension process (StEP).

In parallel to anticancer and footprinting applications, AMNs were employed within the field of protein engineering to generate libraries of highly diverse mutant proteins. For this purpose, the cleavage action of a nuclease (*i.e.* DNase I) is usually used to generate various 5′-phosphorylated and 3′-hydroxylated fragments that can be further manipulated and shuffled into new gene variants.[145] This process is known as DNA shuffling and was first introduced in 1994 by Stemmer (Figure I-9A).[146] This technique has major commercial importance for the production of high performance proteins in areas such as affinity antibody development and it involves digestion of a parent gene by DNase I followed by reannealing of the generated DNA fragments in the presence of a primerless DNA polymerase. The shuffled genes are then integrated within a larger plasmid and transformed into *E. coli* bacteria for translation in the corresponding mutant antibody proteins. Recombinant DNA libraries are then sequenced and antigen-binding affinity of antibody variants accurately identified using technology such as surface plasmon resonance. Alternatively, engineered protein libraries can be obtained through the staggered extension process (StEP). This method—first developed in 1998 by Arnold who shared the Nobel prize in 2018 with Smith and Winter—prepares full-length recombinant genes by primers and repeated cycles of denaturation, fast annealing and polymerase catalyzed extension (Figure I-9B).[147] This experimental design allows the growing fragments to anneal to a

different template within each cycle and to acquire sequence information of different parental genes.

Recently, our group employed Cu-Phen cleavage and DNA shuffling to yield a recombinant library of antibodies for prostate-specific antigen (PSA).[148] Despite the oxidative cleavage effects by CuPhen, a fraction of fragments suitable for PCR was generated through direct strand breakage where promoted β-elimination yields intact 5′-adducts through C1′ abstraction. In addition, the Taq DNA polymerase I used in the experiment lacked a functional 3′ → 5′ exonuclease, but its functioning N-terminal 5′ → 3′ exonuclease suggested possible amplification through the nick translation process. DNA shuffling of the fragments restricted using CuPhen and DNase I produced 60 clones with affinity to PSA and five of the top ten best-performing clones were derived from the CuPhen digested library. In addition the top-performing antibodies showed high levels of modification suggesting CuPhen allows accessibility to more gene mutation than DNase I. Results highlighted in this work showed the potential that Cu-AMNs can have within the field of protein engineering and their mutagenesis can be directed by conjugating AMNs to selective organic-based DNA binding agents.[66]

I. 7. Gene editing

Since double strand breaks into genomic DNA are toxic to cells biological systems possess various mechanisms to repair lesions, namely: the non-homologous end joining (NHEJ) and homologous directed repair (HDR). In the NHEJ process two cleaved ends of the damaged duplex are resealed together by a ligase enzyme without requirement for templates and NHEJ can often result in introduction of insertion or deletions that can alter gene function. Conversely homologous directed repair is less error-prone since repair is based on the annealing of the damaged sequence to a matching template.[149] In HDR the 3′-end of one strand recognizes and invades a specific dsDNA sequence forming a Holliday junction structure. Here the invading strand operates as a primer initiating DNA synthesis and damage repair. Both processes have therefore interesting applications in genome engineering in that single base modifications, but also exogenous DNA sequences, can be introduced in the genetic code resulting into gene disruption, mutation or in creation of specific genome-edits.[150] Hence, research has focused on developing gene-editing tools where cleavage by promiscuous nuclease machineries is directed by sequence-specific DNA binding domain (Figure I-10).

I. 7.1. Enzymatic nucleases

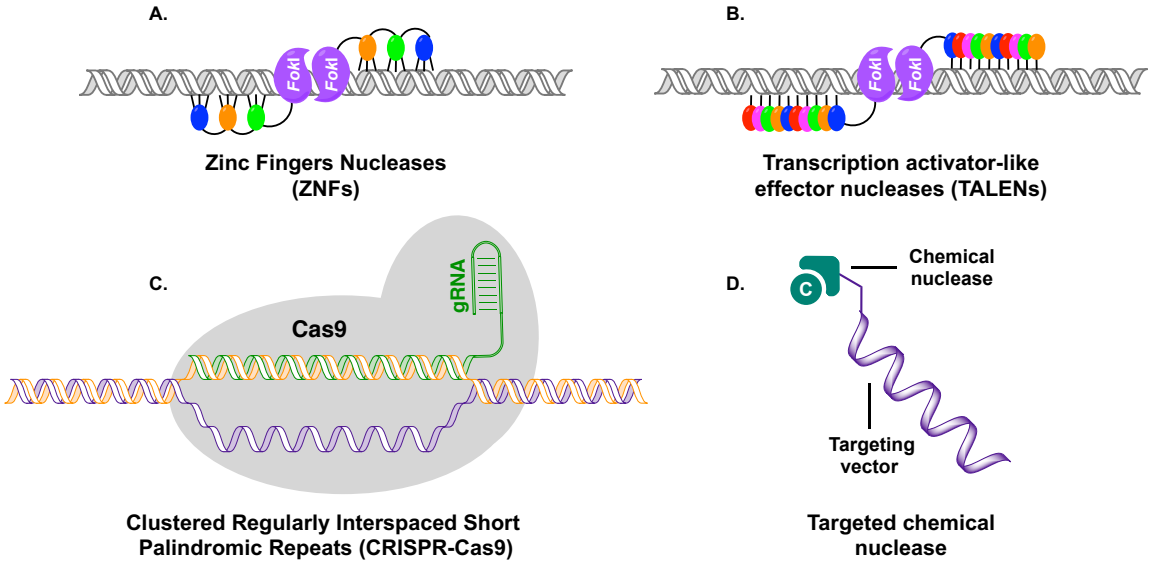

Figure I-10. Cartoon representation of sequence-targeted enzymatic (Zinc finger nuclease, ZNF (**A**); Transcription activator-like effector nuclease, TALEN (**B**); Clustered regularly interspaced short palindromic repeat, CRISPR-Cas9 (**C**)) and chemical nucleases (**D**).

I. 7.1.1. ZFNs

Zinc finger nucleases (ZFNs) are the oldest gene-editing technology and they consist of the cleavage domain of *Fok*I—a Type IIS restriction endonuclease—and a polypeptide chain that recognises specific DNA sequences (Figure I-10 A). The polypeptide is an ensemble of zinc finger domains, also known as Cys_2His_2 due to the coordination environment of zinc which aids structure folding and stabilization. Each finger consists of ~30 amino acids folded into a α-helix and a β-sheet. Sequence specific binding to DNA is provided by the interaction between aminoacidic side chains on the α-helix domain (mainly -1, 3 and 6 from the start of the α-helix) and the nucleobases in the major groove.[151] Each zinc finger can bind 3 bp and recognition of at least 9 bp is required for stable hybridisation to DNA. ZF domains have been developed with specificity to nearly all the 64 possible nucleotide triplets and linked together to assemble combinations capable of targeting a broad range of DNA sequences.[152] Cleavage by ZFN is promoted by the non-specific nuclease domain of *Fok*I after dimerization of two ZFN hybrids on opposite strands. The cleavage moiety is linked to the C terminus of the homing agent and both linker length and distance between the two cleavage agents are important in ruling the effectiveness of the gene-editor. In cells it was found that the best performing spacer length had to be of 6 bp for ZFNs with short linkers (n = 4).[153,154] The complex design of the zinc finger homing agent limits however

application of ZFN in genome engineering and opened the field to simpler systems such as TALENs and CRISPRs.

I. 7.1.2. TALENs

Transcription activator-like effector nucleases (TALENs) are a class of gene-editing tools introduced as an advancement to zinc finger nucleases. Despite both editors sharing the same cleavage domain (*Fok*I), in TALENs specific recognition is provided by a DNA binding protein: the transcription activator-like effector (TALE; Figure I-10B). TALEs are a class of proteins secreted by plant-pathogenic bacteria (*Xanthomonas*) to bind and activate genes that aid infection.[155] These proteins are constituted by repeats of 33-35 amino acids mostly conserved among the modules apart from the 12th and 13th residues—known as repeat variable *di*-residues (RVD)—which control base pair recognition. In the RVD, amino acid 13 binds to the nucleobase while residue 12 side chain folds back to promote stabilizing interactions with the other residues in the module.[156,157] TALE single base interaction provides a more flexible design than triplet recognition by ZF domains and TALE repeat combinations have been reported to virtually recognize any DNA sequence. Canonical TALENs share the same *Fok*I cleavage domain common in ZFNs (hence requiring dimerization) but several variants with nucleases, transcriptional activators and recombinases were developed in the literature.[158–160] In contrast to ZFNs, TALENs require some additional protein on both ends of the DNA binding domain. Two modules with similar structure but different sequences to the TALE repeats are located upstream and are responsible for the contacts with a T nucleobase (the preferential base at the start of the binding site); while additional residues separate the C termini of TALE from the FokI domain probably to aid folding and stability.[158,161]

I. 7.1.3. CRISPR-Cas

CRISPR-Cas systems are currently the key players within gene engineering due to their simple design, generation and modification compared to ZFNs and TALENs. CRISPR-Cas originates from an adaptive immune system common in prokaryotes such as bacteria and archaea.[162] These organisms integrate deleterious exogenous DNA (*e.g.* from hostile viruses and plasmids) within their genome in between copies of repeated sequences called clustered regularly interspaced short palindromic repeats (CRISPRs). The process generates a cellular memory of the past invader and if the same exogenous DNA penetrates the cell, the prokaryote will recognize it and degrade it.[163] In detail, the cellular immune

response starts with transcription of the CRISPR site to form pre-crRNA and with generation of a trans-activating CRISPR-RNA (tracrRNA) from a genomic locus upstream the CRISPR gene. Part of pre-crRNA and its complementary tracrRNA site anneal to form a dsRNA which elicit cleavage by RNAse III. This process yields the crRNA:tracrRNA complex which is then bound by a Cas enzyme to generate the active gene-editor. tracrRNA aids hybridisation of the RNA complex to the nuclease machinery while crRNA acts as a homing vector directing cleavage of the protein to the target sequence (Figure I-10C).[164] In addition to crRNA, also the Cas enzyme has intrinsic sequence selectivity provided by a DNA-binding domain that recognizes a specific nucleobase combination called proto-spacer adjacent motif (PAM). Various Cas nucleases with different PAM bias were found in prokaryotes and the most commonly used *Streptococcus pyogenes* SpCas9 binds 5′-NGG-3′ sequences through specific interaction between two arginine residues and the guanine nucleobases on the noncomplementary strand. When the CRISPR-Cas9 complex is formed the enzyme skims the genome searching for its PAM site. Here arginine-guanine interaction unwinds DNA and aids identification of complementarity between the flanking DNA and sgRNA.[165] At the targeted loci, the cooperative effect of HNH and RuvC-like domains of Cas9 promotes blunt, hydrolytic cleavage of the complementary and non-complementary strands, respectively.[166]

Uncovering this adaptive immune mechanism quickly led to applications of CRISPR-Cas in gene-editing and ever since these systems have been engineered in order to improve their design, increase their binding specificity or widen their applications.[150,167] Jinek *et al*. joined the tracrRNA and crRNA to form a single guide RNA (sgRNA) that efficiently directed Cas9 cleavage.[162] Similarly Brown *et al*. used azide-alkyne chemical ligation to join a fixed tracrRNA strand to the variable crRNA sequence as an efficient tool for the high-throughput generation of wide sgRNA libraries.[168] In parallel to the homing agent, the enzyme was modified and its activity optimized for different applications. Cas enzymes from other prokaryotes (*i.e.* Cas9 variants, Cpf1, Cas13) have been employed as editors due to their different sizes, PAM requirements and substrate preferences. The smaller sizes of NmCas9 (*Neisseria meningitides*), SaCas9 (*Staphylococcus aureus*), CjCas9 (*Campylobacter jejuni*) allow the therapeutic delivery challenge posed by packaging the large SpCas9 variant within Adeno associated viruses (AAV) to be overcome. As a trade-off to their reduced size, these nucleases however require longer and complex PAM sequences limiting the flexibility of their application.[169] Another class of

Cas enzymes—the Cpf1 variants—cleave DNA in a different fashion to Cas9 at the 3′ site of 5′-TTN-3′ PAM yielding staggered rather than blunt ends.[170] The generated 5′-overhangs are of particular interest because they can be exploited for introducing exogenous DNA fragments through complementation and ligation of the "sticky" ends.

Point mutations in Cas9 enzymes can be used to deactivate either one or both of the cleaving domains resulting in nickase or catalytically inactive variants.[171] Cas systems that can induce only single strand breaks (SSB) are particularly interesting as a solution to off-target effects often linked to gene editing with CRISPR-Cas technologies. In this case dimerization of two hybrids with sequence specificity on opposite strands is required for cleavage to occur.[172] On the other hand, catalytically inactive CRISPR-Cas can be employed to recognize, bind and deactivate specific genes of interest. Alternatively, the carboxy or amino terminus of 'dead' Cas (dCas) can be fused to fluorescent probes, transcription activators or epigenetic modifiers.[164] The latter case has particular therapeutic relevance because most of known human pathogenic mutations are represented by point modification—also known as single-nucleotide polymorphism (SNPs). Base editors crossbred to CRISPR-Cas systems can induce pinpointed epigenetic conversions of CG bp to AT bp (and *vicerversa*) without requirement for deleterious strand breaks, hence reversing SNPs and restoring gene function.[171,173–175]

I. 7.2. Targeted chemical nucleases

For many years scientists have tried to develop chimeric systems that act as biomimetics of enzymatic nucleases exploiting the cooperation of a sequence-specific vector with a small molecule that promotes reactivity and cleavage at the DNA interface (Figure I-10D). Strand scission is promoted either through hydrolysis of the phosphate backbone or by oxidative damage of the deoxyribose moiety by ROS production.[112,176] The type of DNA cleavage mechanism adopted by metal complexes is highly dependent on the nature of the metal centre and on its coordination environment. Hydrolytic strand scissions are particularly relevant for the introduction of genomic modifications as they yield 3′-OH and 5′-PO_4 products that are biocompatible for enzymatic manipulation. Conversely, DNA oxidation can provide a wide range of deoxyribose and nucleobase modifications—dependent on the reaction site and nature of the radical—which can result either in epigenetic modifications, DNA damage or gene knockdown. This type of cleavage has been extensively employed to prepare DNA structural probes, footprinting agents as well as gene-silencers.[176,177]

Table I-1. Examples of hybrid chemical editors where reactivity is targeted by DNA-specific binders, oligonucleotides or structural recognition (Ox = oxidative; Mut = mutation; Hyd = hydrolitic; Cov = covalent; Non-Cov = non-covalent; ss = single strand; ds = double strand).

Group	Hybrid	Cleavage	Approach	Substrate	Reference
AMN-DNA binder hybrids					
Dervan	Fe(II)-EDTA-EtBr	Ox	Cov	dsDNA	*J. Am. Chem. Soc.* 1982, *104*, 313.[178]
Dervan	Fe(II)-EDTA-Distamycin	Ox	Cov	dsDNA	*J. Am. Chem. Soc.* 1982, *104*, 6861.[179]
Meunier	3-Clip-Phen-Distamycin	Ox	Cov	dsDNA	*Nucleic Acid Res.* 2000, *28*, 4856.[39]
AMN-oligonucleotide (ON) hybrids					
Dervan	Fe(II)-EDTA-ON	Ox	Cov	ssDNA	*Proc. Natl. Acad. Sci. U.S.A.* 1985, *82*, 968.[180]
Orgel	Fe(II)-EDTA-ON	Ox	Cov	ssDNA	*Proc. Natl. Acad. Sci. U.S.A.* 1985, *82*, 963.[181]
Sigman	Cu(II)-Phen-ON	Ox	Cov	ssDNA	*Proc. Natl. Acad. Sci. U.S.A.* 1986, *83*, 7147.[182]
Dervan	Fe(II)-EDTA-ON	Ox	Cov	dsDNA	*Science* 1987, *283*, 645.[183]
Hélène	Cu(II)-Phen-ON	Ox	Cov	dsDNA	*Proc. Natl. Acad. Sci. U.S.A.* 1989, *86*, 9702.[184]
Glazer	Psoralen-ON	Mut	Cov	dsDNA	*Proc. Natl. Acad. Sci. U.S.A.* 1993, *90*, 7879.[185]
Kodama	Ce(IV)-iminodiacetate-ON	Hyd	Cov	ssDNA	*Supramol. Chem.* 1994, *4*, 31.[186]
Krämer	Zr(IV)-tris(hydroxymethyl)-aminomethane-ON	Hyd	Cov	ssDNA	*Inorg. Chem.* 2003, *42*, 8618.[187]
Ganesh	Cu(II)/Co(III)- metallodesferal-ON	Ox	Cov	ss/dsDNA	*Biochim. Biophys. Acta* 1994, *1201*, 454.[188]
Meunier	Mn(III)-porphyrin-ON	Ox	Cov	dsDNA	*Nucleic Acids Res.* 1995, 23, 3894.[189]
Zarytova	Bleomycin-ON	Ox	Cov	ss/dsDNA	*Russ. Chem. Rev.* 1996, *65*, 355.[190]
Structure-specific AMNs					
Komiyama	Ce(IV)-EDTA	Hyd	Non-Cov	dsDNA	Chem. Soc. Rev 2011, 40, 5657.[191]
Hélène	Fe(II)-EDTA-BQQ	Ox	Non-Cov	H-DNA	Chem. Biol. 1999, 6, 771.[192]

To achieve sequence specific cleavage the chemical nuclease can be either covalently bound to the homing agent or recognize specific secondary structures induced by hybridisation of the vector to DNA. In the covalent approach the gene-editor is directly bound to the homing agent and sequence specific cleavage is caused by enhanced local concentration of the chemical nuclease at the scission site. For this purpose, a wide range of alkylating agents and complexes (*i.e.* Ce^{4+}, Fe^{2+}, Zr^{4+}, Rh^{2+} and Cu^{2+}) have been conjugated to various sequence-directing groups such as proteins, polyamides and polynucleotides (Figure I-11).[193] This review focuses on mainly on Fe(II)-EDTA and Cu-Phen hybrid systems.

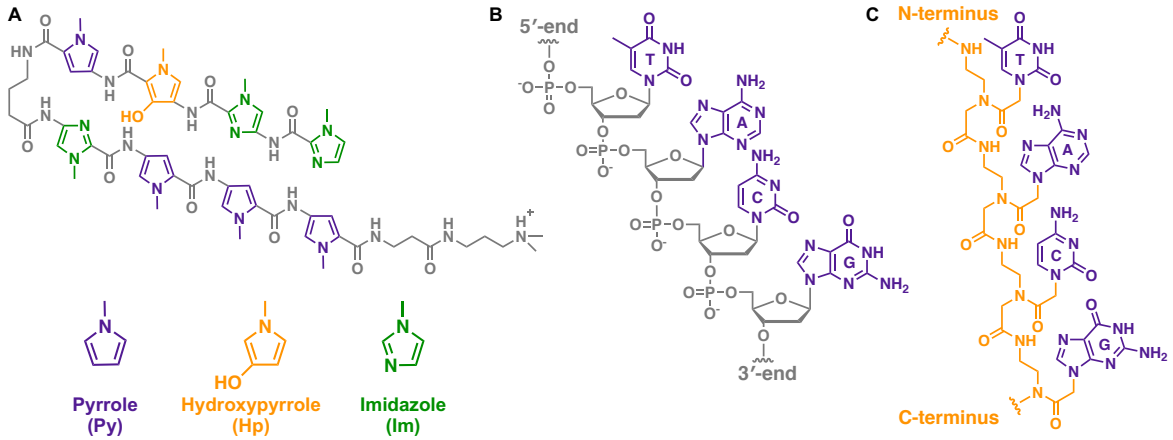

Figure I-11. Molecular structure of **A** polyamide, **B** DNA and **C** PNA based homing agents. Binding specificity by polyamides is provided by pairs of noncanonical amino acids capable of recognizing individual base pair combinations. In the case of DNA and PNA sequence recognition is given by base pairing of the nucleobases (purple).

I. 7.2.1. AMN conjugated to sequence-specific binders

Fe(II)-EDTA was the first complex modified for targeted DNA oxidation by conjugation with the intercalator methydium-propylamine. Despite this derivative showing enhanced cleavage activity in the presence of dithiothreitol and efficiency comparable to bleomycin, it lacked any sequence specificity.[178] To restrict AMN activity to defined sequences, Dervan *et al*. linked the antibiotic distamycin (DE)—an oligopeptide containing three *N*-methylpyrrole carboxamides—to the complex by peptide chemistry.[179] Distamycin binds the minor groove of poly[d(A-T)$_2$] tracts through a combination of electrostatic interactions, hydrogen bonds and van der Waals contacts between the polyamide *N*-methylpyrrole groups and DNA nucleobases.[38,39,194] The Fe(II)-EDTA-DE derivative had higher specificity than bleomycin, cleaving fewer sites on restriction fragments from pBR322 and predominantly at 5′-ATTT-3′.[179] Extension of the targeting moiety to five *N*-methylpyrrole carboxamides enhanced DNA recognition and cleavage efficiency at 5′-TTTTTA-3′ sequences.[195] In parallel to the iron-EDTA conjugates, Cu-Phen and derivatives were conjugated to distamycin to direct nuclease action by the complex. Similar to free Fe(II)-EDTA, Cu-Phen complexes induce promiscuous DNA cleavage which, once tethered to distamycin, is restricted to nucleobases close to poly[d(A-T)$_2$] tracts. Among the Cu-Phen hybrids, 3-Clip-Phen had the highest cleavage efficiency suggesting relevance of the serinol bridge in oxygen activation. In this case DNA damage was slower but more efficient than the cleavage induced by the untethered AMN. In addition, while free [Cu(3-Clip-Phen)]$^{2+}$ induce radical damage at C1′, C4′ and C5′ positions of the deoxyribose ring, in the case of the hybrid C1′ oxidation is reduced

probably due to steric hindrance that promotes interaction at the edge of the minor groove.[39,196] Inspired by DNA recognition of distamycin and to expand specificity of polyamides to other sequences, Dervan *et al.* synthesized a series of hairpin pyrrole-imidazole polymers capable of recognizing defined Watson-Crick base pairs through the minor groove of DNA (Figure I-11A). In this strategy unsymmetrical ring pairs of three non-canonical amino acids (imidazole, pyrrole and hydroxypyrrole) are combined to distinguish the four base pair combinations (AT, TA, GC, CG) through the specific stereochemistry of their hydrogen bonds, differences in steric bulk and electronic potential surfaces. Later, the high DNA binding specificity of these homing agents has been exploited to deliver various chemical gene silencers and site-selective alkylation and cleavage of DNA was achieved for a class of polyamides with 1-(chloromethyl)-5-hydroxy-1,2-dihydro-3H-benz[e]indole (seco-CBI) moiety.[38,197–199] The overall neutral backbone of polyamides is attractive for cell permeability and delivery but their difficult design and short sequence recognition restrict their targeting when compared to other vectors.

I. 7.2.2. AMN-oligonucleotide hybrids

Oligonucleotides can be programmed to specifically bind long DNA regions and their recognition through canonical base pairing provides an easier design of the homing agent compared to polyamides. In this case however hydrogen bonds established between nucleobases of the vector—either a peptide- (PNA) or deoxyribo- nucleic acid strand (Figure 10B and C)—and the target direct reactivity of the chemical nuclease to the major groove of dsDNA.[200] Here, PNAs can induce various secondary structures dependent on vector length and sequence composition while deoxyribonucleic strands forms triple helical arrangements.[23,201] Much elegant work has been dedicated to designing chimeric agents with oligonucleotides (ON) and sequence-specific reactivity was reported for conjugates carrying photo-inducible crosslinkers, alkylating groups and cleaving agents.[202–206] Fe(II)-EDTA was the first complex to be linked to a 19-nucleotide sequence targeting pBR322 by integration of an thymidine-EDTA-triethylester through phosphoramidite solid phase synthesis (Figure I-12A).[180] Chu and Orgel also conjugated the ferrous-EDTA complex to an oligonucleotide but they used a different synthetic approach and directly attached it to the 5′-phosphate terminii through a ethylenediamine linker (Figure I-12B).[181] In the case of Dervan's hybrid, cleavage of a 167 bp amplicon occurred site-specifically over a range of 16 nucleotides from the site of hybridization suggesting that damage is produced by diffusible radicals, namely $^{\bullet}OH$.[180] The first example of $[Cu(Phen)]^{2+}$-ON hybrid was

reported by Sigman *et al.* who conjugated glycylamido-1,10-phenanthroline to oligonucleotides through their phosphate-imidazolide intermediates. Also in this case targeted cleavage was promoting through hydroxyl radical production by $[Cu(Phen)]^{2+}$ in the presence of H_2O_2 but damage was restricted to fewer sites compared to iron-agents indicating that the ROS produced is not diffusible (Figure I-12C).[182] Despite the above systems promote targeted DNA cleavage, an essential requirement in the experimental design relied on disruption of the pre-existing duplex structure to allow hybridisation of the hybrid.

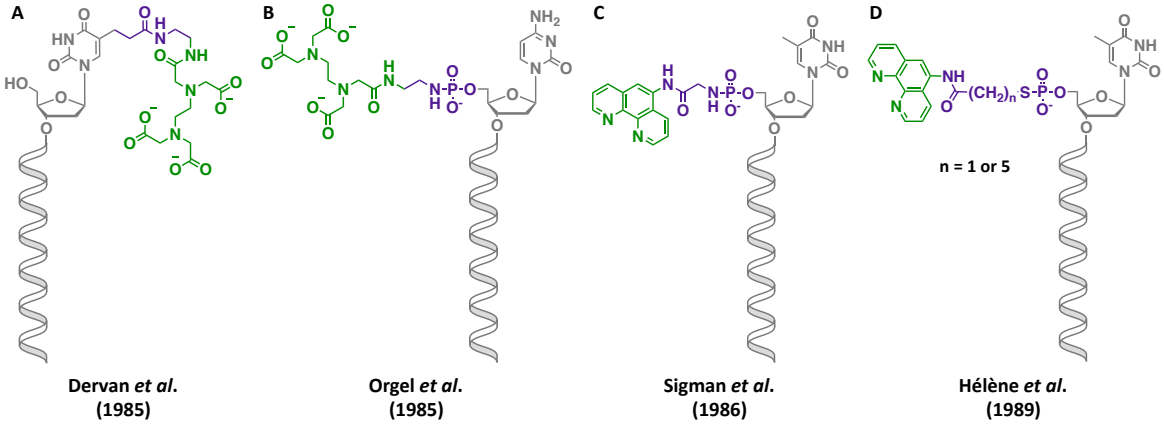

Figure I-12. Molecular structure of the state-of-art targeted-AMNs where an oligonucleotide vector has been coupled to either EDTA (**A** and **B**) or Phen (**C** and **D**) through peptide linkers (highlighted in purple).

In 1987 Dervan and Moser were the first to exploit triplex formation and Hoogsteen recognition of polypurine sequences by polypyrimidine agents to develop nine Fe(II)-EDTA-homopyrimidine probes capable of causing localized double strand breaks in plasmid DNA.[183,207,208] In this work sequence specificity by the targeted chemical nuclease relied significantly on: *i*) buffer composition in that presence of organic solvents induce transition from B- to A-DNA facilitating triplex structure formation; *ii*) pH sensitivity promoting protonation of cytosine bases and triplex stabilization but causing parallel $(EDTA)^{4-}$ quenching and AMN deactivation; *iii*) probe length, temperature and sequence similarities; and *iv*) presence of added cations (i.e. $[Co(NH_3)_6]^{3+}$ or spermine) to reduce phosphate backbone repulsion and stabilize the H-DNA structure.[183] When positioned at the 5′-end of the TFO, the AMN moiety was exposed to the major groove and promoted oxidation of the polypurinic strand toward the 5′-side, indicating parallel directionality with respect to the target strand. On the other hand, internal modifications induced damage of the polypyrimidine sequence for the target purinic sequence is protected by the sugar-phosphate backbone of the TFO. In both cases however damage was distributed over a

range of up to 16 bp due to the diffusible hydroxyl radical.[183] Later work by Hélène reported sequence specific photocrosslinking by a duplex-targeted *p*-azidophenacyl-octathymidylate derivative. Here conversion of crosslinks into chain breaks under alkaline treatment allowed to identify a parallel orientation of the octathymidylate to the target strand.[209] Similarly a phenanthroline-oligonucleotide conjugate reported by the same group induced site-specific cleavage of Simian virus 40 (SV40) DNA in the presence of copper ions and reductant (Figure I-12D). The efficiency of double strand cleavage (70%) was higher than the one reported for Fe(II)-EDTA hybrid (25%).[184,207] In contrast the hybrid reported by Dervan, oxidative damage by the Cu(Phen)-ON was performed at the minor groove of DNA. This behaviour suggested that intercalation of phenanthroline occurs in the major groove while coordination of copper through the minor groove locks the complex close to its cleavage site. In addition, cleavage efficacy was enhanced when a second free Phen intercalator was added to form the active $[Cu(Phen)_2]^{2+}$ complex whereas damage was completely inhibited in the absence of spermine even at high salt concentrations (1 M NaCl).[184,203] With the aim of improving targeted damage, the Cu(Phen)-ON was modified on the other end with an acridine derivative capable of dsDNA intercalation and triple helix stabilization.[203]

Inspired by these systems, reactivity by other chemical agents has been targeted to DNA by oligonucleotide vectors. Psoralen-TFO hybrids were reported to generate triplex mediated adducts upon irradiation both *in vitro* and *in vivo* and these systems have been employed as probes for chromatin structure, inhibitors of transcription and site-specific gene editors.[185,210,211] Chimeric conjugates of Zr^{4+} and Ce^{4+} with peptide nucleic acids or oligonucleotides, respectively, induced site-selective hydrolysis of single-stranded DNA.[186,212,187] In both cases hydrolytic cleavage was mediated by the strong Lewis acids coordinating first to a phosphate group and then triggering scission through water activation. More recent AMN-TFOs include hybrids with bleomycin A_5, Mn(III)-porphyrin and Cu(II)/Co(III)-metallodispheral complexes. All of these chimeric agents showed efficient cleavages of short dsDNA sequences.[188–190] Despite various strategies being employed to induce specific cleavage, conjugation of AMNs to oligonucleotide vectors usually requires complex procedures and usage of cleavable linkers. In addition, most of the aforementioned work on TFO-hybrids relied on the presence of polycationic species for triplex formation.

I. 7.2.3. Targeting AMNs by non-covalent structural recognition

In the non-covalent approach, a biphasic mechanism is involved: i) in the first event, the vector binds and forms a specific type of secondary or tertiary structures; ii) in the second event a conformation specific molecule binds the target site and promotes reactivity. Recently the non-covalent approach has been reported for a class of compounds (ARCUT) that showed higher hydrolysis rates for single-stranded DNA (ssDNA) than for dsDNA. In this case two oligonucleotides were used for dsDNA invasion or to form a gap structure on ssDNA where hydrolysis by a Ce(IV)/EDTA complex was directed toward the ssDNA/dsDNA junctions. Cleavage bias by Ce(IV)/EDTA is due to its different binding constant for ssDNA which is 100 fold higher than for dsDNA.[213,214] The stronger binding originates from the flexible structure of ssDNA that allows a conformational change where three or more phosphodiester groups simultaneously coordinate to the Ce(IV) centre. Complexation to EDTA was essential for discrimination as the 'naked' metal was found to hydrolyse both ssDNA and dsDNA with similar efficiencies. These systems have been successfully employed to introduce genome edits both *in vitro* and *in vivo*.[191] Similarly, formation of triple helical structure has been exploited to direct cleavage by triplex-specific agents. Pentacyclic benzoquinoquinoxaline derivatives (BQQ) bind weakly to double-helical DNA but were shown to strongly stabilize triple helical structures. Therefore, the specific recognition and strong structural discrimination of these intercalators has been exploited to efficiently direct the nuclease action of Fe(II)-EDTA and structure-specific cleavage was achieved both on short linear and plasmid DNA sequences.[192,215]

I. 8. References

[1] A. Travers, G. Muskhelishvili, *FEBS J.* **2015**, *282*, 2279–2295.

[2] P. S. Ho, M. Carter, in *DNA Replication - Current Advances* (Ed.: H. Seligmann), IntechOpen, London, **2011**, pp. 4–28.

[3] L. H. Hurley, *Nat. Rev. Cancer* **2002**, *2*, 188–200.

[4] J. D. Watson, F. H. C. Crick, *Nature* **1953**, *171*, 737–738.

[5] B. Rosenberg, L. V. Camp, T. Krigas, *Nature* **1965**, *205*, 698–699.

[6] E. Chargaff, *Science* **1971**, *172*, 637–642.

[7] S. Harteis, S. Schneider, *Int. J. Mol. Sci.* **2014**, *15*, 12335–12363.

[8] R. Wing, H. Drew, T. Takano, C. Broka, S. Tanaka, K. Itakura, R. E. Dickerson, *Nature* **1980**, *287*, 755–758.

[9] H. R. Drew, R. M. Wing, T. Takano, C. Broka, S. Tanaka, K. Itakura, R. E. Dickerson, *Proc. Natl. Acad. Sci. U.S.A.* **1981**, *78*, 2179–2183.

[10] A. Rich, S. Zhang, *Nat. Rev. Genet.* **2003**, *4*, 566–572.

[11] A. Herbert, *Commun. Biol.* **2019**, *2*, 1–10.

[12] A. Medina-Molner, B. Spingler, *Chem. Commun.* **2012**, *48*, 1961–1963.

[13] J. C. Wang, *Nat. Rev. Mol. Cell Biol.* **2002**, *3*, 430–440.

[14] L. Stefan, B. Bertrand, P. Richard, P. L. Gendre, F. Denat, M. Picquet, D. Monchaud, *ChemBioChem* **2012**, *13*, 1905–1912.

[15] S. Neidle, S. Balasubramanian, Eds., *Quadruplex Nucleic Acids*, Royal Society Of Chemistry, Royal Society of Chemistry, Cambridge, **2007**.

[16] D. R. Boer, A. Canals, M. Coll, *Dalton Trans.* **2008**, 399–414.

[17] H. J. Lipps, D. Rhodes, *Trends Cell Biol.* **2009**, *19*, 414–422.

[18] M. Guéron, J.-L. Leroy, *Curr. Opin. Struct. Biol.* **2000**, *10*, 326–331.

[19] M. Zeraati, D. B. Langley, P. Schofield, A. L. Moye, R. Rouet, W. E. Hughes, T. M. Bryan, M. E. Dinger, D. Christ, *Nat. Chem.* **2018**, *10*, 631–637.

[20] P. A. Khuu, A. R. Voth, F. A. Hays, P. S. Ho, *J. Mol. Recognit.* **2006**, *19*, 234–242.

[21] A. L. Brogden, N. H. Hopcroft, M. Searcey, C. J. Cardin, *Angew. Chem. Int. Ed.* **2007**, *46*, 3850–3854.

[22] K. R. Fox, T. Brown, *Biochem. Soc. Trans.* **2011**, *39*, 629–634.

[23] K. R. Fox, T. Brown, D. A. Rusling, in *DNA-Targeting Molecules as Therapeutic Agents* (Ed.: M.J. Waring), Royal Society of Chemistry, Cambridge, **2018**, pp. 1–32.

[24] F. A. Buske, J. S. Mattick, T. L. Bailey, *RNA Biol.* **2011**, *8*, 427–439.

[25] Y. Taniguchi, S. Sasaki, *Org. Biomol. Chem.* **2012**, *10*, 8336–8341.

[26] A. R. Morgan, R. D. Wells, *J. Mol. Biol.* **1968**, *37*, 63–80.

[27] J. C. Hanvey, M. Shimizu, R. D. Wells, *Nucleic Acids Res.* **1990**, *18*, 157–161.

[28] M. Faria, C. Giovannangeli, *J. Gene Med.* **2001**, *3*, 299–310.

[29] C. J. Cardin, in *Structure and Bonding*, Springer, Berlin, Heidelberg, **2019**, pp. 1–35.

[30] P. Lincoln, L. M. Wilhelmsson, B. Nordén, in *DNA-Targeting Molecules as Therapeutic Agents* (Ed.: M.J. Waring), Royal Society of Chemistry, Cambridge, **2018**, pp. 45–73.

[31] H.-K. Liu, P. J. Sadler, *Acc. Chem. Res.* **2011**, *44*, 349–59.

[32] V. A. Bloomfield, D. M. Crothers, I. Tinoco, *Nucleic Acids: Structures, Properties, and Function.*, University Science Books, Sausalito, **2000**.
[33] A. Kellett, Z. Molphy, C. Slator, V. McKee, N. P. Farrell, *Chem. Soc. Rev.* **2019**, *48*, 971–988.
[34] N. McStay, A. M. Reilly, N. Gathergood, A. Kellett, *ChemPlusChem* **2019**, *84*, 38–42.
[35] N. McStay, Z. Molphy, A. Coughlan, A. Cafolla, V. McKee, N. Gathergood, A. Kellett, *Nucleic Acids Res.* **2017**, *45*, 527–540.
[36] W. D. Wilson, F. A. Tanious, H. J. Barton, R. L. Jones, K. Fox, R. L. Wydra, L. Strekowski, *Biochemistry* **1990**, *29*, 8452–8461.
[37] U. Sehlstedt, S. K. Kim, B. Norden, *J. Am. Chem. Soc.* **1993**, *115*, 12258–12263.
[38] P. B. Dervan, *Isr. J. Chem.* **2019**, *59*, 71–83.
[39] M. Pitié, C. J. Burrows, B. Meunier, *Nucleic Acids Res.* **2000**, *28*, 4856–4864.
[40] M. J. Waring, *J. Mol. Biol.* **1965**, *13*, 269–282.
[41] C. G. Reinhardt, T. R. Krugh, *Biochemistry* **1978**, *17*, 4845–4854.
[42] C. Slator, Z. Molphy, V. McKee, C. Long, T. Brown, A. Kellett, *Nucleic Acids Res.* **2018**, *46*, 2733–2750.
[43] H.-K. Liu, P. J. Sadler, *Acc. Chem. Res.* **2011**, *44*, 349–359.
[44] S. Walsh, A. H. El-Sagheer, T. Brown, *Chem. Sci.* **2018**, *9*, 7681–7687.
[45] A. R. Morgan, J. S. Lee, D. E. Pulleyblank, N. L. Murray, D. H. Evans, *Nucleic Acids Res.* **1979**, *7*, 547–565.
[46] J. P. Hall, P. M. Keane, H. Beer, K. Buchner, G. Winter, T. L. Sorensen, D. J. Cardin, J. A. Brazier, C. J. Cardin, *Nucleic Acids Res.* **2016**, *44*, 9472–9482.
[47] C. Slator, Z. Molphy, V. McKee, A. Kellett, *Redox Biol.* **2017**, *12*, 150–161.
[48] G. Toniolo, M. Louka, G. Menounou, N. Z. Fantoni, G. Mitrikas, E. K. Efthimiadou, A. Masi, M. Bortolotti, L. Polito, A. Bolognesi, et al., *ACS Omega* **2018**, *3*, 15952–15965.
[49] J. Andersson, P. Lincoln, *J. Phys. Chem. B* **2011**, *115*, 14768–14775.
[50] L. Wu, A. Reymer, C. Persson, K. Kazimierczuk, T. Brown, P. Lincoln, B. Nordén, M. Billeter, *Chem. Eur. J.* **2013**, *19*, 5401–5410.
[51] Institute of Medicine (US) Committee on the Survey of the Health Effects of Mustard Gas and Lewisite, in *Veterans at Risk The Health Effects of Mustard Gas and Lewisite* (Eds.: C.M. Pechura, D.P. Rall), National Academies Press (US), Washington D.C., **1993**, pp. 71–80.
[52] M. J. Waring, *Annu. Rev. Biochem.* **1981**, *50*, 159–192.
[53] J. G. Muller, S. J. Paikoff, S. E. Rokita, C. J. Burrows, *J. Inorg. Biochem.* **1994**, *54*, 199–206.
[54] C. Mari, V. Pierroz, S. Ferrari, G. Gasser, *Chem. Sci.* **2015**, *6*, 2660–2686.
[55] E. Wachter, A. Zamora, D. K. Heidary, J. Ruiz, E. C. Glazer, *Chem. Commun.* **2016**, *52*, 10121–10124.
[56] A. F. Westendorf, J. A. Woods, K. Korpis, N. J. Farrer, L. Salassa, K. Robinson, V. Appleyard, K. Murray, R. Grünert, A. M. Thompson, et al., *Mol. Cancer Ther.* **2012**, *11*, 1894–1904.

[57] E. Wachter, D. K. Heidary, B. S. Howerton, S. Parkin, E. C. Glazer, *Chem. Commun.* **2012**, *48*, 9649–9651.
[58] F. S. Mackay, J. A. Woods, H. Moseley, J. Ferguson, A. Dawson, S. Parsons, P. J. Sadler, *Chem. Eur. J.* **2006**, *12*, 3155–3161.
[59] A. Kellett, O. Howe, M. O'Connor, M. McCann, B. S. Creaven, S. McClean, A. Foltyn-Arfa Kia, A. Casey, M. Devereux, *Free Radic. Biol. Med.* **2012**, *53*, 564–576.
[60] J. Cadet, J. R. Wagner, *Cold Spring Harb. Perspect. Biol.* **2013**, *5:a012559*, 1–18.
[61] P. C. Bruijnincx, P. J. Sadler, *Curr. Opin. Chem. Biol.* **2008**, *12*, 197–206.
[62] C. Marzano, M. Pellei, F. Tisato, C. Santini, *Anticancer Agents Med. Chem.* **2009**, *9*, 185–211.
[63] C. Santini, M. Pellei, V. Gandin, M. Porchia, F. Tisato, C. Marzano, *Chem. Rev.* **2014**, *114*, 815–862.
[64] N. P. E. Barry, P. J. Sadler, *Chem. Commun.* **2013**, *49*, 5106–31.
[65] A. Spassky, D. S. Sigman, *Biochemistry* **1985**, *24*, 8050–8056.
[66] N. Fantoni, T. Lauria, A. Kellett, *Synlett* **2015**, *26*, 2623–2626.
[67] G. B. Kauffman, R. Pentimalli, S. Doldi, M. D. Hall, *Platin. Met. Rev.* **2010**, *54*, 250–256.
[68] G. H. W. Milburn, M. R. Truter, *J. Chem. Soc. A* **1966**, 1609–1616.
[69] F. Muggia, R. Leone, A. Bonetti, *Anticancer Res.* **2014**, *34*, 417–417.
[70] H. Shi, C. Imberti, P. J. Sadler, *Inorg. Chem. Front.* **2019**, *6*, 1623–1638.
[71] L. Kelland, *Nat. Rev. Cancer* **2007**, *7*, 573–584.
[72] X. Du, X. Wang, H. Li, H. Sun, *Metallomics* **2012**, *4*, 679–685.
[73] T. C. Johnstone, K. Suntharalingam, S. J. Lippard, *Chem. Rev.* **2016**, *116*, 3436–3486.
[74] M. J. Hannon, *Chem. Soc. Rev.* **2007**, *36*, 280–295.
[75] A. Ratanaphan, S. Wasiksiri, B. Canyuk, P. Prasertsan, *Cancer Biol. Ther.* **2009**, *8*, 890–898.
[76] B. Lippert, *Coord. Chem. Rev.* **1999**, *182*, 263–295.
[77] R. Oun, Y. E. Moussa, N. J. Wheate, *Dalton Trans.* **2018**, *47*, 6645–6653.
[78] V. Brabec, J. Kasparkova, V. Menon, N. P. Farrell, in *Metallo-Drugs: Development and Action of Anticancer Agents* (Eds.: A. Sigel, H. Sigel, E. Freisinger, R.K.O. Sigel), De Gruyter, Berlin, Boston, **2018**, pp. 43–68.
[79] J. B. Mangrum, N. P. Farrell, *Chem. Commun.* **2010**, *46*, 6640–6650.
[80] N. Farrell, S. Spinelli, in *Uses of Inorganic Chemistry in Medicine* (Ed.: N.P. Farrell), Royal Society Of Chemistry, Cambridge, **1999**, pp. 124–134.
[81] J. Kasparkova, N. Farrell, V. Brabec, *J. Biol. Chem.* **2000**, *275*, 15789–15798.
[82] M. S. Davies, D. S. Thomas, A. Hegmans, S. J. Berners-Price, N. Farrell, *Inorg. Chem.* **2002**, *41*, 1101–1109.
[83] N. M. P. Rosa, F. H. do C. Ferreira, N. P. Farrell, L. A. S. Costa, *Front. Chem.* **2019**, *7:307*, 1–12.
[84] S. Komeda, T. Moulaei, K. K. Woods, M. Chikuma, N. P. Farrell, L. D. Williams, *J. Am. Chem. Soc.* **2006**, *128*, 16092–16103.
[85] a. Prisecaru, Z. Molphy, R. G. Kipping, E. J. Peterson, Y. Qu, a. Kellett, N. P. Farrell, *Nucleic Acids Res.* **2014**, *42*, 13474–13487.

[86] A. Levina, A. Mitra, P. A. Lay, *Metallomics* **2009**, *1*, 458–470.
[87] E. S. Antonarakis, A. Emadi, *Cancer Chemother. Pharmacol.* **2010**, *66*, 1–9.
[88] C. X. Zhang, S. J. Lippard, *Curr. Opin. Chem. Biol.* **2003**, *7*, 481–489.
[89] N. P. E. Barry, P. J. Sadler, *Chem. Commun.* **2013**, *49*, 5106–5131.
[90] S. Monro, K. L. Colón, H. Yin, J. Roque, P. Konda, S. Gujar, R. P. Thummel, L. Lilge, C. G. Cameron, S. A. McFarland, *Chem. Rev.* **2019**, *119*, 797–828.
[91] S. Leijen, S. A. Burgers, P. Baas, D. Pluim, M. Tibben, E. van Werkhoven, E. Alessio, G. Sava, J. H. Beijnen, J. H. M. Schellens, *Invest. New Drugs* **2015**, *33*, 201–214.
[92] C. G. Hartinger, S. Zorbas-Seifried, M. A. Jakupec, B. Kynast, H. Zorbas, B. K. Keppler, *J. Inorg. Biochem.* **2006**, *100*, 891–904.
[93] E. Alessio, L. Messori, *Molecules* **2019**, *24*, 1995.
[94] S. Bonnet, *Comment Inorg. Chem.* **2015**, *35*, 179–213.
[95] S. Lazic, P. Kaspler, G. Shi, S. Monro, T. Sainuddin, S. Forward, K. Kasimova, R. Hennigar, A. Mandel, S. McFarland, et al., *Photochem. Photobiol.* **2017**, *93*, 1248–1258.
[96] H. Huang, S. Banerjee, K. Qiu, P. Zhang, O. Blacque, T. Malcomson, M. J. Paterson, G. J. Clarkson, M. Staniforth, V. G. Stavros, et al., *Nat. Chem.* **2019**, 1–8.
[97] F. Harris, L. Pierpoint, *Med. Res. Rev.* **2012**, *28*, 1292–1327.
[98] J. Liu, C. Zhang, T. W. Rees, L. Ke, L. Ji, H. Chao, *Coord. Chem. Rev.* **2018**, *363*, 17–28.
[99] G. Shi, S. Monro, R. Hennigar, J. Colpitts, J. Fong, K. Kasimova, H. Yin, R. DeCoste, C. Spencer, L. Chamberlain, et al., *Coord. Chem. Rev.* **2015**, *282–283*, 127–138.
[100] B. S. Howerton, D. K. Heidary, E. C. Glazer, *J. Am. Chem. Soc.* **2012**, *134*, 8324–8327.
[101] S. M. Hecht, *J. Nat. Prod.* **2000**, *63*, 158–168.
[102] W. Wu, D. E. Vanderwall, J. Stubbe, J. W. Kozarich, C. J. Turner, *J. Am. Chem. Soc.* **1994**, *116*, 10843–10844.
[103] A. D. D'Andrea, W. A. Haseltine, *Proc. Natl. Acad. Sci. U.S.A.* **1978**, *75*, 3608–3612.
[104] A. T. Abraham, X. Zhou, S. M. Hecht, *J. Am. Chem. Soc.* **2001**, *123*, 5167–5175.
[105] L. F. Povirk, M. Hogan, N. Dattagupta, *Biochemistry* **1979**, *18*, 96–101.
[106] J. Chen, J. Stubbe, *Nat. Rev. Cancer* **2005**, *5*, 102–112.
[107] S. A. Kane, S. M. Hecht, *Prog. Nucleic Acid Res. Mol. Biol.* **1994**, *49*, 313–352.
[108] C. Avendaño, J. C. Menéndez, in *Medicinal Chemistry of Anticancer Drugs (Second Edition)* (Eds.: C. Avendaño, J.C. Menéndez), Elsevier, Boston, **2015**, pp. 133–195.
[109] J. C. Wu, J. W. Kozarich, J. Stubbe, *Biochemistry* **1985**, *24*, 7562–7568.
[110] L. E. Rabow, J. Stubbe, J. W. Kozarich, *J. Am. Chem. Soc.* **1990**, *112*, 3196–3203.
[111] M. Pitié, G. Pratviel, *Chem. Rev.* **2010**, *110*, 1018–1059.
[112] F. Mancin, P. Scrimin, P. Tecilla, U. Tonellato, *Chem. Commun.* **2005**, *0*, 2540–2548.
[113] D. S. Sigman, *Biochemistry* **1990**, *29*, 9097–9105.

[114] T. Hirohama, Y. Kuranuki, E. Ebina, T. Sugizaki, H. Arii, M. Chikira, P. Tamil Selvi, M. Palaniandavar, *J. Inorg. Biochem.* **2005**, *99*, 1205–1219.
[115] B. C. Bales, M. Pitié, B. Meunier, M. M. Greenberg, *J. Am. Chem. Soc.* **2002**, *124*, 9062–9063.
[116] T. Oyoshi, H. Sugiyama, *J. Am. Chem. Soc.* **2000**, *122*, 6313–6314.
[117] A. Zaid, J.-S. Sun, C.-H. Nguyen, E. Bisagni, T. Garestier, D. S. Grierson, R. Zain, *ChemBioChem* **2004**, *5*, 1550–1557.
[118] D. S. Sigman, D. R. Graham, V. D'Aurora, A. M. Stern, *J. Biol. Chem.* **1979**, *254*, 12269–12272.
[119] M. M. Meijler, O. Zelenko, D. S. Sigman, *J. Am. Chem. Soc.* **1997**, *119*, 1135–1136.
[120] D. S. Sigman, T. W. Bruice, A. Mazumder, C. L. Sutton, *Acc. Chem. Res.* **1993**, *26*, 98–104.
[121] T. Chen, M. M. Greenberg, *J. Am. Chem. Soc.* **1998**, *120*, 3815–3816.
[122] T. Gimisis, C. Chatgilialoglu, in *Encyclopedia of Radicals in Chemistry, Biology and Materials*, John Wiley & Sons, Inc., **2012**, pp. 1–26.
[123] Z. Molphy, C. Slator, C. Chatgilialoglu, A. Kellett, *Front. Chem.* **2015**, *3*, 1–9.
[124] Z. Molphy, A. Prisecaru, C. Slator, N. Barron, M. McCann, J. Colleran, D. Chandran, N. Gathergood, A. Kellett, *Inorg. Chem.* **2014**, *53*, 5392–5404.
[125] A. Kellett, M. O'Connor, M. McCann, M. McNamara, P. Lynch, G. Rosair, V. McKee, B. Creaven, M. Walsh, S. McClean, et al., *Dalton Trans.* **2011**, *40*, 1024–1027.
[126] B. C. Bales, T. Kodama, Y. N. Weledji, M. Pitié, B. Meunier, M. M. Greenberg, *Nucleic Acids Res.* **2005**, *33*, 5371–5379.
[127] M. Pitié, B. Meunier, *Bioconjug. Chem.* **1998**, *9*, 604–611.
[128] A. Robertazzi, A. V. Vargiu, A. Magistrato, P. Ruggerone, P. Carloni, P. De Hoog, J. Reedijk, *J. Phys. Chem. B* **2009**, *113*, 10881–10890.
[129] P. de Hoog, M. J. Louwerse, P. Gamez, M. Pitié, E. J. Baerends, B. Meunier, J. Reedijk, *Eur. J. Inorg. Chem.* **2008**, *2008*, 612–619.
[130] A. W. Schaefer, M. T. Kieber-Emmons, S. M. Adam, K. D. Karlin, E. I. Solomon, *J. Am. Chem. Soc.* **2017**, *139*, 7958–7973.
[131] G. B. Wijeratne, S. Hematian, M. A. Siegler, K. D. Karlin, *J. Am. Chem. Soc.* **2017**, *139*, 13276–13279.
[132] K. D. Karlin, J. C. Hayes, Y. Gultneh, R. W. Cruse, J. W. McKown, J. P. Hutchinson, J. Zubieta, *J. Am. Chem. Soc.* **1984**, *106*, 2121–2128.
[133] S. T. Frey, H. H. J. Sun, N. N. Murthy, K. D. Karlin, *Inorganica Chim. Acta* **1996**, *242*, 329–338.
[134] T. Ito, S. Thyagarajan, K. D. Karlin, S. E. Rokita, *Chem. Commun.* **2005**, 4812–4814.
[135] K. J. Humphreys, K. D. Karlin, S. E. Rokita, *J. Am. Chem. Soc.* **2002**, *124*, 6009–6019.
[136] K. J. Humphreys, K. D. Karlin, S. E. Rokita, *J. Am. Chem. Soc.* **2002**, *124*, 8055–8066.
[137] L. Li, N. N. Murthy, J. Telser, Lev. N. Zakharov, G. P. A. Yap, A. L. Rheingold, K. D. Karlin, S. E. Rokita, *Inorg. Chem.* **2006**, *45*, 7144–7159.

[138] L. Li, K. D. Karlin, S. E. Rokita, *J. Am. Chem. Soc.* **2005**, *127*, 520–521.
[139] Z. Molphy, D. Montagner, S. S. Bhat, C. Slator, C. Long, A. Erxleben, A. Kellett, *Nucleic Acids Res.* **2018**, *46*, 9918–9931.
[140] L. Q. Hatcher, K. D. Karlin, *J. Biol. Inorg. Chem.* **2004**, *9*, 669–683.
[141] D. J. Galas, a Schmitz, *Nucleic Acids Res.* **1978**, *5*, 3157–3170.
[142] H. R. Drew, *J. Mol. Biol.* **1984**, *176*, 535–557.
[143] H. R. Drew, A. A. Travers, *Cell* **1984**, *37*, 491–502.
[144] K. R. Fox, Ed. , *Drug-DNA Interaction Protocols*, Humana Press, New York, **2010**.
[145] D. Suck, C. Oefner, *Nature* **1986**, *321*, 620–625.
[146] W. P. Stemmer, *Rapid Evolution of a Protein in Vitro by DNA Shuffling.*, **1994**.
[147] H. Zhao, L. Giver, Z. Shao, J. A. Affholter, F. H. Arnold, *Nat Biotechnol* **1998**, *16*, 258–261.
[148] R. Larragy, J. Fitzgerald, A. Prisecaru, V. McKee, P. Leonard, A. Kellett, *Chem. Commun.* **2015**, *51*, 12908–12911.
[149] P. Mali, L. Cheng, *Stem Cells* **2012**, *30*, 75–81.
[150] D. M. Thurtle-Schmidt, T.-W. Lo, *Biochem. Mol. Biol. Educ.* **2018**, *46*, 195–205.
[151] C. O. Pabo, E. Peisach, R. A. Grant, *Annu. Rev. Biochem.* **2001**, *70*, 313–340.
[152] T. Gaj, C. A. Gersbach, C. F. Barbas, *Trends Biotechnol.* **2013**, *31*, 397–405.
[153] J. Smith, M. Bibikova, F. G. Whitby, A. R. Reddy, S. Chandrasegaran, D. Carroll, *Nucleic Acids Res.* **2000**, *28*, 3361–3369.
[154] M. Bibikova, D. Carroll, D. J. Segal, J. K. Trautman, J. Smith, Y.-G. Kim, S. Chandrasegaran, *Mol. Cell Biol.* **2001**, *21*, 289–297.
[155] A. J. Bogdanove, D. F. Voytas, *Science* **2011**, *333*, 1843–1846.
[156] J. Boch, H. Scholze, S. Schornack, A. Landgraf, S. Hahn, S. Kay, T. Lahaye, A. Nickstadt, U. Bonas, *Science* **2009**, *326*, 1509–1512.
[157] M. J. Moscou, A. J. Bogdanove, *Science* **2009**, *326*, 1501–1501.
[158] J. C. Miller, S. Tan, G. Qiao, K. A. Barlow, J. Wang, D. F. Xia, X. Meng, D. E. Paschon, E. Leung, S. J. Hinkley, et al., *Nat. Biotechnol.* **2011**, *29*, 143–148.
[159] J. F. Lutz, Z. Zarafshani, *Adv. Drug Deliv. Rev.* **2008**, *60*, 958–970.
[160] A. C. Mercer, T. Gaj, R. P. Fuller, C. F. Barbas, *Nucleic Acids Res.* **2012**, *40*, 11163–11172.
[161] M. Christian, T. Cermak, E. L. Doyle, C. Schmidt, F. Zhang, A. Hummel, A. J. Bogdanove, D. F. Voytas, *Genetics* **2010**, *186*, 757–761.
[162] M. Jinek, K. Chylinski, I. Fonfara, M. Hauer, J. A. Doudna, E. Charpentier, *Science* **2012**, *337*, 816–821.
[163] R. Barrangou, P. Horvath, *Nat. Microbiol.* **2017**, *2*, 1–9.
[164] H. Wang, M. La Russa, L. S. Qi, *Annu. Rev. Biochem.* **2016**, *85*, 227–264.
[165] C. Anders, O. Niewoehner, A. Duerst, M. Jinek, *Nature* **2014**, *513*, 569–573.
[166] T. Yamano, H. Nishimasu, B. Zetsche, H. Hirano, I. M. Slaymaker, Y. Li, I. Fedorova, T. Nakane, K. S. Makarova, E. V. Koonin, et al., *Cell* **2016**, *165*, 949–962.
[167] C. Fellmann, B. G. Gowen, P.-C. Lin, J. A. Doudna, J. E. Corn, *Nat. Rev. Drug. Discov.* **2017**, *16*, 89–100.

[168] L. Taemaitree, A. Shivalingam, A. H. El-Sagheer, T. Brown, *Nat. Commun.* **2019**, *10:1610*, 1–8.
[169] M. Adli, *Nat. Commun.* **2018**, *9:1911*, 1–13.
[170] B. Zetsche, J. S. Gootenberg, O. O. Abudayyeh, I. M. Slaymaker, K. S. Makarova, P. Essletzbichler, S. E. Volz, J. Joung, J. van der Oost, A. Regev, et al., *Cell* **2015**, *163*, 759–771.
[171] H. A. Rees, W.-H. Yeh, D. R. Liu, *Nat. Commun.* **2019**, *10:2212*, 1–12.
[172] F. A. Ran, P. D. Hsu, J. Wright, V. Agarwala, D. A. Scott, F. Zhang, *Nat. Protoc.* **2013**, *8*, 2281–2308.
[173] H. A. Rees, D. R. Liu, *Nat. Rev. Gen.* **2018**, *19*, 770–788.
[174] W.-H. Yeh, H. Chiang, H. A. Rees, A. S. B. Edge, D. R. Liu, *Nat. Commun.* **2018**, *9:2184*, 1–10.
[175] A. C. Komor, Y. B. Kim, M. S. Packer, J. A. Zuris, D. R. Liu, *Nature* **2016**, *533*, 420–424.
[176] A. Erxleben, *Coord. Chem. Rev.* **2018**, *360*, 92–121.
[177] C. Liu, M. Wang, T. Zhang, H. Sun, *Coord. Chem. Rev.* **2004**, *248*, 147–168.
[178] R. P. Hertzberg, P. B. Dervan, *J. Am. Chem. Soc.* **1982**, *104*, 313–315.
[179] P. G. Shultz, J. S. Taylor, P. B. Dervan, *J. Am. Chem. Soc.* **1982**, *104*, 6861–6863.
[180] G. B. Dreyer, P. B. Dervan, *Proc. Natl. Acad. Sci. U.S.A.* **1985**, *82*, 968–972.
[181] B. C. Chu, L. E. Orgel, *Proc. Natl. Acad. Sci. U.S.A.* **1985**, *82*, 963–967.
[182] C. H. Chen, D. S. Sigman, *Proc. Natl. Acad. Sci. U.S.A.* **1986**, *83*, 7147–7151.
[183] H. Moser, P. Dervan, *Science* **1987**, *238*, 645–650.
[184] J. C. François, T. Saison-Behmoaras, C. Barbier, M. Chassignol, N. T. Thuong, C. Hélène, *Proc. Natl. Acad. Sci. U.S.A.* **1989**, *86*, 9702–9706.
[185] P. A. Havre, E. J. Gunther, F. P. Gasparro, P. M. Glazer, *Proc. Natl. Acad. Sci. U.S.A.* **1993**, *90*, 7879–7883.
[186] M. Komiyama, T. Shiiba, Y. Takahashi, N. Takeda, K. Matsumura, T. Kodama, *Supramol. Chem.* **1994**, *4*, 31–34.
[187] F. H. Zelder, A. A. Mokhir, R. Krämer, *Inorg. Chem.* **2003**, *42*, 8618–8620.
[188] R. R. Joshi, K. N. Ganesh, *Biochim. Biophys. Acta* **1994**, *1201*, 454–460.
[189] P. Bigey, G. Pratviel, B. Meunier, *Nucleic Acids Res.* **1995**, *23*, 3894–3900.
[190] D. S. Sergeyev, V. F. Zarytova, *Russ. Chem. Rev.* **1996**, *65*, 355–378.
[191] Y. Aiba, J. Sumaoka, M. Komiyama, *Chem. Soc. Rev.* **2011**, *40*, 5657–5668.
[192] R. Zain, C. Marchand, J. Sun, C. H. Nguyen, E. Bisagni, T. Garestier, C. Hélène, *Chem. Biol.* **1999**, *6*, 771–777.
[193] Z. Yu, J. Cowan, *Curr. Opin. Chem. Biol.* **2018**, *43*, 37–42.
[194] P. B. Dervan, *Science* **1986**, *232*, 464–471.
[195] P. G. Schultz, P. B. Dervan, *Proc. Natl. Acad. Sci. U.S.A.* **1983**, *80*, 6834–6837.
[196] M. Pitié, J. D. Van Horn, D. Brion, C. J. Burrows, B. Meunier, *Bioconjug. Chem.* **2000**, *11*, 892–900.
[197] A. Y. Chang, P. B. Dervan, *J. Am. Chem. Soc.* **2000**, *122*, 4856–4864.
[198] N. R. Wurtz, P. B. Dervan, *Chem. Biol.* **2000**, *7*, 153–161.
[199] S. White, J. W. Szewczyk, J. M. Turner, E. E. Baird, P. B. Dervan, *Nature* **1998**, *391*, 468–471.

[200] C. Giovannangeli, C. Hélène, *Nat. Biotechnol.* **2000**, *18*, 1245–1246.
[201] P. E. Nielsen, M. Egholm, *Curr. Issues Molec. Biol.* **1999**, *1*, 89–104.
[202] M. Boidot-Forget, M. Chassignol, M. Takasugi, N. T. Thuong, C. Hélène, *Gene* **1988**, *72*, 361–371.
[203] J. C. François, T. Saison-Behmoaras, M. Chassignol, N. T. Thuong, C. Helene, *J. Biol. Chem.* **1989**, *264*, 5891–5898.
[204] A. Majumdar, A. Khorlin, N. Dyatkina, F.-L. M. Lin, J. Powell, J. Liu, Z. Fei, Y. Khripine, K. A. Watanabe, J. George, et al., *Nat. Genet.* **1998**, *20*, 212–214.
[205] I. V. Panyutin, A. N. Luu, I. G. Panyutin, R. D. Neumann, *Radiat. Res.* **2001**, *156*, 158–166.
[206] M. P. Knauert, P. M. Glazer, *Hum. Mol. Genet.* **2001**, *10*, 2243–2251.
[207] S. A. Strobel, H. E. Moser, P. B. Dervan, *J. Am. Chem. Soc.* **1988**, *110*, 7927–7929.
[208] S. A. Strobel, P. B. Dervan, *Science* **1990**, *249*, 73–75.
[209] D. Praseuth, L. Perrouault, T. L. Doan, M. Chassignol, N. Thuong, C. Hélène, *Proc. Natl. Acad. Sci. U.S.A.* **1988**, *85*, 1349–1353.
[210] G. Wang, D. D. Levy, M. M. Seidman, P. M. Glazer, *Mol. Cell Biol.* **1995**, *15*, 1759–1768.
[211] N. Puri, A. Majumdar, B. Cuenoud, F. Natt, P. Martin, A. Boyd, P. S. Miller, M. M. Seidman, *J. Biol. Chem.* **2001**, *276*, 28991–28998.
[212] M. Komiyama, N. Takeda, Y. Takahashi, H. Uchida, T. Shiiba, T. Kodama, M. Yashiro, *J. Chem. Soc. Perkin Trans.* **1995**, *2*, 269–274.
[213] M. Komiyama, S. Kina, K. Matsumura, J. Sumaoka, S. Tobey, V. M. Lynch, E. Anslyn, *J. Am. Chem. Soc.* **2002**, *124*, 13731–13736.
[214] W. Chen, T. Igawa, J. Sumaoka, M. Komiyama, *Chem. Lett.* **2004**, *33*, 300–301.
[215] C. Marchand, C. H. Nguyen, B. Ward, J.-S. Sun, E. Bisagni, T. Garestier, C. Hélène, *Chem. Eur. J.* **2000**, *6*, 1559–1563.

Chapter II

Polypyridyl-based copper phenanthrene complexes: a new type of stabilized artificial chemical nuclease

II. 1. Abstract

The building of robust and versatile inorganic scaffolds with artificial metallo-nuclease (AMN) activity is an important research goal for bioinorganic, biotechnology, and metallodrug research fields. Here we report a new type of AMN combining a *tris*-(2-pyridylmethyl)amine (TPMA) scaffold with the copper(II) *N*,*N*′-phenanthrene chemical nuclease core. In designing these complexes, we sought to employ the stabilisation and flexibility of TPMA together with the prominent chemical nuclease activity of copper 1,10-phenanthroline (Phen). A second aspect was the opportunity to introduce designer *N*,*N*′ DNA intercalators (*e.g.* dipyridophenazine; DPPZ) for improved DNA recognition. Five compounds of formula $[Cu(TPMA)(N,N')]^{2+}$ (where *N*,*N*′ is 2,2-bipyridine (Bipy); Phen; 1,10-phenanthroline-5,6-dione (PD); dipyridoquinoxaline (DPQ); or DPPZ) were developed and characterised by single X-ray crystallography. Solution stabilities were studied by cw-EPR, HYSCORE, and ENDOR spectroscopies and demonstrate preferred geometries where phenanthrene is coordinated to the copper(II) TPMA core. Complexes with Phen, DPQ, and DPPZ ligands have enhanced DNA binding activity with DPQ and DPPZ compounds showing excellent intercalative effects. These complexes are effective AMNs and analysis with spin-trapping scavengers of reactive oxygen species and DNA repair enzymes with glycosylase/endonuclease activity demonstrate distinctive DNA oxidation chemistry compared to classical Sigman and Fenton-type reagents.

II. 2. Introduction

Small molecules that cleave DNA play important roles in gene editing and cancer chemotherapy. They mimic the cleavage portion of natural endonuclease machinery by cutting DNA molecules at or near specific base sequences. As they are versatile and amenable to engineering, coordination compounds with artificial metallo-nuclease (AMN) activity are an attractive alternative to natural nucleases where, despite their sequence specificity, limited selectivity impedes precise cleavage of longer DNA fragments.[1–3] AMNs may also offer therapeutic advantages over native nucleases which are sensitive toward degradation by proteolytic enzymes. Additionally to hydrolysis, AMNs provide another pathway for cutting DNA. Here, cleavage occurs by DNA oxidation, mediated by reactive oxygen species (ROS), and contributes toward therapeutic utility by damaging the genome of cancer cells to impede faithful cell replication.[4–6] DNA oxidation by metallo-nucleases is generally irreversible and relies on binding of the activated AMN to its requisite target site *via* groove binding, insertion or intercalation interactions.[7] Since these

interactions rely on the shape and charge of the complex, the synthesis of selective and robust inorganic scaffolds—and the building of effective biomimetic enzymes[8–11]—is an important research goal for assembling bioactive materials and in exploring the requirements for their biological use.

Copper compounds are attractive choices for AMNs given their biologically-accessible redox properties and wide structural variability.[12] Another factor is the bioavailability and essentiality of copper to the human body where a daily uptake of between 1.0 – 3.0 mg is required.[13] Copper ion homeostasis may, therefore, facilitate both tolerance and the active transport of exogenous copper-based AMNs.[14] A wide range of copper(II) AMNs are known[15–17] but one of best studied examples is Sigman's reagent [Cu(1,10-phenanthroline)$_2$]$^{2+}$ (Cu-Phen)[18] which oxidises DNA in the presence of a reductant and/or oxidant. Cu-Phen, in its reduced Cu(I) form, intercalates A-T rich sites in the minor groove before abstracting a hydrogen atom from the C1′ position of deoxyribose to mediate strand excision.[4,19–22] Inspired by Cu-Phen, heteroleptic systems with designer phenazine intercalators (*e.g.* dipyridoquinoxaline (DPQ), dipyridophenazine (DPPZ), and benzo[*i*]dipyridophenazine (DPPN)) have been reported by this group.[23,24] Significantly, the presence of phenazine ligands did not alter the electrochemical profile nor ROS catalysis when compared with Cu-Phen. We, along with others, then identified the value of poly-nuclearity in providing enhanced cleavage capability[25,26] and recently demonstrated TA/TA and AT/AT oligonucleotide steps can be discriminated by a *di*-Cu(II)-Phen complex containing an octanedioate bridge.[27] Despite these developments, a limiting factor of Cu-Phen systems is their poor solution stability where speciation, ligand dissociation, and transmetalation occur. To help circumvent this limitation, AMNs were developed with both phenanthroline ligands linked by aliphatic chains (or 'clips', *e.g.* serinol) to yield new complexes with improved DNA cleavage sensitivity.[28–30] Stabilization of the copper complex may also be achieved by coordination to polypyridyl ligands and multidentate complexes thereof (*e.g. tris*-(2-pyridylmethyl)amine[31]; 2,2′,2″-*tris*-(dipicolylamino)trimethyl- amine[32]; and structurally related ligands containing phenoxide or alkoxide bridges[33,34]) receive considerable attention as inorganic models of enzyme cofactors. By mimicking the imidazole coordination environment provided by histidine residues in copper proteins, catalytic and structural insights of copper-oxygen activation by monooxygenases or copper-oxidases is provided.[35,36] Arising from these observations, Karlin, Rokita and co-workers explored the application of mono- and poly-nuclear polypyridyl scaffolds as novel AMNs. The activation of these nucleases is

dependent on reduction to Cu(I) where, depending on the ligand present, selective copper-oxo intermediates form and promote excision of canonical and non-canonical DNA structures.[32,34,37,38] Direct comparisons to Cu-Phen were in some cases explored but it was generally shown that poly-(2-pyridyl) systems invoke an alternative DNA damage pathway to Sigman's reagent. This body of work demonstrated polypyridyl ligands afford high stability for redox cycling whereby the complex scaffold can facilitate both Cu(II) and Cu(I) geometries.

In this work we combine the TPMA (*tris*-(2-pyridylmethyl)amine) polypyridyl ligand scaffold with the copper(II) 1,10-phenanthroline chemical nuclease core to yield a new type of AMN. In designing these complexes, we sought to employ the stabilisation and coordination flexibility of TPMA together with the prominent nuclease activity of copper phenanthroline. A second aspect of this design strategy was the opportunity to introduce designer DNA intercalators into the complex scaffold to potentially facilitate improved binding interactions and oxidation reactions at the nucleic acid interface. Herein we report the synthesis and X-ray structural analysis of a new AMN type of general formula $[Cu(TPMA)(N,N')]^{2+}$ (where *N*,*N*′ is either 2,2-bipyridine (Bipy); Phen; 1,10-phenanthroline-5,6-dione (PD); DPQ; or DPPZ). The solution stability of these complexes was studied by continuous wave EPR (cw-EPR), Hyperfine Sublevel Correlation (HYSCORE), and Davies Electron Nuclear Double Resonance (ENDOR) spectroscopies and demonstrates, in agreement with solid-state analysis, preferred geometries where the ancillary phenanthrene is clearly coordinated to the Cu(II) TPMA core. Complexes with Phen, DPQ, and DPPZ ligands have enhanced DNA binding activity relative to $[Cu(TPMA)]^{2+}$ with DPQ and DPPZ compounds showing excellent intercalative effects by the topoisomerase I-mediated relaxation assay. The complexes are effective AMNs when reduced to Cu(I) and the damage profiles of Phen, DPQ and DPPZ complexes were studied in comparison to $[Cu(TPMA)]^{2+}$ and Cu-Phen controls using **i.**) major groove recognition elements, **ii.**) spin-trapping scavengers of reactive oxygen species (ROS), and **iii.**) DNA repair enzymes with glycosylase and/or endonuclease activity. The combined results demonstrate a new type of AMN with enhanced cleavage activity compared to $[Cu(TPMA)]^{2+}$ with distinctive DNA oxidation profiles compared to classical Sigman and Fenton reagents.

II. 3. Results and Discussion

II. 3.1. Preparation and characterisation of *N*,*N*' ligands and Cu(II) complexes

1,10-Phenanthroline (phen) was oxidized in an acidic environment to yield 1,10-phenanthroline-5,6-dione (PD) in high yield. The quinoxaline and phenazine ligands (DPQ and DPPZ) were generated through Schiff-base condensation reactions of PD with either ethylenediamine or *o*-phenylenediamine respectively according to procedures previously published by this group.[23] All organic ligands were characterized by ^{1}H and ^{13}C nuclear magnetic resonance and also by Fourier transform infrared (FT-IR) spectroscopies. The Cu-TPMA perchlorate salt was generated by reacting TPMA with an equimolar solution of $Cu(ClO_4)_2$ and was isolated as a blue powder in high yield. Cu-TPMA was reacted with 1 equivalent of either Bipy, PD, Phen, DPQ and DPPZ in MeOH in a one-step reaction yielding the respective Cu-TPMA-*N*,*N*' perchlorate complex. Each Cu(II) complex was isolated in moderate to high yields and characterized by elemental analysis, ESI-MS (Appendix A-1), UV-vis (Appendix A-1) and FT-IR spectroscopies. Crystals suitable for X-ray analysis were obtained by slow diffusion of Et_2O into a CH_3CN solution of the complex. To establish spectroscopic evidence for complex solution stabilities, 5 mM solutions of Cu-TPMA-Phen, Cu-TPMA-DPQ and Cu-TPMA-DPPZ were prepared in DMF. UV-vis spectra were recorded at 24 h intervals over 72 h. The complexes did not appear to undergo speciation or dissociation over 72 h as no differences in the *d-d* transition were noted (Appendix A-1, Figure A-5A). To further identify the stability of this class, 5 mM solutions of Cu-TPMA-Bipy were prepared in acetonitrile and were reduced with 1, 3 or 5 mM Na-*L*-ascorbate, which resulted in loss of the *d-d* transition. Oxygen was then supplied to each cuvette and the *d-d* transition was regenerated in each solution (Appendix A-1, Figure A-5B).

The five Cu-TPMA-*N*,*N*' complexes have broadly similar structures and (Figure II-1 and Appendix A-2 Figure A-6); a common atom numbering scheme is used in each case. The copper(II) ions are best described as 6-coordinate, bound to all four nitrogen atom donors of the tripodal ligand and to the bidentate site of the Bipy/Phen derivative (though one of the Cu-pyridine bonds is very long, see below). As expected, there is a tetragonal Jahn-Teller distortion evident in the cations, the apical bonds (to N2 and N40) are distinctly longer than those in the tetragonal plane (Appendix A-2). The small bite angle of the Bipy/Phen derivative (76 - 78°) means that the angular geometry at the copper ion is not regular. One of the Cu– Bipy/Phen bonds is lengthened by the Jahn-Teller extension,

reducing the bite angle further; the resulting stress is probably responsible for the observed twisting of this ligand – the interplanar angles between the two coordinated 6-membered rings is in the range 3 - 14°. Not surprisingly, the largest twist is seen in the bipyridyl complex, followed by the Cu-TPMA-PD analogue. The tertiary amine and two pyridine groups of the TPMA ligand occupy three of the four coordination sites in the tetragonal plane. These pyridine groups (containing N20 and N30) are approximately coplanar, with interplanar angles in the range 9 - 17°. The remaining pyridine group (containing N40) makes a very long apical bond to the copper ion. The Cu-N40 bond length is variable across the series, from 2.5974(14) in Cu-TPMA-Bipy to 2.907(2) in Cu-TPMA-DPQ. The other three strongly bound meridional donors sites (N10, N20 and N30) impose some geometrical constraints on the orientation of the apical pyridine, causing it to tilt and accounting for the irregular bond angles involving N40; instead of a 90° interplanar angle with the pyridine containing N20, the actual interplanar angles are in the range 33 - 46°. In each structure there are two perchlorate anions for each cation and weak C-H•••O and C-H•••N hydrogen bonds linking the cations and anions. Only [Cu(TPMA)(DPPZ)]$(ClO_4)_2 \cdot CH_3CN$ contains solvate molecules.

A

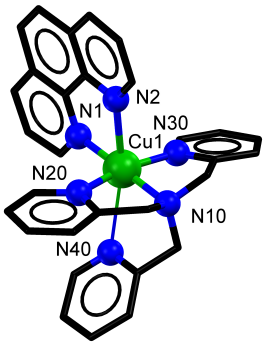

Bond distances (Å)	Cu-TPMA-Bipy	Cu-TPMA-PD	Cu-TPMA-Phen	Cu-TPMA-DPQ	Cu-TPMA-DPPZ
Cu1—N1	2.0071 (13)	2.0083 (19)	2.0207 (14)	2.0373 (19)	2.0037 (15)
Cu1—N2	2.3860 (14)	2.366 (2)	2.3570 (14)	2.2669 (19)	2.3188 (15)
Cu1—N10	2.0337 (13)	2.0292 (19)	2.0329 (14)	2.0386 (19)	2.0233 (15)
Cu1—N20	1.9896 (13)	1.995 (2)	1.9966 (15)	1.9978 (19)	2.0016 (15)
Cu1—N30	2.0049 (13)	2.007 (2)	2.0047 (15)	1.9964 (19)	2.0093 (15)
Cu1—N40	2.5974 (14)	2.667 (2)	2.7678 (15)	2.907 (2)	2.8816 (15)

B

C

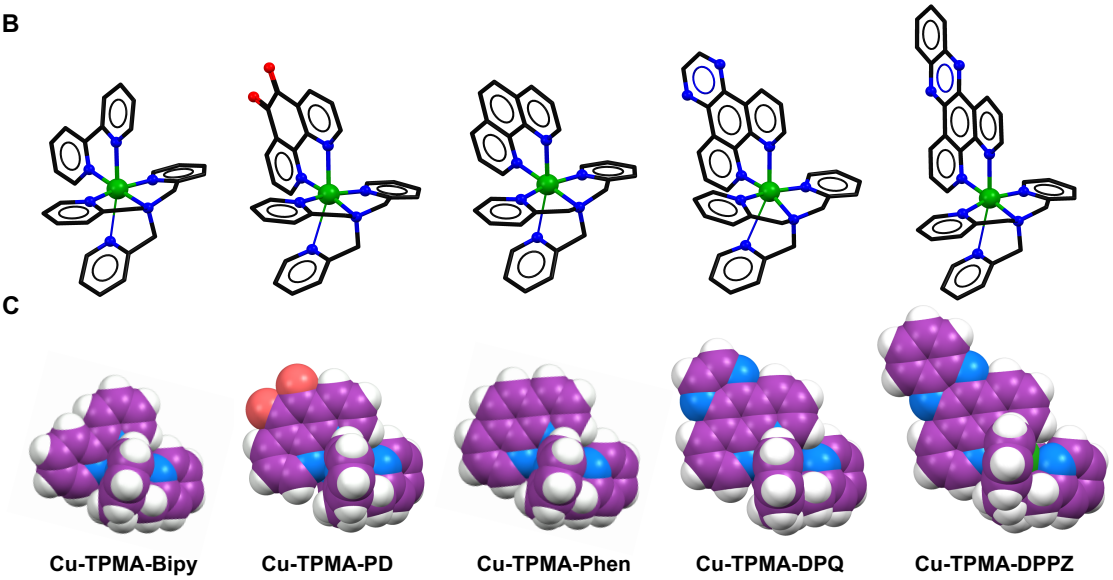

Figure II-1. **A** Perspective view of X-ray crystal structure of Cu-TPMA-Phen cation highlighting the numbering scheme of non-carbon atoms and table outlining the six Cu—N distances found in Cu-TPMA-Bipy, Cu-TPMA-PD, Cu-TPMA-Phen, Cu-TPMA-DPQ and Cu-TPMA-DPPZ complexes respectively; **B** perspective views of the complexes (anions and hydrogen atoms omitted for clarity and the long Cu1—N40 bond is shown as a thin line. Colour scheme: copper, green; nitrogen, blue; carbon, black; oxygen, red); and **C** space filled view of the complex series (Colour scheme: copper, green; nitrogen, blue; carbon, plum; and oxygen, red). See appendix A-2 for further details.

II. 3.2. Electron paramagnetic resonance (EPR)

II. 3.2.1. Continuous Wave (cw-EPR) studies.

cw-EPR was employed to analyze the copper complex solution structures. Depending on the solvent, cw-EPR spectra reflected a distorted octahedral geometry (six-coordinated Cu center), a trigonal bipyramidal (TBP) arrangement (five-coordinated Cu center) or possibly a mixture of these two species (see Appendix A-3 for theory). The EPR spectra of Cu-TPMA-Phen in three different solvents show features that imply contributions from more than one Cu(II) species (Figure II-2A, spectra I). This is evident since at low field (close to $g_{\|}$) a rich structure beyond the typical four-line Cu pattern is observed. Deconvolution analysis then revealed these signals can be simulated assuming two types of spectra: an

almost axial signal with $g_{\|} > g_{\perp}$ and a rhombic signal with $g_x > g_y > g_z$ (Appendix A-3, Figure A-7). The first is typical for elongated tetragonal-octahedral or square-planar geometry with a $d_{x^2-y^2}$ ground state whereas the other occurs for complexes with a d_{z^2} ground state and TBP stereochemistry.[39–41] For all complexes except Cu-TPMA-Bipy both hexa- and penta-coordinated structures contribute to the EPR spectra in organic solvents (Appendix A-3). In the Bipy complex, dissolution in DMF or DMSO yields almost identical spectra where a clear TBP geometry is evident (Figure II-2B). Since similar solvent-dependent spectra are observed for all complexes (Appendix A-3, Figure A-7), an in-depth study was performed using Cu-TPMA-Bipy and Cu-TPMA-Phen.

Upon the addition of excess water (solvent:DI water; 1:19), Cu-TPMA-Phen spectra are dominated by a clean five-coordinate signal (Figure II-2A, spectra II). To elucidate whether this water-induced modification was a transient solvent-dependent effect, the complex was dissolved in the mixtures of DMSO/water (1:19) and CH_3CN/water (1:19), then freeze-dried to remove water and re-dissolved in DMSO and CH_3CN, respectively. In both solvents the initial spectra were recovered, which indicates conformation differences are due to an interaction with the solvent with no permanent modification of the first coordination sphere (Figure II-2A, spectra III).

II. 3.2.2. Pulse EPR studies.

Pulsed EPR experiments such as ENDOR and HYSCORE provide a detailed picture of magnetic interactions between the unpaired Cu(II) *d*-electron and the magnetic nuclei of the ligands. However, these analyses can be performed only on compounds with observable electron spin echo (ESE) and well-defined paramagnetic species with no overlapping EPR spectra. For these reasons, only samples having observable ESE and showing dominant penta-coordinated species such as Cu-TPMA-Bipy in DMF/toluene (1:1) and Cu-TPMA-Phen in DMSO/citrate buffer (1:19) were employed in this analysis. The cw-EPR spectra of both samples are shown in Figure II-2C along with the simulated spectra (generated using parameters given in Table II-1A). The magnetic parameters of the two compounds are identical and resemble reported values for other Cu(II)-TPMA derivatives and complexes with nitrogen-donor ligands characterized by TBP geometry.[39–44] Both complexes are best described by a dominating d_{z^2} ground state, but the non-axial character of the g tensor implies also a possible contribution of the $d_{x^2-y^2}$ orbital, indicative of a penta-coordination halfway between TBP and square-based pyramidal.[41]

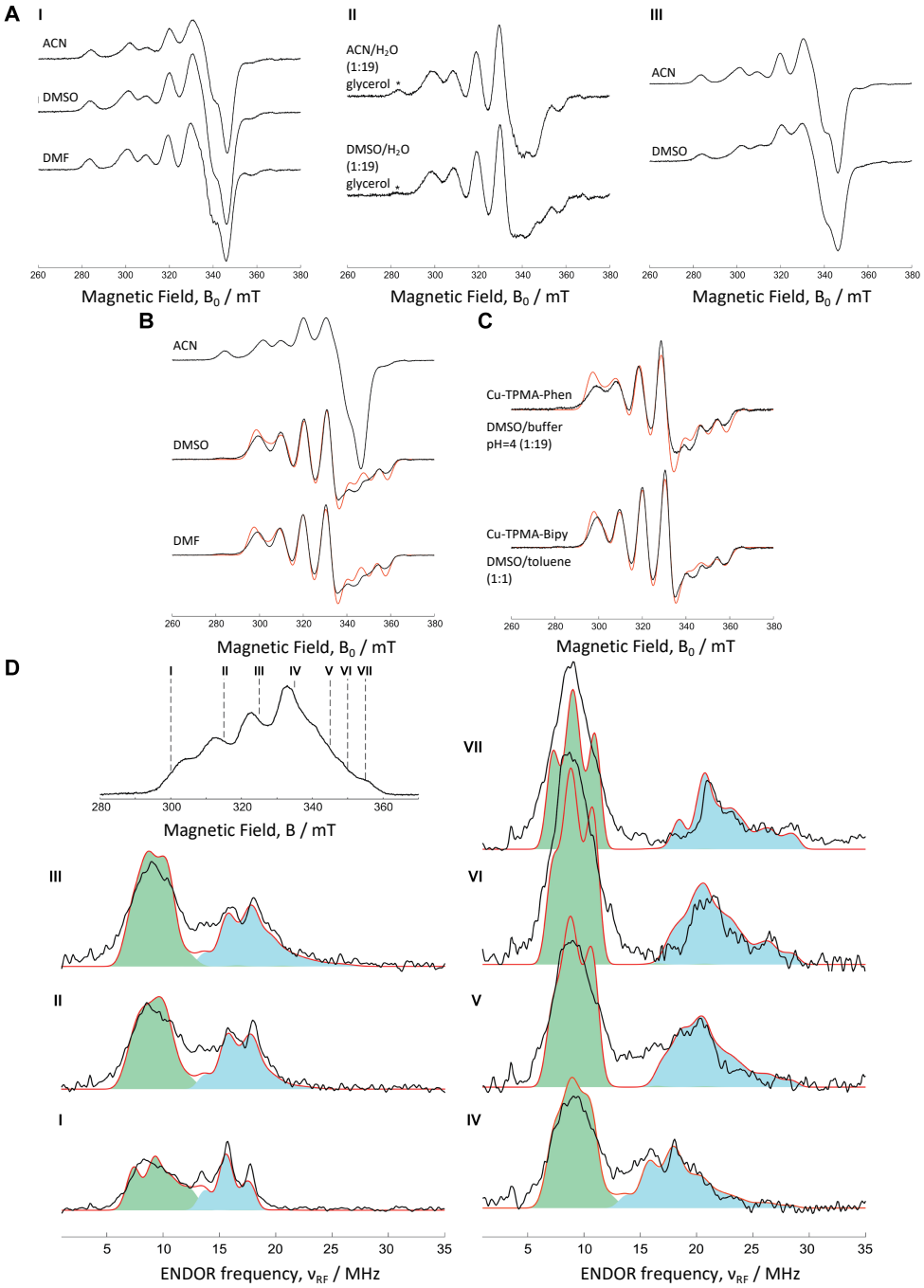

Figure II-2. A cw-EPR spectra of Cu-TPMA-Phen in different frozen solutions measured at 70 K: **I**. Comparison of spectra measured in CH_3CN, DMSO, and DMF showing contributions from both six- and five-coordinated structures; **II**. Spectra in CH_3CN and DMSO after addition of distilled water in excess, showing dominance of the five-coordinated signal. Asterisks denote the position of the low-field transition of the signal assigned to six-coordinated structure; **III**. Recovered spectra in CH_3CN and DMSO after removing water with a freeze-dry process; **B** Cw-EPR spectra of Cu-TPMA-Bipy in different frozen solutions measured at 70 K (black traces) and simulated spectra (red traces) with the paramaters given in Table A-3; **C** Cw-EPR spectra of the two samples Cu-TPMA-Phen (upper) and Cu-TPMA-Bipy (low) in different frozen solutions measured at 70 K (black traces) and simulated spectra (red traces) with the parameters given in Table A-3; and **D** ENDOR spectra of Cu-TPMA-Bipy in DMF/toluene (1:1) frozen solution measured at different observer positions as shown in the field-swept FID-detected EPR spectrum (top left). Black lines: experiment; red lines: simulations. Simulations were performed assuming two axial (light blue) and three equatorial (light green) nitrogen atoms. For parameters see Table II-1B and appendix A-3.

Due to the limited excitation profile of microwave pulses and large anisotropy of the EPR spectrum, only molecules with a specific range of orientations with respect to the direction of the static magnetic field may contribute to the corresponding ENDOR spectrum.[45] Cu-TPMA-Bipy was identified as a suitable complex to analyze (Figure II-2D, spectra VII) and the ENDOR spectrum was measured at high-field (close to g_z) to give a single-crystal like pattern from molecules having their g_z axis parallel to the magnetic field. Here, two sets of peaks were identified: a strong structureless signal in the 5−13 MHz region, centered at ~9 MHz, and a less intense signal centered at ~25 MHz exhibiting a quadruplet structure with a splitting of *ca*. 2.4 MHz. The latter is typical for strongly coupled ^{14}N nuclei, $A > 2\,\nu_N$, where A is the hyperfine coupling constant and $\nu_N = 1.09$ MHz (at $B_0 = 355$ mT) the nuclear Zeeman frequency. In this case the peaks corresponding to the four nuclear transition frequencies are centered about $A/2$ and split by $2\,\nu_N$ and $3P_z$. The parameters $A = 50$ MHz and $P_z = 0.8$ MHz obtained directly from the spectrum are typical for axially coordinated nitrogen atoms in TBP complexes with a d_{z^2} ground state where the large hyperfine coupling occurs from the overlap with the ^{14}N σ donor orbital.[44,46] This is supported by measurements at different field positions away from the z direction which causes a peak shift to lower frequencies. For instance, the ENDOR spectrum (2D I) measured at the low-field end of the EPR line (perpendicular to g_z) shows a triplet centered about 15 MHz, implying $A = 30$ MHz along this direction (Table II-1B). Although these parameters describe the basic features of the signal assigned to the axial nitrogen atom, a detailed inspection in the area above 15 MHz shows that most probably there are additional overlapping signals. This is evident in the spectrum measured along g_z, where a peak close to 21 MHz changes the intensity of the quadruplet. This peak could be assigned to the high-frequency transition due to a proton coupling of 11 MHz as was clearly observed in the corresponding HYSCORE spectrum (*vide infra*). While ENDOR measurements shown in Figure II-2D use short pulses that can indeed suppress signals from weakly-coupled protons (Appendix A-3, Figure A-9), the hyperfine contrast selectivity[47] for a mw π-pulse of 32 ns and a hyperfine coupling of 11 MHz is negligible. This indicates with the current experimental setup, the proton peak is not suppressed. Moreover, as the corresponding low-frequency proton peak at 9 MHz overlaps with the broad signal, it is not possible to unambiguously assign the 21 MHz peak to additional strongly-coupled nitrogen. However, the appearance of peaks around 15-17 MHz (i.e. area of effective suppression of weakly-coupled proton signals) suggests the presence of second axially coordinated nitrogen with

similar but slightly modified parameters to the previous one. The assumption of two axially coordinated nitrogen atoms with the parameters of Table II-1A provides good agreement between the experimental and simulated ENDOR spectra.

Table II-1. A EPR parameters of the samples shown in Figure II-2C obtained from simulations of spectra dominated by five-coordinated signals;[a] **B** Hyperfine and nuclear quadrupole coupling parameters and spin densities for axial and equatorial nitrogens directly coordinated to Cu ion as obtained from simulations of ENDOR spectra for Cu-TPMA-Bipy.[b]

A

Sample	g_x	g_y	g_z	$A^{Cu}{}_x$ (MHz)	$A^{Cu}{}_y$ (MHz)	$A^{Cu}{}_z$ (MHz)
Cu-TPMA-Phen*	2.214	2.181	1.999	327	249	216
Cu-TPMA-Bipy**	2.208	2.180	1.999	339	268	196

[a] The uncertainty in the determination of the hyperfine coupling (absolute values) is 20 MHz and in *g* values is 0.002.* in DMSO/buffer; ** in DMF/toluene.

B

N atom	A_x (MHz)	A_y (MHz)	A_z (MHz)	a_{iso} (MHz)	ρ_{2s}	ρ_{2p}	ρ_{2p}/ρ_{2s}	e^2qQ/h (MHz)	η
axial	30.8 ±0.2	30.8 ±0.2	50.5 ±0.2	37.4 ±0.2	0.024	0.138	5.75	3.8 ±0.4	0
axial	30.8 ±0.5	30.8 ±0.5	43.5 ±0.2	35.0 ±0.4	0.023	0.089	3.87	2.4 ±0.4	0
equatorial[c]	20.0 ±1.0	17.5 ±1.0	17.5 ±1.0	18.3 ±1.0	0.012			2.8 ±1.0	0.1

[b] In all cases the *z*-axis of the quadrupole coupling tensor (largest *P* value) is along the direction of each Cu-N bond. [c] The numerical simulations shown in Figure 2D use three equatorial nitrogen atoms with values ranging within the given limits.

The analysis of the broad ENDOR signal is less straightforward due to the lack of a pattern with well-resolved lines. The centre frequency (~9 MHz) of the broad line implies a strong coupling of A~18 MHz whereas its insensitivity on the observer position of the measurement indicates a hyperfine coupling of modest anisotropy. Although there are few ENDOR studies on Cu(II) TBP complexes in the literature, similar signals have been reported and assigned to equatorial nitrogen atoms[44,48] based on the possibility of their much weaker interaction with the d_{z^2} orbital. In this study, the lack of fine structure, even in the single-crystal like observer position (B_0 = 355 mT), indicates inequality of the three equatorial nitrogens or/and hyperfine strain effects due to structural disorder of complexes. In this respect, the magnetic parameters given in Table II-1B for the equatorial nitrogens are mean values obtained by spectral simulations in order to reproduce the basic features of the experimental spectra. Interestingly, the overall simulations, including two axial and three equatorial nitrogens, reproduce quite accurately the positions of peaks as well as their relative intensities.

The spin densities on the two strongly-coupled nitrogens can be directly obtained from the parameters of Table II-1B, assuming the anisotropic hyperfine coupling to be mainly determined by the through-bond dipolar hyperfine coupling. The latter describes the *p*-

character of the bond between the metal d_{z^2} orbital and the nitrogen σ hybrid orbital. This approximation is valid when the through-space dipolar coupling is much smaller than the total magnitude of the nitrogen hyperfine coupling. Assuming 100% of spin density as localized on the metal ion, the point-dipole approximation of Eq. A-2 gives:

$$T_d = \frac{\mu_0}{4\pi h}\frac{g\beta_e g_n \beta_n}{r^3} \qquad (1)$$

where g and g_n are the electron and ^{14}N nuclear g factors, respectively, β_e and β_n are the Bohr and nuclear magnetons, respectively, and r is the metal–nitrogen distance. Using a distance of r = 2.0 Å (e.g. Cu-N10 distance from crystal structure) we estimate T_d = 0.71 MHz which verifies the validity of approximation. From a_{iso} and $T = a_{iso} - A_{||}$, the spin density on the nitrogen 2*s* and 2*p* orbitals, $\rho_{2s} = a_{iso} / a_0$ and $\rho_{2p} = T / T_0$, respectively, can be calculated with a_0 = 1538 MHz and T_0 = 47.8 MHz.[49] The hybridization states of the nitrogen atoms can be probed through the ρ_{2p}/ρ_{2s} ratios determined from the ENDOR analysis. Interestingly, for one of the two axial atoms the ratio 5.75 is much larger than 2 and 3 expected for regular sp^2 and sp^3 hybrids, respectively. Similar large ratios have been observed earlier for the case of Cu(II) complexes with TBP geometry and have been assigned to the amine nitrogen of the tripodal ligand.[44,48] Although hybridization ratios are not simply determined by geometry, the large deviation from the regular sp^3 value can be explained in terms of a small distortion of about 4° in the Cu−N−C bond angle θ from the normal tetrahedral value of 109.5° (in good agreement with the crystal structure where the Cu-N-C bond angle is in between 105-111°). On the other hand, the second axial nitrogen with the ratio 3.87 is closer to sp^2 hybridization and can be assigned to a pyridyl nitrogen. This is also supported by the estimated nuclear quadruple coupling constant which is in good agreement with the corresponding values found for Cu(II)–pyridine complexes.[50] Finally, the small hyperfine coupling anisotropy of 0.8 MHz obtained for equatorial nitrogens shows that it is mainly determined by the through-space dipolar coupling. Assuming sp^2 hybridization, and based on ρ_{2s} = 0.012, one would expect ρ_{2p} = 0.024 that corresponds to a dipolar coupling of about 1.1 MHz. Since this is comparable to the experimental error, a safe conclusion about ρ_{2p} of the equatorial nitrogen atoms cannot be made on this occasion. Nevertheless, the above analysis and the data given in Table II-1B show that the total spin density distributed among the ligand atoms amounts to about 34%.

Similar ENDOR spectra were obtained for Cu-TPMA-Phen in DMSO/buffer. Although the signals assigned to equatorial nitrogen atoms are the same with Cu-TPMA-

Bipy in DMF/toluene, the signal of the axial amine nitrogen shows a small but observable shift of about 0.6 MHz to lower frequencies (Appendix A-3, Figure A-10). This corresponds to a reduction of hyperfine coupling constants by approximately 1.2 MHz resulting in $a_{iso} \cong 36$ MHz. This change implies a smaller distribution of spin density on the ligand atoms and can be attributed to the slightly different bonding properties of the two ligands, i.e. Bipy and Phen, or to solvent effects. The same trend is also observed for a hyperfine coupling which is assigned to a hydrogen atom of the ligands located in an axial position (vide infra).

II. 3.2.3. ^{1}H and ^{14}N HYSCORE studies.

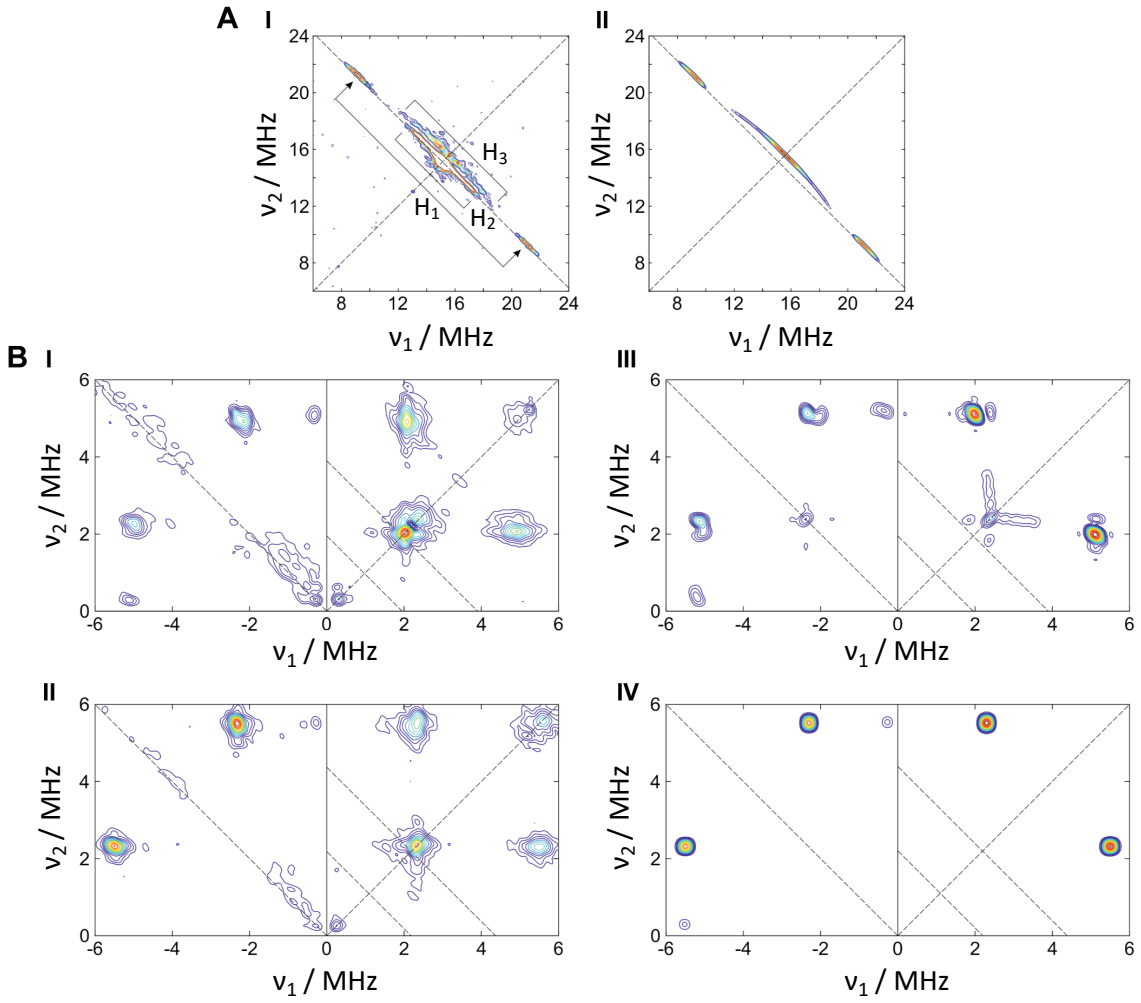

Figure II-3. A ^{1}H-HYSCORE spectra of Cu-TPMA-Bipy in DMF/toluene (1:1) frozen solution measured along g_z (B_0 = 355 mT). **I.** Experimental spectrum. **II.** Simulated spectrum assuming two proton couplings, H_1 with A = [8.7, 8.7, 14.7] MHz and H_3 with A = [-7.13, -7.13, 8.74] MHz. Anti-diagonal lines denote the ^{1}H-Larmor frequency. **B** ^{14}N-HYSCORE spectra Cu-TPMA-Bipy in DMF/toluene (1:1) frozen solution measured at two different observer positions: **I.** B_0 = 317 mT and **II.** B_0 = 355 mT. **III.** and **IV.** show the corresponding simulated spectra. Anti-diagonal lines denote harmonics of the ^{14}N-Larmor frequency at ν_N and $2\,\nu_N$. For simulation parameters see text.

Smaller hyperfine couplings with atoms out from the first coordination sphere can be probed with the 2D-HYSCORE method. The HYSCORE spectrum of Figure II-3A, spectra I, reveals three sets of correlation peaks that lie on the ^{1}H anti-diagonal of the (+,+) quadrant. Therefore, these peaks are assigned to weakly- coupled protons of the ligands and/or solvent molecules. More specifically, the intense peaks marked as H_2 in Figure II-3A, spectra I, are very close to the anti-diagonal and spread over a range of about 5 MHz, implying small values for both the isotropic and the anisotropic hyperfine coupling constants. These proton peaks are typically ascribed to ligand hydrogen atoms that are away from the Cu(II) ion and contribute, together with solvent hydrogen atoms (so-called matrix protons), to an intense signal around the ^{1}H Larmor frequency. Contrary to this, the signal marked as H_1 is characterized by two peaks which are well-separated by about 11 MHz and show a small deviation from the anti-diagonal. Assuming axial hyperfine coupling interaction with isotropic component a_{iso} and anisotropic tensor $[-T, -T, 2T]$, the hyperfine coupling tensor in the principal axes system is given by $[A_1, A_2, A_3] = [a_{iso} - T, a_{iso} - T, a_{iso}+2T]$. With the reasonable assumption that the anisotropic part for protons is mainly determined by the dipolar coupling given in Eq.1 ($T=T_d >0$), the detailed analysis of the spectrum (Appendix A-3, Figure A-11) reveals T = 2.0 ± 0.2 MHz and two possible solutions for a_{iso}, namely a_{iso} = 10.7 ± 0.1 MHz and a_{iso} = –12.7 ± 0.1 MHz. From the determined dipolar coupling T and Eq.1 the electron-proton distance r = 3.4 ± 0.2 Å can be inferred. Moreover, as shown in Figure II-3A, spectra II, a good complete spectrum simulation with these parameters requires the use of an angle $\theta = 35° \pm 5°$ between the g_z direction and the electron-proton vector. Although the sign of a_{iso} cannot be directly determined from the HYSCORE spectrum, the large $|a_{iso}|$ of both solutions implies considerable spin densities on neighboring atoms. A negative isotropic hyperfine coupling constant results from spin polarization when the unpaired electron is delocalized only into the ligand π system. On the other hand, when the unpaired electron is transferred into the σ system of the ligands, e.g. when the metal and the ligand are covalently bonded, the isotropic hyperfine coupling of protons is dominated by this transfer and becomes positive. The magnitude of the experimentally determined $|a_{iso}|$ favors the solution with a_{iso} = 10.7 ± 0.1 MHz.

The determined distance r and the orientation of the hyperfine coupling tensor in the g-frame (described by angle θ) can give information about the origin of that proton. Based on the crystal structure, the distance 3.4 Å is within experimental error compatible with

hydrogen atoms in CH_2 fragments of the tripodal ligand (attached to C21, C31 or C41 atoms, Appendix A-2, Figure A-6A). Moreover, the angle $\theta = 35°$ supports further this assignment because it is in line with the amine nitrogen occupying an axial position as revealed from the ENDOR analysis. In addition, the corresponding signal (H_1) for the case of Cu-TPMA-Phen in DMSO shows a small but measurable difference in the hyperfine coupling parameters. More specifically, the analysis gives $a_{iso} = 9.8 \pm 0.1$ MHz and $T = 1.7 \pm 0.2$ MHz (Appendix A, Figure A-12). The smaller hyperfine coupling of the H_1 signal together with the smaller ^{14}N coupling found for the amine nitrogen in the case of Cu-TPMA-Phen, is in line with the assumption that the corresponding hydrogen atom occupies a more or less axial position.

The correlation ridge marked as H_3 in Figure II-3A, spectra I, is distinguished by a large anisotropy as can be seen from its significant displacement from the ^1H anti-diagonal line. Following the same analysis and assuming $T > 0$, we find $T = 5.3 \pm 0.2$ MHz that corresponds to the electron-proton distance $r = 2.5 \pm 0.2$ Å. It should be noticed that in this case both alternative solutions $a_{iso} = -1.8 \pm 0.2$ MHz and $a_{iso} = -3.5 \pm 0.2$ MHz give negative values which means that for this proton coupling a_{iso} is determined by spin polarization effects. The complete simulation shown in Figure II-3A, spectra II, gives best results for $\theta = 25° \pm 5°$. Based on these findings we can tentatively assign signal H_3 to a pyridine hydrogen atom (either from the TPMA or Bipy moieties) where the associated nitrogen occupies an equatorial position. Given that the z axis coincides with the N1-Cu-N10 direction, possible candidates for this coupling are hydrogen atoms attached to C26, C36, C46, or C10, with the latter being favored due to a better agreement of the orientation with $\theta = 25°$. Note that no such proton coupling was detected in the HYSCORE spectrum of Cu-TPMA-Phen in DMSO (Appendix A-3, Figure A-12).

The HYSCORE spectra of Cu-TPMA-Bipy in DMF/toluene show additional cross-peaks at low frequencies in both (-,+) and (+,+) quadrants as illustrated in Figure II-3B, spectra I and II. The most intense peaks appear at (4.9, 2.1) MHz and (2.1, 4.9) MHz for the measurement perpendicular to g_z, and at (-5.5, 2.3) MHz and (-2.3, 5.5) MHz for the measurement along g_z. The signals are typical for weak ^{14}N hyperfine couplings A which are close to the so-called "cancellation condition", $A \approx 2\nu_N$. The largest (in absolute value) frequency is assigned to the double-quantum transition ($\Delta m_I = 2$) of one of the two electron spin manifolds (Eq A-5) and is observed at approximately $2\nu_N + a_{iso}$, whereas- the other correlation frequency is assigned to one of the three nuclear quadrupole resonance (NQR)

frequencies, $\nu_0 = 2K\eta$ and $\nu_\pm = K(3\pm\eta)$. From this first-order analysis a hyperfine coupling constant of a_{iso} = 3 MHz can be inferred. The complete simulated spectra shown in Figure II-3B, spectra III and IV reproduce well the basic features of experimental spectra and revealed the parameters $[A_x, A_y, A_z] = [2.5, 2.6, 2.9] \pm 0.2$ MHz for the hyperfine interaction and $e^2qQ/h = 2.8 \pm 0.1$ MHz, $\eta = 0.15 \pm 0.05$ for the nuclear quadrupole coupling. The assumption of the Euler angle $\beta = 90°$ for tensor **P** was mandatory in order to get correct intensities for the correlation peaks.

The value a_{iso} = 2.7 MHz is in the range observed for the so-called "remote" nitrogen atoms that possess some spin density due to the overlap with the orbital of the unpaired electron but are not directly coordinated to the metal ion.[51] Interestingly, the observed a_{iso} exceeds considerably the typical value of 1.3-1.4 MHz found for nitrogen atoms two bonds away from the Cu(II) ion.[52] However, it is known that details of spin delocalization and polarization may determine decisively the strength of a_{iso} and give values of up to 5 MHz even for nitrogen atoms three bonds away.[53] Therefore, the assignment of remote nitrogen atoms based exclusively on a_{iso} is not possible. On the other hand, we can attempt to estimate the Cu–N distance assuming the dipolar coupling constant $T = 0.12 \pm 0.05$ MHz obtained from the simulation of HYSCORE spectra. Eq. A-2 gives $r = 3.6 \pm 0.5$ Å which is compatible with a configuration where one of the pyridine moieties of TPMA is dissociated and the corresponding N40 atom occupies a remote position. In this scenario, the necessary spin density on N40 is transferred through the strongly-coupled amine nitrogen (N10) which is directly coordinated to Cu ion and possesses large spin density due to the overlap of its 2s and 2p atomic orbitals with the d_{z^2} orbital. Moreover, the estimated nuclear quadrupole coupling constant is very close to that of pyridine nitrogens and this further supports the previous assignment.

HYSCORE measurements on Cu-TPMA-Phen in DMSO/citrate buffer with pH=4 (1:19) did not reveal this ^{14}N spectrum which raised the question whether the observed signal in Cu-TPMA-Bipy stems from the nitrogen atom of an axially coordinated solvent (DMF) molecule. Measurements of Cu-TPMA-Bipy in DMSO/toluene did not show such signal, however, this result cannot be safely evaluated because the phase memory time was very fast in this occasion. On the other hand, a comparison with Cu-TPMA-Phen in pure solvents (without water) cannot be done since in this case a mixture of two species is observed (Figure II-2A, spectra I). Therefore, the origin of the remote nitrogen signal of Figure II-3B is not completely established yet.

II. 3.3. DNA Binding Experiments

II. 3.3.1. Competitive Ethidium Bromide displacement and topoisomerase I-mediated relaxation.

DNA binding constants of the complexes were determined by high-throughput saturation binding analysis using the fluorogenic intercalator EtBr with calf thymus DNA. The procedure involves treating a limited concentration of DNA with an excess of EtBr which saturates available intercalative binding sites between DNA bases resulting in significant fluorescence enhancement from the inhibition of excited state proton transfer to polar solvent molecules upon binding to DNA.[15] Only Cu-TPMA-Phen, Cu-TPMA-DPQ, and Cu-TPMA-DPPZ complexes had detectable binding to ctDNA with K_{app} values in the range of *ca*. 3 x 10^5 $M(bp)^{-1}$ (Table II-2). These binding constants are in line with a number of *mono*- and *di*-nuclear phenanthroline systems previously reported by this group including $[Cu(Phen)_2]^{2+}$, $[Cu(Ph)(Phen)_2]$, [Cu(Ph)(Phen)], and $[\{Cu(Phen)_2\}_2(\mu\text{-Terph})]$ (where Ph = phthalate; Terph = terephthalate)[55–57] but are lower than $[Cu(Phen)(Phenazine)]^{2+}$ based complexes, possibly due to steric factors imposed by the TPMA ligand.[23]

To characterise the intercalative activity of Phen, DPQ and DPPZ complexes, topoisomerase-I (Topo I) mediated relaxation of negatively supercoiled DNA (pUC19) was examined.[27,58,59] This enzyme is fundamental in biological systems as DNA supercoiling is generated during cellular processes including gene transcription, DNA replication, recombination and repair; it acts by forming a transient break in the DNA backbone permitting topological relaxation to occur prior to strand resealing. Unwinding by copper(II) complexes was examined between 0.1 – 400 μM (Figure II-4) and compared directly to EtBr.[58] Although Cu-TPMA-Phen could not unwind pUC19 below 50 μM, Cu-TPMA-DPQ and Cu-TPMA-DPPZ complexes fully relaxed (0) the plasmid at 1.0 μM with higher concentrations generating a positively (+) supercoiled DNA indicating a strong propensity to intercalate. Both DPQ and DPPZ complexes compare favourably to the EtBr control where 0.5 μM unwound pUC19 under identical conditions.

Table II-2. Binding constants of Cu-TPMA-*N,N′* complexes to calf thymus DNA.

Cu-TPMA-*N,N′*	C_{50}[a]	K_{app} (M bp^{-1})[b]
Cu-TPMA-Bipy	>500	–
Cu-TPMA-PD	>500	–
Cu-TPMA-Phen	487.26	2.28 x 10^5
Cu-TPMA-DPQ	263.88	4.20 x 10^5
Cu-TPMA-DPPZ	351.78	3.15 x 10^5

[a]C_{50} = concentration (μM) required to reduce fluorescence by 50%. [b]$K_{app} = K_e \times 12.6/C_{50}$ where $K_e = 8.8 \times 10^6$ M(bp)$^{-1}$

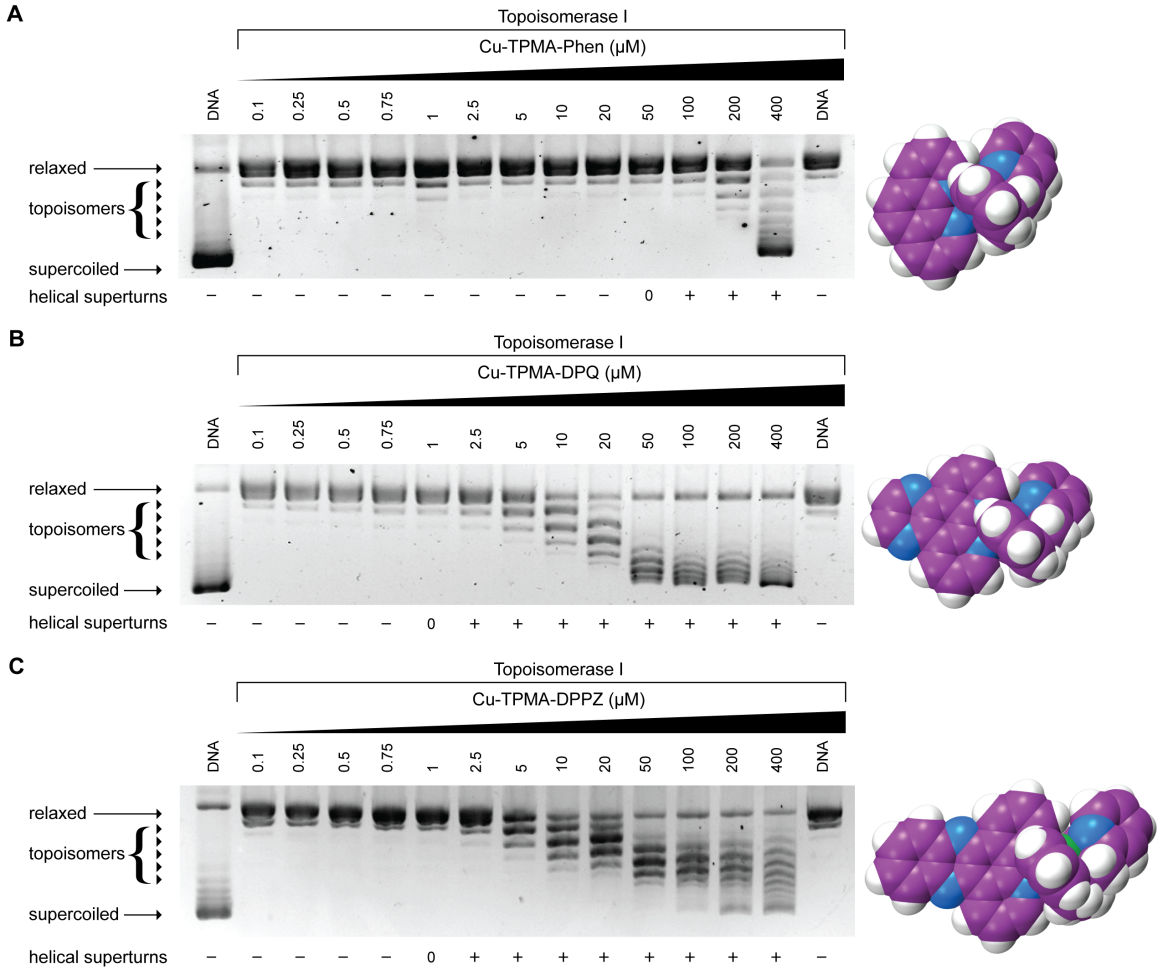

Figure II-4. Release of topological tension from supercoiled plasmid DNA using the topoisomerase I-mediated relaxation assay in the presence of increasing concentrations of **A** Cu-TPMA-Phen; **B** Cu-TPMA-DPQ and **C** Cu-TPMA-DPPZ along with space-filling view of respective complex. Colour scheme: copper, green; nitrogen, blue; carbon, plum; and oxygen, red).

II. 3.3.2. Artificial Chemical Nuclease Activity

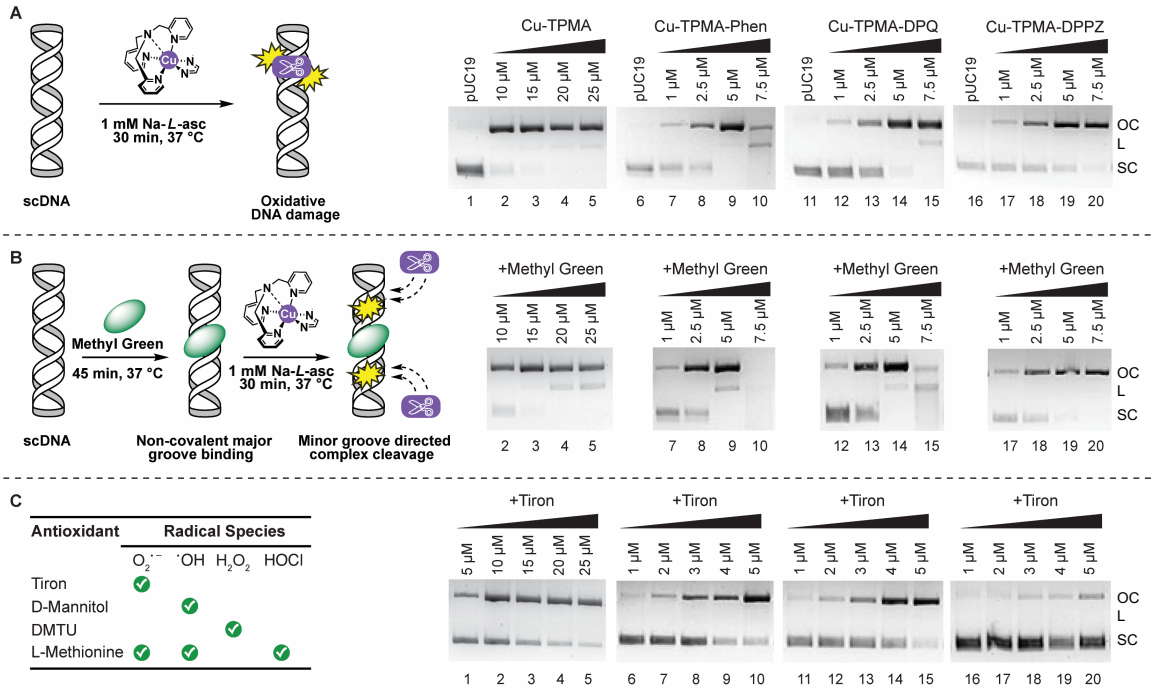

Figure II-5. A Cartoon representation of nuclease experiment where 400 ng pUC19 supercoiled DNA was treated with increasing concentrations of Cu-TPMA (lanes 2-5), Cu-TPMA-Phen (lanes 7-10), Cu-TPMA-DPQ (lanes 12-15) and Cu-TPMA-DPPZ (lanes 17-20) in the presence of 1 mM Na-*L*-ascorbate. **B** Cartoon representation of DNA cleavage in the presence of non-covalent agent methyl green when 400 ng pUC19 supercoiled plasmid was pre-treated with the major groove binding agent methyl green prior to the introduction of Cu-TPMA (lanes 2-5), Cu-TPMA-Phen (lanes 7-10), Cu-TPMA-DPQ (lanes 12-15) and Cu-TPMA-DPPZ (lanes 17-20) in the presence of 1 mM Na-*L*-ascorbate. **C** Table showing ROS scavenging species employed in this study where 400 ng pUC19 supercoiled DNA was treated with increasing concentrations of Cu-TPMA (lanes 1-5), Cu-TPMA-Phen (lanes 6-10), Cu-TPMA-DPQ (lanes 11-15) and Cu-TPMA-DPPZ (lanes 16-20) in the presence of 1 mM Na-*L*-ascorbate and 10 mM scavenging species 4,5-dihydroxy-1,3-benzenedisulfonic acid (Tiron). (Related gels can be found in appendix A-4).

Since DNA damage is dependent on a number of factors including, but not limited to, plasmid conformation, exogenous oxidant and/or reductant, competing chelating agents and complex exposure concentration/time, a number of experimental conditions were explored. The most suitable conditions to compare this series involved the addition of exogenous reductant (ascorbate) to the complex, followed by 30 min incubation with pUC19, and finally deactivation with excess sodium ethylenediaminetetraacetate (EDTA). Under these conditions Cu-TPMA (10 – 25 µM) was found to nick DNA and fully convert supercoiled (SC) to open circular (OC) DNA (Figure II-5A, lanes 1 – 5) while Cu-TPMA-Bipy and Cu-TPMA-PD were incapable of mediating appreciable oxidative DNA damage (Appendix A–4, Figure A-13). Cu-TPMA-Phen, Cu-TPMA-DPQ and Cu-TPMA-DPPZ complexes however, all produced OC DNA at lower concentrations (1.0 – 7.5 µM) with

linear conformations (L) arising with Cu-TPMA-Phen and Cu-TPMA-DPQ complexes (Figure II-5A, lanes 6-20). The overall trend in chemical nuclease activity is Cu-TPMA-Phen > Cu-TPMA-DPQ > Cu-TPMA-DPPZ >> Cu-TPMA which indicates the ancillary *N*,*N*′ phenanthrene group is critical to ROS catalysis at the DNA interface.

II. 3.3.3. Oxidative DNA cleavage in the presence of non-covalent DNA binding agents

To probe the potential site of DNA oxidation, the major groove binding agent methyl green (MG) was pre-incubated with supercoiled plasmid DNA prior to the addition of each test complex in a reducing environment. MG significantly enhanced the oxidative chemical nuclease activity of Cu-TPMA-Phen (Figure II-5B lanes 7-10) and Cu-TPMA-DPQ (Figure II-5B lanes 12-15) when compared with MG-free experiments (Figure II-5A lanes 10 and 15). Here, plasmid DNA was completely degraded by 7.5 μM of Cu-TPMA-Phen with extensive shearing evident in the Cu-TPMA-DPQ treated sample (Figure II-5B lanes 9-10 and 14-15). MG-directed enhancement of Cu-TPMA and Cu-TPMA-DPPZ complexes also occurred where the emergence of linear (L) DNA with 25 μM treatment of Cu-TPMA (Figure II-5B lane 5), and full conversion of SC to OC by 5.0 μM of Cu-TPMA-DPPZ (Figure II-5B lane 20) was observed. These results indicate the minor groove as the main site of oxidative DNA damage; by limiting access to the major groove with MG, the minor groove becomes 'primed' for DNA-metal complex interactions[24] and, for this series significant additional damage was observed.

II. 3.3.4. DNA damage mechanism

In the absence of added reductant, neither Cu-TPMA or the five Cu-TPMA-*N,N*′ derivatives fully converted SC-DNA to OC-DNA over an extended concentration range (Appendix A-4, Figure A-14). This result suggests AMN activity requires exogenous reductant to release the active Cu(I) species that catalyses ROS generation at the DNA interface. To shed further light on this pathway, a variety of ROS specific scavengers of disodium 4,5-dihydroxy-1,3-benzenedisulfonate (tiron), D-mannitol, L-methionine, and *N*,*N*′-dimethylthiourea (DMTU) were employed to probe the role of superoxide ($O_2^{\bullet-}$), the hydroxyl radical ($^{\bullet}OH$), hydrogen peroxide (H_2O_2), hypochlorous acid (HOCl) or a combination thereof. Results suggest $O_2^{\bullet-}$ is the most prevalent radical species involved in the cleavage mechanism as in all cases, pre-incubation with tiron significantly impeded AMN activity (Figure II-5C). In these experiments, delayed onset of OC-DNA formation, inhibition of L-DNA, and the protection of SC-DNA were evident. H_2O_2 is also generated

as part of the mechanism as DMTU somewhat impeded chemical nuclease activity (data not shown). Interestingly, scavenging the •OH radical had no influence on DNA cleavage and these results were validated in two independent experiments using D-mannitol and DMSO. These findings contrast with the DNA damage mechanism of Cu-Phen-Phenanthrene type complexes where the most prevalent species are •OH and H_2O_2.[24] To our knowledge, this DNA oxidation profile is unique for *mono*-nuclear systems and the closest examples are from the *di*-nuclear [Cu_2(*tetra*-(2-pyridyl)-NMe-naphthalene)Cl_4] (Cu_2TPNap) complex[25] and some other multi-nuclear systems.[33,37] Additionally, since the •OH radical is not significant here, AMN activity departs from classical Fenton-type or Haber-Weiss pathways.

II. 3.3.5. DNA repair enzyme recognition

Repair enzymes are intrinsic check-points present in pathways such as the base-excision repair (BER) mechanism to restore spontaneous DNA decomposition and mis-incorporation of mismatch sites, oxidized lesions and/or alkylated bases during the cell cycle.[60] A range of enzymes isolated from both prokaryotic and eukaryotic sources can recognize specific nucleoside modifications and excise the damage site to prime for subsequent repair processes. We designed cleavage experiments to identify the mechanism of oxidative damage utilizing a selected range of repair enzymes. Repair proteins with sole or combined lesion recognition, known as glycoylases, can incise DNA, removing the base and generating abasic sites (AB). Glycoylases and several repair endonucleases also recognise AP (apurine / apyrimidine) sites and mediate strand nicking adjacent to the base-free lesion (Figure II-6A) which can be identified by increased nicked, linear, and sheared forms of plasmid DNA. Specific lesions acted upon by repair enzymes in this study are listed in Figure II-6B and include: formamidopyrimidine [fapy]-DNA glycosylase (Fpg)[61,62] and endonuclease (Endo) III[62,63] that are bifunctional glycosylases with associated AP lyase activity; human alkyladenine (alkyl purine) glycosylase (hAAG)[64,65] that possess base modified recognition properties; and both Endo IV[66] and Endo V[67–70] that nick DNA at AB sites *via* endonuclease activity.

Reaction conditions for Cu-TPMA-Phen, Cu-TPMA-DPQ, Cu-TPMA-DPPZ (0.5 – 2.5 μM) complexes were optimized to initiate cleavage of pUC19 SC-DNA to OC and L forms (Figure II-6C – D lanes 2 – 4) prior to repair enzyme addition (Figure II-6A). These reactions were compared to 1 h exposure of pUC19 to each complex in the absence of repair enzymes (lanes 1-4, Figure II-6C and D). Overall, enhanced cleavage activities in the order

hAAG > Endo V > Endo III > Fpg were identified (see Appendix A-4, Figure A-17 for the full set of results) with limited change or inhibition occurring in the presence of Endo IV (Figure II-6D). Control experiments involving Cu-Phen (0.5 – 2.5 μM), Cu-TPMA (1.0 – 20.0 μM) and the hydroxyl radical (•OH) generated from a $Cu^{+/2+}/H_2O_2$ Fenton system were examined for comparative purposes (Figure II-6C and Appendix A-4, Figure A-16). Here, enhanced activity by Cu-Phen in the presence of Endo III (APyrimidine) but not FpG (APurine) indicates preferential oxidative damage of thymine residues. pUC19 in the presence of Fenton's reagent underwent additional cleavage by FpG, Endo III, and Endo IV which supports formation of oxidized purine and pyrimidine bases together with abasic sites by the •OH radical. Interestingly, DNA damage by phenanthroline-containing complexes (Cu-TPMA-Phen and Cu-Phen) was attenuated upon addition of Endo IV and we propose that this inhibition arises from covalent stabilization of the DNA-adduct Endo IV complex. Additionally, since Endo IV had limited effects with Cu-TPMA, Cu-TPMA-DPQ, and Cu-TPMA-DPPZ this interaction seems phenanthroline ligand-specific. Previous work by Greenberg *et al*.[19,21],[71] on the radical oxidation mechanism of Cu-Phen proposed generation of an abasic 2′-deoxyribonolactone intermediate that was preceded by superoxide radical generation. These results are in good agreement with that work since trapping $O_2^{\bullet-}$ with tiron (Figure II-5C) and stabilizing Endo IV with Phen complexes reduces oxidative DNA damage.

hAAG enhanced the cleavage activity of $[Cu(TPMA)(N,N')]^{2+}$ complexes but not $[Cu(TPMA)]^{2+}$ and, when combined with observations of additional DNA damage with Endo V, it seems reasonable to suggest that deoxyinosine (dI) or free-base hypoxanthine is generated by these ternary compounds. dI is a naturally occurring noncanonical base that arises from deamination of adenine,[72] however it can be formed from radical generation of Ade-N6-yl.[73] The Ade-N6-yl radical may also be generated by Cu^{2+}/H_2O_2 with elegantly designed immuno-spin trapping experiments establishing its formation *via* a 5,5′-dimethyl-1-pyrroline *N*-oxide (DMPO) nucleoside adduct.[74] The extent of hAAG-mediated DNA damage observed here is dependent on the ancillary ligand choice with bulkier intercalators giving rise to more extensive shearing (DPPZ > DPQ > Phen) suggesting a possible alternative deoxyinosine oxidation pathway for future study.

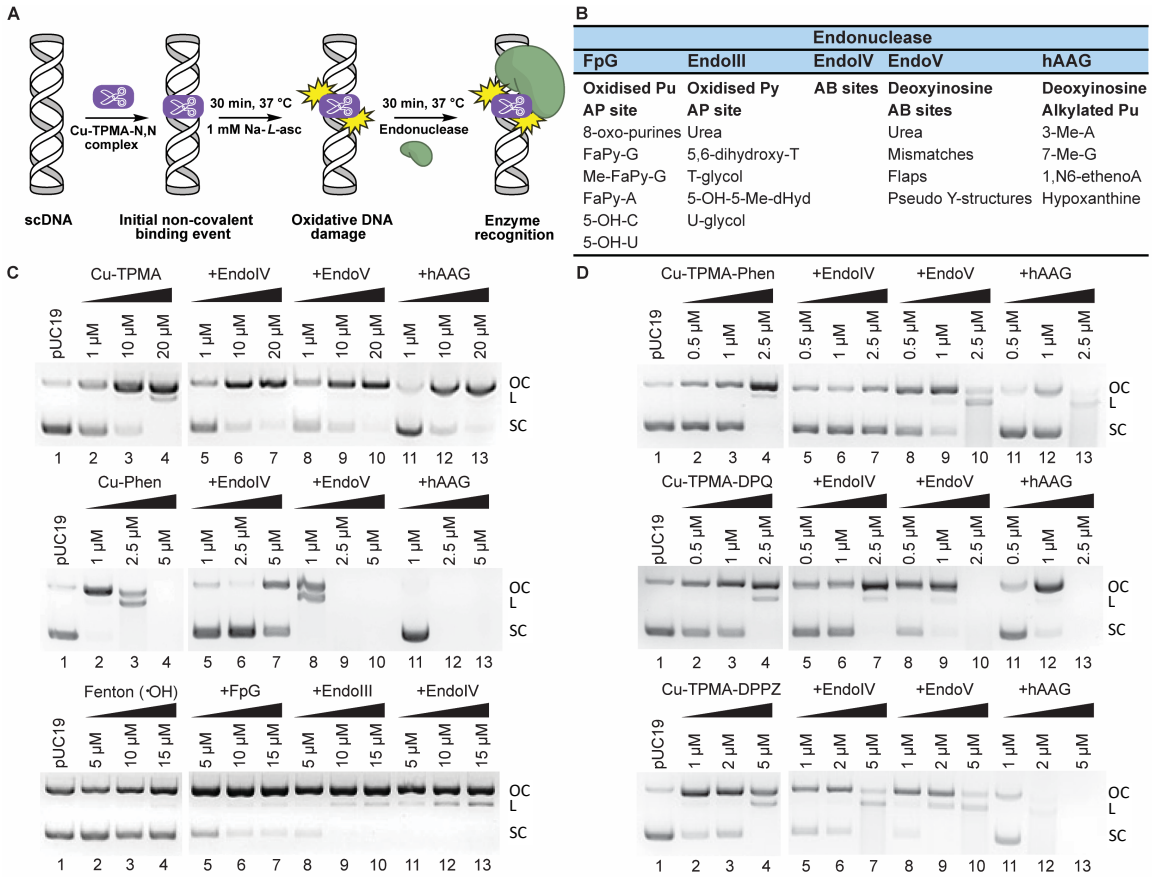

Figure II-6. **A** Cartoon representation of repair enzyme experiments; **B** Table highlighting base lesion recognised or excised by respective repair enzymes. Abbreviations are as follows: A = adenine, G = guanine, T= thymine, C = cytosine, U = uracil, Pu = purines (A and G), Py = pyrimidines (C, T and U), Me = methyl, OH = hydroxy, H = hydro, dH = dihydro, FaPy = formamidopyrimidine, dHyd = deoxyhydanton, Me-Tar-U = methyltartronylurea, dI = deoxyinosine, dU = deoxyuracil; **C** 400 ng pUC19 supercoiled DNA treated with increasing concentrations of Cu-TPMA and Cu-Phen (lanes 2-4) in the presence of 1 mM Na-*L*-ascorbate and 2 U repair enzymes Endo IV[62] (lanes 5-7), Endo V[63-66] (lanes 8-10) and hAAG[60,61] (lanes 11-13). Hydroxyl radical generated from Cu^{2+}/H_2O_2 Fenton-system (lanes 2-4) in the presence of 1 mM Na-*L*-ascorbate and 2 U repair enzymes Fpg[57,58] (lanes 5-7), Endo III[58-59] (lanes 8-10) and Endo IV (lanes 11-13); **D** Cu-TPMA-Phen, Cu-TPMA-DPQ and Cu-TPMA-DPPZ (lanes 2-4) in the presence of 1 mM Na-*L*-ascorbate (lanes 2-4) in the presence of 1 mM Na-*L*-ascorbate and 2 U repair enzymes Endo IV (lanes 5-7), Endo V (lanes 8-10) and hAAG (lanes 11-13). pUC19 only controls in the presence of repair enzymes are shown in appendix A–4, Figure A-17.

II. 4. Conclusions

Copper(II) complexes are attractive choices in the design of new artificial metallo-nucleases (AMNs). The complex scaffold, however, is essential for controlling stability and reactivity at the nucleic acid interface and its shape, charge, and geometry are intrinsic to oligonucleotide recognition. To develop new chemical nucleases beyond the current repertoire of AMNs, this work explored combining the polypyridyl stabilizing ligand

TPMA (*tris*-(2-pyridylmethyl)amine) with the DNA oxidizing properties of Cu(II)-phenanthrene systems. Five new compounds of formula [Cu(TPMA)(*N*,*N*′)]$(ClO_4)_2$ (where *N*,*N*′ is either 2,2-bipyridine (Bipy); 1,10-phenanthroline (Phen); 1,10-phenanthroline-5,6-dione (Phendio); dipyridoquinoxaline (DPQ); or dipyridophenazine (DPPZ)) were generated and their structures determined by single crystal X-ray diffraction. In the solid state, the compounds have broadly similar 6-coordinate structures with four nitrogen donor atoms of the tripodal ligand combining with a chelating Bipy/Phen derivative. One of the apically bound Bipy/Phen N-donor atoms along with a single TPMA pyridine N-donor atom are lengthened by Jahn-Teller distortion with the pyridine nitrogen atom making a long axial bond that varies between 2.5974 and 2.907 Å depending on the *N*,*N*′ ligand present. This long contact was identified in solution by continuous wave (cw) and pulse (ENDOR and HYSCORE) EPR studies where pentacoordination halfway between trigonal bipyramidal and square-based pyramidal geometries dominate with a characteristic dz^2 ground state. Upon addition of excess water, the spectra of Cu-TPMA-Phen modulated to a five-coordinate signal, but this water-induced modification is transient since freezing-drying and re-suspending in DMSO or CH_3CN recovered the identical initial solvent spectrum. ^{14}N ENDOR identified two axially coordinated nitrogen atoms, namely the amine TPMA nitrogen and a Bipy/Phen nitrogen atom, and provided strong evidence of equatorial coordination with three additional pyridine nitrogens. ^{1}H and ^{14}N 2-D HYSCORE analysis were used to probe Cu(II) interactions with atoms outside the first coordination sphere. The ^{1}H spectrum of Cu-TPMA-Bipy—which contains the longest axial Cu-N(pyridine) contact of 2.907 Å—in DMF/toluene (1:1) identified an electron-proton distance of *ca*. 3.4 Å and an orientation of 35° with respect to z-direction which is compatible with hydrogen atoms in CH2 fragments of the TPMA ligand. Moreover, the corresponding ^{14}N-HYSCORE analysis supports a solution configuration where one of the pyridine N-donor atoms is dissociated to a remote position. However, comparisons between Cu-TPMA-Bipy and Cu-TPMA-Phen complexes are less clear-cut and suggest the remote nitrogen atom may originate from an axially coordinated DMF solvent; in either event, the remote contact clearly provides solution access to the Cu(II) centre which is an important aspect of the catalytic design imposed by the TPMA ligand.

DNA binding was identified using indirect ethidium bromide quenching where Phen, DPQ and DPPZ complexes had the greatest overall affinity of the series. Topoisomerase I-mediated relaxation, however, revealed the importance of *N*,*N*′ ligand

choice to intercalation as Cu-TPMA-DPQ and Cu-TPMA-DPPZ complexes unwound supercoiled pUC19 DNA with similar efficiency to an ethidium bromide control. In good agreement with DNA binding observations, oxidation in the presence of exogenous reductant (ascorbate) was pronounced with Cu-TPMA-Phen, Cu-TPMA-DPQ, and Cu-TPMA-DPPZ complexes and attenuated with $[Cu(TPMA)]^{2+}$ or Bipy and Phendio-containing agents. Further analysis showed the minor groove as the preferred site for AMN activity as pre-exposure to a major groove binder (methyl green) enhanced overall oxidative damage sensitivity to supercoiled pUC19 DNA. In terms of the oxidative mechanism, trapping experiments designed to capture the hydroxyl radical, hydrogen peroxide, superoxide, and hypochlorite show the complexes do not follow classical Fenton-type or Haber-Weiss processes but instead generate superoxide- and, to a somewhat lower extent, hydrogen peroxide during the catalytic ROS process. To delineate this activity from that of classical copper-bis-1,10-phenanthroline (Cu-Phen), Fenton-type systems, and the $[Cu(TPMA)]^{2+}$ cation, DNA repair enzyme recognition experiments were conducted. DNA damage lesions formed by Cu-TPMA-Phen, -DPQ, and -DPPZ complexes were not recognized by FpG or Endo III which suggests—in contrast with Cu-Phen and Fenton's reagent—an oxidation pathway independent of oxidized purine and pyrimidine bases, respectively. The activity of Endo IV, which recognizes both apurine and apyrimidine sites, was inhibited by Cu-Phen and Cu-TPMA-Phen and it appears likely, therefore, that a covalent DNA-complex-enzyme adduct is realized. Finally, the role of deoxyinosine (dI) in the DNA damage process was established since hAAG and Endo V both enhanced cleavage activity of $[Cu(TPMA)(N,N')]^{2+}$ complexes; the ancillary ligand choice is important here with bulkier intercalators giving rise to more extensive hAAG-mediated shearing in the order DPPZ > DPQ > Phen.

In summary, these results point toward an effective strategy for the development of a new stabilized AMNs. Given their enhanced solution stability and catalytic flexibility, these agents represent exciting therapeutic leads for the treatment of human cancer and in conjugation strategies for the development of chimeric gene-directed restriction hybrids.[22,28,29,75] Identification of the sequence-specific requirements for intercalation by Cu-TPMA-DPQ and DPPZ complexes and the characterization of specific oxidative DNA damage lesions generated by $[Cu(TPMA)(N,N')]^{2+}$ complexes are important avenues for future research.

II. 5. Materials and methods

My contribution to these experiments was to design and synthesise a series of Cu(II)-TPMA-Phenanthrene complexes. Characterisation of the ligands and complexes were conducted by me. X-ray spectroscopy was performed by Prof. Vickie McKee. EPR, HYSCORE and ENDOR studies were conducted by Dr. Gianluca Toniolo and Dr. George Mitrikas. The DNA binding studies were conducted by me in collaboration with my colleague Dr. Zara Molphy. Dr. Zara Molphy performed topoisomerase-I relaxation assays. Dr. Zara Molphy, Dr. Creina Slator and Dr. Georgia Menounou conducted the oxidative damage analyses. Prof. Chryssostomos Chatgilialoglu supervised the EPR studies. Prof. Andrew Kellett supervised the project.

Chemicals and reagents were sourced from Sigma-Aldrich (Ireland) or Tokyo Chemical Industry (TCI, UK Ltd) and were used without any further purification required. High performance liquid chromatography (HPLC) grade chloroform, MeOH and CH_3CN were used with no further purification. All other solvents were used as supplied. ^{1}H and ^{13}C NMR spectra were obtained on Bruker AC 400 and 600 MHz NMR spectrometers. pH was monitored by a Mettler Toledo InLab Expert Pro-ISM pH probe. Electrospray ionization mass spectra (ESI-MS) were recorded using a Thermo Fisher Exactive Orbitrap mass spectrometer coupled to an Advion TriVersa Nanomate injection system with samples being prepared in 100% HPLC-grade CH_3CN prior to ESI-MS analysis. UV-Visible spectrometry studies were carried out on a Shimadzu UV-2600. FT-IRs were conducted on a Perkin Elmer Spectrum Two Spectrometer.

II. 5.1. $[Cu(TPMA)](ClO_4)_2 \bullet 1.2H_2O$

A solution of *tris*-(2-pyridylmethyl)amine (TPMA) (0.3152 g, 1.09 mmol) in 5 mL of MeOH was added dropwise to a solution of copper(II) perchlorate hexahydrate (0.4024 g, 1.09 mmol) in 10 mL of MeOH. The solution was left stirring for 10 min whereupon the colour changed from light blue to blue aquamarine. The solvent volume was reduced *in vacuo*, the product was precipitated with diethyl ether (45 mL) and the supernatant was decanted to afford a blue aquamarine powder. The solid was washed with Et_2O and dried by desiccation (0.5294 g, yield = 88.2%). ESI-MS (positive mode, $[M + ClO_4^-]^+$) calc.: *m/z* 452.0, found: *m/z* 452.0 Elem. anal. Calc.: C, 37.72; H, 3.59; N, 9.78; Cl, 12.21; Cu, 10.99, found: C, 37.61; H, 3.15; N, 9.38; Cl, 12.40; Cu, 11.09. IR (ATR, cm^{-1}): 1608, 1441, 1072, 1018, 767, 759.

II. 5.2. General procedure for the synthesis [Cu(TPMA)(*N*,*N*')](ClO$_4$)$_2$ complexes (where *N*,*N*' = 2,2′-Bipyridine (Bipy), 1,10-phenanthroline (Phen), 1,10-phenanthroline-5,6-dione (PD), dipyrido[3,2-f:2′,3′-h]quinoxaline (DPQ) and dipyrido[3,2-a:2′,3′-c]phenazine (DPPZ).

A solution of either Bipy (0.0410 g, 0.26 mmol), Phen (0.0467 g, 0.26 mmol), PD (0.0539 g, 0.26 mmol), DPQ (0.0600 g, 0.26 mmol) or DPPZ (0.0727 g, 0.26 mmol) dissolved in a minimal volume of MeOH was added dropwise to a solution of [Cu(TPMA)](ClO$_4$)$_2$ (0.14 g, 0.25 mmol) in 15 mL of MeOH. The resulting solution was left stirring at room temperature for 1 h whereupon a precipitate formed. The solid was vacuum filtered and washed with a minimum volume of ice-cold MeOH and Et_2O. The powders were dried and crystallized by slow diffusion of Et_2O into an CH_3CN solution of the complex.

[Cu(TPMA)(Bipy)](ClO$_4$)$_2$ (0.1137 g, yield = 62.6%). Elem. anal. calc.: C, 47.43; H, 3.70; N, 11.85; Cl, 10.00; Cu, 8.96; found: C, 47.07; H, 3.65; N, 11.62; Cl, 9.69; Cu, 9.11. IR (ATR, cm^{-1}): 1613, 1594, 1477, 1438, 1289, 1079, 1024, 1001, 972, 901, 814, 759, 735, 654. Solubility: CH_3CN, DMF, DMSO.

[Cu(TPMA)(1,10-Phen)](ClO$_4$)$_2$ (0.1064 g, yield = 57.0%). ESI-MS (positive mode, [M]$^{2+}$) calc.: *m/z* 266.5, found: *m/z* 266.6 Elem. anal. calc.: C, 49.16; H, 3.58; N, 11.47; Cl, 9.67; Cu, 8.67; found: C, 48.84; H, 3.45; N, 11.24; Cl, 9.26; Cu, 8.84. IR (ATR, cm^{-1}): 1614, 1598, 1578, 1514, 1486, 1450, 1424, 1292, 1077, 1031, 1006, 969, 905, 847, 770, 755, 729, 657. Solubility: CH_3CN, DMF, DMSO.

[Cu(TPMA)(PD)](ClO$_4$)$_2$ • 0.5 H$_2$O (0.0955 g, yield = 49.1%). Elem. anal. calc.: C, 46.67; H, 3.26; N, 10.89; Cl, 9.18; Cu, 8.23; found: C, 46.42; H, 3.11; N, 10.65; Cl, 8.82; Cu, 8.25. IR (ATR, cm^{-1}): 1707, 1613, 1598, 1577, 1476, 1450, 1427, 1303, 1291, 1076, 1027, 1004, 973, 936, 896, 883, 816, 773, 734, 713, 696, 653. Solubility: CH_3CN, DMF, DMSO.

[Cu(TPMA)(DPQ)](ClO$_4$)$_2$ • H$_2$O (0.1191 g, yield = 59.3%). ESI-MS (positive mode, [M]$^{2+}$) calc.: *m/z* 292.6, found: *m/z* 292.5 Elem. anal. calc.: C, 47.85; H, 3.51; N, 13.95; Cu, 7.91; found: C, 47.88; H, 3.43; N, 13.47; Cu, 8.10. IR (ATR, cm^{-1}): 1612, 1591, 1579, 1477, 1449, 1438, 1406, 1388, 1288, 1078, 1056, 1031, 1004, 966, 814, 766, 736, 707, 656. Solubility: CH_3CN, DMF, DMSO.

[Cu(TPMA)(DPPZ)](ClO$_4$)$_2$ • 1.2H$_2$O (0.1440 g, yield = 67.1%). ESI-MS (positive mode, [M]$^{2+}$) calc.: *m/z* 317.6, found: *m/z* 317.5 Elem. anal. calc.: C, 50.47; H, 3.58; N,

13.07; Cu, 7.42; found: C, 50.49; H, 3.34; N, 12.85; Cu, 7.56. IR (ATR, cm^{-1}): 1612, 1577, 1496, 1485, 1448, 1419, 1360, 1343, 1287, 1164, 1073, 1033, 996, 969, 874, 816, 768, 735, 709, 657. Solubility: CH_3CN, DMF, DMSO.

II. 5.3. X-Ray Crystallography

The data for Cu-TPMA-DPPZ were collected at 100(1)K on a Synergy, Dualflex, AtlasS2 diffractometer using CuK_α radiation (λ = 1.54184 Å) . The other four data sets were collected at 150(2)K on a Bruker-Nonius Apex II CCD diffractometer using MoK_α radiation (λ = 0.71073Å). All were corrected for Lorentz-polarisation effects and absorption. The structures were solved by dual space methods (SHELXT[76]) and refined on F^2 using all the reflections (SHELXL-2014 or SHELXL-2017[77]). All the non-hydrogen atoms were refined using anisotropic atomic displacement parameters and hydrogen atoms bonded to carbon were inserted at calculated positions using a riding model, hydrogen atoms bonded to other atoms were located from difference maps and their coordinates refined. One of the perchlorate anions in $[Cu(TPMA)(Bipy)](ClO_4)_2$ was disordered and was modelled with 55% and 45% occupancy of two orientations related by rotation about one Cl–O bond. Parameters for data collection and refinement are summarised in appendix A-2. CCDC 1853194-1853198 contain the supplementary crystallographic data for this paper. These data can be obtained free of charge from The Cambridge Crystallographic Data Centre via www.ccdc.cam.ac.uk/data_request/cif

II. 5.3.1. Crystal Data:

$[Cu(TPMA)(Bipy)](ClO_4)_2$, $C_{28}H_{26}N_6O_8Cl_2Cu$, M = 708.99 g/mol, monoclinic, space group $P2_1/n$, blue, a = 11.9305(7) Å, b = 18.1422(13) Å, c = 13.9257(9) Å, β = 104.534(2)°, V = 2917.7(3) $Å^3$, Z = 4, T = 150.0(2) K, R_1 = 0.031 ($I > 2\sigma(I)$), wR_2 = 0.077 (all data), GOF = 1.04.

$[Cu(TPMA)(Phen)](ClO_4)_2$, $C_{30}H_{26}N_6O_8Cl_2Cu$, M = 733.01 g/mol, monoclinic, space group $P2_1/n$, blue, a = 12.0959(7) Å, b = 17.0569(9) Å, c = 15.5156(8) Å, β = 104.934(2)°, V = 3093.0(3) $Å^3$, Z = 4, T = 150.0(2) K, R_1 = 0.064 ($I > 2\sigma(I)$), wR_2 = 0.190 (all data), GOF = 1.04.

$[Cu(TPMA)(PD)](ClO_4)_2$, $C_{30}H_{24}N_6O_{10}Cl_2Cu$, M = 762.99 g/mol, monoclinic, space group $P2_1/n$, blue, a = 19.2320(12) Å, b = 8.4888(5) Å, c = 19.9513(13) Å, β =

111.169(3)°, V = 3037.4(3) Å^3, Z = 4, T = 150.0(2) K, R_1 = 0.033 ($I > 2\sigma(I)$), wR_2 = 0.082 (all data), GOF = 1.05.

[Cu(TPMA)(DPQ)](ClO$_4$)$_2$, $C_{32}H_{26}N_8O_8Cl_2Cu$, M = 785.05 g/mol, triclinic, space group $P\bar{1}$, blue, a = 10.7763(6) Å, b = 12.0465(7) Å, c = 13.9004(9) Å, α = 83.429(3)°, β = 75.265(2)°, γ = 67.580(2)°, V = 1612.94(17) Å^3, Z = 2, T = 150.0(2) K, R_1 = 0.044 ($I > 2\sigma(I)$), wR_2 = 0.124 (all data), GOF = 1.04.

[Cu(TPMA)(DPPZ)](ClO$_4$)$_2$•CH$_3$CN, $C_{38}H_{31}N_9O_8Cl_2Cu$, M = 876.16 g/mol, monoclinic, space group $P2_1/c$, blue, a = 13.39827(10) Å, b = 18.82423(12) Å, c = 14.65700(11) Å, β = 93.3180(10)°, V = 3690.48(5) Å^3, Z = 4, T = 100.00(11) K, R_1 = 0.0354 ($I > 2\sigma(I)$), wR_2 = 0.0922 (all data), GOF = 1.03.

II. 5.4. EPR Spectroscopy

The samples were measured in frozen solutions of CH_3CN, DMF, DMSO or water with concentrations ranging between 1 and 5 mM. For pure organic solvents, an equal volume or excess of toluene was used whereas for aqueous solutions an equal volume of glycerol was added to ensure good glass formation. Continuous-wave (cw) EPR measurements at X-band were performed on a Bruker ESP 380E spectrometer equipped with an EN 4118X-MD4 Bruker resonator. Experimental conditions: microwave (mw) frequency, 9.715 GHz; mw power incident to the cavity, 20 μW; modulation frequency, 100 kHz; modulation amplitude, 0.1 mT; temperature, 70 K. Measurements at cryogenic temperatures were performed using a helium cryostat from Oxford Instruments. The microwave frequency was measured using a HP 5350B microwave frequency counter and the temperature was stabilized using an Oxford Instruments ITC4 temperature controller. Pulse EPR measurements at X-band (mw frequency 9.722 GHz) were performed on a Bruker ESP 380E spectrometer equipped with an EN 4118X-MD4 Bruker resonator. The field-swept EPR spectra were recorded via free induction decay (FID) following a pulse length of 500 ns. Davies Electron Nuclear Double Resonance (ENDOR) experiments were carried out with a pulse sequence of π-T-π/2-τ-π-τ-echo, with a π/2 pulse of length 16 ns, a radio frequency pulse of length 10 μs, and a waiting time τ between the pulses of 200 ns. Hyperfine Sublevel Correlation (HYSCORE) spectroscopy with the pulse sequence π/2-τ-π/2-t_1-π-t_2-π/2-τ-echo was carried out with the following instrumental parameters: $t_{\pi/2}$ = 16 ns; starting values of the two variable times t_1 and t_2, 56 ns; time increment, Δt = 24 ns (data

matrix 180 x 180). In order to eliminate blind-spot artefacts, up to four spectra were recorded with τ = 96, 120, 144, and 168 ns. A four-step phase cycle was used to remove undesired echoes. The data were processed with the program MATLAB (The MathWorks, Natick, MA). The HYSCORE time traces were baseline corrected with a second-order exponential, apodized with a Gaussian window, and zero filled. After a two-dimensional Fourier transform the absolute-value spectra were calculated. The experimental cw-EPR, HYSCORE and ENDOR spectra were simulated using the EasySpin package.[78]

II. 5.5. DNA Binding Studies

II. 5.5.1. Competitive Ethidium Bromide Displacement

The competitive ethidium bromide (EtBr) displacement assay was conducted according to the method previously reported by Kellett *et al*.[79] Briefly, a working solution was prepared containing 20 μM UltraPure calf thymus DNA (ctDNA, Invitrogen 15633-019, ε_{260} = 12,824 M $(bp)^{-1}$ cm^{-1}), 25.2 μM EtBr buffer and 40 mM NaCl in HEPES buffer. Serial aliquots of each metal complex were added to working solutions in a 96 well plate format. The volume of each well was adjusted to 100 μL such that the final concentration of ctDNA and EtBr were 10 μM and 12.6 μM, respectively. The plate was incubated at room temperature (~20 °C) before being analyzed using a Bio-Tek synergy HT multi-mode microplate reader with excitation and emission wavelengths of 530 and 590 nm, respectively. The plates were analyzed hourly over 3 h. Concentrations of the complexes were optimized such that fluorescence was reduced to 50% of the initial working solution control at their highest reading. Each drug concentration was measured in triplicate and apparent binding constants were calculated using $K_{app} = K_e$ x $12.6/C_{50}$ where $K_b = 8.8 \times 10^6$ M $(bp)^{-1}$.

II. 5.5.2. Topoisomerase I inhibition assay

400 ng of pUC19 plasmid DNA (NEB, N3041) was exposed to varying concentrations of each copper complex (0.1 - 400 μM) for 30 min at room temperature (~20 °C) in a final volume of 20 μL containing 80 mM HEPES buffer (pH 7.2), 10× CutSmart® buffer (NEB, B7204), and 100× BSA (NEB, B9000). 1 unit of topoisomerase I (*E. coli*) (NEB, M0301) was added to the reaction mixture and incubated for 20 min at 37 °C to ensure relaxation of supercoiled plasmid DNA. The reaction was stopped through the addition of 0.25% SDS and 250 μg/mL protein kinase (Sigma Aldrich). To remove protein from the DNA, samples

were then incubated for 30 min at 50 °C. DNA supercoiling was assessed by agarose gel electrophoresis in the absence of EtBr. 6× loading dye was added and topoisomers of DNA were separated by electrophoresis in 1× TBE buffer at room temperature for 240 min at 40 V and 180 minutes at 50 V. The agarose gel was post-stained using an EtBr bath and photographed using a UV transilluminator.

II. 5.6. DNA Damage Studies

II. 5.6.1. DNA cleavage in the presence of added reductant

Stock solutions of the complexes were initially prepared in DMF and further dilutions prepared in 80 mM HEPES buffer (pH 7.2). 400 ng superhelical pUC19 plasmid DNA was exposed to increasing concentrations of each test complex in the presence of 25 mM NaCl and 1 mM Na-*L*-ascorbate. Reaction mixtures were vortexed and incubated at 37 °C for 30 min. 6× loading buffer (Fermentas) containing 10 mM Tris-HCl, 0.03% bromophenol blue, 0.03% xylene cyanole FF, 60% glycerol, 60 mM EDTA was added to each sample before loading onto a 1.2 % agarose gel containing 4 μL EtBr. Electrophoresis was carried out at 70 V for 90 minutes in 1× TAE buffer and photographed using a UV transilluminator.

II. 5.6.2. DNA cleavage in the presence of non-covalent DNA binding agents

400 ng pUC19 was pre-incubated with 25 mM NaCl, 1 mM Na-*L*-ascorbate and 8 μM of methyl green in 80 mM HEPES for 45 min at 37 °C. Samples were vortexed and varying concentrations of test complexes were then introduced (Cu-TPMA: 10, 15, 20, 25 μM and Cu-TPMA-Phen / Cu-TPMA-DPQ / Cu-TPMA-DPPZ: 1, 2.5, 5, 7.5 μM). The reaction mixture was further incubated at 37 °C for 30 min and subjected to gel electrophoresis (prepared and stained as previously described).

II. 5.6.3. DNA cleavage in the presence of ROS scavangers

The assay was conducted according to the method recently reported by Slator *et al*.[27] Briefly, to a final volume of 20 μL, 80 mM HEPES, 25 mM NaCl, 1 mM Na-*L*-ascorbate, and 400 ng of pUC19 DNA were treated with varying drug concentrations (Cu-TPMA: 5, 10, 15, 20, 25 μM and Cu-TPMA-Phen / Cu-TPMA-DPQ / Cu-TPMA-DPPZ: 1, 2, 3, 4, 5 μM) in the presence ROS scavengers; 4,5-Dihydroxy-1,3-benzenedisulfonic acid (Tiron) (10 mM), D-Mannitol (10 mM), N′-dimethylthiourea (10 mM), L-methionine (10 mM), KI (10 mM), DMSO (10 %) and EDTA (100 μM). Reactions were vortexed and incubated at 37 °C for 30 min and electrophoresis carried out as previously stated.

II. 5.6.4. DNA cleavage in the presence repair enzymes

Supercoiled pUC19 DNA (400 ng) in 8 mM HEPES, 25 mM NaCl, 1 mM Na-*L*-ascorbate in a final volume of 20 µL nuclease free H_2O, was pre-incubated with test series for 30 min at 37 °C at various concentrations. The following reactions were supplemented with associated buffers as per manufacturer recommendations; those with Fpg contained 1 mg/mL BSA and 1× NEB Buffer 1, Endo III with 1× NEB Buffer 1, Endo IV with 1× NEB Buffer 3, Endo V with 1× NEB Buffer 4 and hAAG with 1× ThermoPol. Subsequently, 2U of repair enzymes FpG (NEB, M0240S), endonuclease (Endo) III (NEB, M0268S), Endo IV (NEB, M0304S), Endo V (NEB, M0305S) and hAAG (NEB, M0313S) were added to the reaction mixture and incubated for 30 min, 37 °C. Samples were denatured with 0.25 % SDS, 250 µg/mL proteinase K and heated to 50 °C for 20 min. Reactions solutions were loaded onto a 1.2% agarose gel (4 µL EtBr) with 6× loading buffer and subjected to electrophoresis at 70 V for 70 min and imaged using UV transilluminator.

II. 6. References

[1] D. A. Links, F. Mancin, P. Scrimin, P. Tecilla, *Chem. Commun.* **2012**, 5545–5559.

[2] B. Armitage, *Chem. Rev.* **1998**, *98*, 1171–1200.

[3] J. Chen, J. Stubbe, *Nat. Rev. Cancer* **2005**, *5*, 102–112.

[4] D. S. Sigman, A. Mazumder, D. M. Perrin, *Chem. Rev.* **1993**, *93*, 2295–2316.

[5] M. Pitié, G. Pratviel, *Chem. Rev.* **2010**, *110*, 1018–1059.

[6] R. Larragy, J. Fitzgerald, A. Prisecaru, V. McKee, P. Leonard, A. Kellett, *Chem. Commun.* **2015**, *51*, 12908–12911.

[7] A. C. Komor, J. K. Barton, *Chem. Commun.* **2013**, *49*, 3617–30.

[8] F. R. Xavier, A. Neves, A. Casellato, R. A. Peralta, A. J. Bortoluzzi, B. Szpoganicz, P. C. Severino, H. Terenzi, Z. Tomkowicz, S. Ostrovsky, et al., *Inorg. Chem.* **2009**, *48*, 7905–7921.

[9] R. A. Peralta, A. J. Bortoluzzi, B. de Souza, R. Jovito, F. R. Xavier, R. A. A. Couto, A. Casellato, F. Nome, A. Dick, L. R. Gahan, et al., *Inorg. Chem.* **2010**, *49*, 11421–11438.

[10] S. J. Smith, R. A. Peralta, R. Jovito, A. Horn, A. J. Bortoluzzi, C. J. Noble, G. R. Hanson, R. Stranger, V. Jayaratne, G. Cavigliasso, et al., *Inorg. Chem.* **2012**, *51*, 2065–2078.

[11] P. U. Maheswari, S. Roy, H. Den Dulk, S. Barends, G. Van Wezel, B. Kozlevčar, P. Gamez, J. Reedijk, *J. Am. Chem. Soc.* **2006**, *128*, 710–711.

[12] C. Santini, M. Pellei, V. Gandin, M. Porchia, F. Tisato, C. Marzano, *Chem. Rev.* **2014**, *114*, 815–862.

[13] J. McC. Howell, J. M. Gawthorne, *Copper in Animals and Man*, *Vol. 1*, CRC Press, Boca Raton, **1987**.

[14] A. K. Boal, A. C. Rosenzweig, *Chem. Rev.* **2009**, *109*, 4760–4779.

[15] J. A. Cowan, *Chem. Rev.* **1998**, *98*, 1067–1088.

[16] J. A. Cowan, *Curr. Opin. Chem. Biol.* **2001**, *5*, 634–642.

[17] Z. Yu, M. Han, J. A. Cowan, *Angew. Chem. Int. Ed.* **2015**, *54*, 1901–1905.

[18] D. S. Sigman, D. R. Graham, V. D'Aurora, A. M. Stern, *J. Biol. Chem.* **1979**, *254*, 12269–12272.

[19] T. Chen, M. M. Greenberg, *J. Am. Chem. Soc.* **1998**, *120*, 3815–3816.

[20] D. S. Sigman, *Biochemistry* **1990**, *29*, 9097–9105.

[21] B. C. Bales, M. Pitié, B. Meunier, M. M. Greenberg, *J. Am. Chem. Soc.* **2002**, *124*, 9062–9063.

[22] B. C. Bales, T. Kodama, Y. N. Weledji, M. Pitié, B. Meunier, M. M. Greenberg, *Nucleic Acids Res.* **2005**, *33*, 5371–5379.

[23] Z. Molphy, A. Prisecaru, C. Slator, N. Barron, M. McCann, J. Colleran, D. Chandran, N. Gathergood, A. Kellett, *Inorg. Chem.* **2014**, *53*, 5392–5404.

[24] Z. Molphy, C. Slator, C. Chatgilialoglu, A. Kellett, *Front. Chem.* **2015**, *3*, 1–9.

[25] Z. Molphy, D. Montagner, S. S. Bhat, C. Slator, C. Long, A. Erxleben, A. Kellett, *Nucleic Acids Res.* **2018**, *46,* 9918-9931.

[26] A. Prisecaru, M. Devereux, N. Barron, M. McCann, J. Colleran, A. Casey, V. McKee, A. Kellett, *Chem. Commun.* **2012**, *48*, 6906–6908.

[27] C. Slator, Z. Molphy, V. McKee, C. Long, T. Brown, A. Kellett, *Nucleic Acids Res.* **2018**, *46*, 2733–2750.
[28] M. Pitié, B. Meunier, *Bioconjugate Chem.* **1998**, *9*, 604–611.
[29] M. Pitié, J. D. Van Horn, D. Brion, C. J. Burrows, B. Meunier, *Bioconjugate Chem.* **2000**, *11*, 892–900.
[30] M. Pitié, B. Sudres, B. Meunier, *Chem. Commun.* **1998**, *0*, 2597–2598.
[31] K. J. Humphreys, K. D. Karlin, S. E. Rokita, *J. Am. Chem. Soc.* **2002**, *124*, 6009–6019.
[32] K. J. Humphreys, K. D. Karlin, S. E. Rokita, *J. Am. Chem. Soc.* **2001**, *123*, 5588–5589.
[33] L. Li, N. N. Murthy, J. Telser, L. N. Zakharov, G. P. A. Yap, A. L. Rheingold, K. D. Karlin, S. E. Rokita, *Inorg. Chem.* **2006**, *45*, 7144–7159.
[34] K. J. Humphreys, K. D. Karlin, S. E. Rokita, *J. Am. Chem. Soc.* **2002**, *124*, 8055–8066.
[35] S. Kim, J. W. Ginsbach, J. Y. Lee, R. L. Peterson, J. J. Liu, M. A. Siegler, A. A. Sarjeant, E. I. Solomon, K. D. Karlin, *J. Am. Chem. Soc.* **2015**, *137*, 2867–2874.
[36] M. Bhadra, J. Y. C. Lee, R. E. Cowley, S. Kim, M. A. Siegler, E. I. Solomon, K. D. Karlin, *J. Am. Chem. Soc.* **2018**, *140*, 9042–9045.
[37] L. Li, K. D. Karlin, S. E. Rokita, *J. Am. Chem. Soc.* **2005**, *127*, 520–521.
[38] S. Thyagarajan, N. N. Murthy, A. A. Narducci Sarjeant, K. D. Karlin, S. E. Rokita, *J. Am. Chem. Soc.* **2006**, *128*, 7003–7008.
[39] F. Jiang, K. D. Karlin, J. Peisach, *Inorg. Chem.* **1993**, *32*, 2576–2582.
[40] G. Kokoszka, K. D. Karlin, F. Padula, J. Baranowski, C. Goldstein, *Inorg. Chem.* **1984**, *23*, 4378–4380.
[41] B. J. Hathaway, D. E. Billing, *Coord. Chem. Rev.* **1970**, *5*, 143–207.
[42] Z. Lu, C. Duan, Y. Tian, X. You, X. Huang, *Inorg. Chem.* **1996**, *35*, 2253–2258.
[43] A. Hazell, *Polyhedron* **2004**, *23*, 2081–2083.
[44] M. Q. Ehsan, Y. Ohba, S. Yamauc, *Bull. Chem. Soc. Japan* **1996**, *69*, 2201–2209.
[45] G. G. Hurst, T. A. Henderson, R. W. Kreilick, *J. Am. Chem. Soc.* **1985**, *107*, 7294–7299.
[46] S. V. Doorslaer, R. Bachmann, A. Schweiger, *J. Phys. Chem. A* **1999**, *103*, 5446–5455.
[47] A. Schweiger, G. Jeschke, *Principles of Pulse Electron Paramagnetic Resonance*, Oxford University Press, Oxford, New York, **2001**.
[48] M. Q. Ehsan, Y. Ohba, S. Yamauchi, M. Iwaizumi, *Chem. Lett.* **1995**, *24*, 151–152.
[49] A. K. Koh, D. J. Miller, *At. Data Nucl. Data Tables* **1985**, *33*, 235–253.
[50] Z. G. Lada, Y. Sanakis, C. P. Raptopoulou, V. Psycharis, S. P. Perlepes, G. Mitrikas, *Dalton Trans.* **2017**, *46*, 8458–8475.
[51] F. Jiang, J. Peisach, *Inorg. Chem.* **1994**, *33*, 1348–1353.
[52] V. Kofman, J. J. Shane, S. A. Dikanov, M. K. Bowman, J. Libman, A. Shanzer, D. Goldfarb, *J. Am. Chem. Soc.* **1995**, *117*, 12771–12778.
[53] C. Calle, A. Schweiger, G. Mitrikas, *Inorg. Chem.* **2007**, *46*, 1847–1855.
[54] J. Olmsted, D. R. Kearns, *Biochemistry* **1977**, *16*, 3647–3654.

[55] A. Kellett, M. O'Connor, M. McCann, M. McNamara, P. Lynch, G. Rosair, V. McKee, B. Creaven, M. Walsh, S. McClean, et al., *Dalton Trans.* **2011**, *40*, 1024–1027.
[56] C. Slator, N. Barron, O. Howe, A. Kellett, *ACS Chem. Biol.* **2016**, *11*, 159–171.
[57] A. Kellett, O. Howe, M. O'Connor, M. McCann, B. S. Creaven, S. McClean, A. Foltyn-Arfa Kia, A. Casey, M. Devereux, *Free Radical Biol. Med.* **2012**, *53*, 564–576.
[58] C. Slator, Z. Molphy, V. McKee, A. Kellett, *Redox Biol.* **2017**, *12*, 150–161.
[59] P. Peixoto, C. Bailly, M.-H. David-Cordonnier, in *Drug-DNA Interaction Protocols* (Ed.: K.R. Fox), Humana Press, **2010**, pp. 235–256.
[60] T. Lindahl, *Nature* **1993**, *362*, 709–715.
[61] J. Tchou, V. Bodepudi, S. Shibutani, I. Antoshechkin, J. Miller, A. P. Grollman, F. Johnson, *J. Biol. Chem.* **1994**, *269*, 15318–15324.
[62] Z. Hatahet, Y. W. Kow, A. A. Purmal, R. P. Cunningham, S. S. Wallace, *J. Biol. Chem.* **1994**, *269*, 18814–18820.
[63] M. Dizdaroglu, J. Laval, S. Boiteux, *Biochemistry* **1993**, *32*, 12105–12111.
[64] C. W. Abner, A. Y. Lau, T. Ellenberger, L. B. Bloom, *J. Biol. Chem.* **2001**, *276*, 13379–13387.
[65] G. Dianov, T. Lindahl, *Nucleic Acids Res.* **1991**, *19*, 3829–3833.
[66] J. D. Levin, A. W. Johnson, B. Demple, *J. Biol. Chem.* **1988**, *263*, 8066–8071.
[67] M. Yao, Z. Hatahet, R. J. Melamede, Y. W. Kow, *J. Biol. Chem.* **1994**, *269*, 16260–16268.
[68] M. Yao, Y. W. Kow, *J. Biol. Chem.* **1994**, *269*, 31390–31396.
[69] M. Yao, Y. W. Kow, *J. Biol. Chem.* **1996**, *271*, 30672–30676.
[70] M. Yao, Y. W. Kow, *J. Biol. Chem.* **1997**, *272*, 30774–30779.
[71] N. Fantoni, T. Lauria, A. Kellett, *Synlett* **2015**, *26*, 2623–2626.
[72] P. M. Keane, J. P. Hall, F. E. Poynton, B. C. Poulsen, S. P. Gurung, I. P. Clark, I. V. Sazanovich, M. Towrie, T. Gunnlaugsson, S. J. Quinn, et al., *Chem. Eur. J.* **2017**, *23*, 10344–10351.
[73] J. Cadet, J. R. Wagner, *Cold Spring Harb. Perspect. Biol.* **2013**, *5*, 1–18.
[74] S. Bhattacharjee, L. J. Deterding, S. Chatterjee, J. Jiang, M. Ehrenshaft, O. Lardinois, D. C. Ramirez, K. B. Tomer, R. P. Mason, *Free Radical Biol. Med.* **2011**, *50*, 1536–1545.
[75] C. Boldron, S. A. Ross, M. Pitié, B. Meunier, *Bioconjugate Chem.* **2002**, *13*, 1013–1020.
[76] G. M. Sheldrick, *Acta Crystallogr. Sect. A* **2015**, *71*, 3–8.
[77] G. M. Sheldrick, *Acta Crystallogr. Sect C* **2015**, *71*, 3–8.
[78] S. Stoll, A. Schweiger, *J. Magn. Reson.* **2006**, *178*, 42–55.
[79] M. McCann, J. McGinley, K. Ni, M. O'Connor, K. Kavanagh, V. McKee, J. Colleran, M. Devereux, N. Gathergood, N. Barron, et al., *Chem. Commun.* **2013**, *49*, 2341–2343.

Chapter III

Design and development of *di*-(2-pyridylmethyl)amine copper phenanthrene chemical nucleases

III. 1. Introduction

The development of small molecules capable of binding and reacting with DNA is an intensive area of research and finds applications in DNA footprinting[1], protein engineering[2] and anticancer therapy[3]. Transition metals offer flexibility because of the wide variety of binding modes and reactivities dependent on the metal centre, shape and charge of the inorganic scaffold.[4] The ability of metal complexes to introduce unique reactivity not accessible to organic molecules makes them particularly interesting as potential chemotherapeutics with alternative cytotoxic mechanisms.[5,6] *Cis*-diamminedichloroplatinum(II) (cisplatin)—a cornerstone of modern chemotherapy— is a square planar Pt(II)-complex that binds the N7 position of purine residues (47-50 % *cis*-GG and 23-28 % *cis*-AG) primarily causing 1,2-intrastrand cross-links. DNA platination induces a kink in the DNA structure that ultimately leads to replication inhibition and apoptosis. Cisplatin and derivatives (*i.e.* carboplatin and oxaliplatin) have been used alone or in combination therapies for the treatment of various forms of neoplasia such as ovarian, testicular, colorectal and pancreatic tumours.[7,8] Among these, pancreatic ductal adenocarcinoma (PDAC) is one of the most lethal and chemoresistant types of cancer and it is usually treated with ineffective therapies aimed mostly to improve the quality of life.[9,10] The main chemotherapeutic treatments used against PDAC are gemcitabine, Abraxane® (nab-Paclitaxel) and Folfirinox®—a combination therapy including oxaliplatin together with folinic acid, fluorouracil and irinotecan. Folfirinox® has shown improved median survival in patients with widespread metastatic disease but the low safety profile associated with high dose limiting side-effects restricts its application to younger patients.[9,11] The poor efficacy of current PDAC chemotherapeutics together with the intrinsic toxicity of oxaliplatin and general platinum-therapeutics spurred scientists to search for new metal-based drugs effective against this form of cancer.[12–14]

Several metal complexes capable of Fenton or Haber-Weiss chemistry have been developed as potential anticancer drugs. In particular, recent research has focused on the design of copper complexes due to the natural bioavailability of copper, the variability of its coordination environment and its ability to biomimetically activate oxygen.[15,16] Among these chemotypes, $[Cu(1,10\text{-phenanthroline})_2]^{2+}$ (Cu-Phen) and derivatives have been quite widely studied for their oxidation mechanism and biological applications.[16–21] However the cleavage efficacy of Cu-Phen is limited by its poor solution stability where dissociation of the second coordinated ligand causes formation of the less active $[Cu(Phen)]^{+}$

species.[18,22] In order to prevent dissociation and transmetallation of the copper centre we, along with others, exploited the stabilizing properties provided by polypyridyl ligands.[23,24] In the previous chapter we sought to develop a class of stabilized AMNs by combining the coordination flexibility of *tris*-(2-pyridylmethyl)amine (TPMA) with the oxidative profile of Cu(II)-phenazine systems.[23] One of these compounds, Cu-TPMA-Phen, showed promising preclinical chemotherapeutic activity on human neuroblastoma-derived cells (NB100) with EC_{50} values within the micromolar range.[20] However, even with the inclusion of designer phenazine intercalators such as DPQ or DPPZ, limited DNA binding was observed and this is likely due to the steric hindrance imposed by TPMA.

In this study we sought to identify whether a less hindered polypyridyl ligand, *di*-(2-pycolylamine) (DPA), facilitates enhanced intercalation to provide a greater balance between complex stabilization and enhanced DNA binding. In addition, the penta-coordination of Cu-DPA-Phenanthrene might be expected to expose a labile site for augmented biological potential. To this end, this chapter reports the synthesis and characterization of complexes of general formula Cu-DPA-*N,N′*(where *N,N′*= Phen, DPQ or DPPZ). The coordination geometry of these compounds was analysed by single-crystal X-ray crystallography. The solution stability of Cu-DPA-*N,N′* was delineated by continuous-wave EPR (cw-EPR), hyperfine sub-level correlation (HYSCORE), and Davies electron-nuclear double resonance (ENDOR) spectroscopies. DNA binding and cleavage was identified using a range of biophysical and molecular biological assays to establish the nucleic acid binding properties of the complex series. Our overall aim was to develop a new chemotype with enhanced DNA binding and reactivity at the nucleic acid interface and target this toward pancreatic cancer cells. We therefore tested these Cu-DPA-*N,N′* complexes against four pancreatic cell lines including PT 127, Panc-1, MiaPaCa-2, and HPAC (isolated from a patient-derived xenograft).

III. 2. Results and Discussion

III. 2.1. Synthesis and characterisation

1,10-Phenanthroline was obtained from Sigma Aldrich while quinoxaline and phenazine ligands (DPQ and DPPZ) were generated through Schiff-base condensation reactions of 1,10-phenanthroline-5,6-dione with ethylenediamine and o-phenylenediamine according to procedures developed by our group.[25] Organic ligands were characterized by ^{1}H and ^{13}C nuclear magnetic resonance (NMR) and Fourier transform infrared (FTIR) spectroscopies. The DPA ligand was generated by reacting a solution of 2-picolylamine with a slight excess of 2-pyridinecarboxaldehyde in MeOH. The imine was reduced through the addition of $NaBH_4$ and the product was extracted with CH_2Cl_2 and isolated as a yellow oil in moderate yield. Cu-DPA perchlorate salt was generated by reacting DPA with an equimolar solution of $Cu(ClO_4)_2$ at room temperature. Cu-DPA was reacted with 1 equivalent of either Phen, DPQ or DPPZ in MeOH to yield the respective Cu-DPA-*N,N'* perchlorate complex in moderate yield (Figure III-1). Each copper(II) complex was characterised by FTIR spectroscopy, ESI-MS, elemental analysis, and UV-vis absorption. Crystals suitable for X-ray analysis were obtained by slow evaporation of methanolic solutions of the complexes. All complexes are readily soluble in CH_3CN, DMF and DMSO. UV-vis absorption spectra were recorded at 24-hour intervals over 72 h to determine solution stability. Cu-DPA-Phen and Cu-DPA-DPQ did not appear to undergo speciation or dissociation over 72 h as no differences in the *d–d* transition were noted. Slight changes were however noted in Cu-DPA-DPPZ solution which may be due to solvent rearrangement around the copper centre. Fresh stocks were therefore prepared daily for all biological studies.

The crystal structure of $[Cu(DPA)(Phen)](ClO_4)_2$ (Figure B-6A) shows that all of the nitrogen donors in both DPA and Phen are coordinated to the copper ion. The geometry at the metal ion is best described as trigonal bipyramidal, with N2, N21 and N31 making up the trigonal plane; the N21 – Cu1 – N31 angle is 132.80(7)° and the τ parameter[26] is 0.77° (Table B-1). This geometry contrasts with that found for complexes $[Cu(DPA)(DPQ)](NO_3)_2$ and $[Cu(DPA)(DPPZ)](ClO_4)_2$ and also with the nitrate analogue $[Cu(DPA)(Phen)](NO_3)_2 \cdot 2H_2O$ (Appendix B) where the geometry is closer to square pyramidal with a weaker interaction to a sixth ligand and disorder of the Phen groups. The observation of different geometries for the $[Cu(DPA)(Phen)]^{2+}$ cation supports the conclusion that they are very similar in energy with the observed conformation depending on other factors, such as interionic interactions in the solid state. One perchlorate anion is

hydrogen bonded to the amine group of DPA (N11 – O14 2.956 (2) Å) and this is the most striking interaction between ions. There are a number of (aryl) C-H$\cdots$$OClO_3$ interactions but no significant C-H$\cdots\pi$ or π–π features.

Cu-DPA-DPQ crystallised as $[Cu(DPA)(DPQ)](NO_3)_2 \cdot 0.565EtOH \cdot 0.435H_2O$, with the solvate disordered between water and ethanol molecules, overlapped and sharing the oxygen site. Again, all of the nitrogen donors are coordinated to the copper ion but in this case the geometry is closer to square-pyramidal Figure B-6B. The Cu – N1 bond is significantly longer than the others though the DPQ bite angle prevents it from orienting perpendicular to the basal plane. On the open side there is a very long interaction to one of the nitrate anions (Cu1 – O62, 2.8900(17) Å). The DPA amine forms a bifurcated hydrogen bond with the second nitrate anion (2.930(2) and 3.065(2) Å for N11 – O52 and N1 – 053, respectively). There is a further hydrogen bond between the solvate ethanol/water molecule and this nitrate (O41 – O53 2.845(2) Å). The DPQ molecules are involved in some $\pi - \pi$ stacking and there are both C-H$\cdots\pi$ and (aryl) C-H$\cdots$$ONO_2$ interactions linking the ions (Figure B-6B).

$[Cu(DPA)(DPPZ)](ClO_4)_2$ crystallises with four independent cations in the asymmetric unit, one of these is shown in Figure B-6C and the others are very similar (Table B-1, Figure B-6C). The coordination sphere resembles that of complex $[Cu(DPA)(DPQ)](NO_3)_2$, i.e. approximately square pyramidal geometry with a long sixth "bond" to an anion and a hydrogen bond from the amine to a second anion. There is some disorder at the amine nitrogen in two of the cations and two perchlorate anions. Again, there is some π–π stacking, C-H$\cdots\pi$ and (aryl)C-H$\cdots$$OClO_3$ interactions linking the ions (Figure B-6C)

A

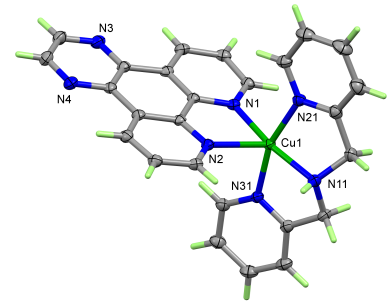

Bond distances (Å)	Cu-TPMA-Phen*	Cu-DPA-Phen	Cu-TPMA-DPQ*	Cu-DPA-DPQ	Cu-TPMA-DPPZ*	Cu-DPA-DPPZ†
Cu1 – N1	2.0083(19)	1.9973(19)	2.0373 (19)	2.0326(15)	2.0037 (15)	2.0715(19)
Cu1 – N2	2.366(2)	2.1428(18)	2.2669 (19)	2.2910(15)	2.3188 (15)	2.247(2)
Cu1 – N11	2.0292(19)	1.9968(19)	2.0386 (19)	2.0076(15)	2.0233 (15)	2.017(2)
Cu1 – N21	2.007(2)	2.0142(18)	1.9978 (19)	2.0012(15)	2.0016 (15)	2.0148(19)
Cu1 – N31	1.995(2)	2.0489(18)	1.9964 (19)	2.0174(15)	2.0093 (15)	1.987(2)
Cu1 – N41	2.667(2)	-	2.907 (2)	-	2.8816 (15)	-
τ	-	0.77	-	0.09	-	0.15

B

C

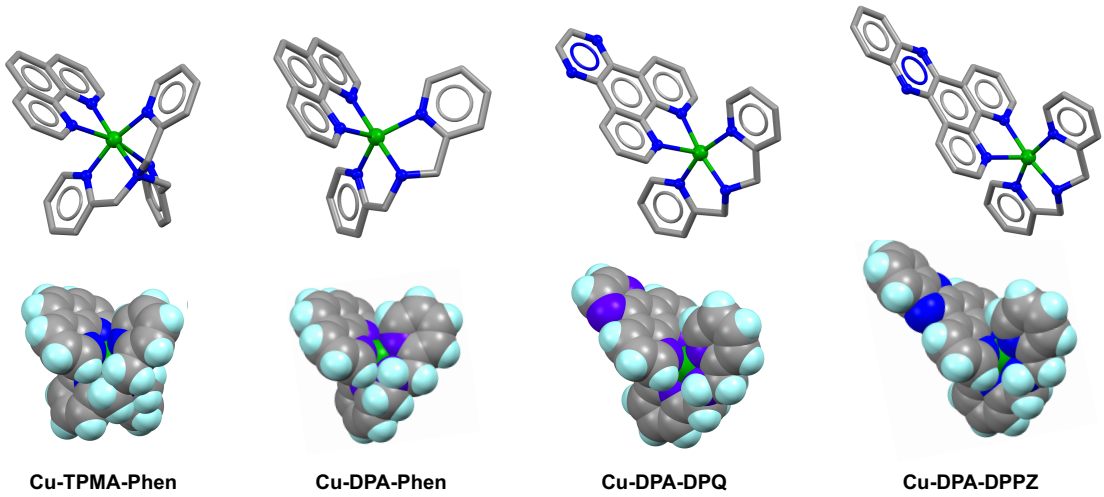

Figure III-1. A Perspective view of X-ray crystal structure of Cu-DPA-DPQ cation highlighting the numbering scheme of non-carbon atoms and table outlining the five Cu—N distances found in Cu-DPA-Phen, Cu-DPA-DPQ and Cu-DPA-DPPZ compared to Cu-TPMA- *N,N′*; * = Data from reference [23]; † = Data for one of 4 independent but similar cations. **B** Perspective view of X-ray crystal structure of Cu-TPMA-Phen and the Cu-DPA-Phenazine series (anions and hydrogen atoms omitted for clarity. Colour scheme: copper, green; carbon, grey; nitrogen, blue). **C** Space-filled view of the complex series (colour scheme: copper, green; carbon, grey; nitrogen, blue; hydrogen, light blue).

III. 2.2. Electron paramagnetic resonance (EPR)

III. 2.2.1. Continuous Wave (cw-EPR) studies.

The continuous wave (cw) EPR spectra of Cu-DPA-Phen, Cu-DPA-DPQ and Cu-DPA-DPPZ samples measured in frozen solution are shown in Figure III-2. All spectra exhibit axial symmetry with $g_{\parallel} > g_{\perp}$ which implies a $d_{x^2-y^2}$ ground state being consistent with a square pyramidal geometry in the first coordination sphere.[27] This is also supported by the g_z = 2.233 ± 0.005 and Cu $|A_z|$=555 ± 10 MHz principal values which are in line with a $d_{x^2-y^2}$ ground state and a {CuN5} chromophore where the axially coordinated N atom tends to increase g_z=2.2 and decrease $|A_z|$=600 MHz values that are expected for a square planar {CuN5} chromophore.[28] The close similarity of g and ^{Cu}A parameters between the three samples (Figure III-2C) indicates a common square conformation for all species

despite the fact that their X-ray crystal structures range from distorted square pyramidal to trigonal bipyramidal. Such structural changes upon dissolution are often encountered in systems interacting weakly with solvent molecules and have been previously reported for two of the three complexes studied here, namely, Cu-DPA-Phen and Cu-DPA-DPQ.[29] In order to shed light into structural details of the complexes in solution, we employed pulsed EPR methods like electron nuclear double resonance (ENDOR) and hyperfine sublevel correlation (HYSCORE) spectroscopies.[30]

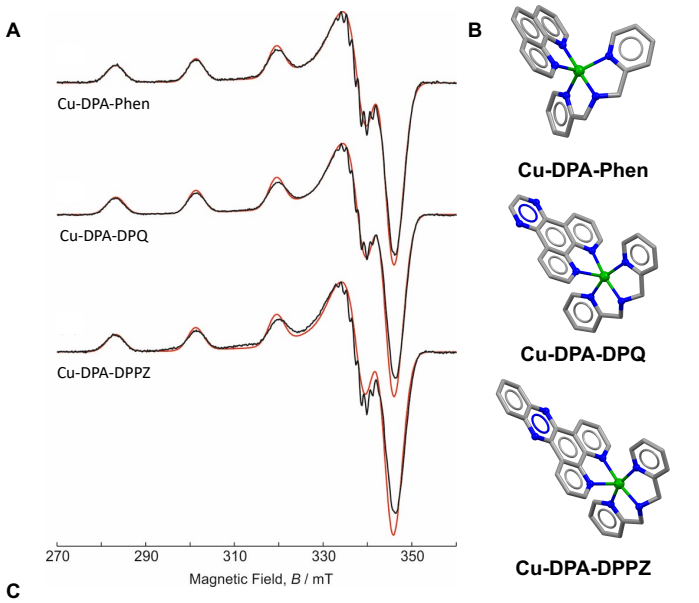

C

Complex	g_x	g_y	g_z	g_{iso}	$^{Cu}A_1$ (MHz)	$^{Cu}A_2$ (MHz)	$^{Cu}A_3$ (MHz)
Cu-DPA-Phen							
Cu-DPA-DPQ	2.052	2.052	2.233	2.112	40 ±10	40 ±10	-555 ±10
Cu-DPA-DPPZ							

^{14}N-ENDOR (equatorial) and ^{14}N-HYSCORE (axial) results for Cu-DPA-Phen

	A_1 (MHz)	A_2 (MHz)	A_3 (MHz)	A_{iso} (MHz)	(α, β, γ) (°)
N_1	28.2 ±0.5	26.2 ±0.5	36.0 ±0.5	30.1 ±0.5	(0, -90, 90)
N_2	32.5 ±0.5	31.5 ±0.5	40.0 ±0.5	34.7 ±0.5	(-90, 90, -90)
N_3	32.5 ±0.5	32.5 ±0.5	40.0 ±0.5	35.0 ±0.5	(-90, 90, -90)
N_4	28.2 ±0.5	26.2 ±0.5	36.0 ±0.5	30.1 ±0.5	(0, -90, 90)
N_5	-1.03 ±0.1	-1.03 ±0.1	0.41 ±0.1	-0.55 ±0.1	(0, 15, 0)
	$\|K\|$ (MHz)		η		(α, β, γ) (°)
N_1	0.55 ±0.1		0.2 ±0.1		(0, -90, 90)
N_2	0.74 ±0.1		0.2 ±0.1		(-90, 90, -90)
N_3	0.61 ±0.1		0.2 ±0.1		(-90, 90, -90)
N_4	0.56 ±0.1		0.2 ±0.1		(0, -90, 90)
N_5	1.00 ±0.1		0.2 ±0.1		(0, 20, 0)

Figure III-2. **A** X-band cw-EPR spectra of Cu-DPA-Phen, Cu-DPA-DPQ, and Cu-DPA-DPPZ in DMF/toluene (1:1) frozen solution measured at 70 K. Black traces: experiment; red traces: simulation; **B** Perspective view of X-ray crystal structure of Cu-DPA-Phen, Cu-DPA-DPQ and Cu-DPA-DPPZ (anions and hydrogen atoms omitted for clarity. Colour scheme: copper, green; carbon, black; nitrogen, blue) **C** Summary of magnetic parameters from CW-EPR for all three samples, and ENDOR, HYSCORE measurements for Cu-DPA-Phen. The Euler angles α, β, γ, define the active rotation of the g tensor axes system (molecular frame) to the hyperfine (A) or nuclear quadrupole (P) principal axes systems, e.g. $\mathbf{A} = \mathbf{R}^{+}(\alpha, \beta, \gamma)\, \mathbf{A}_{\mathbf{diagonal}}\, \mathbf{R}\, (\alpha, \beta, \gamma)$.

III. 2.2.2. Pulse EPR studies

Figure III-3A (lower trace I) shows the ENDOR spectrum measured close to $g_{\|}$ for which only molecules having their *g*-tensor *z*-axis parallel to magnetic field ***B*** contribute to the signal. The spectrum consists of four peaks centred at 15 MHz and split by *ca.* twice the nuclear Zeeman frequency of ^{14}N, $2\nu_N$=2.0 MHz. This spectrum is typical for strongly coupled nitrogens with a hyperfine coupling of 30 MHz. Moreover, the shift of spectra to higher frequencies (i.e. larger hyperfine couplings) as the observer position is moving towards $g_{\perp}$, implies equatorial coordination for these nitrogen atoms. A more detailed inspection of the spectrum measured along $g_{\|}$ (Figure III-3A, spectra I) shows that the four peaks have different intensities and splittings as well. This picture is different than the triplet spectrum (with intensity ratio 1:2:1) typically observed along $g_{\|}$ for strongly-coupled nitrogens of Cu(II)-pyridine complexes where all atoms are magnetically equivalent and the nuclear quadrupole interaction P_z along this direction is such that the condition $3P_z = 2\nu_N$ is fulfilled.[31–33] In the present case, the ENDOR features cannot be reproduced assuming only one set of magnetic parameters and, since this spectrum corresponds to a single-crystal like position, this provides strong evidence that the interacting nitrogen atoms are non-equivalent. Although ENDOR spectroscopy does not allow for determining the number of interacting nuclei, a safe assumption of four strongly-coupled equatorially coordinated nitrogen atoms can be done on the basis of the above-mentioned inequivalency and the g_z-$|A_z|$ correlation. The best simulation of all experimental spectra under this assumption occurs when the magnetic interactions are equivalent in pairs: two nitrogen atoms with isotropic coupling constant $A_{iso} \approx 30$ MHz, and another two with $A_{iso} \approx 35$ MHz. Moreover, the nuclear quadrupole coupling constant $K = e^2Qq/4h$ and the asymmetry parameter η, which define the principal values $P_1 = -K(1-\eta)$, $P_2 = -K(1+\eta)$, and $P_3 = 2K$ obtained by simulation for the corresponding ^{14}N atoms (I=1, see Table I), are in very good agreement with the values found for Cu(II)-pyridine complexes.[31,32] This is also the case for the orientation of the tensors, where the principal field gradient axis (P_3) coincides with the direction of the maximum hyperfine splitting (Cu-N bond), whereas the direction of minimum (in absolute value) quadrupole coupling P_1, lies in the pyridine ring (perpendicular to g_z). It should be noted that, due to the limited resolution of ENDOR spectra at X-band and the small differences between interactions, the combination of the obtained magnetic parameters of Figure III-2C may not be unique. However, the very good agreement between experiment and simulations provides strong evidence on the concept of

four strongly coupled pyridine nitrogens occupying equatorial positions in a more or less square planar arrangement.

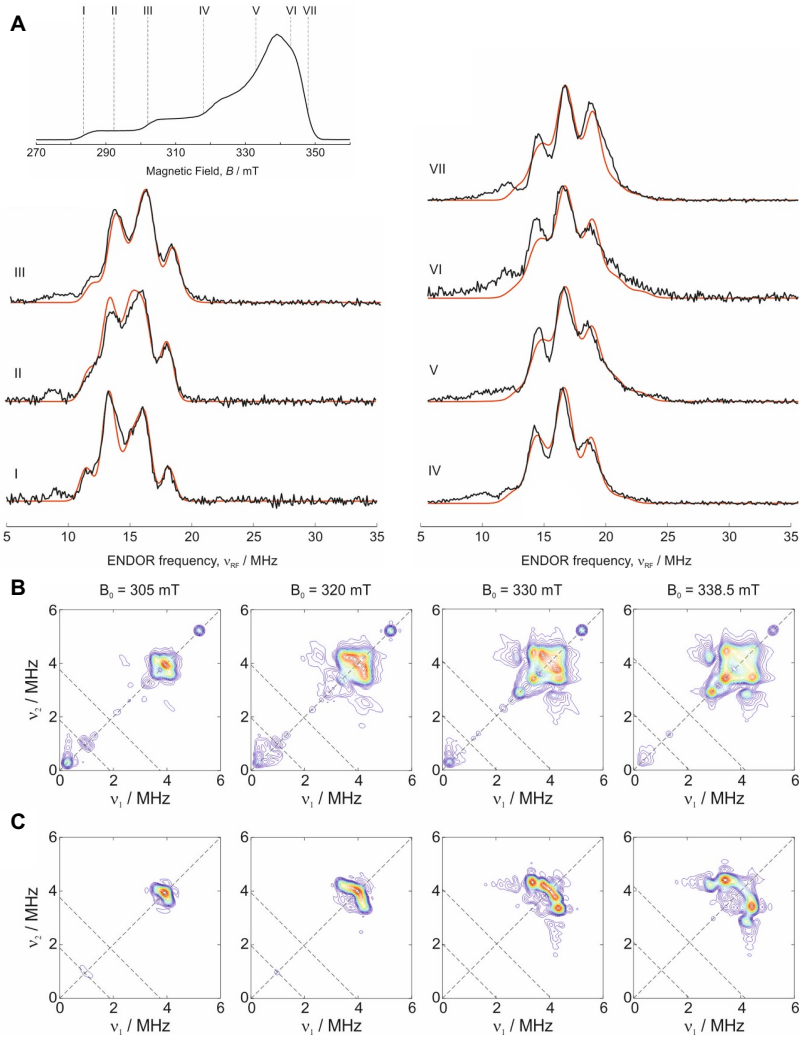

Figure III-3. **A** Field-swept FID-detected EPR spectrum of Cu-DPA-Phen in DMF/toluene (1:1) frozen solution indicating the different observer positions of ENDOR measurements together with Davies ENDOR spectra obtained at different field positions. Black lines: experiment; red lines: simulations. Simulations were performed assuming four equatorial nitrogen atoms. For parameters, see Figure III-2C; **B** Experimental ^{14}N-HYSCORE spectra of Cu-DPA-Phen in DMF/toluene (1:1) frozen solution measured at four different observer positions B_0. Anti-diagonal lines denote harmonics of the ^{14}N Larmor frequency at ν_N and $2\nu_N$; **C** Corresponding simulated spectra using parameters of N_5 shown in Figure III-2C.

HYSCORE spectroscopy also revealed the existence of a weakly-coupled nitrogen atom, as can be seen in Figure III-3. The spectrum measured at a field position close to $g_{||}$ (Figure III-3B, left pattern) consists of a correlation peak close to the diagonal at about (4.0, 4.0) MHz. The close proximity of this peak to the diagonal and the large separation from the anti-diagonal line at $2\nu_N$, indicates a very weak hyperfine coupling where the nuclear quadrupole coupling is the prevailing interaction term. The detailed simulations of HYSCORE spectra measured at four different field positions (Figure III-3C) show that the

principal values of the hyperfine coupling tensor fulfil the condition $|A_1|=|A_2|>|A_3|$, which occurs when the isotropic and the anisotropic parts of the hyperfine interaction have opposite signs. Assuming an axially symmetric hyperfine coupling tensor $[A_1, A_2, A_3]=[A_{iso}-T, A_{iso}-T, 2T]$, where A_{iso} and T is the isotropic and the anisotropic part of the hyperfine interaction, respectively, the determined values of A_1, A_2 and A_3 given in Figure III-2C (entry for N_5) result into two possibilities: i) A_{iso} = -0.55 MHz and T = 0.48 MHz, or ii) A_{iso} = 0.55 MHz and T = -0.48 MHz. The first solution implies a spin polarization mechanism creating the negative A_{iso} on the nitrogen atom. Moreover, assuming that the electron spin is 100% localized on the metal ion, the through space dipole-dipole interaction T_d is given by:[30]

$$T_d = \frac{\mu_0}{4\pi h}\frac{g\beta_e g_n \beta_n}{r^3} \quad (\mathrm{III}-1)$$

where g and g_n are the electron and ^{14}N nuclear g factors, respectively, β_e and β_n are the Bohr and nuclear magnetons, respectively, and r is the metal-nitrogen distance. Assuming that the main contribution to the anisotropic part of the hyperfine interaction is the through space dipole-dipole interaction, i.e. T_d = 0.48 MHz, equation (III-1) gives r = 2.3 ± 0.1 Å. This distance together with the obtained orientation of the corresponding tensor (β = 15°), is compatible with a nitrogen atom occupying an axial position. Comparison of Cu-DPA-*N,N′* with Cu-TPMA-*N,N′* derivatives show similar geometries in solution, both characterized by a $d_{x^2-y^2}$ ground state and penta-coordination between TBP and square-based pyramidal. However, in contrast to the TPMA derivatives, Cu-DPA-*N,N′* lacked a signal in the range of the "remote" nitrogen atom. Indeed the ^{14}N HYSCORE signal consistent with the presence of a remote nitrogen in Cu-TPMA-Bipy was unclear and can be attributed to either a dissociated pyridine or a solvent molecule. Cu-DPA-*N,N′* analysis now strongly suggests that this signal originates from a pyridine N-donor dissociated to a remote position.

III. 2.3. DNA studies

III. 2.3.1. Binding affinity and topoisomerase-I-mediated relaxation

An indirect fluorescence assay based on the fluorescence of the intercalator ethidium bromide (EtBr) was used to calculate the binding constants of the complexes against calf thymus DNA (ctDNA). Cu-DPA-Phen and Cu-DPA-DPQ showed medium to high apparent binding constants (K_{app}) to ctDNA. Cu-DPA-DPPZ had the highest binding (1.49×10^7 M bp^{-1}) with K_{app} close to the best Cu-intercalator complexes reported in the literature thereby demonstrating the influence of this extended intercalator.[25] Data here contrasts with the binding affinity of Cu-TPMA- *N,N′* complexes where all values were found to be approximately in the region 10^5 M bp^{-1} (Figure III-4A and B).

A

Complex	C_{50}[a]	K_{app} [M bp^{-1}][b]
Cu-DPA	337.54	3.29×10^5
Cu-DPA-Phen	238.44	4.65×10^5
Cu-DPA-DPQ	20.90	5.31×10^6
Cu-DPA-DPPZ	7.45	1.49×10^7
Cu-TPMA-Phen‡	487.26	2.28×10^5
Cu-TPMA-DPQ‡	263.88	4.20×10^5
Cu-TPMA-DPPZ‡	351.78	3.15×10^5

[a] C_{50}=concentration (μM) required to reduce fluorescence by 50%.
[b] $K_{app}=K_b \times 12.6/C_{50}$, where $K_b = 8.8 \times 10^6$ Mbp^{-1}
‡ Previously reported

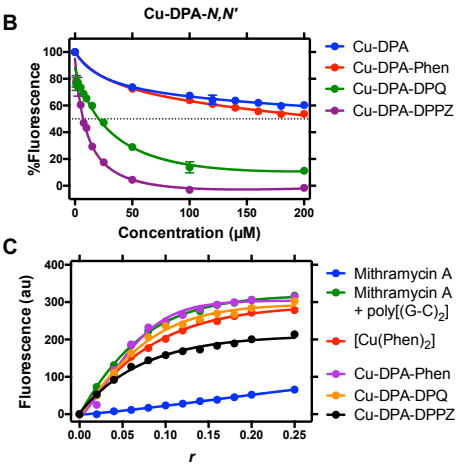

Figure III-4. A Comparison between the binding constants of Cu-DPA-*N,N′* and previously reported Cu-TPMA-*N,N′*[23] complexes to calf thymus DNA; **B** Binding of Cu-DPA-*N,N′* to EtBr-saturated solutions of ctDNA upon titration of complex (Data points presented as an average of triplicate fluorescence measurement ± standard deviation (S.D.); **C** fluorescence binding of mithramycin A (MithA) to poly[d(G-C)$_2$] in the presence and absence of $[Cu(Phen)_2]^{2+}$ or Cu-DPA-*N,N′* (r = 0.10).

The preferential DNA binding site of the complexes was identified using a competitive assay based on the fluorescence of mithramycin A (MithA), an aureolitic acid-type antibiotic.[24] In this experiment, poly[d(G-C)$_2$] is primed with Cu-DPA-*N,N′* and then titrated with the minor groove binder MithA. Here, sequence-specific binding of MithA is directed by hydrogen bonding between the OH-8 group on the tricyclic aromatic polyketide core of the fluorophore and the C2′ amino group on the guanines. Wrapping and interaction of the two oligosaccharide chains in the minor groove stabilize the MithA-DNA interaction.[34–37] Priming poly[d(G-C)$_2$] with Cu-DPA-Phen and Cu-DPA-DPQ (r = 0.10 [drug]/[nucleotide]) prior to titration with MithA did not inhibit fluorophore binding. On the contrary, MithA fluorescence is considerably reduced in the case of Cu-DPA-DPPZ

suggesting preferential binding by this complex in the minor groove of poly[d(G-C)$_2$] (Figure III-4C).

Intercalation by Cu-DPA-*N,N′* was then studied by topoisomerase-I (Topo I)-mediated relaxation of negatively supercoiled DNA (pUC19).[21,38,39] Unwinding experiments were examined between 0.1-400 μM and compared to the relaxation profiles of Cu-TPMA-*N,N′* agents. While Cu-DPA-Phen fully relaxed (0) pUC19 at 0.1 μM, DPQ and DPPZ derivatives mediated complete unwinding at lower concentration (Figure III-5). For both complexes, nicking (SSBs) to the relaxed form at higher loading (above 10 μM) was observed indicating onset of a permanent OC form. In good agreement with the K_{app} experiment, Cu-DPA-*N,N′* are notably better intercalators than Cu-TPMA-*N,N′*.

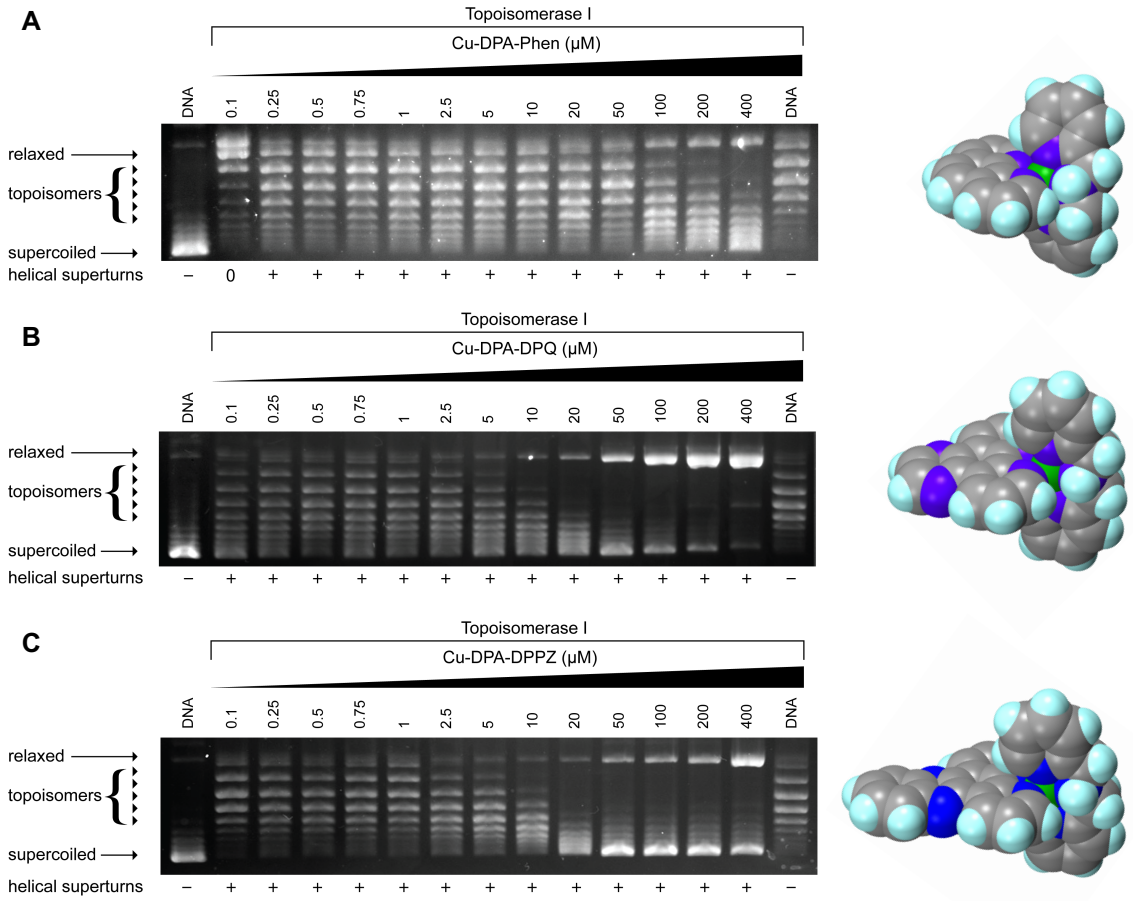

Figure III-5. Topoisomerase I-mediated relaxation assay in the presence of increasing concentrations of **A** Cu-DPA-Phen, **B** Cu-DPA-DPQ and **C** Cu-DPA-DPPZ along with space-filling view of respective complex (Color scheme: copper green; nitrogen, blue; carbon, plum; and hydrogen, white).

III. 2.3.2. DNA Damage

To investigate the oxidative properties of the complexes, DNA cleavage was analysed in the absence and presence of exogenous reductant, over various exposure times and in the presence of radical oxygen species scavengers and repair enzymes. Nuclease-mimetic activity by the complexes was both time and concentration dependent (Figure B-7). For the purpose of our studies however, optimal cleavage conditions were identified by treating the plasmid with the complexes for 30 min at 37 °C in the presence of added reductant (1 mM Na-*L*-Asc). Under these conditions, complete nicking to OC form was achieved at 4 μM loading of Cu-DPA-Phen and Cu-DPA-DPQ whereas Cu-DPA and Cu-DPA-DPPZ induce the same effect at 10 μM. For the latter two complexes partial onset of the linear form (L) was observed at higher drug concentrations (20 μM and 15 μM, respectively). The overall trend in oxidative damage follows Cu-DPA-Phen ~ Cu-DPA-DPQ > Cu-DPA-DPPZ > Cu-DPA (Figure B-8).

The type of radical chemistry involved in the oxidative DNA damage was delineated by analysing the nuclease activity by the complexes in the presence of ROS scavengers including 4,5-dihydroxy-1,3-benzenedisulfonic acid (tiron, $O_2^{\bullet-}$), *D*-mannitol ($^{\bullet}OH$), *L*-methionine ($O_2^{\bullet-}$, $^{\bullet}OH$ and HOCl) and *N,N′*-dimethylthiourea (DMTU, H_2O_2). Co-treatment of pUC19 with tiron (or at a lesser extent *L*-methionine) significantly protected DNA from AMN activity indicating that DNA damage is predominantly dependent on production of superoxide radical. Scavenging $O_2^{\bullet-}$ by tiron caused delayed formation of OC and complete inhibition of L-DNA. In the case of Cu-DPA, H_2O_2 was also produced as DMTU impeded nicking of the plasmid (Figure B-8). Overall the oxidative profile of Cu-DPA-*N,N′* resembles that of Cu-TPMA-*N,N′* and other polypyridyl multinuclear complexes[23] and departs from Cu-Phen-type systems where classical Fenton-type or Haber-Weiss pathways dominate.[40]

III. 2.3.3. DNA-repair enzyme recognition

During cell cycles DNA can undergo spontaneous decay and various types of damage are introduced within the genome such as the incorporation of mismatch sites, alkylated bases and/or oxidised lesions. To restore genetic information prokaryotic and eukaryotic systems developed a wide range of enzymes able to identify specific types of damage, excise the modified nucleoside/nucleobase and prime DNA for the repair mechanism.[41] In this study, we employed a range of glycosylases capable of recognising various specific lesions and of mediating strand nicks (Figure III-6A).[23]

SC-DNA was pre-treated with the complexes to induce single and double strand cleavage prior to addition of the repair enzyme and reactions were compared to a control where the plasmid was treated for 1 h with Cu-DPA-*N,N′* in the absence of repair enzymes. An increase in DNA damage was observed after treatment with EndoV and hAAG indicating formation of deoxyinosines (dI) or free-base hypoxanthines as major oxidation products (Figure III-6B-E). This behaviour emulates the oxidation profile previously observed for Cu-TPMA-*N,N′* and also for Cu-DPA-*N,N′* where hAAG-mediated damage was found dependent on the ancillary intercalator in that extended aromatic ligands caused enhanced cleavage. Treatment with Endo IV inhibited cleavage for all complexes with the exception of Cu-DPA-DPPZ (Figure III-6E). Here recognition of abasic sites by Endo IV suggests an oxidation mechanism similar to that reported by Greenberg *et al*.[17,42,43] for Cu-Phen systems where generation of superoxide radical caused formation of an abasic 2'-deoxyribonolactone intermediate. No major change occurred in the nuclease activity across the series after treatment with FpG and Endo III indicating a radical chemistry different from Fenton reaction where •OH production causes generation of oxidized purines and pyrimidines (Figure B-9).

A

Endonuclease				
FpG	**Endo III**	**Endo IV**	**Endo V**	**hAAG**
Oxidized Purines	**Oxidized Pyrimidine**	**AB sites**	**Deoxyinosine AB sites**	**Deoxyinosine Alkylated Purine**
8-oxo-purines	Urea		Urea	3-Me-A
FaPy lesions	5,6-dihydroxy-T		Mismatches	7-Me-G
5-OH-C	T-glycol		Flaps	1,N6-ethenoA
5-OH-U	5-OH-5-Me-dHyd		Pseudo Y-structures	Hypoxanthine

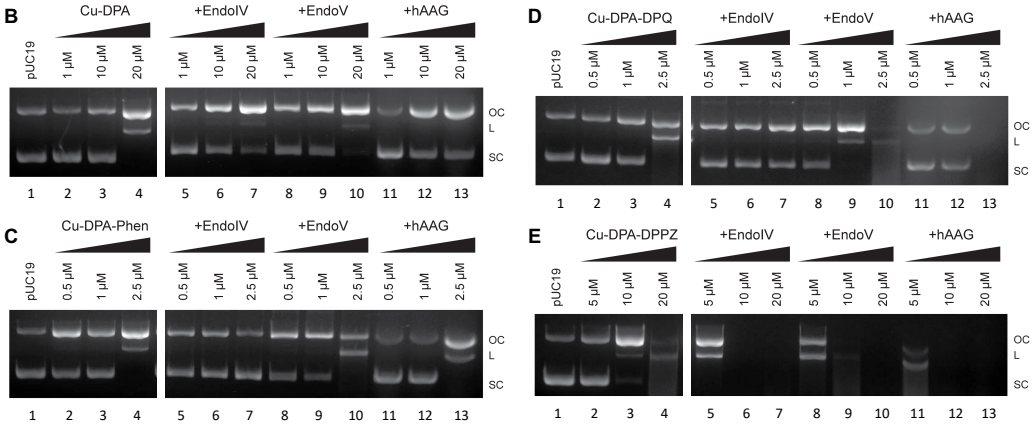

Figure III-6. A Repair enzymes and base lesion recognized or excised by the respective enzymes. Abbreviations are as follows: A=adenine, G=guanine, T=thymine, C=cytosine, U=uracil, Me=methyl, OH=hydroxy, FaPy=formamidopyrimidine, dHyd=deoxyhydantoin. Nuclease activity of **B** Cu-DPA, **C** Cu-DPA-Phen, **D** Cu-DPA-DPQ and **E** Cu-DPA-DPPZ (lanes 2–4) in the presence of 1 mM Na-*L*-ascorbate and repair enzymes Endo IV (lanes 5–7), Endo V (lanes 8–10) and hAAG (lanes 11–13).

III. 2.4. Antiproliferative activity

The *in vitro* cytotoxic activity of the Cu-DPA-*N,N′* series was identified against four pancreatic cancer cell lines including PT127, MiaPaCa-2, Panc-1 and HPAC (isolated from patient derived xenograft). Cells were exposed to increasing concentrations of the complexes and dose-dependent curves were derived from sigmoidal non-linear regression fitting (Figure III-7A-D). IC_{50} were calculated after 5 days of continuous incubation using an acid phosphatase assay[44] and the activity profile of the complexes was compared to oxaliplatin (Figure III-7E). Oxaliplatin was chosen as a reference drug for this study due to its clinical chemotherapeutic role in the treatment of pancreatic ductal adenocarcinoma.[10] The cytotoxic activity of the complexes follows the trend Cu-DPA-DPPZ > Cu-DPA-DPQ > Cu-DPQ-Phen with activities within the low micromolar range. In general, the complexes showed similar or higher *in vitro* cytotoxicity than oxaliplatin against all tested cell lines. Cu-DPA-DPPZ was the most potent among the tested drugs and had an IC_{50} in the nanomolar range against PT127 (0.20 µM) and HPAC (0.32 µM).

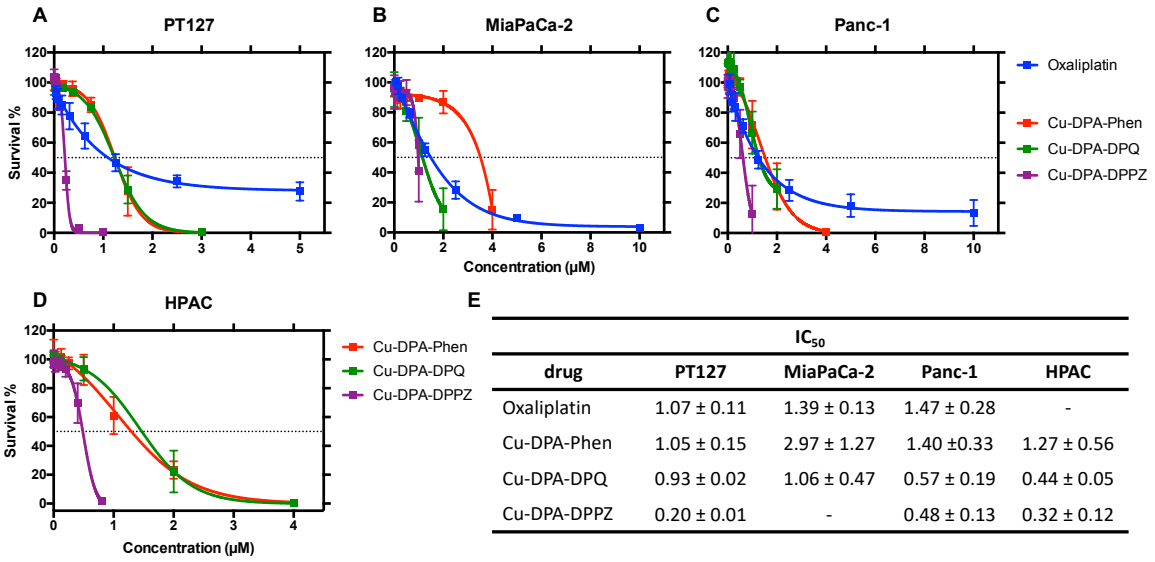

	IC_{50}			
drug	PT127	MiaPaCa-2	Panc-1	HPAC
Oxaliplatin	1.07 ± 0.11	1.39 ± 0.13	1.47 ± 0.28	-
Cu-DPA-Phen	1.05 ± 0.15	2.97 ± 1.27	1.40 ±0.33	1.27 ± 0.56
Cu-DPA-DPQ	0.93 ± 0.02	1.06 ± 0.47	0.57 ± 0.19	0.44 ± 0.05
Cu-DPA-DPPZ	0.20 ± 0.01	-	0.48 ± 0.13	0.32 ± 0.12

Figure III-7. Dose response inhibition of the Cu-DPA-*N,N′* and the clinical agent oxaliplatin against **A** PT127, **B** MiaPaCa-2, **C** Panc-1, **D** HPAC cell lines together with **E** IC_{50} values after 5 days of drug exposure.

III. 3. Conclusion

Cancer is currently one of the leading causes of death and pancreatic ductal adenocarcinoma (PDAC) is among the most chemoresistant types due to the broad heterogeneity of genetic mutations and dense stromal environment. The main treatments used for PDAC include gemcitabine or Folfirinox®, a combination treatment made of folinic acid, fluorouracil, irinotecan and oxaliplatin.[11,45] Copper complexes offer an attractive alternative because of their diverse cytotoxic mechanism—based on DNA oxidation—and of the essential nature of copper to the human body which can aid both tolerance and drug uptake. To further advance the biological potential of previously reported Cu-TPMA-Phenanthrene complexes and introduce stronger DNA binding and nuclease activities, we combined the lower hindrance by DPA [*di*-(2-pycolylamine)] with the oxidation profile provided by Cu(II)-phenanthrene core. Three compounds of formula [Cu(DPA)(*N,N′*)]$(ClO_4)_2$ (where *N,N′* = Phen, dipyridoquinoxaline (DPQ), or dipyridophenazine (DPPZ)) were developed and X-ray crystallography showed a penta-coordinated structure where all nitrogen atoms of DPA and of the intercalating scaffold (Phen, DPQ or DPPZ) are connected to the copper centre. While [Cu(DPA)(DPQ)]$(NO_3)_2$, [Cu(DPA)(DPPZ)]$(ClO_4)_2$ and [Cu(DPA)(Phen)]$(NO_3)_2$ displayed a geometry close to square pyramidal, [Cu(DPA)(Phen)]$(ClO_4)_2$ was best described as trigonal bipyramidal with one phenanthroline and two pyridine nitrogen atoms on the trigonal plane. Cw-EPR study showed coordination rearrangement in solution where all the complexes acquired a

square-pyramidal conformation with $d_{x^2-y^2}$ ground state. ENDOR and HYSCORE analyses identified four nitrogen atoms—presumably from the pyridine rings on DPA and Phen, DPQ or DPPZ—occupying equatorial positions in a more or less square planar arrangement. A fifth nitrogen, possibly the NH nitrogen of DPA, was coordinated in an out of plane position only slightly deviating from axial orientation. Comparison of these results with the ^{14}N HYSCORE spectra of Cu-TPMA-Bipy confirmed the nature of its remote nitrogen signal originating from a pyridine N-donor dissociated to a remote position rather than an axially coordinated DMF solvent.

Ethidium bromide displacement assay showed enhanced affinity by Cu-DPA-*N,N′* compared to Cu-TPMA-*N,N′*. Cu-DPA-DPPZ was the best binder across the series displaying a K_{app} close to the best Cu(II)-phenazine intercalators reported in literature (K_{app} ~ 10^7). Mithramycin A competitive binding assay revealed intercalation in the minor groove of poly[d(G-C)$_2$] by Cu-DPA-DPPZ in contrast to Phen and DPQ derivatives. The trend in intercalation was supported also by topoisomerase-I-mediated relaxation assay where enhanced unwinding of SC-DNA was directly related to the extension of the aromatic intercalator (Cu-DPA-DPPZ ≈ Cu-DPA-DPQ > Cu-DPA-Phen >> Cu-DPA).

In the presence of reductant, pronounced DNA damage was observed by Cu-DPA-Phen and Cu-DPA-DPQ while Cu-DPA and Cu-DPA-DPPZ induced attenuated cleavage. Trapping experiments designed to scavenge various ROS showed that the complexes damage DNA through production of the superoxide radical. This trend resembles that identified for Cu-TPMA-*N,N′* where a role in ROS production by the ancillary *N,N′* intercalator was hypothesized and where the type of radical chemistry promoted by the complexes deviates from classical Fenton-type or Haber-Weiss systems. These results were supported by nuclease experiments in the presence of specific DNA-repair enzymes where DNA lesions by the complexes were not recognized by FpG and Endo III suggesting a oxidation mechanism divergent from Fenton reaction. Similar to Cu-TPMA-*N,N′*, enhanced cleavage was observed for Cu-DPA-*N,N′* in the presence of Endo V and hAAG indicating formation of deoxyinosine and extension in aromaticity of the ancillary ligand augmented hAAG shearing following the trend DPPZ > DPQ > Phen. Overall, comparison between the two families showed enhanced DNA binding by Cu-DPA-*N,N′* but similar nuclease profiles. The solution rearrangement of Cu-TPMA-*N,N′* characterized by dissociation of one pyridine ring suggests a coordination environment—hence a catalytic

chemistry—similar to Cu-DPA-*N,N′* but where the distal pyridine prevented the complete intercalation accessible to DPA derivatives.

Antiproliferative assays against four different pancreatic cell lines (PT127, MiaPaCa-2, Panc-1 and HPAC) showed that the complexes have higher cytotoxic activities than the reference drug oxaliplatin and follow the trend Cu-DPA-DPPZ > Cu-DPA-DPQ > Cu-DPQ-Phen. In particular the high potency of Cu-DPA-DPPZ against PT127 and the patient derived xenograft HPAC make this complex highly interesting for future development as potential chemotherapeutic against PDAC.

In summary, three stabilized AMNs were developed through rational design inspired by previous studies on Cu-Phen-like systems incorporating polypyridyl scaffolds. Enhanced solution stability and a promising cytotoxic profile of Cu-DPA-*N,N′* open interesting prospects for their further development and application as chemotherapeutics in the treatment of pancreatic cancer. The use of conjugation strategies to develop hybrids with directed nuclease activity to specific cancer-related genes may offer improved targeting and low toxicities.

III. 4. Materials and methods

My contribution to this chapter was to design and synthesise a series of Cu(II)-DPA-Phenanthrene complexes. Characterisation of the ligands and complexes were conducted by me. X-ray spectroscopy was performed by Prof. Vickie McKee. EPR, HYSCORE and ENDOR studies were conducted by Dr. George Mitrikas. The DNA binding studies were conducted by me in collaboration with my colleague Dr. Zara Molphy. Dr. Zara Molphy performed topoisomerase-I relaxation assays. Dr. Zara Molphy and Dr. Georgia Menounou analysed the oxidative profile by the complexes. Dr. Sandra Roche performed the cell studies. Prof. Andrew Kellett supervised the project.

Chemicals, reagents and high-performance liquid chromatography (HPLC) grade solvents including $CHCl_3$, MeOH and CH_3CN were sourced from Sigma–Aldrich (Ireland) or Tokyo Chemical Industry (TCI, UK Ltd) and used without further purification. ^{1}H and ^{13}C NMR spectra were obtained on a Bruker AC 400 and 600 MHz NMR spectrometer. pH was monitored by a Mettler Toledo InLab Expert Pro-ISM pH probe. Electrospray ionization mass spectrometry (ESI-MS) measurements were recorded using a ion trap Bruker HCT mass spectrometer with samples being prepared in 100% HPLC-grade CH_3CN prior to ESI-MS analysis. UV/Vis absorption spectroscopy studies were carried out on a Shimadzu UV-2600 spectrophotometer. FTIR measurements were conducted on a

PerkinElmer Spectrum Two spectrometer. Fluorescence DNA binding studies were carried out on a Perkin Elmer LS55 Fluorescence Spectrometer.

III. 4.1. Synthesis of *di*-(2-picolyl)amine (DPA)

Di-(2-picolyl)amine was synthesized according to a literature procedure previously reported by Hamann *et al*.[46] To a solution of 2-picolylamine (2.0113 g, 18.6 mmol) in 10 mL of MeOH brought to 0 °C, a solution of 2-pyridinecarboxaldehyde (2.0249 g, 18.9 mmol) in 10 mL of MeOH was added dropwise. The solution was stirred for 1 h at room temperature and $NaBH_4$ (0.7043 g, 18.6 mmol) was added slowly to the solution at 0 °C. After stirring the solution at room temperature for 16 h, the colour of the solution changed from dark yellow to orange-red, and finally to light yellow. A minimal amount of water was added to the solution and MeOH was removed *in vacuo.* Conc. HCl was added over ice to reach pH ~ 4 and the water phase was extracted with CH_2Cl_2 (6 x 20 mL). The aqueous layer was kept and Na_2CO_3 was slowly added to reach pH ~ 8 . The product was extracted with CH_2Cl_2 (3 x 25 mL) and the combined organic layers were dried over $MgSO_4$. Solvent was removed *in vacuo* to afford a yellow oil. (1.761 g, yield= 47.5 %). ^{1}H-NMR (600 MHz, $CDCl_3$): δ 8.55 (dq, J = 4.9, 1.9, 1.0 Hz, 1H), 7.64 (td, J = 7.7, 1.9 Hz, 1H), 7.35 (d, J = 7.8 Hz, 1H), 7.15 (qd, J = 7.5, 4.8, 1.2 Hz, 1H), 3.98 (s, 2H). ^{13}C-NMR (151 MHz, $CDCl_3$): δ 159.6, 149.2, 136.3, 122.2, 121.8, 54.7. ESI-MS: *m/z* calcd: 200.1 $[M + H]^+$; found: 200.1.

III. 4.2. General procedure for the synthesis of [Cu(DPA)(*N*,*N*')](ClO$_4$)$_2$ complexes (where *N*,*N*' = Phen, DPQ and DPPZ)

[Cu(DPA)(*N*,*N*')]$(ClO_4)_2$ complexes were prepared according to a literature procedure previously reported by Ramakrishnan *et al.*, with some modifications.[29] A solution of DPA (0.1177 g, 0.6 mmol) in MeOH (5 mL) was added dropwise to a solution of copper(II) perchlorate hexahydrate (0.2188 g, 0.6 mmol) in MeOH (5 mL). After stirring for 10 minutes at room temperature a solution of either Phen, (0.1170 g, 0.6 mmol), DPQ (0.1445 g, 0.6 mmol), or DPPZ (0.1813 g, 0.6 mmol) in MeOH (35 mL) was added and the reaction mixture heated to 50 °C overnight. The solution was filtered and crystals of the complexes were obtained by slow evaporation of MeOH.

[Cu(DPA)(1,10-Phen)]$(ClO_4)_2$ (0.2292 g, yield = 60.5%); ATR-FTIR: $\tilde{\nu}$ 1612, 1522, 1488, 1443, 1432, 1076, 1028, 972, 928, 869, 845, 772, 763, 724, 647, 621, 496, 487, 462, 441, 415 cm^{-1}; ESI-MS: *m/z* calcd: 541.1 $[M + ClO_4^-]^+$; found: 541.0; elemental analysis

calcd: C 44.91, H 3.30, N 10.91, Cu 9.90; found: C 44.60, H 3.02, N 10.77, Cu 9.97; solubility: CH_3CN, DMF, DMSO.

[Cu(DPA)(DPQ)](ClO$_4$)$_2$ (0.2142 g, yield = 52.3%); ATR-FTIR: $\tilde{\nu}$ 1611, 1578, 1531, 1481, 1448, 1406, 1389, 1287, 1080, 1028, 929, 818, 766, 737, 709, 655, 621, 438, 417 cm^{-1}; ESI-MS: *m/z* calcd: 493.1 $[M - H^+]^+$; found: 493.1; elemental analysis calcd: C 45.00, H 3.05, N 14.13, Cu 9.16; found: C 42.24, H 2.61, N 13.10, Cu 8.86; solubility: CH_3CN, DMF, DMSO.

[Cu(DPA)(DPPZ)](ClO$_4$)$_2$ (0.2798 g, yield = 63.7%); ATR-FTIR: $\tilde{\nu}$ 1611, 1575, 1500, 1445, 1424, 1360, 1342, 1287, 1064, 1029, 819, 764, 730, 655, 620, 574, 426, 419 cm^{-1}; ESI-MS: *m/z* calcd: 543.1 $[M - H^+]^+$; found: 543.1; elemental analysis calcd: C 48.43, H 3.12, N 13.18, Cu 8.54; found: C 48.48, H 2.76, N 12.93, Cu 8.23; solubility: CH_3CN, DMF, DMSO.

III. 4.3. X-ray crystallography

The data were collected at 100(1)K on a Synergy, Dualflex, AtlasS2 diffractometer using Cu*K*α radiation (λ = 1.54184 Å) and the *CrysAlis PRO* 1.171.39.27b suite[47]. Using SHELXLE[48] and Olex2[49] the structure was solved by dual space methods (SHELXT[50]) and refined on F^2 using all the reflections (SHELXL-2018/3[51]). Except where mentioned below, the non-hydrogen atoms were refined using anisotropic atomic displacement parameters, hydrogen atoms bonded to carbon were inserted at calculated positions using a riding model, and hydrogen atoms bonded to nitrogen were located from difference maps and their coordinates refined.

In Cu-DPA-Phen the oxygen atoms of uncoordinated perchlorate anion showed disorder and were modelled with 0.888/0.112 occupancies of two tetrahedra, related by rotation about Cl2. The atoms of the minor component were refined isotropically. In Cu-DPA-DPQ the structure contains disordered solvate modelled with site occupancies of 0.565 for ethanol and 0.435 for water and the oxygen atoms coincident. In Cu-DPA-DPPZ two of the four independent cations have disorder at the DPA amine group, each modelled with 0.85/0.15 occupancy of the two related sites. This results in the amine hydrogen bond being directed on the opposite side of the DPA plane. Additionally, two perchlorate ions were modelled with 0.65/0.35 and 0.6/0.4 occupancy of overlapping sites. Additional figures are included in B-2 and crystal data, data collection and structure refinement details are

summarised in Table B-2. CCDC [X], [Y], [Z]. This data is provided free of charge by The Cambridge Crystalographic Data Centre.

III. 4.3.1. Crystallographic Data

Crystal Data for [Cu(DPA)(Phen)](ClO$_4$): $C_{24}H_{21}N_5O_8Cl_2Cu$ (M =641.90 g/mol): monoclinic, space group $P2_1/n$ (no. 14), a = 13.2485(2) Å, b = 9.10540(10) Å, c = 22.0943(3) Å, β = 106.707(2)°, V = 2552.79(6) Å^3, Z = 4, T = 100.00(10) K, μ(CuKα) = 3.669 mm^{-1}, *Dcalc* = 1.670 g/cm^3, 20935 reflections measured (8.356° ≤ 2θ ≤ 153.446°), 5299 unique (R_{int} = 0.0268, R_{sigma} = 0.0208) which were used in all calculations. The final R_1 was 0.0375 (I > 2σ(I)) and wR_2 was 0.0994 (all data).

Crystal Data for [Cu(DPA)(DPQ)](NO$_3$)$_2$•0.56EtOH•0.435H$_2$O: $C_{27.132}H_{25.264}N_9O_7Cu$ (M =652.95 g/mol): monoclinic, space group $P2_1/n$ (no. 14), a = 15.12969(19) Å, b = 12.63595(13) Å, c = 15.5323(2) Å, β = 114.5564(16)°, V = 2700.85(7) Å^3, Z = 4, T = 100.00(10) K, μ(CuKα) = 1.720 mm^{-1}, *Dcalc* = 1.606 g/cm^3, 49272 reflections measured (6.856° ≤ 2θ ≤ 148.992°), 5513 unique (R_{int} = 0.0425, R_{sigma} = 0.0204) which were used in all calculations. The final R_1 was 0.0361 (I > 2σ(I)) and wR_2 was 0.0994 (all data).

Crystal Data for [Cu(DPA)(DPPZ)](ClO$_4$)$_2$: $C_{30}H_{23}N_7O_8Cl_2Cu$ (M =743.99 g/mol): triclinic, space group P-1 (no. 2), a = 13.6561(2) Å, b = 17.1834(2) Å, c = 26.2578(4) Å, α = 75.2210(10)°, β = 89.3210(10)°, γ = 88.9110(10)°, V = 5956.53(15) Å^3, Z = 8, T = 100.01(10) K, μ(CuKα) = 3.264 mm^{-1}, *Dcalc* = 1.659 g/cm^3, 54137 reflections measured (6.964° ≤ 2θ ≤ 153.96°), 24296 unique (R_{int} = 0.0254, R_{sigma} = 0.0325) which were used in all calculations. The final R_1 was 0.0409 (I > 2σ(I)) and wR_2 was 0.1109 (all data).

III. 4.4. EPR spectroscopy

The samples were measured in frozen solutions of DMF with an equal volume or excess of toluene to ensure good glass formation and final complex concentrations ranging between 1 and 5 mM. Continuous-wave (cw) EPR measurements at X-band were performed on a Bruker ESP 380E spectrometer equipped with an EN 4118X-MD4 Bruker resonator. Experimental conditions: microwave (mw) frequency, 9.702 GHz; mw power incident to the cavity, 20 μW; modulation frequency, 100 kHz; modulation amplitude, 0.1 mT; temperature, 70 K. Measurements at cryogenic temperatures were performed using a helium cryostat from Oxford Instruments. The microwave frequency was measured using a HP 5350B microwave frequency counter and the temperature was stabilized using an

Oxford Instruments ITC4 temperature controller. Pulse EPR measurements at X-band (mw frequency 9.724 GHz) were performed on a Bruker ESP 380E spectrometer equipped with an EN 4118X-MD4 Bruker resonator. The field-swept EPR spectra were recorded via free induction decay (FID) following a pulse length of 500 ns. Davies Electron Nuclear Double Resonance (ENDOR) experiments were carried out with a pulse sequence of π-T-$\pi/2$-τ-π-τ-echo, with a $\pi/2$ pulse of length 16 ns, a radio frequency pulse of length 10 μs, and a waiting time τ between the pulses of 200 ns. Hyperfine Sublevel Correlation (HYSCORE) spectroscopy with the pulse sequence $\pi/2$-τ-$\pi/2$-t_1-π-t_2-$\pi/2$-τ-echo was carried out with the following instrumental parameters: $t_{\pi/2}$ = 16 ns; starting values of the two variable times t_1 and t_2, 56 ns; time increment, Δt = 24 ns (data matrix 180 x 180). In order to eliminate blind-spot artefacts, up to four spectra were recorded with τ = 96, 120, 144, and 168 ns. A four-step phase cycle was used to remove undesired echoes. The data were processed with the program MATLAB (The MathWorks, Natick, MA). The HYSCORE time traces were baseline corrected with a second-order exponential, apodized with a Gaussian window, and zero filled. After a two-dimensional Fourier transform the absolute-value spectra were calculated. The experimental cw-EPR, HYSCORE and ENDOR spectra were simulated using the EasySpin package.[52]

III. 4.5. DNA Binding Studies

Competitive EtBr displacement[25], Mithramycin A assay[24] and topoisomerase I-mediated relaxation[23] assays were carried out as previously reported.

III. 4.6. DNA damage studies

III. 4.6.1. DNA cleavage in absence of exogenous reductant

In a total volume of 20 μL HEPES (pH 7.2), 25 mM NaCl 400 ng of pUC19 plasmid DNA (NEB, N3041) was treated with increasing concentrations of each DPA-phenazine complex (10 μM, 20 μM, 30 μM, 40 μM and 50 μM) in the absence of reductant. Complexes were initially prepared in DMF and further diluted in HEPES buffer. Samples were incubated at 37 °C for 30 min. Reactions were quenched by adding 6× loading buffer (Fermentas) containing 10 mM Tris-HCl, 0.03% bromophenol blue, 0.03% xylene cyanole FF, 60% glycerol, 60 mM EDTA and samples were loaded onto an agarose gel (1.2%) containing 4 μL EtBr. Electrophoresis was completed at 70 V for 90 min in 1× TAE buffer.

III. 4.6.2. Time dependent DNA cleavage in presence of exogenous reductant

1000 ng of pUC19 plasmid DNA was treated with 5 μM of each DPA-Phenazine complex in the presence of 1 mM Na-*L*-ascorbate and 25 mM NaCl. Incubated at 37 °C for from 1-6 hrs.

III. 4.6.3. DNA cleavage in the presence of repair enzymes

This experiment was carried out according to the literature procedure reported previously.[23] Controls with only pUC19 in the presence of repair enzymes are shown in section B-3 and Figure B-9 in Appendix B.

III. 4.7. Cell studies

III. 4.7.1. Cell-lines and Reagents

Panc-1, Mia-PaCa-2, and HPAC cells were obtained from ATCC. PT-127 cells were derived from a first generation pancreatic ductal adenocarcinoma patient-derived xenograft. Panc-1 and Mia PaCa-2 cell lines were maintained in DMEM medium supplemented with 5% fetal bovine serum (FBS) (Gibco) and 2% L-glutamine (supplier). HPAC were maintained in RPMI media supplemented with 5% FBS. PT-127 cells were maintained in DMEM F-21/Hams media, supplemented with 10% FBS. All cell lines were maintained at 37 °C in a 5 % CO_2 incubator. Oxaliplatin was obtained from St Vincent's University Hospital (Dublin, Ireland). Cell culture media, DMSO, DMF were obtained from Sigma-Aldrich (Dublin, Ireland). Cu-DPA-Phen and Cu-DPA-DPQ stock solution (10 mM) was prepared in DMF and stored at -20°C. Cu-DPA-DPPZ was prepared fresh daily in DMF.

III. 4.7.2. Proliferation assay *in vitro*

Proliferation was measured using an acid phosphatase assay[44]. Cells were seeded in 96 plates at the following densities and incubated for 24 hours prior to the addition of drug; MiaPaCa-2 $1x10^3$ cells/well; Panc-1 2 $x10^3$ cells/well; HPAC 3 $x10^3$ cells/well. After 5 days of drug treatment cells were washed with PBS. 10 mM paranitrophenol phosphate substrate (Sigma-Aldrich) in 0.1 M sodium acetate buffer with 0.1% Triton X (Sigma Aldrich) was added to each well and incubated at 37°C for 2 hours. The reaction was stopped with 50 μL of 1 M NaOH and the absorbance was read at 405 nm (reference - 620 nm). Growth of drug treated cells was calculated relative to control untreated cells in biological triplicate. IC_{50} data was calculated using Calcusyn software

III. 5. References

[1] D. S. Sigman, A. Mazumder, D. M. Perrin, *Chem. Rev.* **1993**, *93*, 2295–2316.

[2] R. Larragy, J. Fitzgerald, A. Prisecaru, V. McKee, P. Leonard, A. Kellett, *Chem. Commun.* **2015**, *51*, 12908–12911.

[3] A. Casini, A. Vessières, S. M. Meier-Menches, Eds. , *Metal-Based Anticancer Agents*, The Royal Society Of Chemistry, **2019**.

[4] A. Kellett, Z. Molphy, C. Slator, V. McKee, N. P. Farrell, *Chem. Soc. Rev.* **2019**, *48*, 971–988.

[5] T. C. Johnstone, K. Suntharalingam, S. J. Lippard, *Chem. Rev.* **2016**, *116*, 3436–3486.

[6] P. C. Bruijnincx, P. J. Sadler, *Curr. Opin. Chem. Biol.* **2008**, *12*, 197–206.

[7] L. Kelland, *Nat. Rev. Cancer* **2007**, *7*, 573–584.

[8] H. Shi, C. Imberti, P. J. Sadler, *Inorg. Chem. Front.* **2019**, *6*, 1623–1638.

[9] F. Hand, K. C. Conlon, *Surgery (Oxford)* **2019**, *37*, 319–326.

[10] A. Adamska, O. Elaskalani, A. Emmanouilidi, M. Kim, N. B. Abdol Razak, P. Metharom, M. Falasca, *Advances in Biological Regulation* **2018**, *68*, 77–87.

[11] C. Thierry, D. Françoise, Y. Marc, B. Olivier, G. Rosine, B. Yves, A. Antoine, R. Jean-Luc, G.-B. Sophie, *N. Engl. J. Med.* **2011**, *364*, 1817–1825.

[12] R. Oun, Y. E. Moussa, N. J. Wheate, *Dalton Trans.* **2018**, *47*, 6645–6653.

[13] N. P. E. Barry, P. J. Sadler, *Chem. Commun.* **2013**, *49*, 5106–31.

[14] S. Monro, K. L. Colón, H. Yin, J. Roque, P. Konda, S. Gujar, R. P. Thummel, L. Lilge, C. G. Cameron, S. A. McFarland, *Chem. Rev.* **2019**, *119*, 797–828.

[15] C. Santini, M. Pellei, V. Gandin, M. Porchia, F. Tisato, C. Marzano, *Chem. Rev.* **2014**, *114*, 815–862.

[16] A. Kellett, Z. Molphy, V. McKee, C. Slator, in *Metal-Based Anticancer Agents* (Eds.: A. Casini, A. Vessières, S.M. Meier-Menches), **2019**, pp. 91–119.

[17] B. C. Bales, M. Pitié, B. Meunier, M. M. Greenberg, *J. Am. Chem. Soc.* **2002**, *124*, 9062–9063.

[18] B. C. Bales, T. Kodama, Y. N. Weledji, M. Pitié, B. Meunier, M. M. Greenberg, *Nucleic Acids Res.* **2005**, *33*, 5371–5379.

[19] M. Pitié, G. Pratviel, *Chem. Rev.* **2010**, *110*, 1018–1059.

[20] G. Toniolo, M. Louka, G. Menounou, N. Z. Fantoni, G. Mitrikas, E. K. Efthimiadou, A. Masi, M. Bortolotti, L. Polito, A. Bolognesi, et al., *ACS Omega* **2018**, *3*, 15952–15965.

[21] C. Slator, Z. Molphy, V. McKee, C. Long, T. Brown, A. Kellett, *Nucleic Acids Res.* **2018**, *46*, 2733–2750.

[22] M. Pitié, B. Meunier, *Bioconjug. Chem.* **1998**, *9*, 604–611.

[23] N. Zuin Fantoni, Z. Molphy, C. Slator, G. Menounou, G. Toniolo, G. Mitrikas, V. McKee, C. Chatgilialoglu, A. Kellett, *Chem. Eur. J.* **2019**, *25*, 221–237.

[24] Z. Molphy, D. Montagner, S. S. Bhat, C. Slator, C. Long, A. Erxleben, A. Kellett, *Nucleic Acids Res.* **2018**, *46*, 9918–9931.

[25] Z. Molphy, A. Prisecaru, C. Slator, N. Barron, M. McCann, J. Colleran, D. Chandran, N. Gathergood, A. Kellett, *Inorg. Chem.* **2014**, *53*, 5392–5404.

[26] A. W. Addison, T. N. Rao, J. Reedijk, J. van Rijn, G. C. Verschoor, *J. Chem. Soc., Dalton Trans.* **1984**, 1349–1356.
[27] B. J. Hathaway, D. E. Billing, *Coord. Chem. Rev.* **1970**, *5*, 143–207.
[28] J. Peisach, W. E. Blumberg, *Arch. Biochem. Biophys.* **1974**, *165*, 691–708.
[29] S. Ramakrishnan, M. Palaniandavar, *J. Chem. Sci.* **2005**, *117*, 179–186.
[30] A. Schweiger, G. Jeschke, *Principles of Pulse Electron Paramagnetic Resonance*, Oxford University Press, Oxford, New York, **2001**.
[31] G. V. Rubenacker, T. L. Brown, *Inorg. Chem.* **1980**, *19*, 392–398.
[32] G. H. Rist, J. S. Hyde, *J. Chem. Phys.* **1969**, *50*, 4532–4542.
[33] Z. G. Lada, Y. Sanakis, C. P. Raptopoulou, V. Psycharis, S. P. Perlepes, G. Mitrikas, *Dalton Trans.* **2017**, *46*, 8458–8475.
[34] M. W. Van Dyke, P. B. Dervan, *Biochemistry* **1983**, *22*, 2373–2377.
[35] K. R. Fox, N. R. Howarth, *Nucleic Acids Res.* **1985**, *13*, 8695–8714.
[36] M. A. Keniry, D. L. Banville, P. M. Simmonds, R. Shafer, *J. Mol. Biol.* **1993**, *231*, 753–767.
[37] F. Barceló, C. Scotta, M. Ortiz-Lombardía, C. Méndez, J. A. Salas, J. Portugal, *Nucleic Acids Res* **2007**, *35*, 2215–2226.
[38] C. Slator, Z. Molphy, V. McKee, A. Kellett, *Redox Biol.* **2017**, *12*, 150–161.
[39] P. Peixoto, C. Bailly, M.-H. David-Cordonnier, in *Drug-DNA Interaction Protocols* (Ed.: K.R. Fox), Humana Press, Totowa, NJ, **2010**, pp. 235–256.
[40] Z. Molphy, C. Slator, C. Chatgilialoglu, A. Kellett, *Front. Chem.* **2015**, *3*, 1–9.
[41] T. Lindahl, *Nature* **1993**, *362*, 709–715.
[42] T. Chen, M. M. Greenberg, *J. Am. Chem. Soc.* **1998**, *120*, 3815–3816.
[43] N. Fantoni, T. Lauria, A. Kellett, *Synlett* **2015**, *26*, 2623–2626.
[44] A. Martin, M. Clynes, *In Vitro Cell. Dev. Biol.* **1991**, *27A*, 183–184.
[45] F. Scheufele, D. Hartmann, H. Friess, *Transl. Gastroenterol. Hepatol.* **2019**, *4:32*, 1–7.
[46] J. N. Hamann, M. Rolff, F. Tuczek, *Dalton Trans.* **2015**, *44*, 3251–3258.
[47] Rigaku Oxford Diffraction, *CrysAlisPro Software System*, Rigaku Corporation, Oxford, UK, **2018**.
[48] C. B. Hübschle, G. M. Sheldrick, B. Dittrich, *J. Appl. Cryst.* **2011**, *44*, 1281–1284.
[49] O. V. Dolomanov, L. J. Bourhis, R. J. Gildea, J. a. K. Howard, H. Puschmann, *J. Appl. Cryst.* **2009**, *42*, 339–341.
[50] G. M. Sheldrick, *Acta Cryst. A* **2015**, *71*, 3–8.
[51] G. M. Sheldrick, *Acta Cryst. C* **2015**, *71*, 3–8.
[52] S. Stoll, A. Schweiger, *J. Magn. Reson.* **2006**, *178*, 42–55.

Chapter IV

Design and development of Cu(II)-TFO hybrids *via* click chemistry for targeted oxidative DNA cleavage

IV. 1. Introduction

There have recently been remarkable advances in therapies that target nucleic acids. For example, the sequence-specific recognition of RNA is central to antisense oligonucleotide (ASO) technologies in which short interfering RNA (siRNA) and ASOs target mRNA, which then becomes a cleavage substrate for Argonaute or RNase H respectively. Although intervention at the mRNA level is effective, it does not alter the genetic code, hence gene silencing is transient. Antigene technologies, however, provide a potential means to permanently alter the mammalian genome.[3] New CRISPR-Cas technologies provide a tractable method for gene editing compared to ZFNs and TALENs [4–6] by cleaving DNA using an endonuclease (*e.g.* Cas9) complexed to a short guide RNA (sgRNA) vector. The enzyme scans the genome to identify sequences where complementarity between DNA and sgRNA occurs. Hydrolytic cleavage is then triggered,[7] but these breaks are easily resealed by cellular repair mechanisms, limiting their application as permanent gene-silencers. Gene knockdown by CRISPR-Cas9 therefore relies on the inclusion of disruptions (*i.e.* insertions or deletions) during the mammalian repair processes: non-homologous end joining (NHEJ) or homology directed repair (HDR).[8] Attempts to repurpose CRISPR have uncovered base editors that heritably change the genetic sequence by modifying the underlying nucleobase sequence.[9]

Artificial metallo-nucleases (AMNs) provide an alternative cleavage strategy to endonucleases whereby redox metal ions can generate reactive oxygen species (ROS) that damage nucleotides to initiate strand excision.[10,11] AMNs are characterised by the metal ion present and the shape and charge of the DNA-coordinating ligand. Copper-based AMNs are attractive due to their versatile coordination environments, oxygen activation mechanisms, intrinsic bioavailability and tolerance within biological systems.[12] The first discovered AMN $[Cu(1,10\text{-phenanthroline})_2]^{2+}$ (Cu-phen) was shown to semi-intercalate and oxidise DNA from the minor groove in the presence of an exogenous reductant (*e.g.* ascorbate) [13,14] and other polypyridyl copper-binding architectures have since been identified.[15–17] Cu-phen-based AMNs have been used in DNA footprinting,[13] recombinant protein production,[18] chemotherapy,[19] and nucleobase discrimination.[20] Efforts to engineer site-specific copper nucleases have focused on tethering the AMN to sequence-directing groups such as DNA-binding proteins, polyamides, and polynucleotides.[14,21–26] While much elegant work has been dedicated to designing chimeric iron(II),[27,28] cerium(IV),[29] zirconium(IV),[30] rhenium(I),[31] technetium(I),[32]

and rhodium(II)[33] systems, considerable challenges remain in the development of copper-based hybrids.[25,34,35] These include: low metal complex stability; complex preparative methods; non-selective (*off*-target) cleavage; the requirement of an adjuvant (*e.g.* spermine) to stabilise triplex formation; and undesirably high hybrid loading to achieve appropriate binding and cleavage effects.

Here, we present a new strategy for targeted oxidative DNA cleavage using triplex forming oligonucleotides (TFOs) loaded with copper AMNs. These hybrid materials are generated by coupling an azide-functionalised AMN with an alkyne-modified TFO using the copper catalysed azide-alkyne cycloaddition (CuAAC) 'click' reaction to facilitate scalable and high-throughput generation of hybrid libraries. We employed polypyridyl ligands to strongly ligate copper ions and designed TFOs to bind a specific region of a plasmid containing the green fluorescent protein (GFP) gene by formation of parallel triplexes with the Hoogsteen face of a sequences of varying lengths. By exploiting the unique base-triplet recognition properties of TFOs, purine-rich tracts were targeted and efficiently cleaved by copper-bound hybrids. Finally, we delineate the chemistry-based cleavage mode of AMN-TFO hybrids from well-studied and optimised hydrolytic enzymes including type II restriction endonucleases and CRISPR-Cpf1. We also reveal how engineering the TFO strand with strain-promoted alkyne substituents and thiazole orange (TO) intercalators confers enhanced triplex stabilisation for future *in vitro* applications.

IV. 2. Results and Discussion

IV. 2.1. Design of azide-modified copper-binding scaffolds

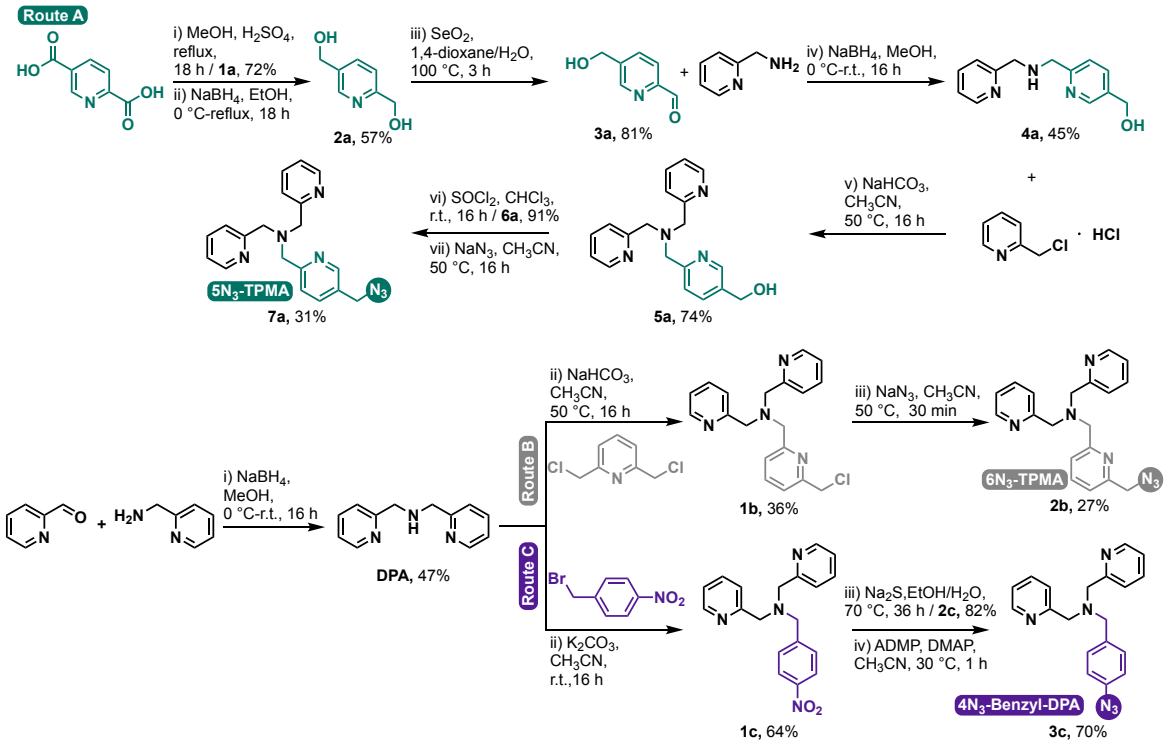

Figure IV-1. Preparation of AMN ligands: N-5-(azidomethyl)pyridine-N-di-(2-picolyl)amine ($5N_3$-TPMA, route a, 7a), N-6-(azidomethyl)pyridine-N-di-(2-picolyl)amine ($6N_3$-TPMA, route b, 2b) and N-4-azidobenzyl-N-di-(2-picolyl)amine ($4N_3$-Benzyl-DPA, route c, 3c).

We developed synthetic routes to introduce an azide-modification into copper binding polypyridyl ligands TPMA (*tris*-(2-picolyl)amine) and DPA (*di*-(2-picolyl)amine) (Appendix C-1). The three synthetic strategies were designed, where possible: *i*) to use canonical 'click' reaction conditions (modularity, insensitivity toward oxygen and water, regiospecificity and stereospecificity); *ii*) to keep in consideration green chemistry criteria (employment of safer solvents, chemicals and easily removable catalysts or reactants); and *iii*) to allow potential industrial upscalability. In route A, an asymmetric pyridine (**3a**) was prepared from 2,5-pyridinedicarboxylic acid using regioselective functional group conversions. The use of SeO_2 to prepare **3a** allows for regiospecific oxidation of the 2-hydroxyl group due to the interaction between the selenium atom with the neighbouring nitrogen atom. Schiff-base condensation of **3a** with picolylamine, followed by nucleophilic substitution of **4a** on 2-picolylchloride afforded 5OH-TPMA (**5a**), which was used as a substrate to release the $5N_3$-TPMA target (**7a**). In route B and C, 2,6-*bis*-(chloromethyl)pyridine and 4-nitrobenzyl bromide were treated with DPA to form **1b** and

1c, respectively. Nucleophilic substitution of NaN_3 on **1b** then afforded $6N_3$-TPMA (**2b**). In route C, we introduced the azide group by NO_2 reduction of **1c** followed by a diazotransfer reaction on the *N*-4-amminobenzyl linker of **2c**. Here, NaS_2 provided an alternative way to reduce the nitro- to amine-group avoiding potentially pyrophoric and oxygen sensitive conditions such as those typical of palladium on carbon hydrogenations. Similarly, using 2-azido-1,3-dimethylimidazolinium hexafluorophosphate (ADMP) offered a safer option to sodium azide which is the common reactant in diazotransfer reactions. The isolated copper-binding ligands $5N_3$-TPMA (**7a**), $6N_3$-TPMA (**2b**) and $4N_3$-benzyl-DPA (**3c**) (Figure IV-1A) were all characterised by ^{1}H-, ^{13}C- and 2D-NMR and ESI-MS (Appendix C-1). Our motivation for developing the $5N_3$-TPMA ligand stemmed from single X-ray analysis of the $[Cu(6N_3\text{-TPMA})(NO_3)](NO_3)\cdot\frac{1}{2}CH_3CN$ complex (Figure IV-1B and Appendix C-2). Comparison with the structure of $[Cu(TPMA)(Phen)]^{2+}$ (Figure C-46) suggests the methylene carbon in $6N_3$-TPMA prevents accessibility of an additional phenanthrene ligand (or, at least, that the apical pyridine and the phen cannot both bind) due to interaction of the methylene hydrogen atoms with those of the phenanthrene. The azide in $5N_3$-TPMA is remote by comparison reducing the potential for steric hindrance around the metal when clicked to the alkyne-TFO.

IV. 2.2. Engineering Cu(II)-TFO hybrids with click chemistry

Several factors were taken into account in the design of parallel TFOs: an oligopyrimidine strand for Hoogsteen base recognition of the targeted duplex; an acidic environment to form stable C^+-GC triplets;[3,36,37] and triplet inversions (*e.g.* G-TA) should be minimised to avoid destabilisation. More complex approaches have been developed to circumvent these sequence and pH limitations on triplex stability, but they were not required in this study.[38] We prepared Cu(II)-TFO hybrids (*cf.* Figure IV-2C) by clicking [39] the azide-modified $5N_3$-TPMA, $6N_3$-TPMA, and $4N_3$-Benzyl-DPA ligands to alkyne-modified oligonucleotides. Click reactions were performed in anaerobic environment to prevent oxygen activation by the copper catalyst and possible oxidation of the oligonucleotide probe. Three alkyne TFO variations were considered—5′-phosphate-, terminal base-, and internally base-modified sequences. 5′-hexynyl-dN (Mod A), 5-octadiynyl-dC (Mod B), or internal octadiynyl-dU (Mod C) (Figure IV-2D) TFOs were then clicked by CuAAC to the AMN ligands (Figure IV-2A). The final library of AMN-TFOs ranged between 16 – 32 nt in length (TFO 1-5; Figure IV-2E). Triplexes contained either one (TFO1) or two (TFOs 2, 4, and 5) G-TA inversions when bound to their target, while TFO3 was fully

complementary. The 5′-phosphate modification (Mod A) has the flexibility to target both the major and minor groove of DNA while modifications B and C were developed to target only the major groove. The full alkyne-TFO and AMN-TFO library is available in Table C-3 & C-4.

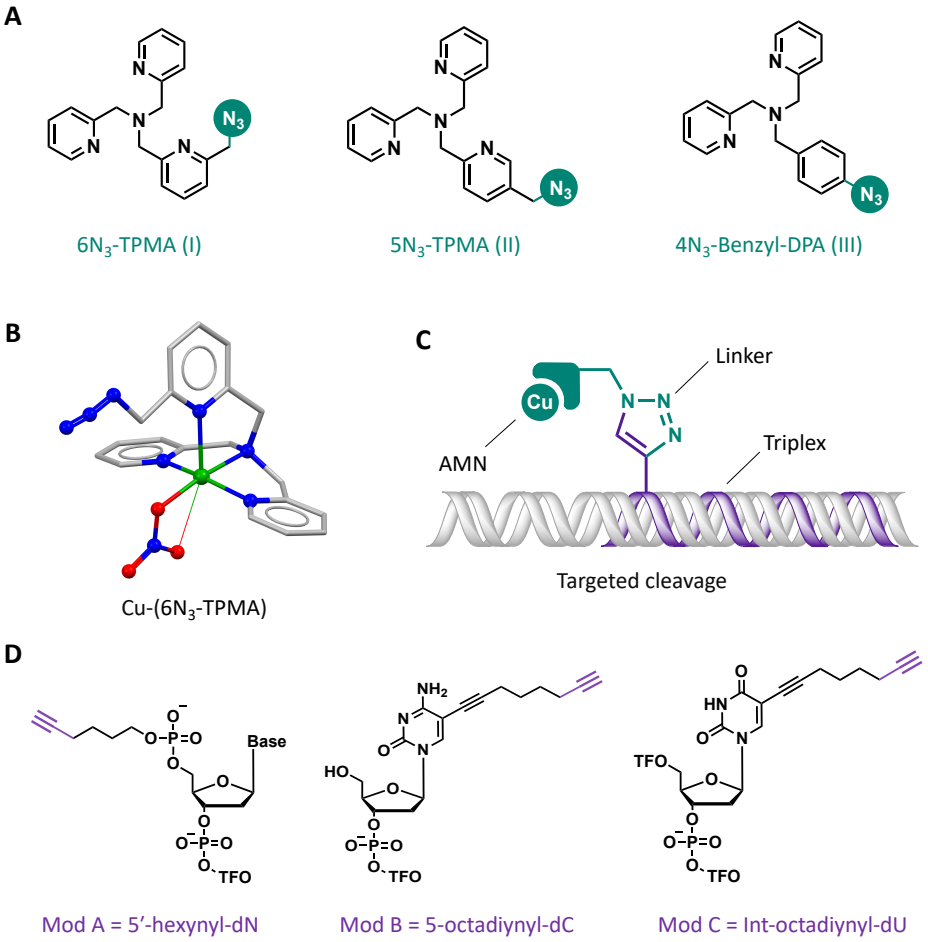

Figure IV-2 A Azide-modified AMN ligands. **B** X-ray crystal structure of $[Cu(6N_3\text{-TPMA})]^{2+}$. **C** AMN-TFO hybrid bound to a target duplex. **D** Alkyne modified nucleotides. **E** TFO sequences (purple) targeting specific regions of a plasmid containing the GFP gene (grey).

IV. 2.3. Triplex formation and targeted cleavage by AMN-TFO hybrids

Thermal melting experiments were conducted with duplex sequences from the GFP plasmid containing 10 flanking base pairs on each side of the TFO binding site (Figure IV-2E). We conducted these studies under physiological conditions (10 mM PO_4^{3-}, 150 mM NaCl, 2 mM $MgCl_2$) at pH 6.0 to ensure cytosine protonation (Table C-5 and Fig. C-49). Alkyne-modified TFOs were first examined for their ability to form triplexes (Figure IV-3A). Although G-TA inverted triplets are the most stable X-TA triplex combination (where X = A, C, G or T),[40] the presence of two inversion sites in TFO2 (16 nt) and TFO5 (17 nt) resulted in triplexes that were not stable above 12 °C and were not further investigated. We identified that TFO1, a 16 nt sequence containing a single G-TA inversion, formed stable triplexes with melting temperatures (T_M) in the range of 19.3 - 24.6 °C depending on the AMN 'click' modification introduced. TFO3A, a 20 nt sequence with no inversion sites, had a T_M value of ~45 °C while TFO4 (32 nt)—containing two inverted triplets—also formed stable triplexes with melting temperatures of ~45 °C or above. Upon conjugating AMNs to TFO sequences, a slight lowering of triplex stability was identified with exception of terminal base modified AMNs (Mod B) (Figure IV-3B and Table C-5). These effects may be attributed to steric hindrance exerted by the bulky polypyridyl ligands at the 5′-phosphate termini, while base stacking interactions by the ligands are feasible when positioned at the terminal nucleobase. Coordination of a Cu(II) ion introduced in the form of $Cu(ClO_4)_2$ to AMN-TFO hybrids enhanced triplex stability up to 6 °C (Figure IV-3C and Table C-5). As expected, this effect was not observed in the absence of a copper-binding AMN (*i.e.* alkyne-TFOs). Therefore, enhanced stability is likely due to a combination of charge neutralisation and Cu(II)-phosphate binding of the target duplex by the metal-bound AMN—an effect recently identified in a major groove binding copper(II) polypyridyl complex.[41] Although a range of organic modifications for augmenting triplex stability have been reported,[42] to our knowledge this is the first evidence of triplex stabilisation induced by a metal binding adduct.

We next identified the cleavage activity of selected AMN-TFO hybrids by real-time PCR (qPCR). Internally modified TFO4C hybridised to $6N_3$-TPMA (I), $5N_3$-TPMA (II) and $4N_3$-Benzyl-DPA (III) ligands were selected as they displayed high sequence discrimination during preliminary electrophoretic analysis. During qPCR a specific region of intact DNA (a 113 bp amplicon in this case) is exponentially amplified by *Taq* DNA polymerase, while the relative concentration of DNA is monitored through SYBR green I

fluorescence. The initial concentration of intact duplex present is directly related to the number of PCR cycles required to achieve a fluorescent signal (threshold cycle, C_T). In the presence of the Cu-TPMA and alkyne-TFO (non-clicked) no significant damage is observed until 250 equivalents of reductant are present (fold change at 250 eq. Na-*L*-asc = 0.58). However, DNA damage was observed for Cu(II)-bound AMN-TFO hybrids in the absence of reductant (fold change for 0 eq. Na-*L*-asc = 0.54, 0.54 and 0.42 for TFO4CI, TFO4CII and TFO4CIII, respectively) while in the presence of ascorbate—a reductant natively present in biological systems—the target was ablated. Comparing C_T values for the hybrids reveals an overall cleavage efficiency of TFO4CIII ($4N_3$-benzyl-DPA) > TFO4CII ($5N_3$-TPMA) > TFO4CI ($6N_3$-TPMA) while attenuated cleavage by the non-clicked Cu(II)-TPMA complex with alkyne-TFO was observed.

A

Oligo	T_M Mod A (°C)	T_M Mod B (°C)	T_M Mod C (°C)
TFO1	22.4 ± 0.2	19.3 ± 0.1	24.6 ± 0.0
TFO3	45.2 ± 0.7	-	-
TFO4	47.3 ± 0.4	45.2 ± 0.1	45.1 ± 0.2

B

Oligo	T_M (°C) − Cu	T_M (°C) + Cu	ΔT_M (°C)
TFO4A	47.3 ± 0.4	47.3 ± 0.6	0
TFO4AI	45.8 ± 0.4	47.8 ± 0.6	2.0
TFO4B	45.2 ± 0.1	44.6 ± 0.8	-0.6
TFO4BI	46.4 ± 0.4	47.9 ± 1.0	1.5
TFO4C	45.1 ± 0.2	46.2 ± 0.6	1.1
TFO4CI	40.8 ± 0.3	44.3 ± 1.5	3.5

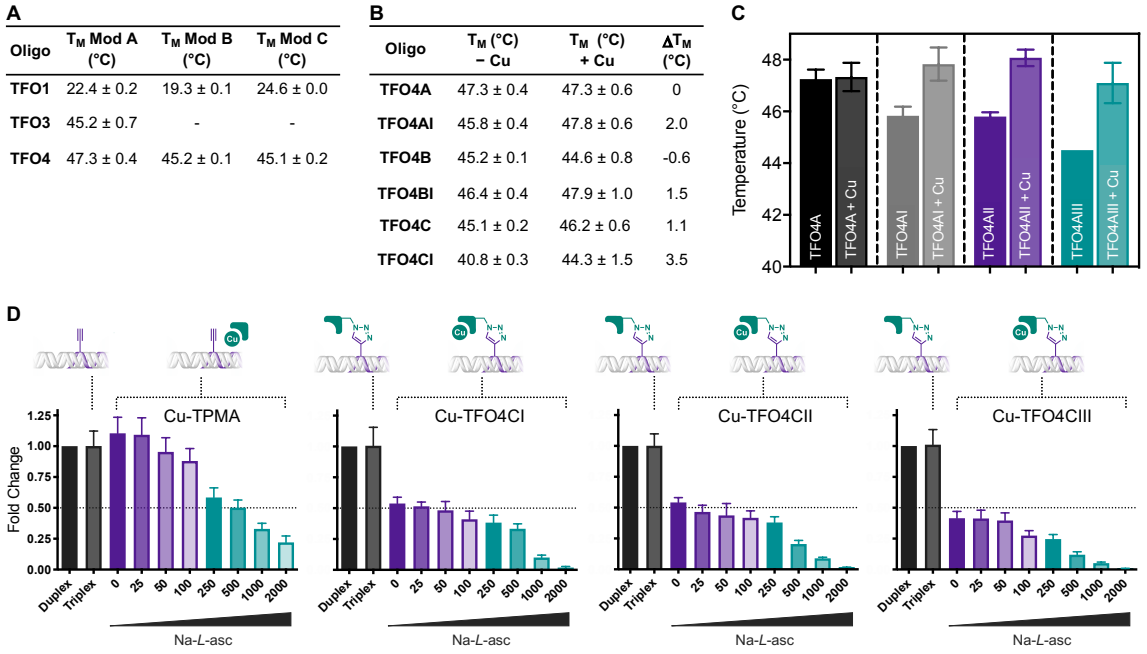

Figure IV-3 A T_M of alkyne-modified TFOs. **B** T_M of TFO4A hybrids modified with either $6N_3$-TPMA (I), $5N_3$-TPMA (II) or $4N_3$-Benzyl-DPA (III) in the absence or presence of 1 eq Cu(II). **C** ΔT_M of TFO4 hybrids containing alkyne modifications clicked to $6N_3$-TPMA (I) in the absence or presence of 1 eq Cu(II). **D** Target duplex (0.625 pmol) treated with 25 eq of TFO4CI, TFO4CII, TFO4CIII and non-clicked Cu(II)-TPMA complex in the presence of increasing concentrations of Na-*L*-asc (0-2000 eq. to TFO4C derivative). Resulting DNA damage was analysed by qPCR where the change in threshold cycle between the target (6 h) and control sample (0 h) (target C_T – control C_T) was calculated (ΔC_T). ΔC_T was plotted as linear values ($2^{-\Delta CT}$).

IV. 2.4. Targeted oxidative cleavage by AMN-TFO hybrids

We initially assessed triplex formation and oxidative cleavage by Cu(II)-TFO hybrids against a 52 bp sequence from a plasmid containing the GFP gene using polyacrylamide gel electrophoresis (PAGE) (*cf.* Figure C-50). Our studies focused on TFO3 and TFO4

since they formed stable triplexes above 37 °C. Alkyne-modified TFO (TFO4A) in the presence of Cu(II) salt and increasing ascorbate produced no cleavage effects towards either the target or *off*-target duplex present *in situ* (Figure C-51). Oxidative damage of the target sequence was also monitored in the presence of the non-clicked Cu(II)-TPMA complex, alkyne-TFO, an *off*-target sequence, and increasing equivalents of reductant (Figure IV-4A). This mixture, as expected from earlier qPCR analysis, was not efficient at depleting the target with similar degradation effects observed on the *off*-target. Identical experiments with Cu(II)-bound AMN-TFO hybrids demonstrated targeted cleavage and excellent sequence discrimination at low reductant loading (Figure C-52). The presence of an internally clicked AMN results in significant depletion (*cf.* TFO4CII Figure IV-4B) with the target being degraded faster than the *off*-target sequence (72% versus 24% knockdown with 100 eq. Na-*L*-asc, respectively, Figure IV-3b). Finally, comparisons between the hybrids showed cleavage efficiencies following the trend: TFO3AI > TFO4CII > TFO4BI (Figure IV-4B and Figure C-52) but sequence discrimination was found to be significantly higher for TFOs bearing base modifications (*i.e.* Mod B & C). DNA damage is also dependent on the type and position of the alkyne modification with increased discrimination by TFO4CII suggesting the internal position contributes to lower *off*-target cleavage effects.

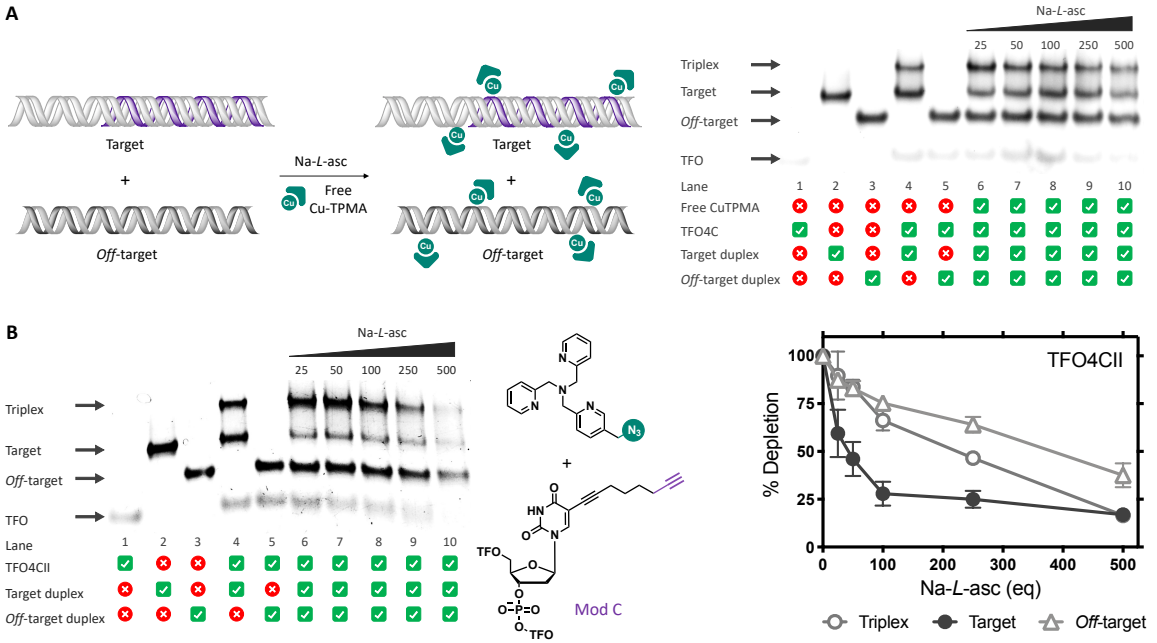

Figure IV-4. A Cartoon of target and *off*-target duplex treated with free AMN (left), duplex target and *off*-target (1.25 pmol) treated with a 25 eq mixture of free Cu-TPMA and TFO4C (Cu-TPMA/TFO4C; 1:1) in the presence of increasing concentrations of Na-*L*-asc (25-500 eq to Cu-TPMA/TFO4C; lanes 6-10, right). **B** 25 eq. of Cu(II) bound hybrid TFO4CII was exposed to the target and an *off*-target duplex (1.25 pmol) in the presence of increasing concentrations of Na-*L*-asc (25-500 eq). Densitometry analysis showing target discrimination and cleavage (right).

IV. 2.5. Mechanistic studies and comparisons with state-of-art nucleases

We analysed the cleavage effects of TFO4CII using a closed circular pCSanDI-HYG plasmid (6389 bp) containing the target sequence. The AMN-hybrid in the presence of Na-*L*-asc completely converted supercoiled (SC) plasmid to an open circular (OC) form with the linear (L) form arising at 100 equivalents of reductant (Figure IV-5A). To probe radical species involved in the cleavage pathway experiments were performed with ROS scavengers tiron (superoxide, $O_2^{\bullet-}$), *D*-mannitol (hydroxyl radical, $^{\bullet}OH$), *L*-histidine (singlet oxygen, $^1O_2$), and *L*-methionine (H_2O_2, $^{\bullet}OH$, and HOCl). It is clear that AMN-hybrids excise DNA primarily through superoxide radical production (presumably as Cu(II)-$O_2^{\bullet-}$ adducts)[35] as preincubation with tiron impedes damage of SC-DNA to delay the onset of nicking and inhibits double strand damage (Figure IV-5B, lanes 1-3). Other radical species are involved to a lesser extent and follow an inhibition profile of $H_2O_2 > {}^1O_2 > {}^{\bullet}OH$. Differences between the chemistry-based cleavage mechanism of the AMN hybrid and state-of-art enzymatic nucleases EcoRI and CRISPR-Cas12a were next examined. Although hydrolysis of DNA releases 3′-OH and 5′-PO_4 products that can be resealed by ligases (*e.g*. T4 ligase), oxidative AMNs produce fragments that are not recognized by ligase enzymes resulting in repair inhibition. The pCSanDI-HYG vector was cleaved with TFO4CII (Figure IV-5C, lane 8) and the purified products treated with T4 DNA ligase (Figure IV-5C, lane 9). Parallel re-ligation experiments were performed with restriction endonuclease EcoRI (Figure IV-5C, lane 2 & 3) and CRISPR-Cas12a enzymes (Figure IV-5C, lane 4-7) targeted to genomic sites close to the TFO4CII binding region. EcoRI and CRISPR/Cas12a restriction fragments (Figure IV-5C lanes 3, 5 & 7) produced re-ligation patterns—re-emergence of open circular and concatameric forms—consistent with hydrolytic cleavage while DNA cleaved by TFO4CII remained in its original restricted form (Figure IV-5C lanes 8 & 9; Figure C-53). These results suggest AMN-TFOs provide a different cleavage mechanism to knockdown pGFP whereby intact 5′ phosphate and 3′ hydroxyl termini are not available for re-ligation.

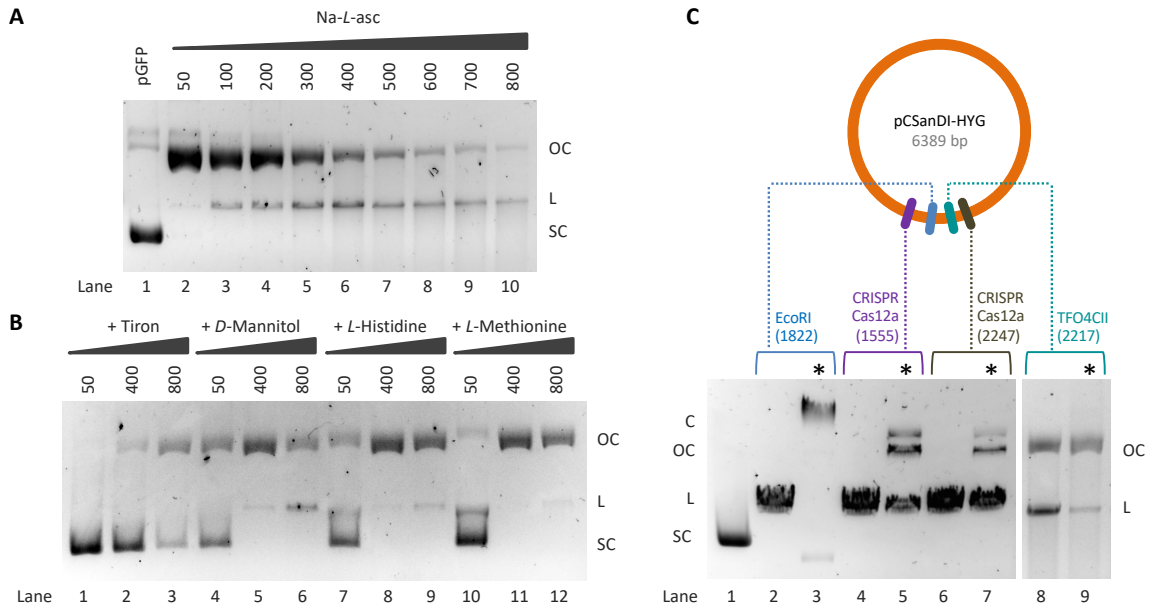

Figure IV-5. A Catalytic nuclease activity of TFO4CII on pGFP supercoiled DNA; pGFP (200 ng) treated with 250 eq of TFO4CII in the presence of increasing concentrations of Na-*L*-asc (50-800 eq to TFO4CII, lanes 2-10). **B** pGFP (200 ng) treated with 250 eq of TFO4CII with increasing Na-*L*-asc (50-800 eq, lanes 2, 6, and 10 in part **A** in the presence of 10 mM scavenging species 4,5-dihydroxy-1,3-benzenedisulfonic acid (tiron, lanes 1-3), D-mannitol (lanes 4-6), L-histidine (lanes 7-9) and L-methionine (lanes 10-12). **C** T4 DNA re-ligation study of pGFP cleaved by EcoRI (lanes 2,3), CRISPR-1555-Cas12a (lanes 4-5), CRISPR-2247-Cas12a (lanes 6-7) and TFO4CII (lanes 8,9). (SC = supercoiled; L = linear; OC = open circular; C = concatemer; * = T4 Ligase).

IV. 2.6. Application of strain-promoted and thiazole orange substituents

To expand the scope of this technology attempts to develop AMN-TFOs using bio-orthogonal chemistry—a selective reaction possible in living systems without interference to the native biochemical process—were investigated. One type of bio-orthogonal reaction is strain-promoted azide-alkyne cycloaddition (SPAAC) which operates *in-situ* without the need for copper catalysis.[43] We functionalised TFO4 with a 5′-phosphate-BCN (bicyclo[6.1.0]nonyne; Mod D) and successfully coupled the azide-modified ligands I-III *via* SPAAC (Figure IV-6A). Similar to CuAAC hybrids, AMN ligands clicked to TFO4D displayed lower T_M values with the introduction of 1 equivalent of Cu(II) affording additional triplex stability. To develop the AMN-TFO probes even further, the introduction of an intercalator that can overcome triplex instability was explored.[42] TFO4D was modified with a 5-(1-propargylamino)-2′-deoxyuridine (pdU) internally (iTOTFO) and towards the 3′-end (tTOTFO) to allow NHS ester labelling of the TFO with thiazole orange (TO), an intercalating fluorophore known to increase the stability of triplexes. The introduction of TO greatly enhances the stability of TOTFO4D (+18.4 °C) and this stability remains when the AMN ligands are clicked (Figure IV-6B). With enhanced stability, AMN-TOTFOs maintain their cleavage capability suggesting TO intercalation does not

affect strand scission (Figure IV-6C). Comparison of the triplex band in lane 5 and 6 show stronger binding effects of TOTFO4D compared to TFO4D. It is also evident from the depletion of this band in lane 8 compared to lane 6 that efficient cleavage is occurring with minimal *off*-target cleavage effects.

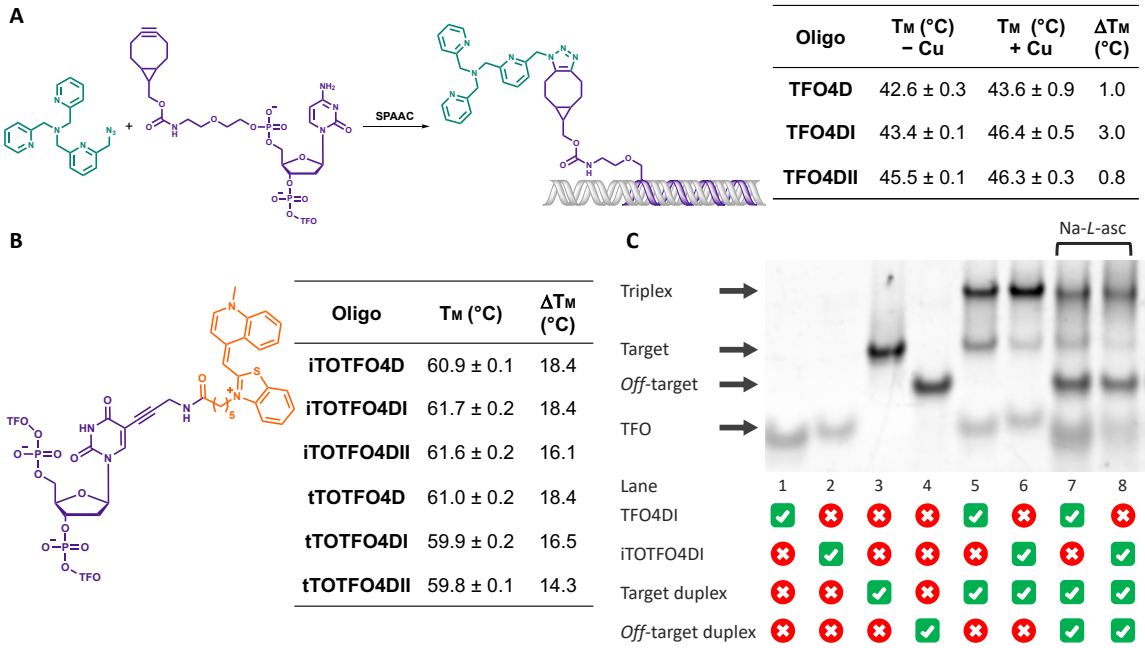

Oligo	T_M (°C) − Cu	T_M (°C) + Cu	ΔT_M (°C)
TFO4D	42.6 ± 0.3	43.6 ± 0.9	1.0
TFO4DI	43.4 ± 0.1	46.4 ± 0.5	3.0
TFO4DII	45.5 ± 0.1	46.3 ± 0.3	0.8

Oligo	T_M (°C)	ΔT_M (°C)
iTOTFO4D	60.9 ± 0.1	18.4
iTOTFO4DI	61.7 ± 0.2	18.4
iTOTFO4DII	61.6 ± 0.2	16.1
tTOTFO4D	61.0 ± 0.2	18.4
tTOTFO4DI	59.9 ± 0.2	16.5
tTOTFO4DII	59.8 ± 0.1	14.3

Figure IV-6. A Generation of AMN hybrid TFO4DI using SPAAC. **B** Structure of pdU modification with thiazole orange dye conjugated to the TFO (left), T_M of TOTFOs; t = TO attached towards 3'-end of TFO, i = internally attached TO, ΔT_M = change in T_M between TFO4D and TOTFOD4. **C** GFP target and off-target (1.25 pmol) treated with a 25 eq of copper(II) bound hybrids TFO4DI and iTOTFO4DI in the presence of 1000 eq of Na-*L*-asc (lane 7 and 8).

IV. 3. Conclusions

We have applied click chemistry and bio-orthogonal methods to engineer a new class of chemistry-based targeted nucleases. Two components are principally required: *i*.) a parallel triplex forming oligonucleotide (TFO) that binds sequence specifically, to a gene fragment, and *ii*.) a copper binding artificial metallo-nuclease (AMN) that is conjugated *via* nucleic acid click chemistry to the TFO probe strand. The use of click chemistry provides a facile method to engineer library combinations that vary in probe length (16-32 nt), modification placement, and copper-binding scaffold. By exploiting the unique base-triplet recognition properties of TFOs, purine-rich tracts of the green fluorescent protein (GFP) gene were targeted and cleaved by copper-bound hybrids. TFOs represent a strategic choice since the Hoogsteen base pairing makes them easily programmable to target extended sequences that do not require disruption of the dsDNA structure for recognition. Quantitative PCR analysis and visualisation of triplexes by polyacrylamide gel electrophoresis identified cleavage

responses consistent with oxidative damage and the cleavage sensitivity of copper-bound hybrids can be enhanced in the presence of a reducing agent. Significantly, the chemical-based DNA cutting mechanism by AMN-TFOs provides a unique type of cleavage mechanism compared to state-of-art enzymatic nucleases, including CRISPR-Cas, which hydrolytically cleave target sequences rendering them amenable to resealing/repair by ligases. To extend the boundaries of this technology, hybrid systems were engineered using bio-orthogonal methods involving strain-promoted substituents with thiazole orange modifications introduced to augment triplex stability. Further refinements to progress these materials towards cellular applications include the development of AMNs that provide damage specificity (double strand breaks vs. nicking) with catalytic cores that limit diffusible radical production to reduce undesirable *off*-target cleavage effects. Exploiting synthetic triplex motifs with backbone and ribose modifications may offer improved resistance to free radical oxidation and provide cellular targeting advantages to this type of chemistry-based hybrid knockout system.

IV. 4. Materials and methods

My contribution to this chapter was to design, synthesise and characterise a series of azide modified polypyridyl scaffolds. Design, synthesis of the oligonucleotides and 'click' reactions were conducted by me in collaboration with Dr. Daniel Singleton. I designed and conducted the experiments to analyse triplex formation, *off*-target discrimination and oxidative damage on plasmid DNA. X-ray spectroscopy was performed by Prof. Vickie McKee. qPCR experiments were conducted by my colleague Bríonna McGorman. Experiments with thiazole orange modified oligonucleotides were conducted by Sarah Walsh in collaboration with Dr. Afaf El-Sagheer. Prof. Andrew Kellett and Prof. Tom Brown supervised the project.

Chemicals, reagents and high-performance liquid chromatography (HPLC) grade solvents including $CHCl_3$, MeOH and CH_3CN were purchased from Merck (Ireland) or Tokyo Chemical Industry (TCI, UK Ltd) and used without further purification. ^1H, ^{13}C NMR and 2D-NMR spectra were obtained on a Bruker AC 600 MHz NMR spectrometer (C-1). pH was monitored using a Mettler Toledo InLab Expert Pro-ISM pH probe. Electrospray ionization mass spectrometry (ESI-MS) measurements were recorded on a Bruker HCT-MS with samples prepared in 100% HPLC-grade CH_3CN prior to ESI-MS analysis. UV/Vis absorption spectroscopy studies were carried out on a Shimadzu UV-2600 spectrophotometer. FTIR measurements were conducted on a PerkinElmer Spectrum Two spectrometer. Thermal melting analysis was carried out on an Agilent Cary 100 dual beam spectrophotometer equipped with a 6 × 6 Peltier multicell system and temperature controller or an Agilent Cary 4000 UV-Visible spectrophotometer from Varian. PAGE and agarose gels were photographed using a Syngene G:Box mini 9 imaging system. Real-time PCR (qPCR) analysis was performed on a Roche LightCycler® 480 II using SYBR Green I Master mix (Roche). X-ray diffraction data were collected at 100(2)K on a Synergy, Dualflex, AtlasS2 diffractometer using CuKα radiation. The structure was solved by dual space methods and refined on F^2 using all the reflections (SHELXL-2018).

IV. 4.1. Route A: Synthesis of *N*-5-(azidomethyl)pyridine-*N*-*di*-(2-picolyl)amine ($5N_3$-TPMA)

IV. 4.1.1. 2,5-Pyridine dicarboxylic acid dimethyl ester (1a)

1a was synthesized according to a procedure previously reported by Kramer *et al*.[44] A suspension of 2,5-pyridinedicarboxylic acid (20.011 g, 119.74 mmol) in MeOH (55 mL) and conc. H_2SO_4 (4.5 mL) was refluxed overnight, neutralized with a saturated aqueous

solution of $NaHCO_3$, and extracted with $CHCl_3$ (3 × 150 mL). The combined organic phases were dried over $MgSO_4$ and the solvent removed *in vacuo* to yield the diester product **1a** as a white solid (16.712 g, yield = 71.5%). ^{1}H-NMR (600 MHz, $CDCl_3$): δ 9.24 (dd, J = 2.1, 0.7 Hz, 1H), 8.39 (dd, J = 8.1, 2.1 Hz, 1H), 8.15 (dd, J = 8.1, 0.7 Hz, 1H), 3.98 (s, 3H), 3.93 (s, 3H). ^{13}C-NMR (151 MHz, $CDCl_3$): δ 164.9, 164.8, 150.8, 150.7, 138.3, 128.6, 124.7, 53.2, 52.7.

IV. 4.1.2. 2,5-Bis(hydroxymethyl)pyridine (2a)

2a was synthesized according to a procedure previously reported by Kramer *et al*.[44] $NaBH_4$ (0.390 g, 10.30 mmol) was added slowly to a suspension of **1a** (0.502 g, 2.57 mmol) in EtOH (10 mL) at 0 °C. The solution was stirred for 1 h at 0 °C, then for 3 h at room temperature, and finally at reflux overnight. The solvent was removed and the resulting yellow oil was dissolved in a mixture of acetone (50 mL) and saturated aqueous solution of K_2CO_3 (50 mL), refluxed for 1 h and the yellow organic phase collected from a bi-phasic mixture. The solvent was removed and the crude product purified *via* dry column vacuum chromatography (DCVC silica gel, CH_2Cl_2:MeOH, 7:1 v/v) to yield the diol **2a** as a yellow, hygroscopic oil (0.204 g, yield = 57.0%). ^{1}H-NMR (600 MHz, MeOD-d_4): δ 8.46 (d, J = 1.6 Hz, 1H), 7.84 (dd, J = 8.0, 2.0 Hz, 1H), 7.54 (d, J = 8.0 Hz, 1H), 4.70 (s, 2H), 4.65 (s, 2H). ^{13}C-NMR (151 MHz, MeOD): δ 161.2, 148.1, 137.6, 137.3, 121.8, 65.4, 62.4.

IV. 4.1.3. 2-Formyl-5-hydroxymethylpyridine (3a)

3a was synthesized according to a procedure reported by Dawson *et al*.[45] Under inert atmosphere, **2a** (8.277 g, 59.49 mmol) was dissolved in 1,4-dioxane (80 mL) and H_2O (2 mL) and SeO_2 (3.386 g, 30.51 mmol) was added. The mixture was degassed and heated under argon at 100 °C for 3 h. The solution was then filtered through a celite pad (30 mL dioxane wash), reduced in volume to ~ 5 mL, and purified *via* DCVC (silica gel, hexane:ethylacetate, gradient 50:50 to 25:75 v/v). The fractions of the product were combined, and solvent removed *in vacuo* to yield **3a** as a pale yellow solid (6.633 g, yield = 81.3%). ^{1}H-NMR (600 MHz, $CDCl_3$): δ 10.1 (d, J = 0.8 Hz, 1H), 8.77 (dd, J = 2.0, 0.7 Hz, 1H), 7.97 (dd, J = 8.0, 0.7 Hz, 1H), 7.90 (dq, J = 8.0, 2.1, 0.8 Hz, 1H), 4.87 (s, 2H, CH_2). ^{13}C-NMR (151 MHz, $CDCl_3$): δ 193.2, 152.4, 148.8, 140.9, 135.4, 121.8, 62.5.

IV. 4.1.4. 5-Hydroxomethyl-*di*-(2-pycolyl)amine (4a)

To a solution of 2-picolylamine (0.179 g, 1.65 mmol) in MeOH (20 mL), a solution of **3a** (0.229 g, 1.67 mmol) in MeOH (20 mL) was added at 0 °C, stirred for 1 h at room

temperature and $NaBH_4$ (0.063 g, 1.66 mmol) was added at 0 °C. The reaction was stirred at room temperature overnight. A minimal volume of H_2O was added and MeOH was removed *in vacuo*. The solution was acidified with conc. HCl to pH ~ 4 and extracted with CH_2Cl_2 (6 x 20 mL). $NaHCO_3$ was slowly added to the aqueous layer to reach pH ~ 8, extracted with CH_2Cl_2 (3 x 100 mL) and the combined organic layers were dried over $MgSO_4$. The solvent was removed to afford **4a** as a yellow oil (0.170 g, yield = 44.9%). ^{1}H-NMR (600 MHz, $CDCl_3$): δ 8.56 (dq, J = 4.9, 1.5, 0.8 Hz, 1H), 8.53 (d, J = 1.8 Hz, 1H), 7.67 (dd, J = 8.0, 2.2 Hz, 1H), 7.64 (td, J = 7.6, 1.8 Hz, 1H), 7.37 (d, J = 7.9, Hz, 1H), 7.35 (d, J = 7.9 Hz, 1H), 7.16 (qd, J = 7.4, 4.9, 0.9 Hz, 1H), 4.71 (s, 2H), 3.99 (s, 2H), 3.97 (s, 2H). ^{13}C-NMR (151 MHz, $CDCl_3$): δ 195.8, 149.4, 148.3, 136.6, 135.6, 122.4, 122.3, 122.2, 63.0, 54.8, 54.62.

IV. 4.1.5. 5-Hydroxomethyl-*tris*-(2-pycolyl)amine (5a)

4a (0.130 g, 0.57 mmol) was dissolved in CH_3CN (15 mL) and stirred with $NaHCO_3$ (0.097 g, 1.15 mmol). 2-pycolylchloride (0.072 g, 0.57 mmol) in CH_3CN (15 mL) was added dropwise and the mixture was stirred at 50 °C for 72 h. The solution was filtered and the filtrate evaporated to afford **5a** as a brown oil. (0.135 g, yield = 74.4%) ^{1}H-NMR (600 MHz, $CDCl_3$): δ 8.51 (dq, J = 4.8, 1.6, 0.8 Hz, 2H), 8.47 (d, J = 1.7 Hz, 1H), 7.69 (dd, J = 8.0, 2.2 Hz, 1H), 7.64 (td, J = 7.7, 1.8 Hz, 2H), 7.57 (d, J = 2.7 Hz, 2 H), 7.55 (d, J = 2.9 Hz, 1 H), 7.13 (qd, J = 7.4, 4.9, 1.1 Hz, 2H), 4.68 (s, 2H), 3.85 (s + s, 6H).

IV. 4.1.6. 5-Chloromethyl-*tris*-(2-pycolyl)amine (6a)

A modification of the literature procedure by Sprakel *et al.* was employed.[46] A solution of **5a** (0.396 g, 1.24 mmol) in $CHCl_3$ (5 mL) was added dropwise at 0 °C to a solution of $SOCl_2$ (0.450 mL, 6.18 mmol) in $CHCl_3$ (10 mL) and stirred overnight at room temperature. The solvent was removed *in vacuo* and the green product was dissolved in THF (5 mL) and DIPEA (0.808 mL) and stirred under argon for 3 h at room temperature and filtered through a celite pad (25 mL THF wash). Solvent was removed *in vacuo* to yield **6a** as a brown solid. (0.381 g, yield = 90.9%) ^{1}H NMR (600 MHz, $CDCl_3$): δ 8.54 (dq, J = 4.8, 1.8, 0.9 Hz, 2H), 8.52 (d, J = 1.9 Hz, 2H), 7.69 (dd, J = 8.1, 2.3 Hz, 1H), 7.65 (td, J = 7.7, 1.8 Hz, 2H), 7.60 (d, J = 8.1 Hz, 1 H), 7.56 (d, J = 7.8 Hz, 2 H), 7.14 (qd, J = 7.4, 4.9, 1.2 Hz, 2H), 4.56 (s, 2H), 3.89 (s, 2H), 3.88 (s, 4H).

IV. 4.1.7. 5-Azidomethyl-*tris*-(2-pycolyl)amine (7a)

To a solution of **6a** (0.381 g, 1.12 mmol) in CH_3CN (20 mL), NaN_3 (0.219 g, 3.37 mmol) was added. The mixture was stirred in the dark at 50 °C overnight, filtered through a celite pad and solvent removed. The product was dissolved in $CHCl_3$ (20 mL) and washed with H_2O (3 x 10 mL). The organic phase was dried to yield **7a** as a brown solid (0.148 g, yield = 38.3%) ^{1}H NMR (600 MHz, $CDCl_3$): δ 8.54 (dq, J = 7.2, 2.3, 1.2 Hz, 2H), 8.47 (s, 1H), 7.66 (td, J = 11.5, 2.7 Hz, 4H), 7.63 (d, J = 2.8 Hz, 4H), 7.56 (d, J = 11.6 Hz, 2 H), 7.15 (qd, J = 11.1, 7.4, 1.7 Hz, 2H), 4.35 (s, 2H), 3.90 (s, 2H), 3.89 (s, 4H).

IV. 4.2. Route B: Synthesis of *N*-6-(azidomethyl)pyridine-*N*-*di*-(2-picolyl)amine ($6N_3$-TPMA)

IV. 4.2.1. Synthesis of *di*-(2-picolyl)amine (DPA)

Di-(2-picolyl)amine was synthesized according to a procedure reported by Hamann *et al*.[47] To a solution of 2-picolylamine (2.011 g, 18.6 mmol) in MeOH (10 mL), a solution of 2-pyridinecarboxaldehyde (2.025 g, 18.9 mmol) in MeOH (10 mL) was added dropwise at 0 °C. The solution was stirred for 1 h at room temperature, $NaBH_4$ (0.704 g, 18.6 mmol) was added slowly at 0 °C and stirred at room temperature overnight. A minimal volume of water was added and MeOH was removed *in vacuo.* The solution was acidified with conc. HCl to pH ~ 4 and extracted with CH_2Cl_2 (6 x 20 mL). Na_2CO_3 was added slowly to the aqueous layer until a pH ~ 10 was reached. The product was extracted with CH_2Cl_2 (3 x 25 mL) and the combined organic layers dried over $MgSO_4$. Solvent was removed *in vacuo* to yield DPA as a yellow oil. (1.761 g, yield= 47.5%). ^{1}H-NMR (600 MHz, $CDCl_3$): δ 8.55 (dq, J = 4.9, 1.9, 1.0 Hz, 1H), 7.64 (td, J = 7.7, 1.9 Hz, 1H), 7.35 (d, J = 7.8 Hz, 1H), 7.15 (qd, J = 7.5, 4.8, 1.2 Hz, 1H), 3.98 (s, 2H). ^{13}C-NMR (151 MHz, $CDCl_3$): δ 159.6, 149.2, 136.3, 122.2, 121.8, 54.7. ESI-MS: *m/z* calcd 200.1 $[M + H]^+$; found 200.1.

IV. 4.2.2. *N*-6-(chloromethyl)pyridine-*N*-*di*-(2-picolyl)amine (1b)

1b was prepared according to the method reported by Pope *et al.* with slight modification.[48] To a solution of 2,6-*bis*(chloromethyl)pyridine (0.505 g, 2.86 mmol) in CH_3CN (15 mL), $NaHCO_3$ (0.241 g, 2.87 mmol) was added, followed by 1 eq. of *di*-(2-picolyl)amine (0.571 g, 2.86 mmol) in CH_3CN (15 mL). The mixture was stirred at 50 °C overnight and monitored by ^{1}H-NMR. The solution was filtered and the filtrate evaporated to dryness. The orange, oily residue was purified by column chromatography (silica gel, CH_2Cl_2:MeOH, 95:5 v/v). Fractions of **1b** were combined and the solvent removed to

afford a yellow solid (0.349 g, yield = 36.0%). ^{1}H-NMR (600 MHz, $CDCl_3$): δ 8.53 (dq, J = 4.8, 1.7, 0.9 Hz, 2H), 7.68 (t, J = 7.7 Hz, 1H), 7.65 (td, J = 7.7, 1.8 Hz, 1H), 7.57 (d, J = 7.8 Hz, 2H), 7.54 (d, J = 7.7 Hz, 1H), 7.32 (d, J = 7.6 Hz, 1H), 7.14 (qd, J = 7.4, 4.9, 1.1 Hz, 2H), 4.64 (s, 2H), 3.90 (s, 4H), 3.89 (s, 2H). ^{13}C-NMR (151 MHz, $CDCl_3$): δ 159.4, 156.0, 149.2, 137.6, 136.6, 123.1, 122.3, 122.1, 121.1, 60.3, 60.0, 47.0. ESI-MS: *m/z* calcd: 361.1 $[M+H]^+$; found: 361.1.

IV. 4.2.3. *N*-6-(azidomethyl)pyridine-*N*-*di*-(2-picolyl)amine (2b)

To a solution of **1b** (0.349 g, 1.03 mmol) in CH_3CN (15 mL), NaN_3 (0.214 g, 3.29 mmol) was added, stirred in the dark at 50 °C overnight, filtered over a celite pad and evaporated to dryness. The product was dissolved in $CHCl_3$ (20 mL) and washed with H_2O (3 x 10 mL). The organic phase was dried to yield **2b** as a brown solid (0.097 g, yield = 27.4%). ^{1}H-NMR (600 MHz, $CDCl_3$): δ 8.53 (d, J = 4.4 Hz, 2H), 7.68 (t, J = 7.7 Hz, 1H), 7.65 (td, J = 7.6, 1.8 Hz, 2H), 7.58 (d, J = 7.7 Hz, 2H), 7.54 (d, J = 7.7 Hz, 1H), 7.18 (d, J = 7.6 Hz, 1H), 7.14 (q, J = 6.3, 5.0 Hz, 2H), 4.44 (s, 2H, CH_2), 3.88 (d, 6H, CH_2). ^{13}C-NMR (151 MHz, $CDCl_3$): δ 159.8, 159.5, 155.2, 149.3, 137.5, 136.6, 123.1, 122.3, 122.2, 120.3, 60.4, 60.1, 55.8. ESI-MS: *m/z* calcd: 368.2 $[M+Na]^+$; found: 368.2.

Crystal Data for $[Cu(6N_3\text{-TPMA})(NO_3)](NO_3)\cdot\frac{1}{2}CH_3CN$**:** $C_{20}H_{20.5}N_{9.5}O_6Cu$ (M =553.50 g/mol): triclinic, space group $P\bar{1}$ (no. 2), a = 10.6029(2) Å, b = 14.9442(4) Å, c = 15.8857(4) Å, α = 68.947(2)°, β = 82.439(2)°, γ = 82.246(2)°, V = 2318.19(11) Å^3, Z = 4, T = 100.00(10) K, μ(CuKα) = 1.855 mm^{-1}, D_{calc} = 1.586 g/cm^3, 21435 reflections measured (8.45° ≤ 2θ ≤ 153.396°), 9502 unique (R_{int} = 0.0269, R_{sigma} = 0.0350) which were used in all calculations. The final $R1$ was 0.0350 (I > 2σ(I)) and $wR2$ was 0.0914 (all data).

IV. 4.3. Route C: Synthesis of *N*-4-azidobenzyl-*N*-*di*-(2-picolyl)amine ($4N_3$-Benzyl-DPA)

IV. 4.3.1. *N*-4-nitrobenzyl-*N*-*di*-(2-picolyl)amine (1c)

On a parallel synthesizer, ten reactions were prepared using a modification of a literature procedure reported by Du *et al.*[49] DPA (0.247 g, 1.24 mmol), K_2CO_3 (0.516 g, 3.74 mmol) and *p*-nitrobenzylbromide (0.268 g, 1.24 mmol) were mixed in CH_3CN (10 mL) and stirred overnight at room temperature. The resulting suspension was filtered and solvent removed to yield an orange oil. The crude product was purified *via* column chromatography (silica gel, MeOH:CH_2Cl_2, gradient 0:100 to 20:80 v/v) yielding **1c** as a brown solid. (2.614 g, yield = 64.2%) ^{1}H-NMR (600 MHz, $CDCl_3$): δ 8.54 (dq, J = 4.9, 1.7, 0.9 Hz, 2H), 8.16 (dt,

J = 8.8, 2.3 Hz, 2H), 7.67 (td, J = 7.7, 1.8 Hz, 2H), 7.58 (d, J = 8.8 Hz, 2 H), 7.52 (d, J = 7.8 Hz, 2H), 7.17 (qd, J = 7.4, 4.9, 1.1 Hz, 2H), 3.83 (s, 4H), 3.81 (s, 2H).^{13}C-NMR (151 MHz, $CDCl_3$): δ 159.0, 149.3, 147.3, 136.7, 129.5, 123.7, 123.1, 122.4, 60.3, 57.9. ESI-MS *m/z* calcd: 357.1 $[M+Na]^+$; found: *m/z* 358.1.

IV. 4.3.2. *N*-4-amminobenzyl-*N*-*di*-(2-picolyl)amine (2c)

To a solution of **1c** (0.497 g, 1.49 mmol) in EtOH/H_2O (3:1; 48 mL), Na_2S (2.901 g, 37.23 mmol) was added and stirred at 70 °C for two days. The solvent was reduced and the product extracted with CH_2Cl_2 (3 x 50 mL). The combined fractions were dried over $MgSO_4$ and the solvent removed to afford **2c** as an orange oil that solidifies over time. (0.371 g, yield = 82.0%) ^{1}H-NMR (600 MHz, $CDCl_3$): δ 8.50 (d, J = 4.8 Hz, 2H), 7.65 (td, J = 7.9, 1.4 Hz, 2H), 7.57 (d, J = 7.8 Hz, 2H), 7.18 (d, J = 8.2 Hz, 2 H), 7.12 (q, J = 6.2, 5.1 Hz, 2H), 6.63 (d, J = 8.2 Hz, 2H), 3.77 (s, 4H), 3.55 (s, 2H).^{13}C-NMR (151 MHz, $CDCl_3$): δ 160.2, 149.0, 145.5, 136.5, 130.2, 128.9, 122.9, 122.0, 115.2, 59.9, 58.1. ESI-MS: *m/z* calcd: 372.2 $[M+Na]^+$; found: 372.1.

IV. 4.3.3. *N*-4-azidobenzyl-*N*-*di*-(2-picolyl)amine (3c)

The diazotransfer reagent 2-azido-1,3-dimethylimidazolinium hexafluorophosphate (ADMP) used in the following synthesis was prepared according to a literature procedure previously reported by Kitamura *et al*.[50] To a suspension of *N*-4-amminobenzyl-*N*-*di*-(2-picolyl)amine (0.159 g, 0.52 mmol) and *N,N'*-dimethyl-4-aminopyridine (DMAP; 0.076 g, 0.63 mmol) in CH_3CN (10 mL), ADMP (0.178 g, 0.63 mmol) was added and stirred overnight at 30 °C. The reaction was quenched with a saturated aqueous solution of $NaHCO_3$ and the salted-out product extracted with CH_2Cl_2 (3 x 20 mL). The combined fractions were dried over $MgSO_4$ and the solvent removed. The crude compound was purified by column chromatography (silica gel, CH_3CN:DCM, 40:60 v/v) and combined fractions dried *in vacuo* to afford the product **3c** as a brown solid. (0.121 g, yield = 70%). ^{1}H-NMR (600 MHz, $CDCl_3$): δ 8.52 (dq, J = 4.9, 1.8, 0.9 Hz, 2H), 7.66 (td, J = 7.7, 1.8 Hz, 2H), 7.55 (d, J = 7.8 Hz, 2H), 7.38 (d, J = 8.5 Hz, 2 H), 7.15 (qd, J = 7.4, 4.9, 1.1 Hz, 2H), 6.98 (dt, J = 8.5, 2.5 Hz, 2H), 3.79 (s, 4H), 3.66 (s, 2H). ^{13}C-NMR (151 MHz, $CDCl_3$): δ 149.2, 136.6, 130.4, 123.0, 122.2, 119.1, 60.0, 57.9. ESI-MS: *m/z* calcd: 353.1 $[M+Na]^+$; found: 353.1.

IV. 4.4. Click reactions

IV. 4.4.1. Oligonucleotide synthesis and purification

Alkyne-modified TFOs and dsDNA targets were synthesised by solid phase synthesis using an automated DNA synthesiser (Applied Biosystems 394) according to standard methods. Coupling efficiencies were monitored by the trityl cation conductivity monitoring facility and were greater than 98% for all oligonucleotides (ODNs). Modified phosphoramidites such as Mod A, B and C were purchased from Glen Research and Mod D from Berry and Associates. 5-(1-propargylamino)-dU phosphoramidite as well as thiazole orange was synthesised according to previously determined conditions.[42] ODNs were deprotected and cleaved in standard aqueous ammonia by heating for 5 h at 55 °C and were purified by gradient reverse phase HPLC (C8 size exclusion column) in 0.1 M Triethylammonium acetate (TEAA) buffer with 50% CH_3CN. Gradients of 10-40% over 20 minutes were used with 4 mL/min flow rate before desalting using NAP-25 (GE Healthcare). Purity of TFOs and dsDNA were analysed by ESI-MS (C-3). TFOs containing pdU were labelled with TO following a procedure by Walsh *et al*.[42]

IV. 4.4.2. CuAAC 'click' reaction of TFOs with AMN-ligands

The CuAAC reactions were performed according to the Lumiprobe protocol for click-chemistry labeling of oligonucleotides with minor modifications. In a final volume of 3 mL (50:50, H_2O:DMSO), 60 nmols of the alkyne-modified TFOs, 90 nmols of azide-modified ligand ($6N_3$-TPMA, $5N_3$-TPMA or $4N_3$-Benzyl-DPA) and 1.5 μmols of Na-*L*-asc were added. Reaction mixtures were degassed with nitrogen and 1.5 μmol of Cu-TBTA complex in DMSO (55% aqueous solution) was added. Solutions were further degassed, stirred overnight, quenched with 30 μmol of EDTA and desalted using NAP-25 columns. The volume was reduced and clicked TFOs were purified by gradient (0.1 M NH_4OAc + 50% CH_3CN in NH_4OAc) reverse phase HPLC (C8 size exclusion column) to yield the final products (33-67%). Purity of the AMN-TFOs were determined by ESI-MS (Appendix C-3 and C-4).

IV. 4.5. Triplex formation studies

Thermal melting of the TFO triplexes in absence and presence of Cu(II)

Solutions for thermal melting analysis containing 5 μM TFO and 2 μM target duplex (2.5:1 TFO:duplex) were prepared in a final volume of 100 μL buffer (10 mM PO_4^{3-}, 150 mM NaCl, 2 mM $MgCl_2$, pH ~ 6). Prior to analysis, TFOs and target duplexes were denatured by heating to 90 °C (10 °C/min, 2 min hold) and reannealed at 12 °C (0.5 °C/min, 20 min

hold). In experiments containing Cu(II), 5 μM $Cu(ClO_4)_2$ was added at this point (1:1 ratio with TFO). Thermal melting analysis was recorded at 260 nm using Starna black-walled quartz cuvettes with tight-fitting seals in the range of 12-90 °C (0.5 °C/min, 2 min hold). A total of three heating ramps were carried out and T_M calculated as an average of the first derivative of the sigmoidal regression fit of the triplex melting curve on Graphpad Prism® 6.0 software.

IV. 4.6. DNA damage studies

Stock solutions of AMN-TFOs and target duplexes were initially prepared in nuclease-free water and further dilutions prepared in reaction buffer (10 mM PO_4^{3-}, 150 mM NaCl, 2 mM $MgCl_2$, pH ~ 6). 1 *eq.* of Cu(II) ($Cu(ClO_4)_2$) was added to the AMN-TFO stock solutions and incubated for 15 minutes prior to further use.

IV. 4.6.1. Cleavage efficacy of AMN-TFO hybrids

In a total volume of 5 μL, a target DNA duplex sequence (52 bp, 1.25 pmol) was exposed to increasing eq. of TFO4CII in the presence of Na-*L*-asc (3.125 mM). Reaction mixtures were vortexed and incubated at 37 °C for 6 h, quenched with 6X loading dye and loaded onto a 20% polyacrylamide gel (50 mM Trizma, 5 mM $MgCl_2$, pH ~ 6). Electrophoresis was carried out at 70 V for 6 h in Trizma buffer (50 mM, pH ~ 6) and post-stained with SybrGold.

IV. 4.6.2. Catalytic activity of AMN-TFO hybrids

A target DNA duplex sequence (52 bp, 1.25 pmol) was exposed to TFO4CII (31.25 pmol) in the presence of increasing equivalents of Na-*L*-asc for 6 h at 37 °C with electrophoresis and staining carried out as previously stated.

IV. 4.6.3. qPCR analysis of catalytic activity

A 113 bp region of the pCSanDI-HYG plasmid (containing the target site for TFO4) was amplified by PCR (forward primer: 5'-AAAGGGAGCCCCCGATTTAG-3' and reverse primer: 5'-GTGACCGCTACACTTGCCA-3') and amplicons purified using Monarch® PCR & DNA clean-up kit (NEB, T1030). In a total volume of 12 μL, the target DNA duplex (113-mer, 1.25 pmol) was exposed to each hybrid material (31.25 pmol of either TFO4CI, TFO4CII or TFO4CIII) in the presence of increasing equivalents of Na-*L*-asc. Reaction mixtures were vortexed. At t = 0 h, 6 μL of the reaction volume was quenched with EDTA (90 nmol) and kept as a control. The remaining 6 μL was incubated at 37 °C for 6 h (target) prior to addition of EDTA. Control and target samples were diluted ($1:10^5$) and qPCR

analysis was performed over 45 cycles (LightCyler 480 II). Each sample was prepared as per kit protocol using LightCycler 480 SYBR green I master kit (Roche, 04887352001). The change in threshold cycle (C_T) between the target (6 h) and control sample (0 h) (target C_T – control C_T) was calculated (ΔC_T). ΔC_T were plotted as linear values ($2^{-\Delta CT}$). The $2^{-\Delta CT}$ values were normalised to the untreated duplex yielding a $2^{-\Delta\Delta CT}$ plot.

IV. 4.6.4. Target and *off*-target cleavage discrimination

In a total volume of 5 µL, a mixture of target and *off*-target (no triplex recognition) DNA duplex sequences was exposed to 25 eq of each hybrid material (TFO3AI, TFO4AIII, TFO4BI, TFO4CII or a 1:1 mixture of free Cu-TPMA and TFO4C) in the presence of increasing equivalents of Na-*L*-asc for 6h at 37 °C. Electrophoresis and staining was carried out as previously stated.

IV. 4.6.5. pCSanDI-HYG cleavage efficacy

In a total volume of 5 µL, pCSanDI-HYG (200 ng, 0.05 pmol) was treated with 250 eq of TFO4CII in the presence of increasing concentrations of Na-*L*-asc (50-800 eq to TFO4CII) for 6 h at 37 °C. Reactions were quenched with 6X loading dye and loaded onto a 1% agarose gel containing 10 µL SYBR Safe and subjected to electrophoresis at 70 V for 3 h in TAE buffer (1X).

IV. 4.6.6. pCSanDI-HYG cleavage in the presence of ROS scavengers

In a total volume of 5 µL, pCSanDI-HYG (200 ng, 0.05 pmol) was treated with 250 eq of TFO4CII and increasing concentrations of Na-*L*-asc (50-800 eq to TFO4CII), in the presence of 10 mM scavenging species 4,5-dihydroxy-1,3-benzenedisulfonic acid (tiron), *D*-mannitol, *L*-histidine and *L*-methionine. Control cleavage by nuclease enzymes EcoRI and CRISPR-Cas12a were also performed in the presence of radical scavengers. Reactions were vortexed and incubated at 37 °C for 6 h. Agarose gel electrophoresis carried out as above.

IV. 4.6.7. T4 re-ligation assay

pCSanDI-HYG (2 µg, 0.51 pmol) was initially treated with 250 eq of TFO4CII in the presence of Na-*L*-asc (400 eq to TFO4CII) for 6 h at 37 °C and quenched with Na_2EDTA (100 eq TFO4CII). Control linear (L) DNA was obtained through the treatment of pCSanDI-HYG (2 µg, 0.51 pmol) with either 10 eq of EcoRI (NEB, R0101S) or CRISPR-Cas12a (IDT, 10001272). Both enzymes were heat denaturated for 20 min at 65 °C. Linear DNA products were purified by Monarch® PCR & DNA clean-up kit (NEB, T1030L) and

eluted in 20 µL nuclease free H_2O. 10 µL of purified DNA were kept as control and 10 µL were incubated with 2 µL T4 DNA Ligase (NEB, M0202S).

IV. 5. References:

[1] B. L. Stoddard, A. Khvorova, D. R. Corey, W. S. Dynan, K. R. Fox, *Nucleic Acids Res.* **2018**, *46*, 1563–1564.

[2] X. Shen, D. R. Corey, *Nucleic Acids Res.* **2018**, *46*, 1584–1600.

[3] M. Faria, C. Giovannangeli, *J. Gene Med.* **2001**, *3*, 299–310.

[4] F. A. Ran, P. D. Hsu, J. Wright, V. Agarwala, D. A. Scott, F. Zhang, *Nat. Protoc.* **2013**, *8*, 2281–2308.

[5] H. Wang, M. La Russa, L. S. Qi, *Annu. Rev. Biochem.* **2016**, *85*, 227–264.

[6] C. Fellmann, B. G. Gowen, P.-C. Lin, J. A. Doudna, J. E. Corn, *Nat. Rev. Drug. Discov.* **2017**, *16*, 89–100.

[7] R. Barrangou, P. Horvath, *Nature Microbiology* **2017**, *2*, 17092.

[8] T. Bentin, in *DNA-Targeting Molecules as Therapeutic Agents* (Ed.: M.J. Waring), **2018**, pp. 391–407.

[9] H. A. Rees, D. R. Liu, *Nat. Rev. Gen.* **2018**, *19*, 770–788.

[10] A. Kellett, Z. Molphy, C. Slator, V. McKee, N. P. Farrell, *Chem. Soc. Rev.* **2019**, *48*, 971–988.

[11] J. Cadet, J. R. Wagner, *Cold Spring Harb. Perspect. Biol.* **2013**, *5*, a012559.

[12] C. Marzano, M. Pellei, F. Tisato, C. Santini, *Anticancer Agents Med. Chem.* **2009**, *9*, 185–211.

[13] D. S. Sigman, A. Mazumder, D. M. Perrin, *Chem. Rev.* **1993**, *93*, 2295–2316.

[14] B. C. Bales, T. Kodama, Y. N. Weledji, M. Pitié, B. Meunier, M. M. Greenberg, *Nucleic Acids Res.* **2005**, *33*, 5371–5379.

[15] K. J. Humphreys, K. D. Karlin, S. E. Rokita, *J. Am. Chem. Soc.* **2002**, *124*, 8055–8066.

[16] S. Thyagarajan, N. N. Murthy, A. A. Narducci Sarjeant, K. D. Karlin, S. E. Rokita, *J. Am. Chem. Soc.* **2006**, *128*, 7003–7008.

[17] N. Zuin Fantoni, Z. Molphy, C. Slator, G. Menounou, G. Toniolo, G. Mitrikas, V. McKee, C. Chatgilialoglu, A. Kellett, *Chem. Eur. J.* **2019**, *25*, 221–237.

[18] R. Larragy, J. Fitzgerald, A. Prisecaru, V. McKee, P. Leonard, A. Kellett, *Chem. Commun.* **2015**, *51*, 12908–12911.

[19] A. Kellett, Z. Molphy, V. McKee, C. Slator, in *Metal-Based Anticancer Agents* (Eds.: A. Casini, A. Vessières, S.M. Meier-Menches), **2019**, pp. 91–119.

[20] C. Slator, Z. Molphy, V. McKee, C. Long, T. Brown, A. Kellett, *Nucleic Acids Res.* **2018**, *46*, 2733–2750.

[21] M. Pitié, C. J. Burrows, B. Meunier, *Nucleic Acids Res.* **2000**, *28*, 4856–4864.

[22] D. S. Sigman, T. W. Bruice, A. Mazumder, C. L. Sutton, *Acc. Chem. Res.* **1993**, *26*, 98–104.

[23] J. Gallagher, C. B. Chen, C. Q. Pan, D. M. Perrin, Y.-M. Cho, D. S. Sigman, *Bioconjugate Chem.* **1996**, *7*, 413–420.

[24] P. B. Dervan, *Isr. J. Chem.* **2019**, *59*, 71–83.

[25] J. C. François, T. Saison-Behmoaras, M. Chassignol, N. T. Thuong, C. Helene, *J. Biol. Chem.* **1989**, *264*, 5891–5898.
[26] S. A. Kane, S. M. Hecht, J.-S. Sun, T. Garestier, C. Helene, *Biochemistry* **1995**, *34*, 16715–16724.
[27] H. Moser, P. Dervan, *Science* **1987**, *238*, 645–650.
[28] S. A. Strobel, P. B. Dervan, *Science* **1990**, *249*, 73–75.
[29] Y. Aiba, J. Sumaoka, M. Komiyama, *Chem. Soc. Rev.* **2011**, *40*, 5657–5668.
[30] F. H. Zelder, A. A. Mokhir, R. Krämer, *Inorg. Chem.* **2003**, *42*, 8618–8620.
[31] G. Gasser, A. Pinto, S. Neumann, A. M. Sosniak, M. Seitz, K. Merz, R. Heumann, N. Metzler-Nolte, *Dalton Trans.* **2012**, *41*, 2304–2313.
[32] G. Gasser, K. Jäger, M. Zenker, R. Bergmann, J. Steinbach, H. Stephan, N. Metzler-Nolte, *J. Inorg. Biochem.* **2010**, *104*, 1133–1140.
[33] M. E. Núñez, K. T. Noyes, D. A. Gianolio, L. W. McLaughlin, J. K. Barton, *Biochemistry* **2000**, *39*, 6190–6199.
[34] C. H. Chen, D. S. Sigman, *Proc. Natl. Acad. Sci. U.S.A.* **1986**, *83*, 7147–7151.
[35] B. C. Bales, M. Pitié, B. Meunier, M. M. Greenberg, *J. Am. Chem. Soc.* **2002**, *124*, 9062–9063.
[36] K. R. Fox, T. Brown, *Biochem. Soc. Trans.* **2011**, *39*, 629–634.
[37] K. R. Fox, T. Brown, D. A. Rusling, in *DNA-Targeting Molecules as Therapeutic Agents* (Ed.: M.J. Waring), Royal Society Of Chemistry, Cambridge, **2018**, pp. 1–32.
[38] D. A. Rusling, V. E. C. Powers, R. T. Ranasinghe, Y. Wang, S. D. Osborne, T. Brown, K. R. Fox, *Nucleic Acids Res.* **2005**, *33*, 3025–3032.
[39] J. Gierlich, G. A. Burley, P. M. E. Gramlich, D. M. Hammond, T. Carell, *Org. Lett.* **2006**, *8*, 3639–3642.
[40] E. Wang, S. Malek, J. Feigon, *Biochemistry* **1992**, *31*, 4838–4846.
[41] Z. Molphy, D. Montagner, S. S. Bhat, C. Slator, C. Long, A. Erxleben, A. Kellett, *Nucleic Acids Res.* **2018**, *46*, 9918–9931.
[42] S. Walsh, A. H. El-Sagheer, T. Brown, *Chem. Sci.* **2018**, *9*, 7681–7687.
[43] J. C. Jewett, C. R. Bertozzi, *Chem. Soc. Rev.* **2010**, *39*, 1272–1279.
[44] J. J. P. Kramer, M. Nieger, S. Bräse, *Eur. J. Org. Chem.* **2013**, *2013*, 541–549.
[45] M. I. Dawson, M. Park, R. L. S. Chan, D. Hobbs, R. City, **n.d.**, 9.
[46] V. S. I. Sprakel, J. A. A. W. Elemans, M. C. Feiters, B. Lucchese, K. D. Karlin, R. J. M. Nolte, *Eur. J. Org. Chem.* **2006**, *10*, 2281–2295.
[47] J. N. Hamann, M. Rolff, F. Tuczek, *Dalton Trans.* **2015**, *44*, 3251–3258.
[48] S. J. A. Pope, R. H. Laye, *Dalton Trans.* **2006**, *25*, 3108–3113.
[49] P. Du, S. J. Lippard, *Inorg. Chem.* **2010**, *49*, 10753–10755.
[50] M. Kitamura, S. Kato, M. Yano, N. Tashiro, Y. Shiratake, M. Sando, T. Okauchi, *Org. Biomol. Chem.* **2014**, *12*, 4397–4406.

Chapter V

Thesis Conclusions and Future Work

This work focused on the design and synthesis of stabilised copper(II)-polypyridyl oxidative chemical-nucleases. Particular emphasis was directed to the use of click-chemistry as a major tool for the high-throughput generation of targeted artificial metallo-nucleases (AMNs). Combining a polypyridyl scaffold such as *tris*-(2-pyridylmethyl)amine (TPMA) with copper(II)-phenanthrene cores allowed the limitations imposed by dissociation in solution of Cu-Phen-like system to be overcome. The Cu-TPMA-*N,N′* family showed prominent DNA-oxidation profile with a radical chemistry that deviates from classical Sigman and Fenton-type reagents. Although designer ligands such as DPQ and DPPZ provided enhanced intercalation compared to Cu-TPMA-Phen, the complexes had binding affinities broadly similar to Cu-Phen but consistently lower than previously reported heteroleptic diphenanthrene systems.

Employing a less hindered polypyridyl scaffold such as *di*-(2-pycolylamine) (DPA) facilitated binding and provided improved balance between stabilization by the polypyridyl ligand and enhanced intercalation by the phenanthrene system. The compounds showed solution geometries and catalytic radical chemistry similar to the Cu-TPMA-*N,N′* family but two orders of magnitude higher binding affinity to ctDNA. The antiproliferative activity of the complexes was analysed against various pancreatic ductal adenocarcinoma cell lines (PT127, MiaPaCa-2, Panc-1 and the patient-derived xenograft HPAC). Here, cytotoxicity was found to be higher than oxaliplatin in all four cancer cell lines and the Cu-DPA-DPPZ derivative was the most potent chemotype in the family displaying IC_{50} within the nanomolar range (0.21-0.62 μM).

To target oxidative damage by the complexes to specific genes, both TPMA and DPA polypyridyl scaffolds were modified with an azide moiety through asymmetrical multistep synthesis. The synthetic pathways employed here were designed through a thorough retrosynthetic analysis and were aimed to use basic and upscalable organic chemistry conversions. Reduction of the 2,5-pyridinedicarboxylic methyl ester, followed by regioselective oxidation to 2-formyl-5-hydroxymethylpyridine promptly allowed to introduce an asymmetric 5-hydroxymethylpyridine into the TPMA ligand by Schiff-base condensation and nucleophilic substitution. Both $5N_3$-TPMA and $6N_3$-TPMA were prepared through nucleophilic substitution of NaN_3 on the Cl-TPMA derivatives while $4N_3$-Benzyl-DPA was obtained by reduction of $4NO_2$-Benzyl-DPA followed by diazotransfer reaction on $4NH_2$-Benzyl-DPA. The reaction steps were designed to follow the green chemistry criteria employing, where possible, safer solvents (water or alcoholic solutions),

safer chemicals (*i.e.* ADMP has reduced risks and toxicity compared to sodium azide) and easily removable catalysts or reactants (SeO_2, carbonates or Na_2S). Click-chemistry between the organic azides and the alkyne-modified triplex-forming oligonucleotides allowed generation of a wide library of AMN-TFO hybrids with various targeting and cleavage properties. Here sequence specificity provided by Hoogsteen base pairing and triplex structure hybridization provide an easily programmable means to target extended sequences of dsDNA without requiring disruption of the helical structure for recognition. The hybrids showed catalytic and targeted DNA oxidative cleavage in the presence of reductand and various *off*-target discriminations with internally modified AMN-TFOs promoting 72% versus 24% knockdown of the *on*-target and *off*-target, respectively. Presence of the TFO did not affect the radical chemistry promoted by the Cu(II)-polypyridyl complex and DNA damage was caused by production of Cu-superoxide species. DNA-cleavage by our hybrids deviates from that of classical enzymatic nucleases, including CRISPR-Cas, where strand excision is hydrolytic and amenable to repair. Modification of this technology with bio-orthogonal methods involving strain-promoted substituents with thiazole orange modifications introduced augmented triplex stability without affecting the capability of the hybrids of promoting targeted damage.

As a continuation of this work, targeted chemical nucleases could be modified using various types of backbone modified oligonucleotides such as locked nucleic acids (LNA) or peptide nucleic acids (PNA). The high cellular stability to nucleases and neutral charge of PNA makes its AMN-hybrids an interesting field of research for *in cellulo* or *in vivo* applications. In addition, reactivity by the AMN moiety might be adjusted to achieve enhanced damage at the targeted DNA site by including phenanthrene intercalators or to introduce different types of cleavage and nucleotide modification by changing the metal centre, complex nuclearity or modifying the TPMA scaffold.

Appendix A

Polypyridyl-based Copper Phenanthrene Complexes: A New Type of Stabilized Artificial Chemical Nuclease

A-1 Complex Characterisation

ESI-MS

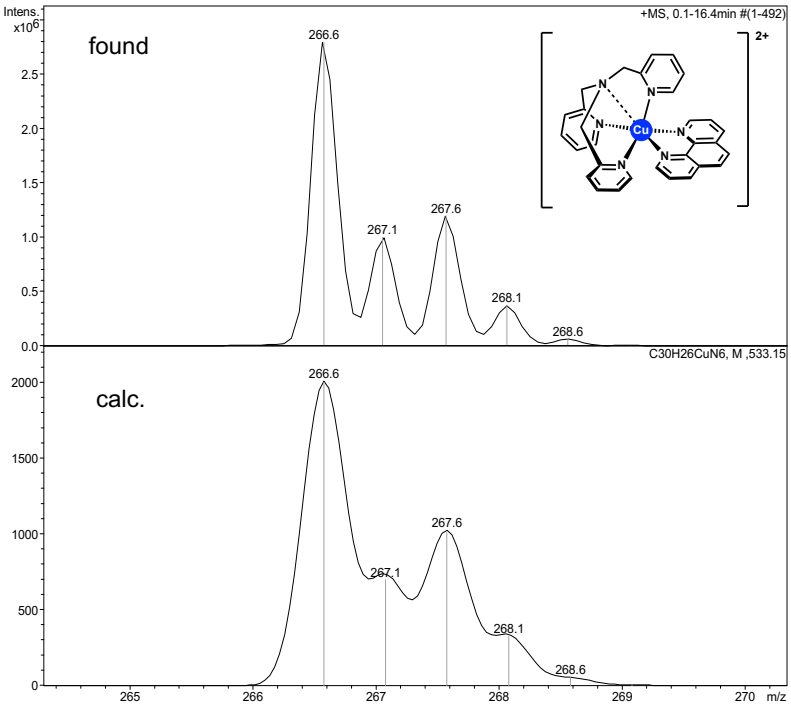

Figure A-1. ESI-MS spectra of $[Cu(TPMA)(Phen)](ClO_4)_2$.

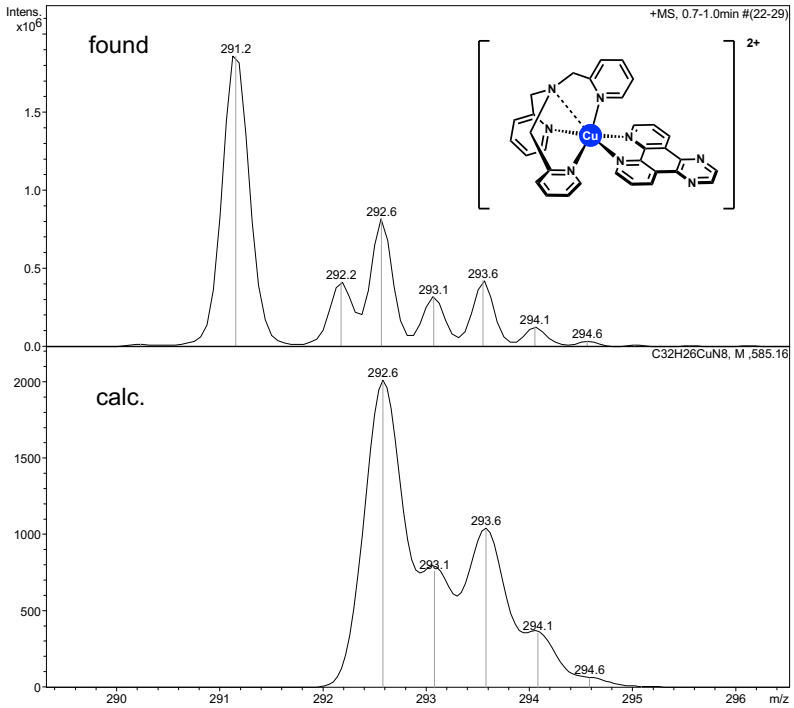

Figure A-2. ESI-MS spectra of $[Cu(TPMA)(DPQ)](ClO_4)_2$.

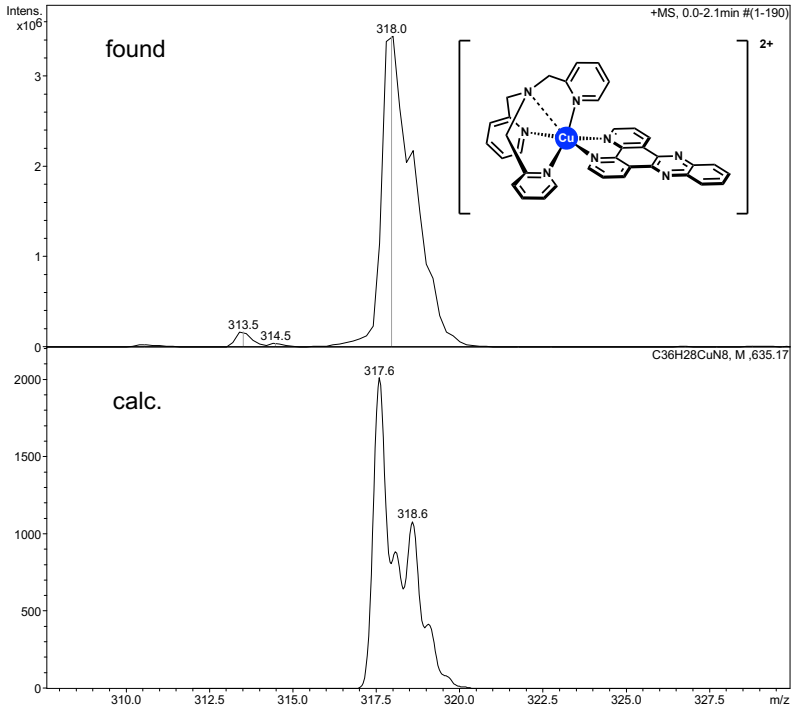

Figure A-3. ESI-MS spectra of $[Cu(TPMA)(DPPZ)](ClO_4)_2$.

UV-Vis Spectra d-d transitions

UV-Vis spectra of the complexes were recorded at a concentration of 5 mM in acetonitrile and ε (M^{-1} cm^{-1}) was plotted against wavelength (λ). Data were recorded every 0.5 nm in the 350-900 nm range.

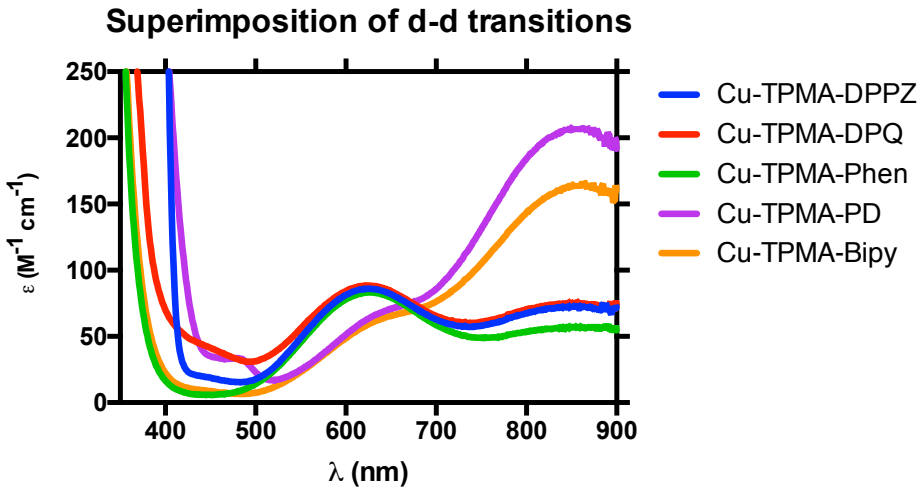

Figure A-4. Superimposition of the UV-Vis spectra of the Cu-TPMA-*N,N'* complexes.

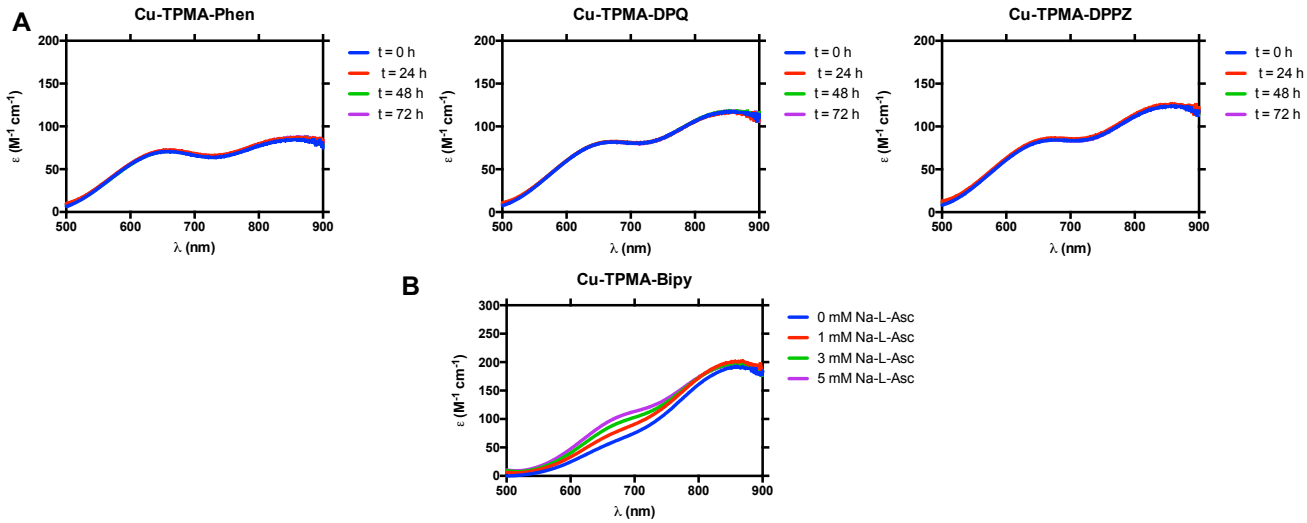

Figure A-5. A UV-Vis stability study of Cu-TPMA-Phen, Cu-TPMA-DPQ and Cu-TPMA-DPPZ (5 mM) in DMF over 72 h and **B** UV-Vis oxidation study of Cu-TPMA-Bipy (5 mM) after reduction with 1, 3, 5 mM Na-*L*-Ascorbate in CH_3CN:H_2O, 50:50.

A-2 X-RAY CRYSTALLOGRAPHY

Table A-1. Crystal data

	Cu-TPMA-Bipy	**Cu-TPMA-Phen**	**Cu-TPMA-PD**	**Cu-TPMA-DPQ**	**Cu-TPMA-DPPZ**
Formula	$C_{28}H_{26}CuN_6 \cdot 2(ClO_4)$	$C_{30}H_{26}CuN_6 \cdot (ClO_4)$	$C_{30}H_{24}CuN_6O_2 \cdot 2(ClO_4)$	$C_{32}H_{26}CuN_8 \cdot 2(ClO_4)$	$C_{36}H_{28}CuN_8 \cdot 2(ClO_4) \cdot CH_3CN$
M_r	708.99	733.01	762.99	785.05	876.16
Crystal Class	Monoclinic	Monoclinic	Monoclinic	Triclinic	Monoclinic
Space group	$P2_1/n$	$P2_1/n$	$P2_1/n$	$P\bar{1}$	$P2_1/c$
a (Å)	11.9305 (8)	12.0959 (7)	19.2320 (12)	10.7763 (6)	13.39827 (10)
b (Å)	18.1422 (13)	17.0569 (9)	8.4888 (5)	12.0465 (7)	18.82423 (12)
c (Å)	13.9257 (9)	15.5156 (8)	19.9513 (13)	13.9004 (9)	14.65700 (11)
α (°)	90	90	90	83.429 (3)	90
β (°)	104.534 (2)	104.934 (2)	111.169 (3)	75.265 (2)	93.318 (1)
γ (°)	90	90	90	67.580 (2)	90
V (Å^3)	2917.7 (3)	3093.0 (3)	3037.4 (3)	1612.94 (17)	3690.48 (5)
Z	4	4	4	2	4
λ (Å)	0.71073	0.71073	0.71073	0.71073	1.54184
μ (mm^{-1})	0.99	0.94	0.97	0.91	2.75
T (K)	150(2)	150(2)	150(2)	150(2)	100(1)
Crystal size (mm^3)	0.32 × 0.22 × 0.12	0.31 × 0.26 × 0.18	0.34 × 0.32 × 0.09	0.24 × 0.21 × 0.19	0.19 × 0.10 × 0.07
Refl measured / R_{int}	54645 / 0.032	36649 / 0.083	33181 / 0.034	30434 / 0.031	40004 / 0.022
Indep. Refl / Obs $I > 2\sigma(I)$	7558 /6524	8538 / 6846	7709 / 6630	8000 / 6919	27370 / 10474

$R[F^2 > 2\sigma(F^2)]$	0.031	0.064	0.033	0.044	0.035
$wR(F^2)$	0.077	0.190	0.082	0.124	0.092
S	1.04	1.04	1.05	1.04	1.03
Param/restraints	434 / 30	424 / 0	442 / 0	460 / 10	524 / 0
Δ>max, min (e Å^{-3})	0.38 , -0.43	1.51, -0.84	0.37, -0.40	0.90, -0.61	1.44, -0.67

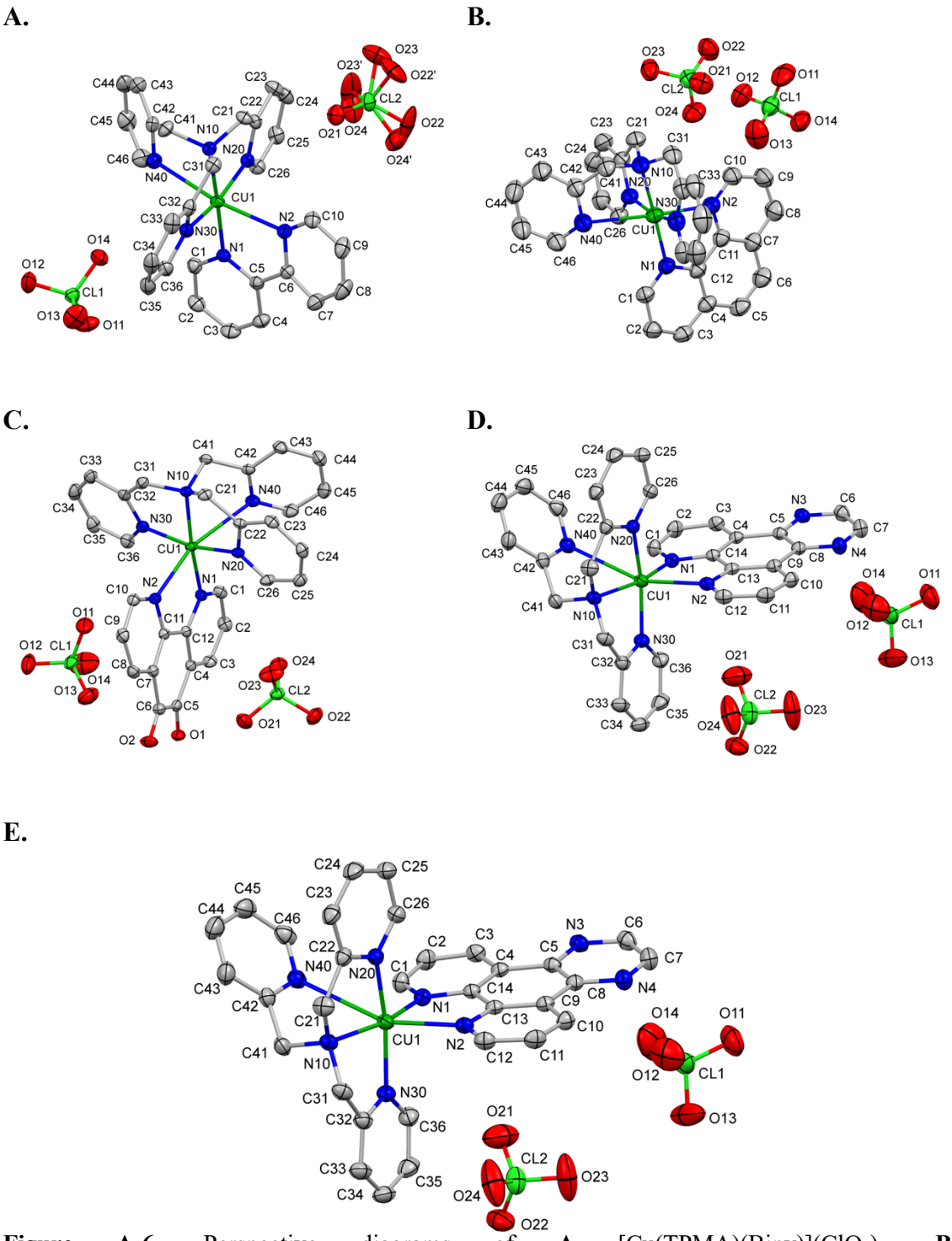

Figure A-6. Perspective diagrams of **A** $[Cu(TPMA)(Bipy)](ClO_4)_2$, **B** $[Cu(TPMA)(Phen)](ClO_4)_2$, **C** $[Cu(TPMA)(PD)](ClO_4)_2$, **D** $[Cu(TPMA)(DPQ)](ClO_4)_2$ and **E** $[Cu(TPMA)(DPPZ)](ClO_4)_2 \cdot CH_3CN$ showing 50% probability ellipsoids and atom labelling scheme. Hydrogen atoms omitted for clarity.

Table A-2. Selected geometric parameters (Å, º)

Bond/angle	Cu-TPMA-Bipy	Cu-TPMA-Phen	Cu-TPMA-PD	Cu-TPMA-DPQ	Cu-TPMA-DPPZ
distances					
Cu1—N1	2.0071 (13)	2.0083 (19)	2.0207 (14)	2.0373 (19)	2.0037 (15)
Cu1—N2	2.3860 (14)	2.366 (2)	2.3570 (14)	2.2669 (19)	2.3188 (15)
Cu1—N10	2.0337 (13)	2.0292 (19)	2.0329 (14)	2.0386 (19)	2.0233 (15)
Cu1—N20	1.9896 (13)	1.995 (2)	1.9966 (15)	1.9978 (19)	2.0016 (15)
Cu1—N30	2.0049 (13)	2.007 (2)	2.0047 (15)	1.9964 (19)	2.0093 (15)
Cu1—N40	2.5974 (14)	2.667 (2)	2.7678 (15)	2.907 (2)	2.8816 (15)
angles					
N1—Cu1—N2	76.27 (5)	77.55 (8)	75.99 (5)	77.67 (7)	77.26 (6)
N1—Cu1—N10	176.99 (5)	177.19 (8)	169.70 (6)	160.20 (8)	173.75 (6)
N1—Cu1—N40	103.46 (5)	101.17 (8)	94.58 (5)	88.53 (7)	99.01 (5)
N2—Cu1—N40	168.14 (5)	164.73 (7)	163.21 (5)	157.72 (6)	167.27 (5)
N10—Cu1—N2	103.88 (5)	104.89 (8)	114.05 (5)	122.12 (7)	108.62 (6)
N10—Cu1—N40	77.03 (5)	76.85 (8)	76.25 (5)	72.66 (7)	75.70 (5)
N20—Cu1—N1	98.79 (5)	97.71 (8)	99.32 (6)	97.01 (8)	99.62 (6)
N20—Cu1—N2	91.44 (5)	87.49 (8)	91.92 (5)	91.79 (7)	95.11 (5)
N20—Cu1—N10	84.21 (5)	83.86 (8)	83.15 (6)	83.38 (8)	82.19 (6)
N20—Cu1—N30	165.89 (5)	165.53 (9)	164.80 (6)	163.87 (8)	163.80 (6)
N20—Cu1—N40	76.83 (5)	77.56 (8)	75.71 (5)	72.40 (7)	73.34 (5)
N30—Cu1—N1	95.26 (5)	96.76 (9)	95.86 (6)	99.09 (8)	95.24 (6)
N30—Cu1—N2	90.72 (5)	95.62 (8)	92.56 (5)	90.61 (7)	94.41 (6)
N30—Cu1—N10	81.74 (5)	81.68 (9)	81.76 (6)	81.84 (8)	82.37 (6)
N30—Cu1—N40	101.09 (5)	99.63 (8)	102.32 (5)	108.99 (7)	98.07 (5)
*Interplanar angles**					
N1/N2	13.67(6)	2.97(13)	12.25(9)	3.46(16)	3.30(9)
N20/N40	45.62(7)	43.61(12)	33.79(8)	37.23(11)	26.79(7)
N20/N30	9.43(11)	12.19(16)	8.40(7)	16.4(3)	17.83(9)

* Angles between mean planes of the 6-membered rings containing the named N atoms

Software used:

Crysalis: Rigaku Oxford Diffraction, (2018), CrysAlisPro Software system, version 1.171.39.27b, Rigaku Corporation, Oxford, UK.

APEX2, SAINT: Bruker (2012). Bruker AXS Inc., Madison, Wisconsin, USA.

ShelXle: C.B. Hübschle, G.M. Sheldrick and B. Dittrich. J. Appl. Cryst., 2011, **44**, 1281-1284.
Olex2: O.V. Dolomanov, L.J. Bourhis, R.J. Gildea, J.A.K. Howard & H. Puschmann. J. Appl. Cryst., 2009, **42**, 339-341
SHELXT: Sheldrick, G.M. Acta Cryst., 2015, **A71**, 3-8.
SHELXL-2014/2017: Sheldrick, G.M. Acta Cryst., 2015, **C71**, 3-8.
Mercury: Macrae, C. F., Edgington, P. R., McCabe, P., Pidcock, E., Shields, G. P. Taylor, R., Towler, M. & J. van der Streek, (2006), *J. Appl. Crystallogr.*, **39**, 453-457.

A-3 EPR Spectroscopy

Theory

The spin Hamiltonian for a spin system of a Cu(II) ion (electronic configuration $3d^9$, S = 1/2, I = 3/2) and m nuclei with spins I_k is given by Eq. A1[1]:

$$H = \beta_e \mathrm{B_0 g S}/h + \sum_k^m \mathrm{S A}_k \mathrm{I}_k - \beta_n \sum_k^m \frac{g_{n,k} \mathrm{B_0 I}_k}{h} + \sum_{I_k > \frac{1}{2}} \mathrm{I}_k \mathrm{P}_k \mathrm{I}_k \qquad \text{(EQ A1)}$$

where the terms describe the electron Zeeman interaction, the hyperfine interaction, the nuclear Zeeman interaction, and the nuclear quadrupole interaction (for nuclei with $I > 1/2$). The electron Zeeman interaction is characterized by the g tensor that is essentially determined by the metal ion and the directly coordinated ligand atoms. The g values observed in the EPR spectrum together with the metal hyperfine coupling can often be used as a fingerprint to identify the metal ion and to provide information on the symmetry of the paramagnetic center. The ligand hyperfine interaction can be written as the sum of the isotropic interaction or Fermi contact interaction $H_F = a_{iso}$SI and the electron–nuclear dipole–dipole coupling H_{DD} = STI. Here a_{iso} is the isotropic hyperfine coupling constant which is directly related to $|\psi_0(0)|^2$, the electron spin density at the nucleus and matrix T describes the anisotropic dipole–dipole coupling. For protons, the anisotropic part of the hyperfine interaction can be approximated using the point-dipole model assuming that the distance r between the unpaired electron and the proton is larger than 0.25 nm. In this case, the point-dipole formula (Equation. A2)

$$T = \frac{\mu_0}{4\pi h} g_e \beta_e g_n \beta_n \frac{(3\tilde{\mathrm{n}}\mathrm{n} - 1)}{r^3} \qquad \text{(EQ A2)}$$

where n is the electron-nucleus vector, can be used to determine the electron-nuclear distance and orientation with respect to the g tensor.

For nuclear spins larger than 1/2, such those of as ^{14}N with I = 1, the nuclear quadrupole principal values $[P_x, P_y, P_z] = [-K(1-\eta), -K(1+\eta), 2K]$ of the traceless P matrix are usually

expressed by the quadrupole coupling constant $K = e^2qQ/4I(2I–1)h$ and the asymmetry parameter $\eta = (P_x–P_y)/P_z$, where Q is the nuclear quadrupole moment and eq is the electric field gradient.

For an S =1/2, I = 1/2 spin system there are two single-quantum nuclear transitions ($|\Delta m_S| = 0$, $|\Delta m_I| = 1$). For the special case when g, A, and P are coaxial and B_0 is along one of the principal axes, the first-order frequencies are given by Eq. A3:

$$\nu_i = |\nu_I \pm A_i/2| \qquad \text{(EQ A3)}$$

where ν_I is the nuclear Zeeman frequency and A_i ($i = x, y, z$) is one of the principal hyperfine values. For $\nu_I > |A_i/2|$ (weak coupling case) the two frequencies are centered at ν_I and separated by A_i. For $\nu_I < |A_i/2|$ (strong coupling case) the two frequencies are centered at $A_i/2$ and split by $2\nu_I$.

For an S = 1/2, I = 1 spin system there are four single-quantum nuclear frequencies given by Eq. A4:

$$\nu_i = |\nu_I \pm A_i/2 \pm 3/2P_i| \qquad \text{(EQ A4)}$$

and two double-quantum nuclear transitions ($|\Delta m_S| = 0$, $|\Delta m_I| = 2$). If the anisotropic hyperfine coupling is small compared to the isotropic hyperfine interaction and the nuclear quadrupole interaction, the latter frequencies are given by Eq. A5:

$$\nu_{\alpha,\beta}^{dq} = 2[(a_{\text{iso}}/2 \pm \nu_I)^2 + K^2(3 + \eta^2)]^{1/2} \qquad \text{(EQ A5)}$$

The EPR technique is well suited for studying the geometric and electronic structure of paramagnetic molecules like the Cu^{II} ($3d^9$, S = 1/2) complexes under study. Although structural details of Cu^{II} complexes in the solid state are provided by single-crystal X-ray crystallography, one cannot a priory decide whether the geometry of the complex is retained in solution or solvent interactions change the structure of the complex. Cw-EPR spectroscopy can probe changes in the first coordination sphere through the analysis of g values and the metal hyperfine coupling constants, A^{Cu}.[2] A more detailed mapping of the spin density distribution over the whole complex is provided by measuring nuclear spin transitions with advanced methods like pulsed ENDOR and HYSCORE.[1,3]

Analysis of cw EPR spectra showing at least 2 species

Figure A-6 shows the frozen solution EPR spectra of Cu-TPMA-Bipy in ACN and DMF. The latter can be simulated with the parameters given in Table A-3 of main text. These parameters are typical of a “reverse” axial spectrum, i.e., $g_{\|} < g_{\perp}$, consistent with a copper(II) ion d_{z^2} ground state, as expected for an ideal or barely distorted trigonal

bipyramidal coordination environment (five-coordinated structure). The subtraction of DMF from the ACN signal gives a regular axial spectrum as can be seen from the black trace of Figure A-6. The simulation with parameters [g_x, g_y, g_z] = [2.037, 2.087, 2.231] and [A_x, A_y, A_z] = [75, 33, 542] MHz reproduces well the difference spectrum and shows that is consistent with a copper(II) ion in the $d_{x^2-y^2}$ ground state as expected for elongated tetragonal-octahedral (6-coordination), square pyramidal (5-coordination), or square-planar geometry.[4–6] This analysis provides strong indication for the existence of both six- and five-coordinated structures in spectra showing mixed signals like the one of Cu-TPMA-Bipy in ACN (and similar of Cu-TPMA-Phen in all pure organic solvents).

Table A-3. EPR parameters of Cu-TPMA-Bipy obtained from simulations of spectra dominated by five-coordinated signals.[a]

Cu-TPMA-Bipy	g_x	g_y	g_z	A^{Cu}_x / MHz	A^{Cu}_y / MHz	A^{Cu}_z / MHz
DMSO	2.206	2.174	1.995	334	258	195
DMF	2.207	2.179	2.001	348	252	199

[a] The uncertainty in the determination of the hyperfine coupling (absolute values) is 20 MHz and in *g* values is 0.002.

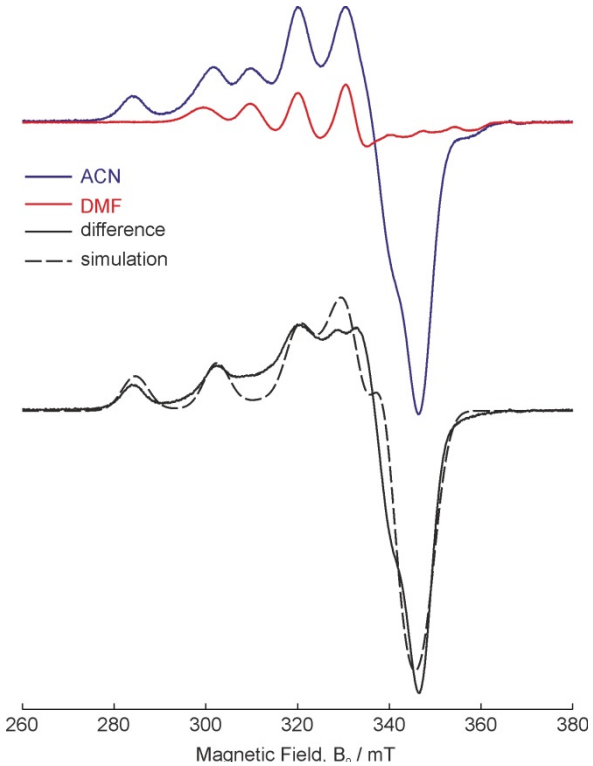

Figure A-7. cw-EPR spectra of Cu-TPMA-Bipy in ACN (blue trace) and DMF (red trace). Their difference spectrum (with the scale shown in figure) gives an almost axial signal with $g_{\|} > g_{\perp}$.

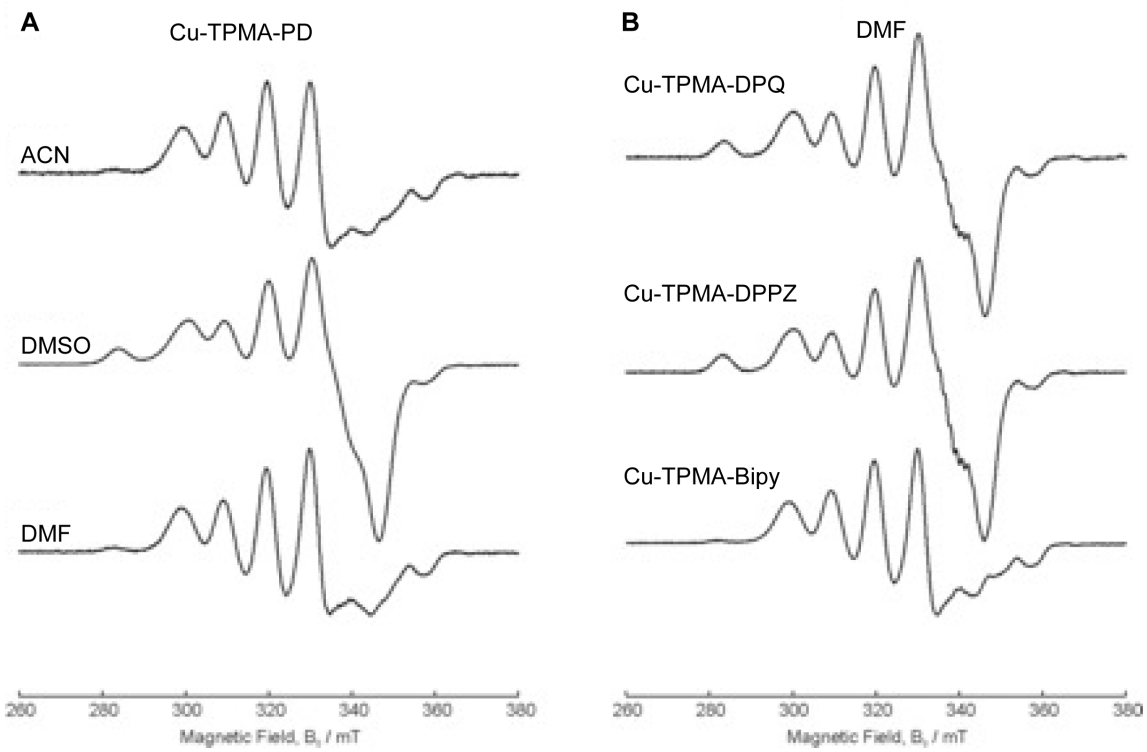

Figure A-8. Frozen-solution cw-EPR spectra (T=70 K) of complexes under study. **A** Complex Cu-TPMA-PD measured in three different solvents, ACN, DMSO and DMF and **B** spectra of complexes Cu-TPMA-DPQ, Cu-TPMA-DPPZ and Cu-TPMA-Bipy in DMF solvent.

ENDOR spectroscopy

Figure A-8 shows the Davies-ENDOR spectra of Cu-TPMA-Bipy in DMF/toluene (1:1) measured with strong and soft mw pulses. In the first case, signals assigned to weakly-coupled protons close to the ^{1}H Larmor frequency are considerably suppressed. Figure A-9 compares the ENDOR spectra of samples Cu-TPMA-Bipy and Cu-TPMA-Phen measured at the same observer positions.

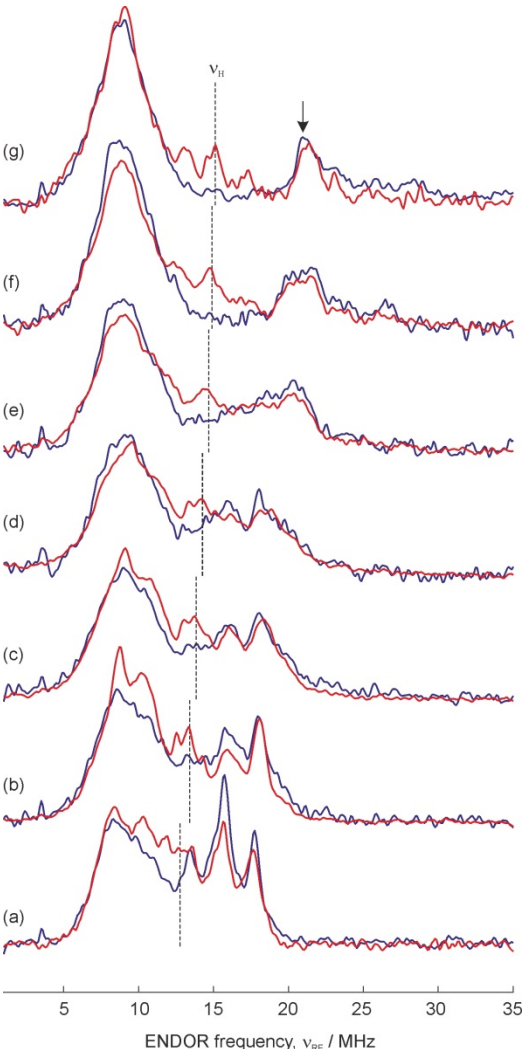

Figure A-9. Davies-ENDOR spectra of Cu-TPMA-Bipy in DMF/toluene (1:1) measured with strong (Δt_π = 32 ns, blue traces) and soft (Δt_π = 128 ns, red traces) mw pulses. Dashed lines denote the ^{1}H Larmor frequency and the arrow marks the frequency position at 21 MHz. The observer magnetic fields are the ones shown in Figure 2D of main text.

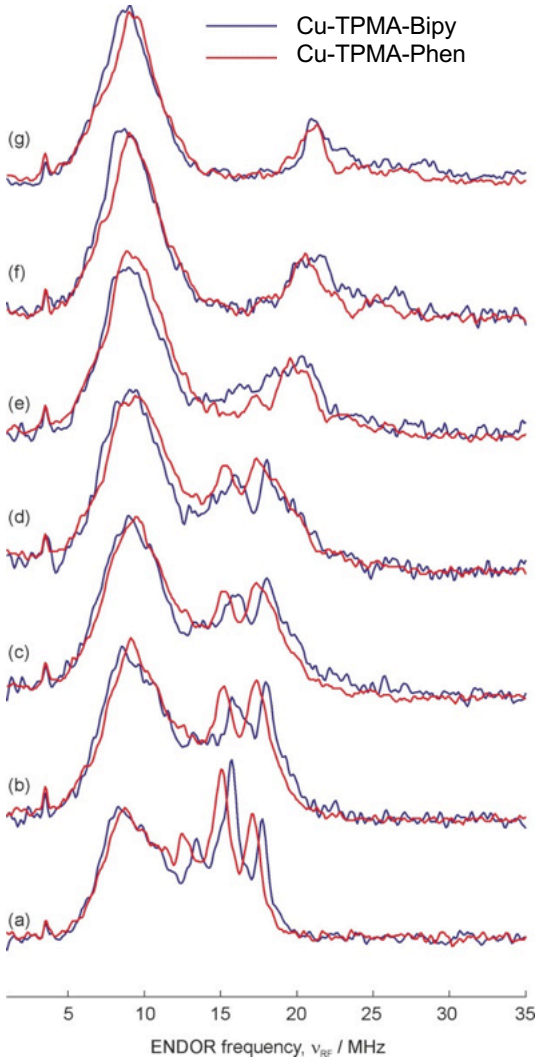

Figure A-10. Davies-ENDOR spectra of Cu-TPMA-Bipy in DMF/toluene (1:1) (blue traces) and Cu-TPMA-Phen in DMSO/citrate buffer with pH=4 (1:19) (red traces). The observer magnetic fields are the ones shown in Figure 2D of main text.

Analysis of ^{1}H-HYSCORE spectra for Cu-TPMA-Bipy

The analysis HYSCORE peaks can be best performed with the methodology developed by Dikanov and co-workers[7,8] which allows the accurate determination of isotropic and anisotropic hyperfine parameters without the need of complete spectrum simulation. Assuming axial hyperfine interaction with isotropic component *a* and anisotropic tensor (-*T*, -*T*, 2*T*), i.e. (A_x, A_y, A_z) = (*a*-*T*, *a*-*T*, *a*+2*T*), the contour line shape in the power 2D spectrum from ^{1}H nuclei is described by Dikanov and Bowman[7]

$$\nu_\beta = \{Q_\beta \nu_\alpha^{\,2} + G_\beta\}^{1/2} \qquad \text{(EQ A6)}$$

with

$$Q_\beta = \frac{T + 2a + 4\nu_I}{T + 2a - 4\nu_I} \qquad \text{(EQ A7)}$$

and

$$G_\beta = -2\nu_I \left(\frac{4\nu_I^{\,2} - a^2 + 2T^2 - aT}{T + 2a - 4\nu_I} \right) \qquad \text{(EQ A8)}$$

where ν_I is the proton nuclear Zeeman frequency. When the square of each pair of cross-peak frequencies is plotted as ν_β^2 versus ν_α^2, the contour line shape is transformed into a straight line whose slope and intercept are given by Q_β and G_β, respectively. From these values one can subsequently obtain two possible sets of the hyperfine coupling parameters *a*, *T*.

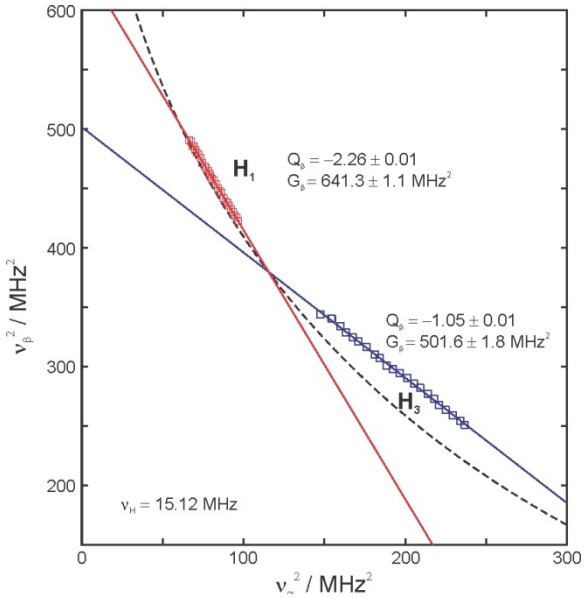

Figure A-11. Points of the two sets of cross-peaks H_1 and H_3 appeared in the HYSCORE spectrum of Cu-TPMA-Bipy shown in Figure II-3A (main paper) in the ν_β^2 versus ν_α^2 representation. The larger coordinate of each point is arbitrarily assigned to ν_β and the smaller coordinate is assigned to ν_α. The straight lines show the linear fits. The dashed line is defined by the equation $|\nu_\alpha+\nu_\beta| = 2\nu_H$.

Figure A-10 shows selected points of HYSCORE peaks for H1 and H3 signals measured at g_z and plotted in the coordinates ν_β^2 versus ν_α^2. Both sets of points fit to the linear regression with a high degree of accuracy. From the straight lines and Eq. A7, Eq. A8, we get the two possible sets of parameters:

$a = 10.7 \pm 0.1$ MHz, $T = 2.0 \pm 0.2$ MHz or $a = 12.7 \pm 0.1$ MHz, $T = -2.0 \pm 0.2$ MHz for H_1
$a = -1.8 \pm 0.2$ MHz, $T = 5.3 \pm 0.2$ MHz or $a = 3.5 \pm 0.2$ MHz, $T = -5.3 \pm 0.2$ MHz for H_3

Analysis of ^{1}H-HYSCORE spectra for Cu-TPMA-Phen

Figure A-11A shows that the HYSCORE spectrum contains similar signals to H_1 and H_2 of Cu-TPMA-Bipy, however no H_3 signal is found. The analysis of H_1 gives the two possible solutions:

$a = 9.8 \pm 0.1$ MHz, $T = 1.7 \pm 0.2$ MHz or $a = 11.5 \pm 0.1$ MHz, $T = -1.7 \pm 0.2$ MHz

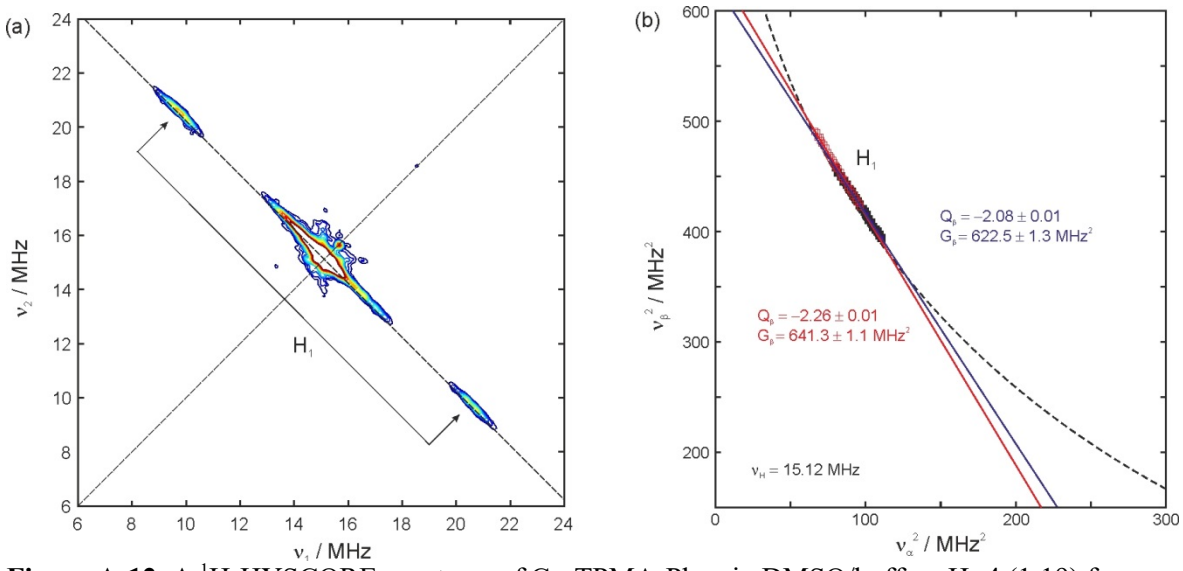

Figure A-12. A ^{1}H-HYSCORE spectrum of Cu-TPMA-Phen in DMSO/buffer pH=4 (1:19) frozen solution measured along g_z (B_0 = 355 mT). **B** Selected points from cross-peaks in ν_β^2 versus ν_α^2 representation. Red open squares: Cu-TPMA-Bipy; Blue filled squares: Cu-TPMA-Phen. The larger coordinate of each point is arbitrarily assigned to ν_β and the smaller coordinate is assigned to ν_α. The straight lines shows the linear fits. The dashed line is defined by the equation $|\nu_\alpha + \nu_\beta| = 2\nu_H$.

A-4 DNA Damage

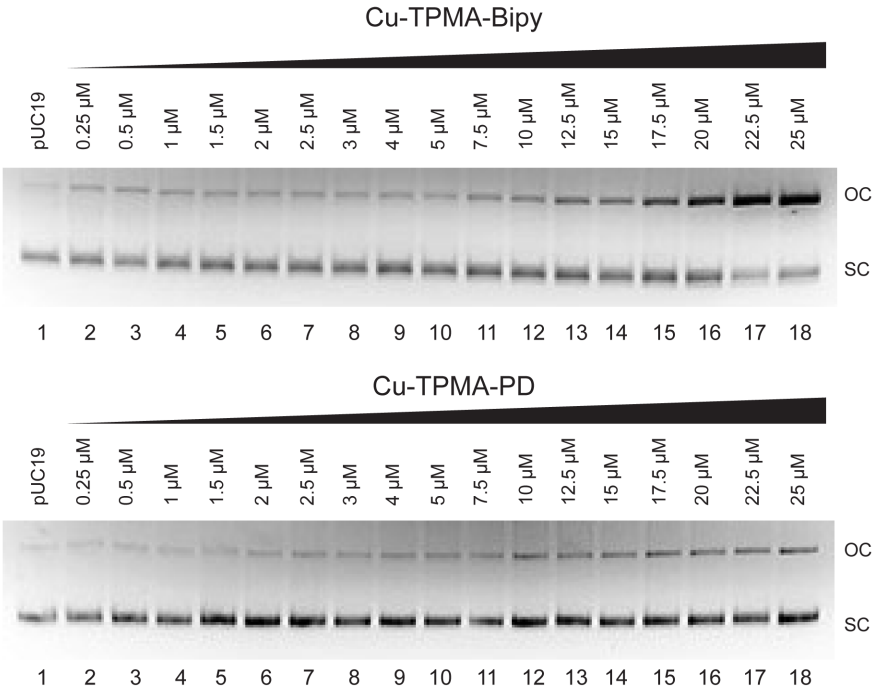

Figure A-13. 400 ng pUC19 supercoiled DNA was treated with increasing concentrations (0.25 µM –25 µM) of Cu-TPMA-Bipy and Cu-TPMA-PD in the presence of 1 mM Na-*L*-ascorbate and incubated at 37 °C for 30 min. Electrophoresis carried out as previously stated.

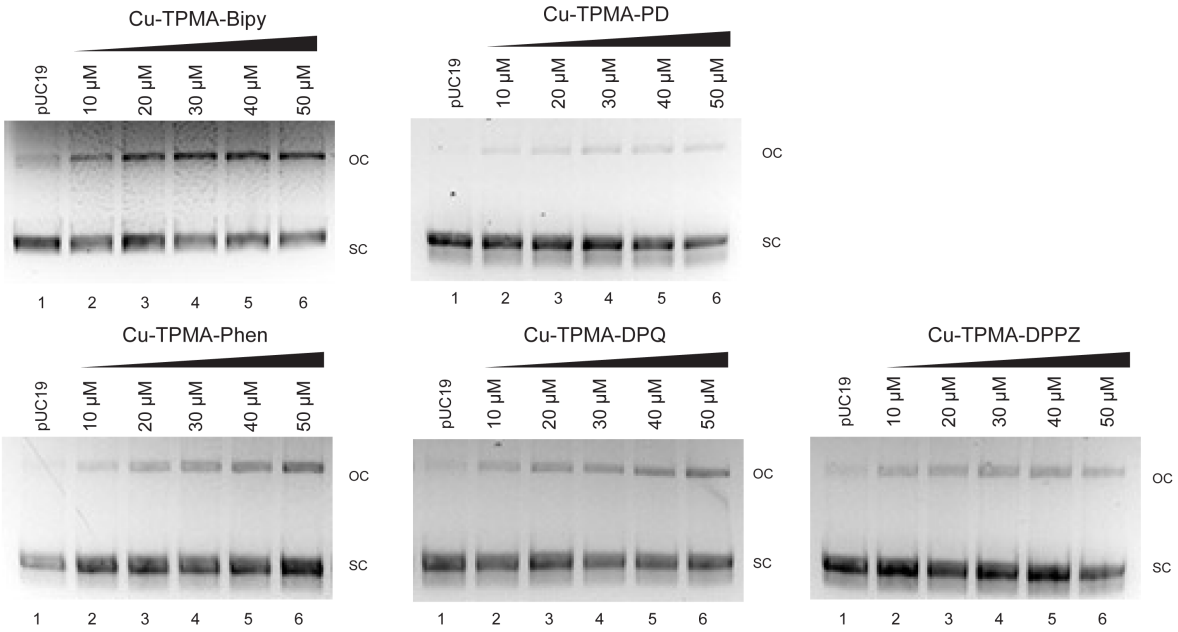

Figure A-14. 400 ng pUC19 supercoiled DNA was treated with increasing concentrations (10, 20, 30, 40, 50 µM) of Cu-TPMA-Bipy, Cu-TPMA-PD, Cu-TPMA-Phen, Cu-TPMA-DPQ and Cu-TPMA-DPPZ in the absence of 1 mM Na-*L*-ascorbate and incubated at 37 °C for 30 min. Electrophoresis carried out as previously stated.

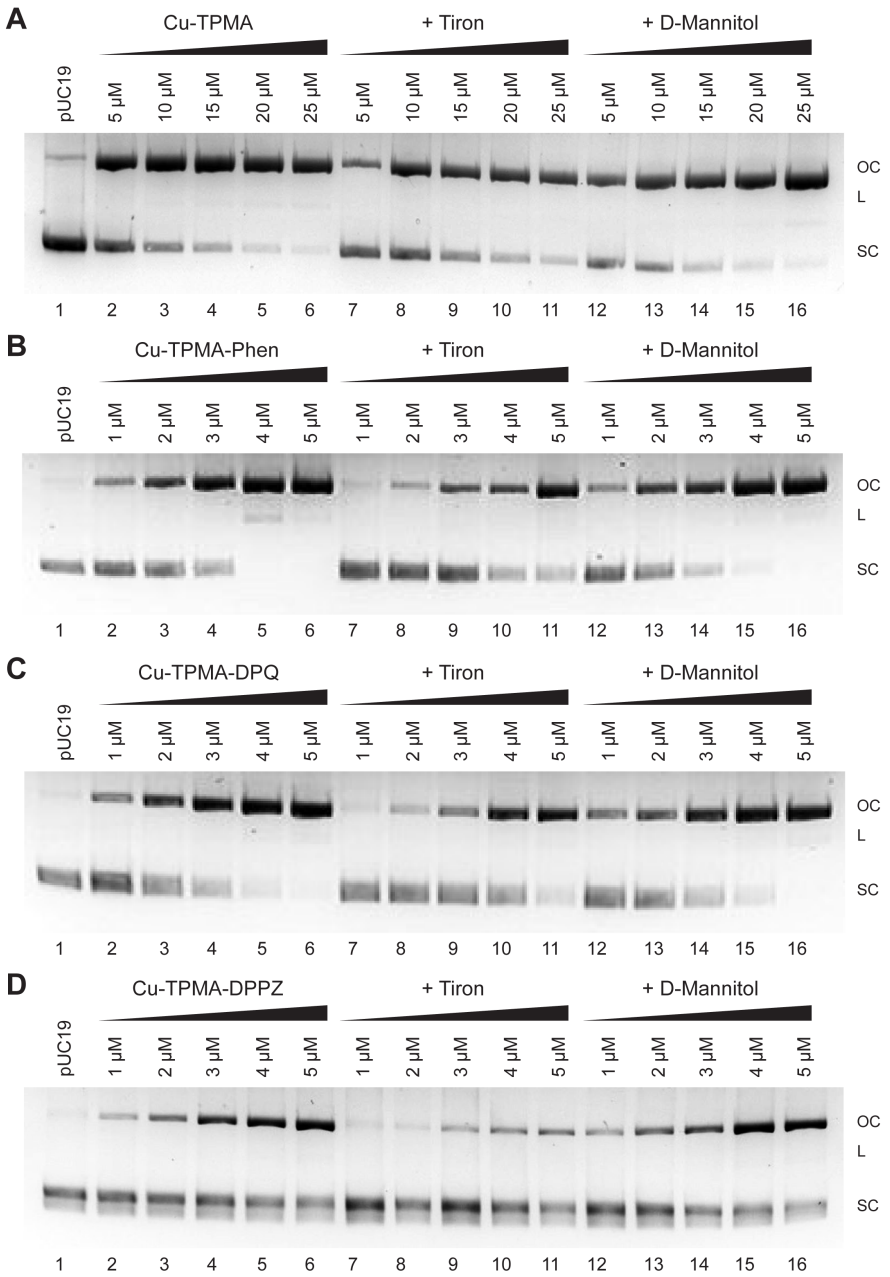

Figure A-15. 400 ng pUC19 supercoiled DNA was treated with increasing concentrations of **A** Cu-TPMA, **B** Cu-TPMA-Phen, **C** Cu-TPMA-DPQ and **D** Cu-TPMA-DPPZ (lanes 1-6) in the presence of 1 mM Na-*L*-ascorbate and 10 mM scavenging species 4,5-Dihydroxy-1,3-benzenedisulfonic acid (Tiron) (lanes 7-11) and D-Mannitol (lanes 12-16).

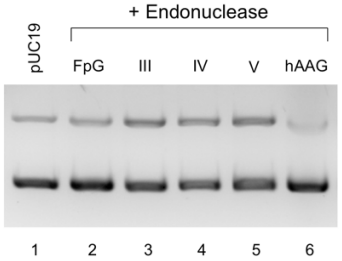

Figure A-16. Enzymatic controls of 400 ng pUC19 supercoiled DNA (lane 1) in the presence of 1 mM Na-*L*-ascorbate and 2U of either FpG (lane 2), Endo III (lane 3), Endo IV (lane 4), EndoV (lane 5) or hAAG (lane 6). For full experimental conditions see main paper.

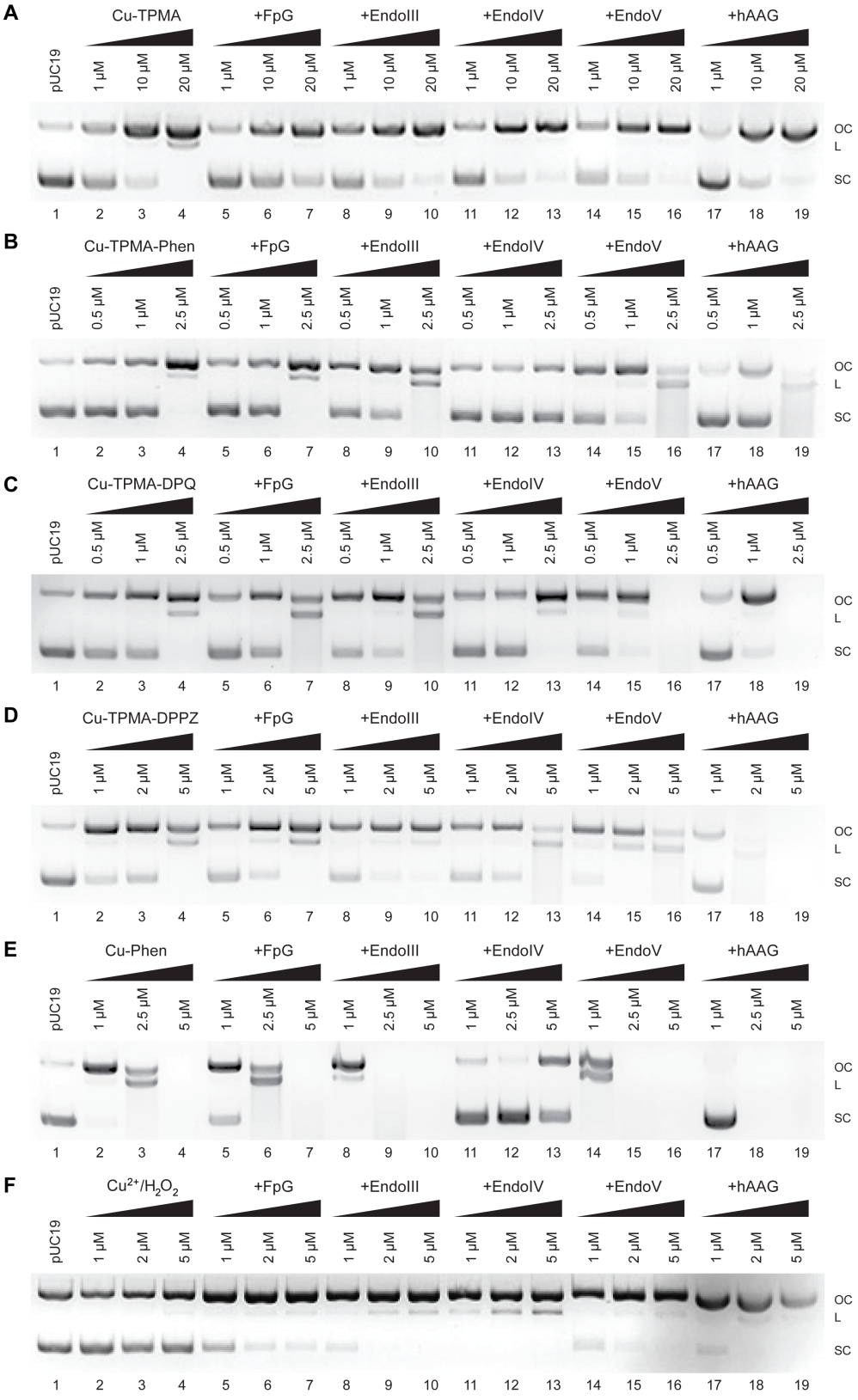

Figure A-17. 400 ng pUC19 supercoiled DNA was treated with increasing concentrations of **A** Cu-TPMA; **B** Cu-TPMA-Phen; **C** Cu-TPMA-DPQ; **D** Cu-TPMA-DPPZ; **E** CuPhen and **F** $^{\bullet}$OH - generated from Cu^{2+}/H_2O_2 Fenton-system (lanes 2-4) in the presence of 1 mM Na-*L*-ascorbate and in the presence of 2U of either FpG (lanes 5-7), Endo III (lanes 8-10), Endo IV (lanes 11-13), EndoV (lanes 14-16) or hAAG (lanes 17-19). For full experimental conditions see main paper.

A-5 REFERENCES

(1) Schweiger, A.; Jeschke, G. *Principles of Pulse Electron Paramagnetic Resonance*; Oxford University Press: Oxford, New York, 2001.

(2) Studies in Inorganic Chemistry. In *Electron Paramagnetic Resonance of d Transition Metal Compounds*; Mabbs, F. E., Collison, D., Eds.; Studies in Inorganic Chemistry; Elsevier, 1992; Vol. 16.

(3) Calle, C.; Sreekanth, A.; Fedin, M. V.; Forrer, J.; Garcia-Rubio, I.; Gromov, I. A.; Hinderberger, D.; Kasumaj, B.; Léger, P.; Mancosu, B.; et al. Pulse EPR Methods for Studying Chemical and Biological Samples Containing Transition Metals. *Helv. Chim. Acta* **2006**, *89* (10), 2495–2521.

(4) Hathaway, B. J.; Billing, D. E. The Electronic Properties and Stereochemistry of Mono-Nuclear Complexes of the Copper(II) Ion. *Coord. Chem. Rev.* **1970**, *5* (2), 143–207.

(5) Jiang, F.; Conry, R. R.; Bubacco, L.; Tyeklar, Z.; Jacobson, R. R.; Karlin, K. D.; Peisach, J. Crystal Structure and Electron Spin Echo Envelope Modulation Study of [Cu(II)(TEPA)(NO2)]PF6 (TEPA = Tris[2-(2-Pyridyl)Ethyl]Amine): A Model for the Purported Structure of the Nitrite Derivative of Hemocyanin. *J. Am. Chem. Soc.* **1993**, *115* (6), 2093–2102.

(6) Lucchese, B.; Humphreys, K. J.; Lee, D.-H.; Incarvito, C. D.; Sommer, R. D.; Rheingold, A. L.; Karlin, K. D. Mono-, Bi-, and Trinuclear CuII-Cl Containing Products Based on the Tris(2-Pyridylmethyl)Amine Chelate Derived from Copper(I) Complex Dechlorination Reactions of Chloroform. *Inorg. Chem.* **2004**, *43* (19), 5987–5998.

(7) Dikanov, S. A.; Bowman, M. K. Cross-Peak Lineshape of Two-Dimensional ESEEM Spectra in Disordered S = 12, I = 12 Spin Systems. *J. Magn. Res. Series A* **1995**, *116* (1), 125–128.

(8) Dikanov, S. A.; Tyryshkin, A. M.; Bowman, M. K. Intensity of Cross-Peaks in Hyscore Spectra of S = 1/2, I = 1/2 Spin Systems. *J. Magn. Res.* **2000**, *144* (2), 228–242.

Appendix B.

Design and development of *di*-(2-pyridylmethyl)amine copper phenanthrene chemical nucleases

B-1 Complex Characterisation

ESI-MS

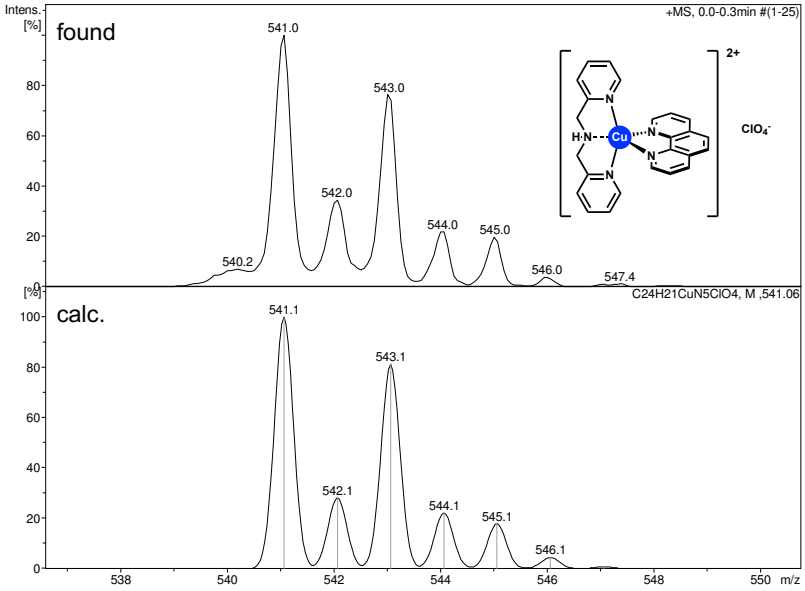

Figure B-1. ESI-MS spectrum of $[Cu(DPA)(Phen)](ClO_4)_2$.

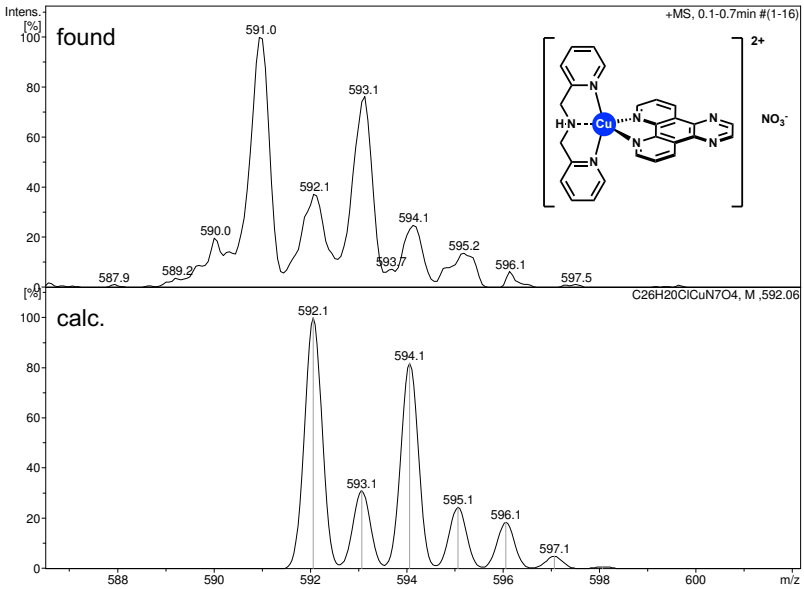

Figure B-2. ESI-MS spectrum of $[Cu(DPA)(DPQ)](ClO_4)_2$.

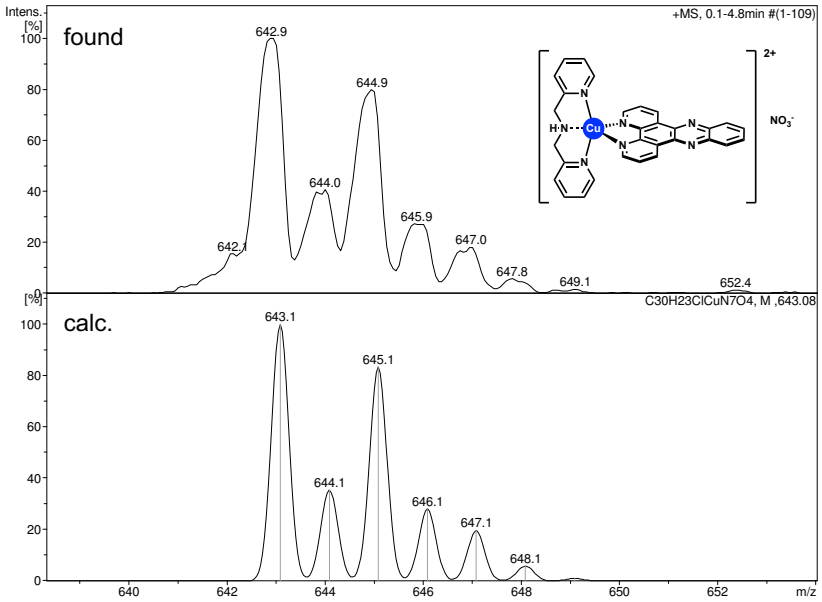

Figure B-3. ESI-MS spectrum of $[Cu(DPA)(DPPZ)](ClO_4)_2$.

UV-Vis Spectra d-d transitions

UV-Vis spectra of the complexes were recorded at a concentration of 5 mM in acetonitrile and ε (M^{-1} cm^{-1}) was plotted against wavelength (λ). Data was recorded every 0.5 nm in the 350-900 nm range.

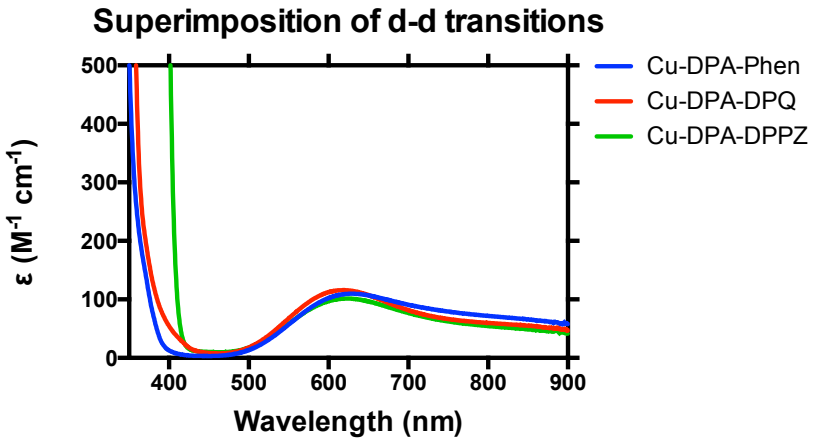

Figure B-4. Superimposition of the UV-Vis spectra of the Cu-DPA-*N,N'* complexes.

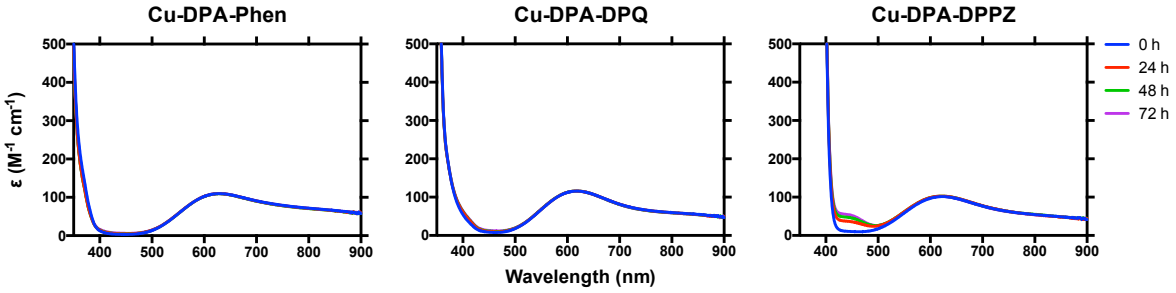

Figure B-5. UV-Vis stability study of Cu-DPA-Phen, Cu-DPA-DPQ and Cu-DPA-DPPZ (5 mM) in CH_3CN over 72 h.

B-2 X-Ray Crystallography

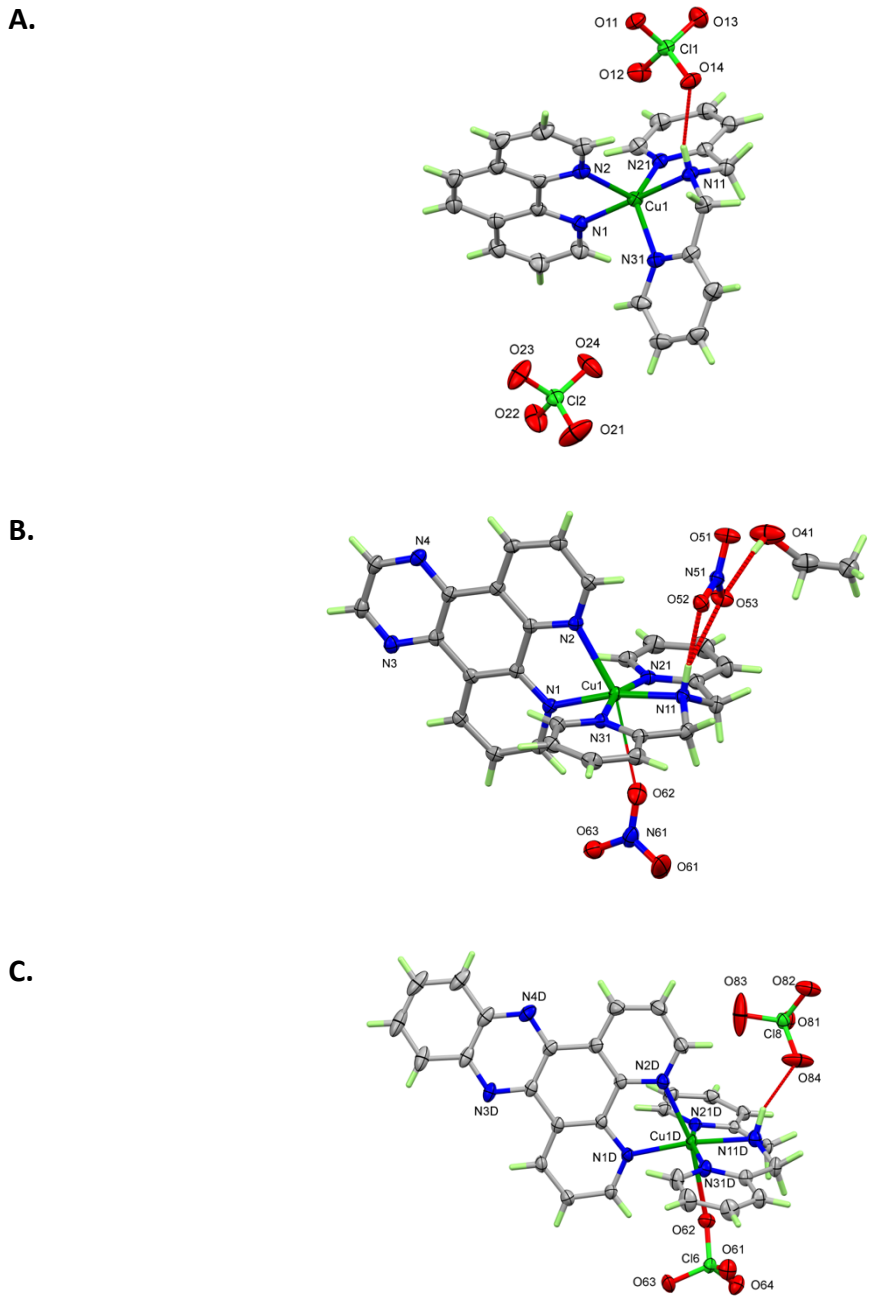

Figure B-6. A [Cu(DPA)(Phen)]$(ClO_4)_2$ showing 50% probability ellipsoids for the non-hydrogen atoms. The hydrogen bond is shown as a dashed red line and the minor component of the disorder in the uncoordinated anion is omitted. **B** [Cu(DPA)(DPQ)]$(NO_3)_2 \cdot 0.565EtOH \cdot 0.435H_2O$, showing 50% probability ellipsoids for the non-hydrogen atoms. The hydrogen bond is shown as a dashed red line, the long sixth "bond" as a dotted black line and the minor (water) component of the disorder is omitted. **C** [Cu(DPA)(DPPZ)]$(ClO_4)_2$, showing 50% probability ellipsoids for the non-hydrogen atoms. The hydrogen bond is shown as a dashed red line.

Table B-1. Selected geometric parameters (Å, º).

	Cu-DPA-Phen	**Cu-DPA-DPQ**		
Cu1—N1	1.9973 (19)	2.2910 (15)		
Cu1—N2	2.1428 (18)	2.0326 (15)		
Cu1—N11	1.9968 (19)	2.0076 (15)		
Cu1—N21	2.0142 (18)	2.0012 (15)		
Cu1—N31	2.0489 (18)	2.0174 (15)		
Cu1—O(anion)		2.8900 (17) (O62)		
N21—Cu1—N31	132.80 (7)	162.42 (6)		
τ parameter	0.77	0.09		
	Cu-DPA-DPPZ Mol A	**Cu-DPA-DPPZ** Mol B	**Cu-DPA-DPPZ** Mol C	**Cu-DPA-DPPZ** Mol D
Cu1—N1	2.0198 (19)	2.0581 (19)	2.0113 (19)	2.0715 (19)
Cu1—N2	2.241 (2)	2.274 (2)	2.242 (2)	2.247 (2)
Cu1—N11	2.030 (2)	2.016 (2)	2.019 (2)	2.017 (2)
Cu1—N21	1.997 (2)	1.994 (2)	2.033 (2)	2.0148 (19)
Cu1—N31	2.0226 (19)	2.0180 (19)	1.995 (2)	1.987 (2)
Cu1—O(anion)	2.808 (4) (O13)	2.6761 (17) (021)	3.045 (3) (O53)	2.6901 (18) (O62)
Cu1A—N11X	*2.007 (12)*		*2.016 (16)*	
N21—Cu1—N31	161.80 (8)	160.99 (8)	160.50 (8)	161.60 (8)
τ parameter	-	-	-	0.15

Entries in italic – minor components of disorder.

Table B-2. Crystal data and structure refinement for Cu-DPA-Phenazine complexes.

Complex	**Cu-DPA-Phen**	**Cu-DPA-DPQ**	**Cu-DPA-DPPZ**
Empirical formula	$C_{24}H_{21}N_5O_8Cl_2Cu$	$C_{27.13}H_{25.26}N_9O_7Cu$	$C_{30}H_{23}N_7O_8Cl_2Cu$
Formula weight	641.90	652.95	743.99
Temperature/K	100.00(10)	100.00(10)	100.01(10)
Crystal system	monoclinic	monoclinic	triclinic
Space group	$P2_1/n$	$P2_1/n$	$P\bar{1}$
a/Å	13.2485(2)	15.12969(19)	13.6561(2)
b/Å	9.10540(10)	12.63595(13)	17.1834(2)
c/Å	22.0943(3)	15.5323(2)	26.2578(4)
α/°	90	90	75.2210(10)
β/°	106.707(2)	114.5564(16)	89.3210(10)
γ/°	90	90	88.9110(10)
Volume/Å^3	2552.79(6)	2700.85(7)	5956.53(15)
Z	4	4	8
ρ_{calc} g/cm^3	1.670	1.606	1.659
μ/mm^{-1}	3.669	1.720	3.264
F(000)	1308.0	1344.0	3032.0
Crystal size/mm^3	0.148 × 0.074 × 0.068	0.154 × 0.135 × 0.026	0.216 × 0.097 × 0.031
Radiation , λ /Å	CuKα, 1.54184	CuKα, 1.54184	CuKα, 1.54184
2θ range /°	8.356 to 153.446	6.856 to 148.992	6.964 to 153.96
Reflections collected	20935	49272	54137
Independent reflections	5299	5513	24296
R_{int} , R_{sigma}	0.0268, 0.0208]	0.0425, 0.0204	0.0254, 0.0325
Data/restraints/parameters	5299/30/381	5513/3/413	24296/1917/1809
Goodness-of-fit on F^2	1.044	1.038	1.018
R1, wR2 [I>=2σ (I)]	0.0375, 0.0973	0.0361, 0.0969	0.0409, 0.1052
R1, wR2 [all data]	0.0402, 0.0994	0.0395, 0.0994	0.0483, 0.1109
+/- Δρ /e Å^{-3}	0.48/-0.58	0.96/-0.53	0.84/-0.56
CCDC			

B-3 DNA Damage

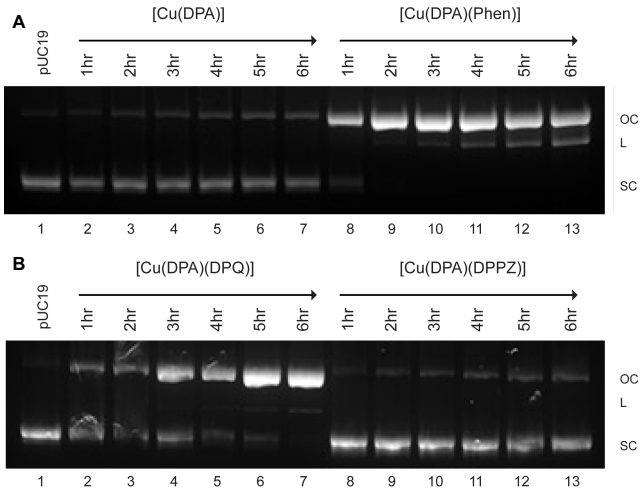

Figure B-7. Time dependent artificial nuclease activity analysed by treating 1000 ng of pUC19 supercoiled DNA with **A** Cu-DPA, CuDPA-Phen or **B** Cu-DPA-DPQ, Cu-DPA-DPPZ in the presence of Na-*L*-ascorbate (1 mM).

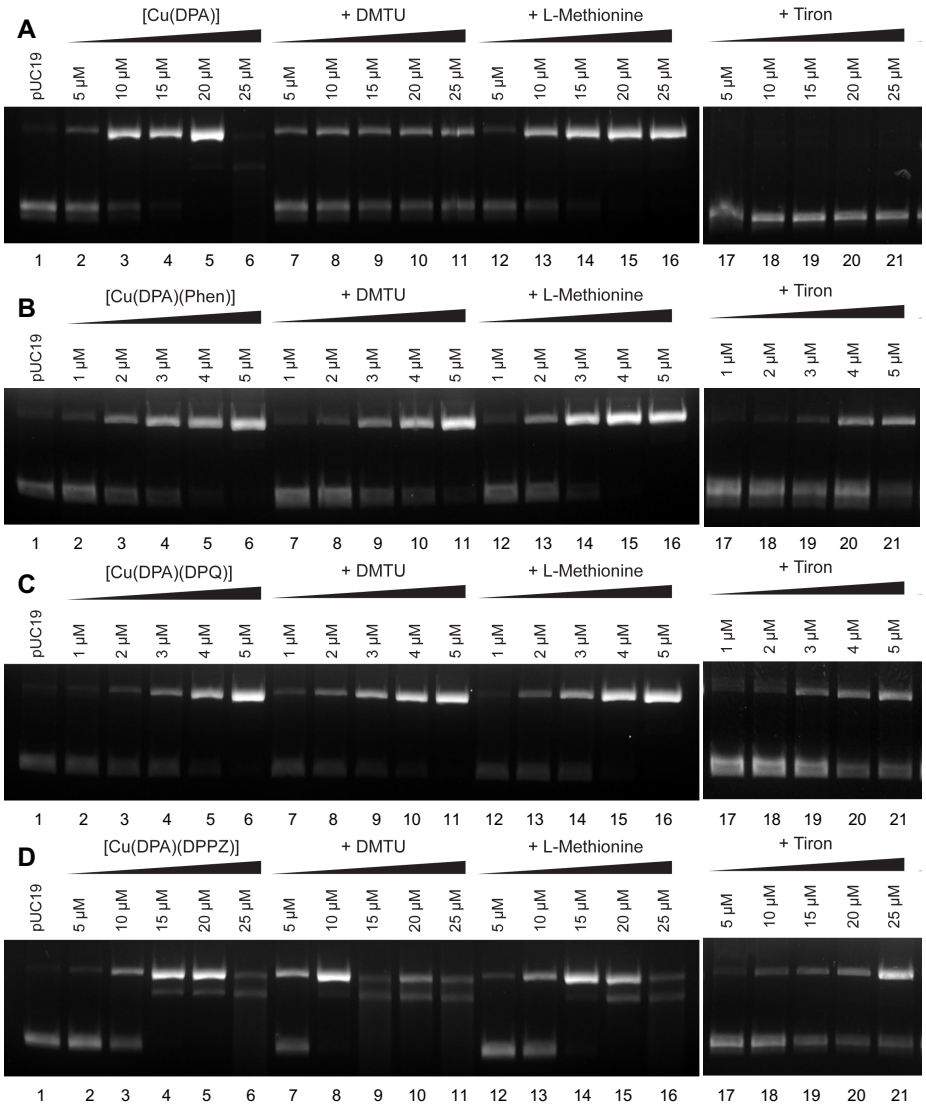

Figure B-8. 400 ng pUC19 supercoiled DNA was treated with increasing concentrations of **A** Cu-DPA, **B** Cu-DPA-Phen, **C** Cu-DPA-DPQ and **D** Cu-DPA-DPPZ (lanes 2-6) in the presence of 1 mM Na-*L*-ascorbate and 10 mM scavenging species *N,N'*-dimethylthiourea (DMTU) (lanes 7-11), *L*-Methionine (lanes 12-16) and 4,5-Dihydroxy-1,3-benzenedisulfonic acid (Tiron) (lanes 17-21).

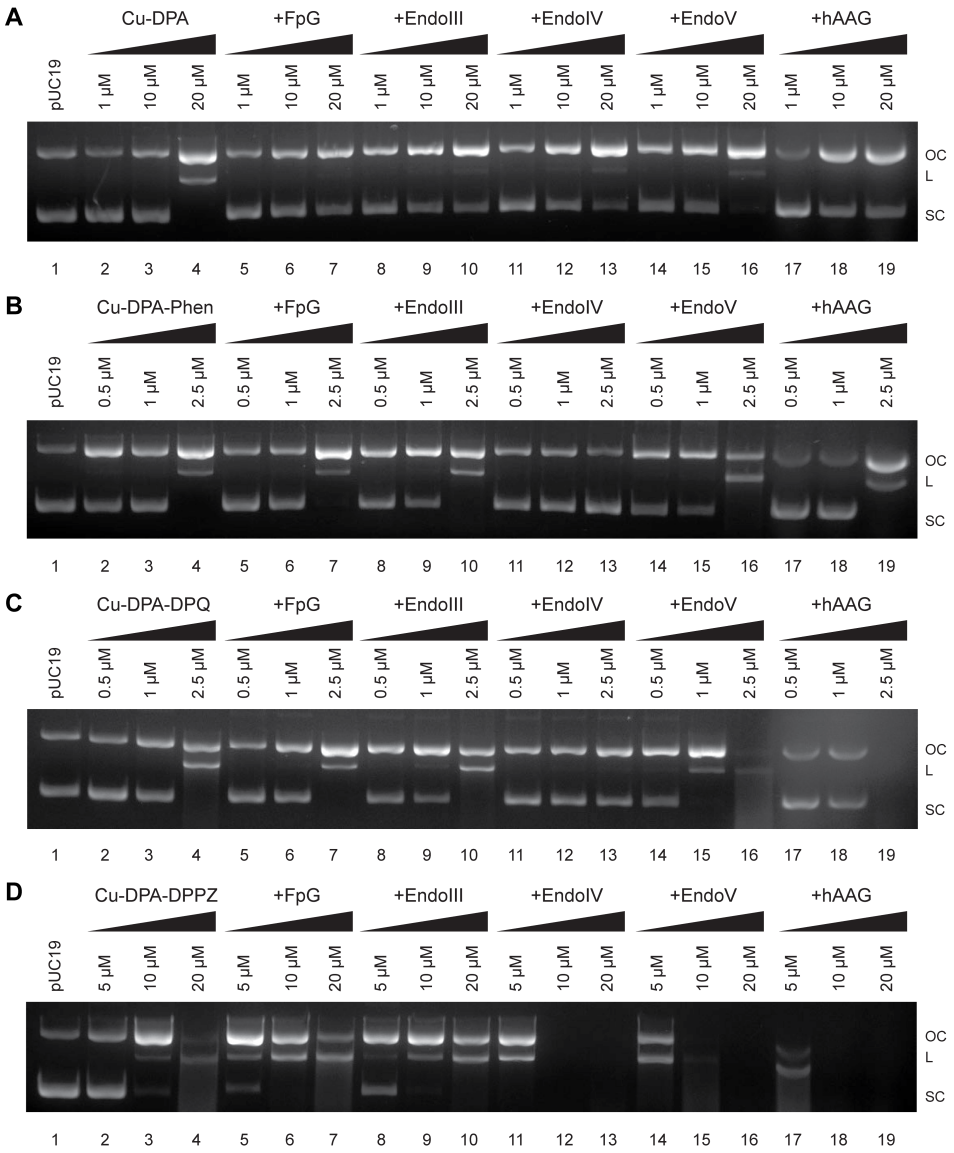

Figure B-9. 400 ng pUC19 supercoiled DNA was treated with increasing concentrations of **A** Cu-DPA; **B** Cu-DPA-Phen; **C** Cu-DPA-DPQ; **D** Cu-DPA-DPPZ; (lanes 2-4) in the presence of 1 mM Na-*L*-ascorbate and in the presence of 2U of either FpG (lanes 5-7), Endo III (lanes 8-10), Endo IV (lanes 11-13), EndoV (lanes 14-16) or hAAG (lanes 17-19). For full experimental conditions see main paper.

Appendix C.

Design and development of Cu(II)-TFO hybrids *via* click chemistry for targeted oxidative DNA cleavage

C-1 Synthetic routes and NMR Spectroscopy

Route A: Synthesis of *N*-5-(azidomethyl)pyridine-*N*-*di*-(2-picolyl)amine (5N$_3$TPMA)

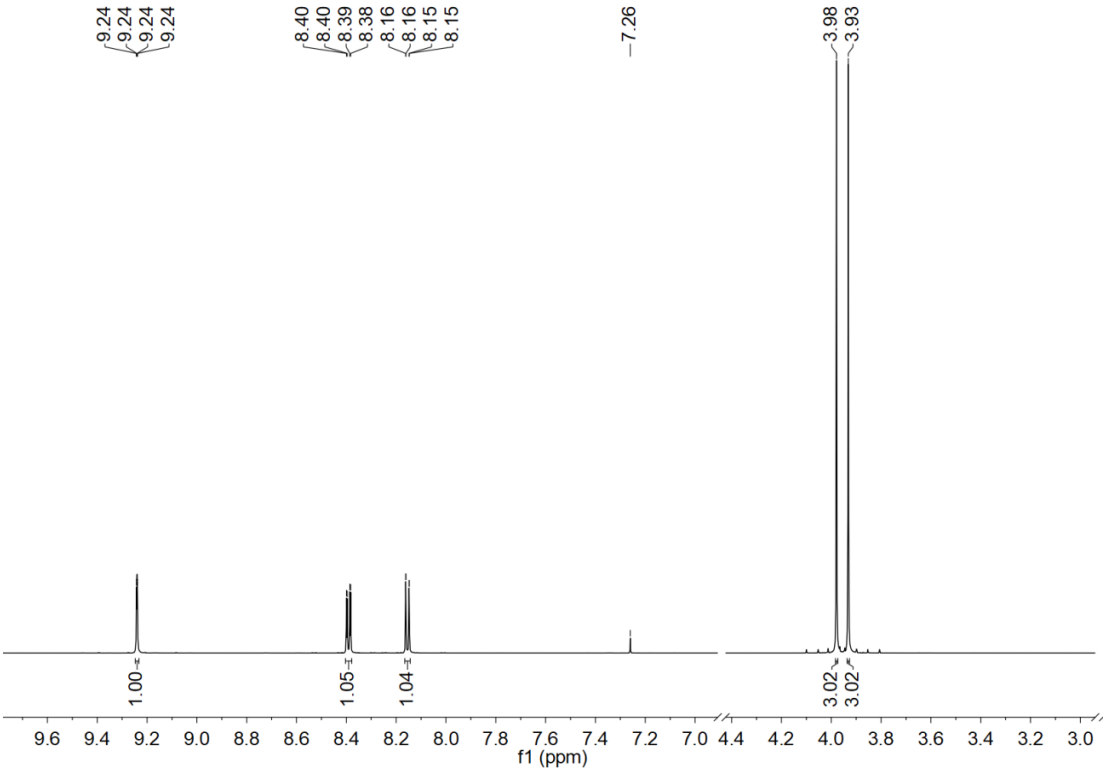

Figure C-1. ^{1}H-NMR spectrum of 2,5-pyridine dicarboxylic acid dimethyl ester (**1a**).

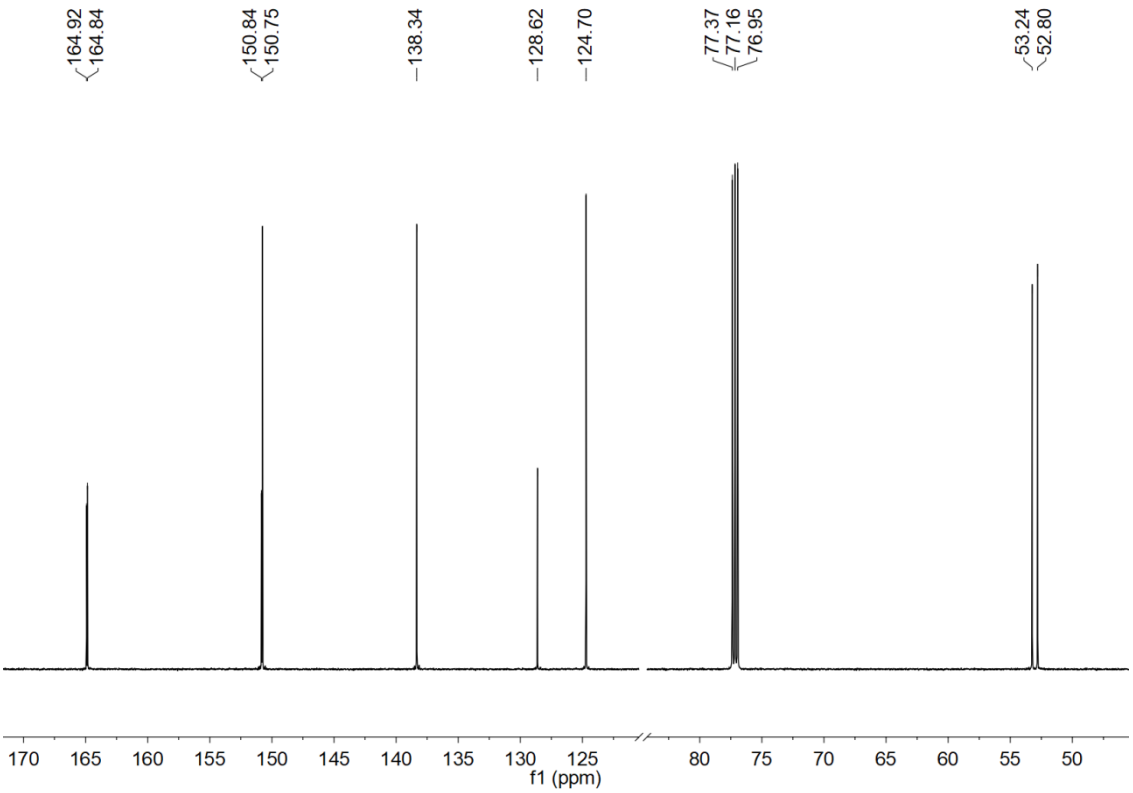

Figure C-2. ^{13}C-NMR spectrum of 2,5-pyridine dicarboxylic acid dimethyl ester (**1a**).

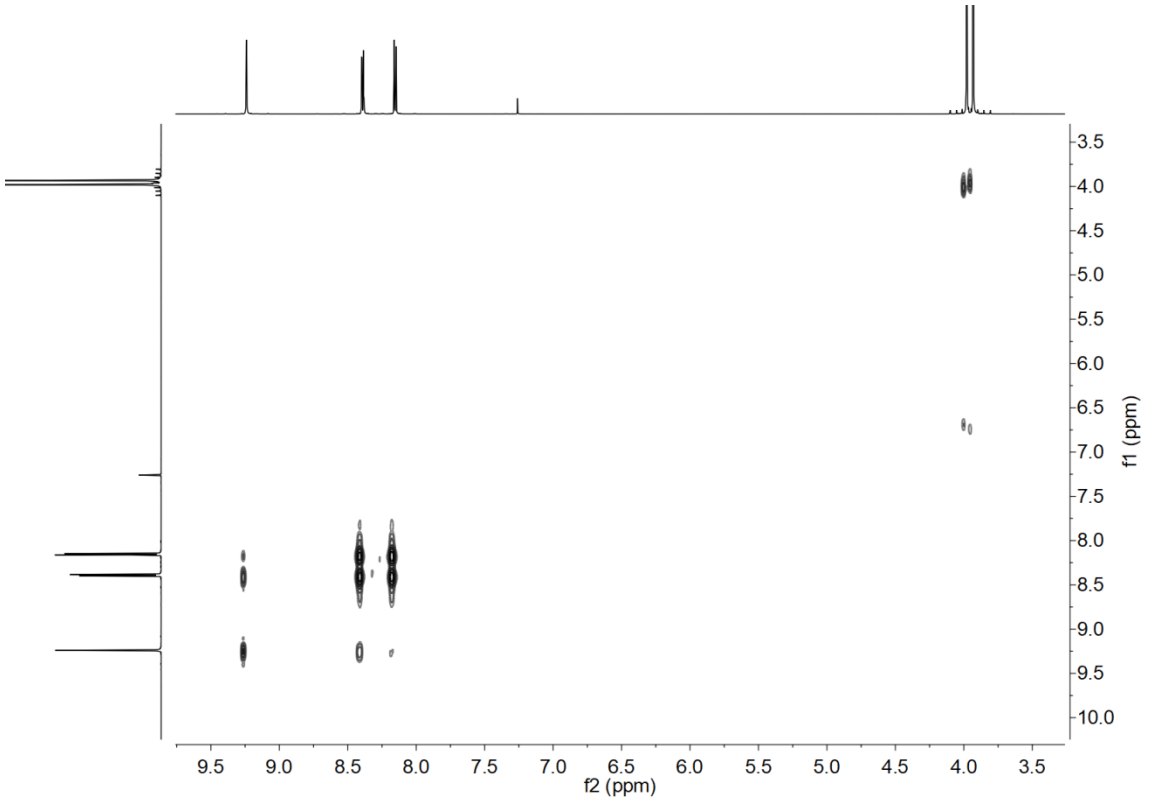

Figure C-3. ^{1}H-^{1}H COSY spectrum of 2,5-pyridine dicarboxylic acid dimethyl ester (**1a**).

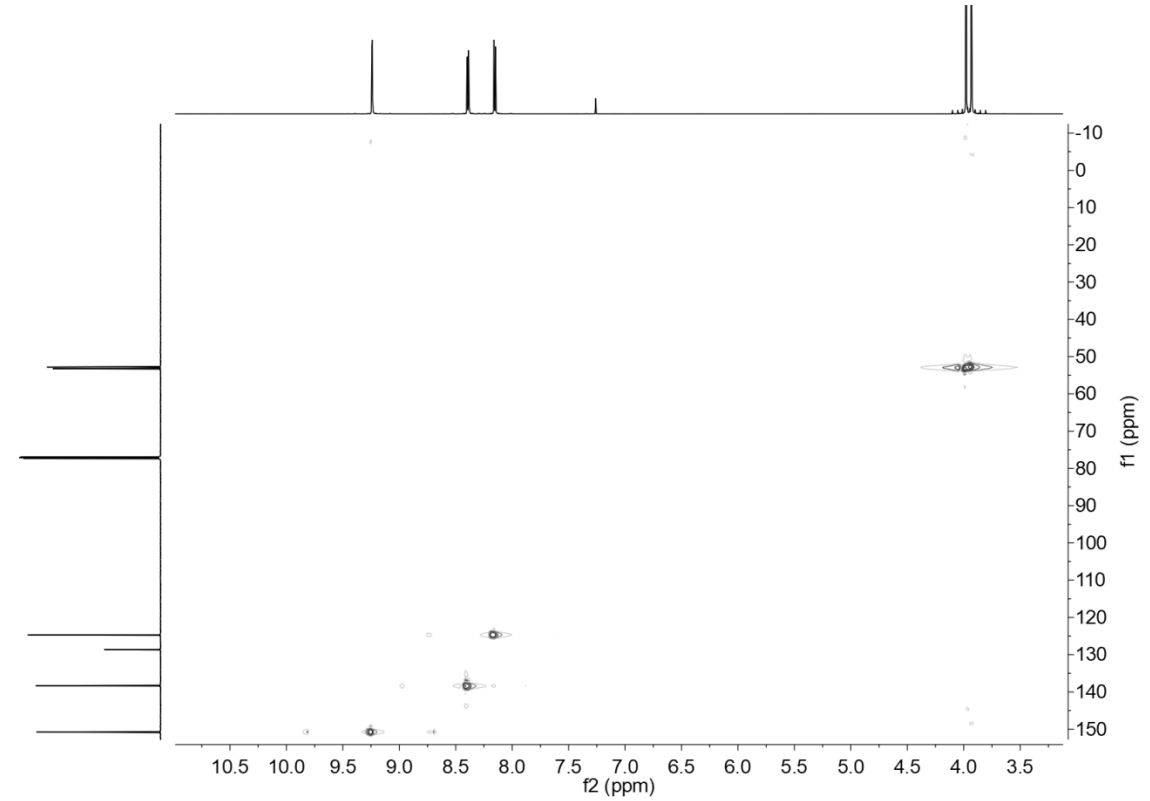

Figure C-4. ^{1}H-^{13}C HSQC spectrum of 2,5-pyridine dicarboxylic acid dimethyl ester (**1a**).

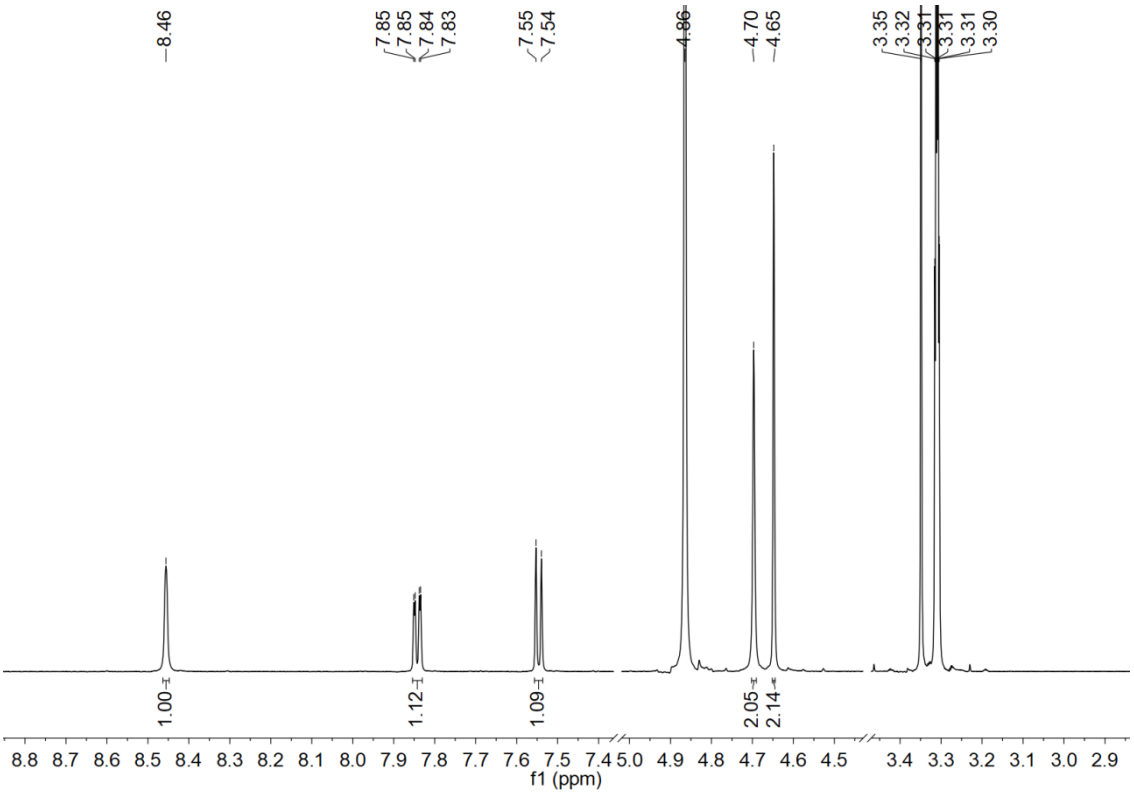

Figure C-5. [1]H-NMR spectrum of 2,5-bis(hydroxymethyl)pyridine (**2a**).

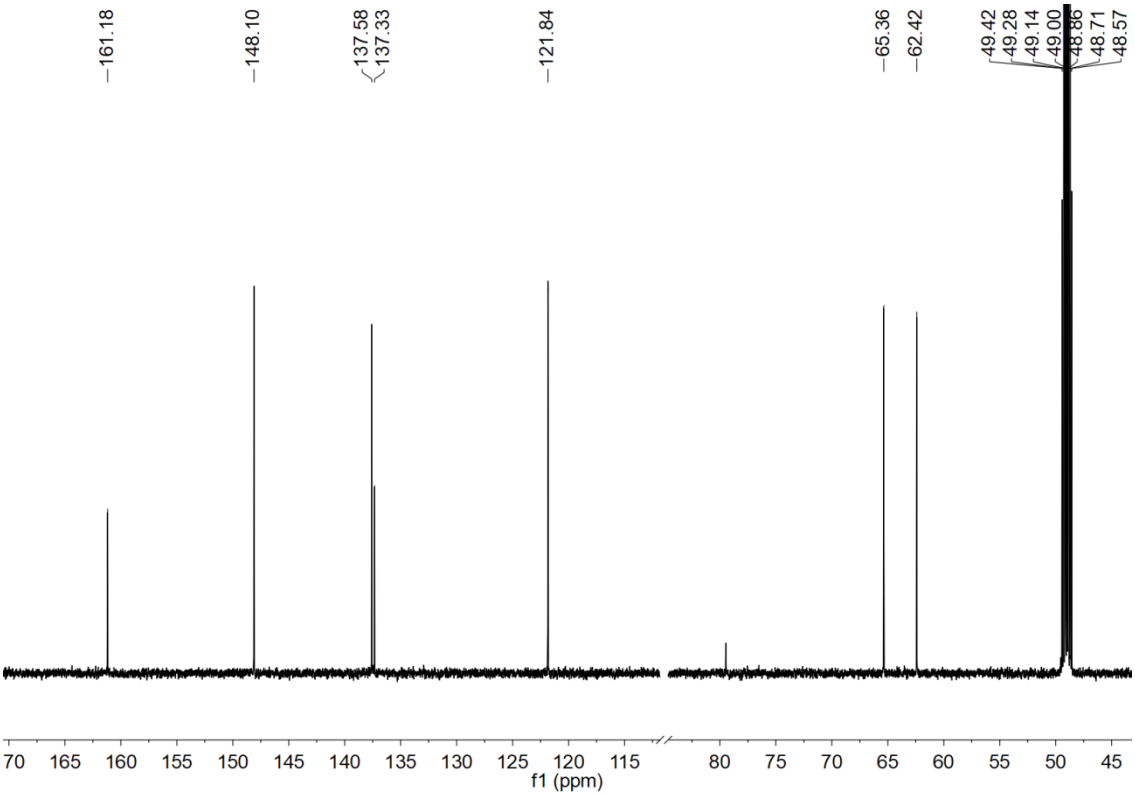

Figure C-6. [13]C-NMR spectrum of 2,5-bis(hydroxymethyl)pyridine (**2a**).

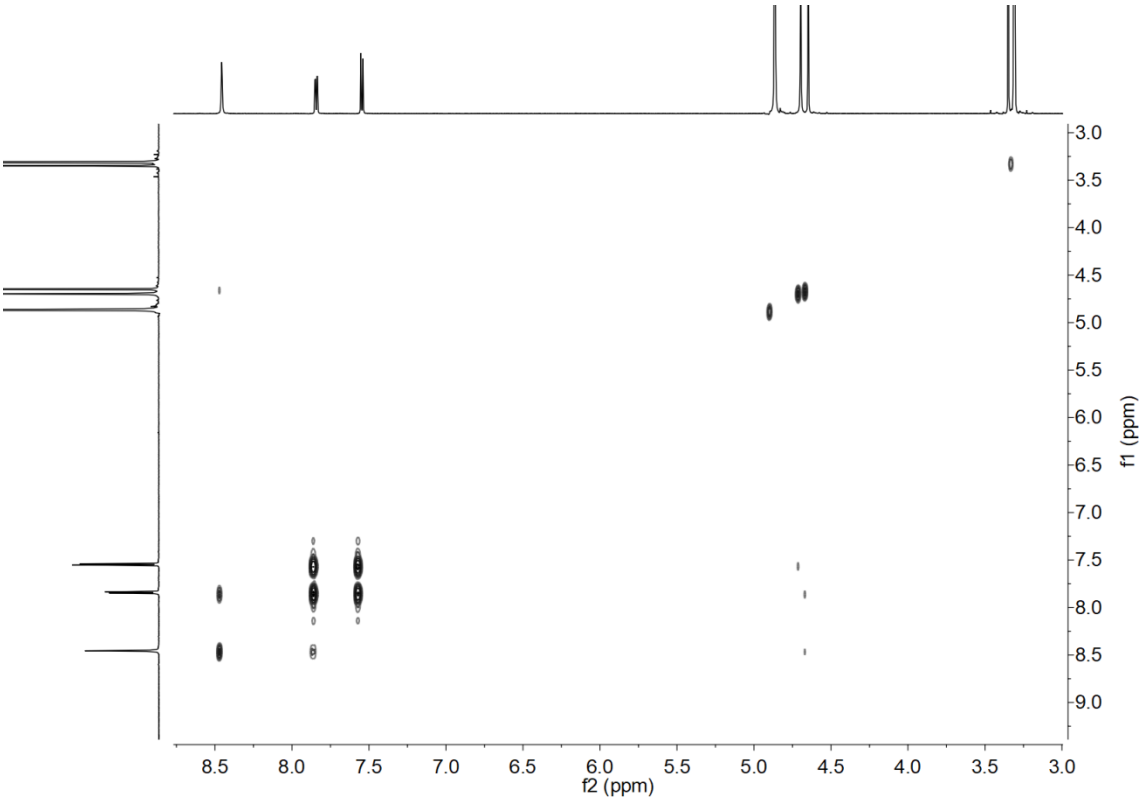

Figure C-7. ^{1}H-^{1}H COSY spectrum of 2,5-*bis*(hydroxymethyl)pyridine (**2a**).

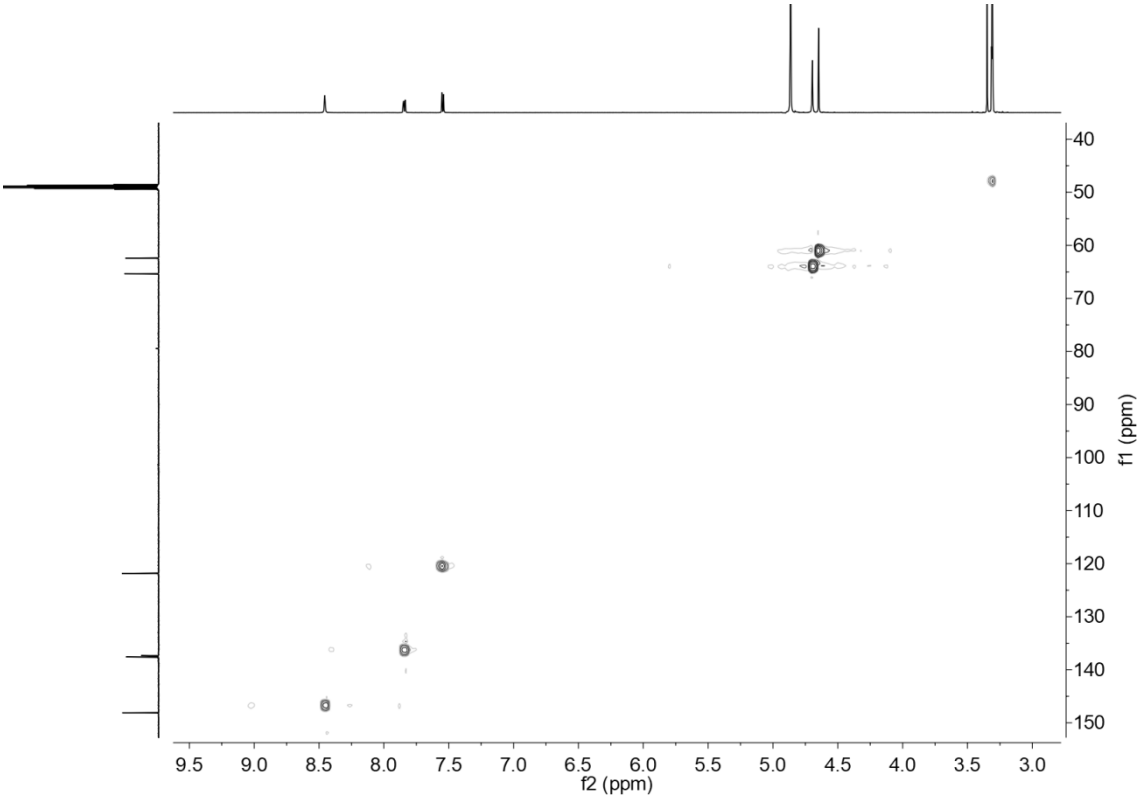

Figure C-8. ^{1}H-^{13}C HSQC spectrum of 2,5-*bis*(hydroxymethyl)pyridine (**2a**).

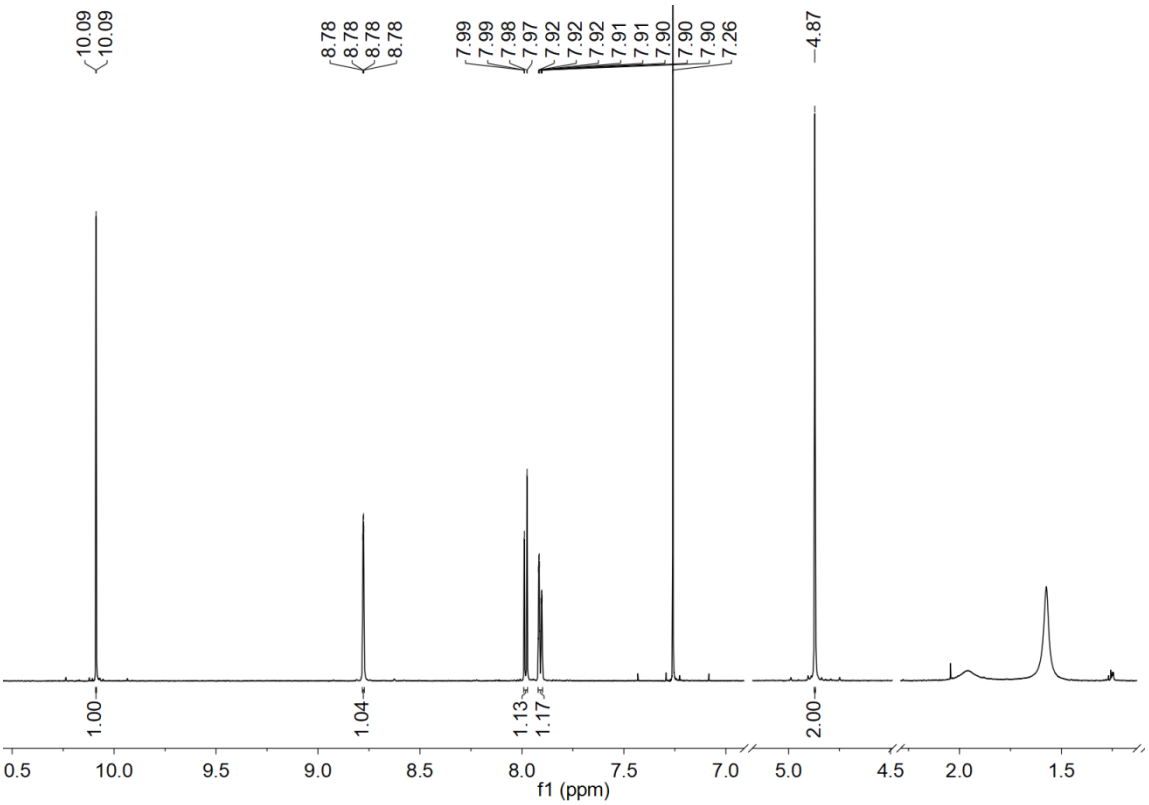

Figure C-9. [1]H-NMR spectrum of 2-formyl-5-hydroxymethylpyridine (**3a**).

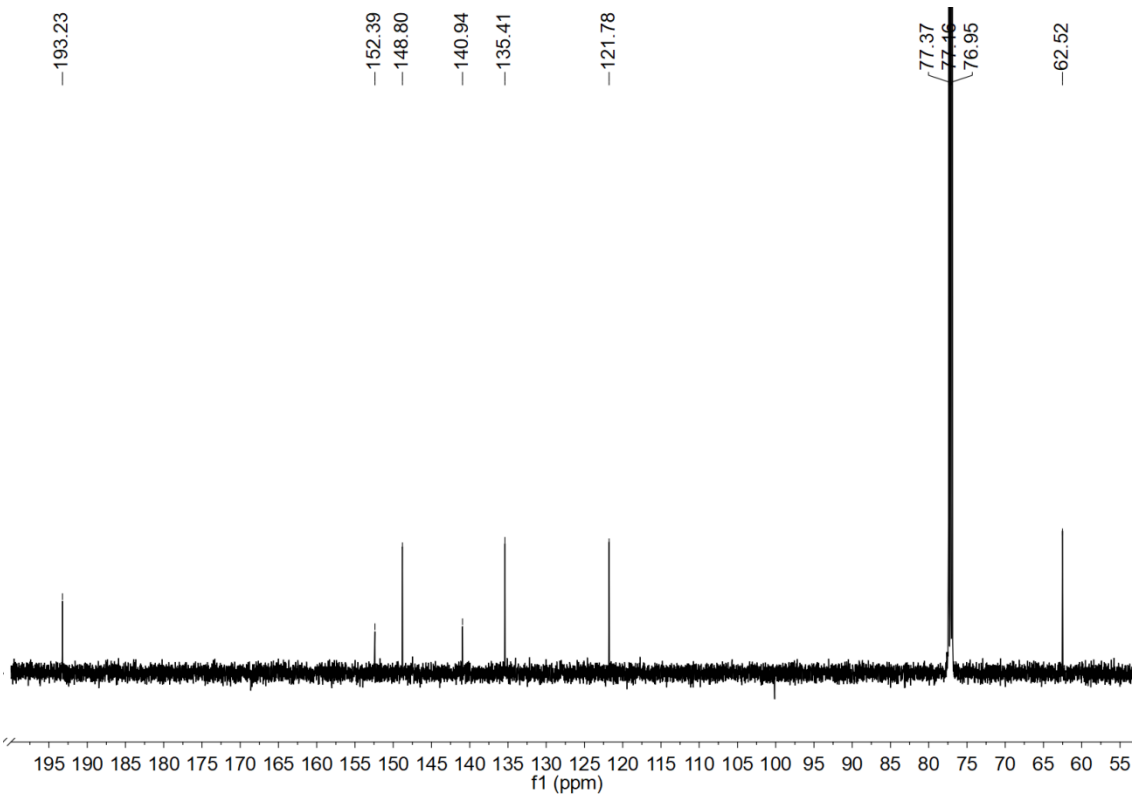

Figure C-10. [13]C-NMR spectrum of 2-formyl-5-hydroxymethylpyridine (**3a**).

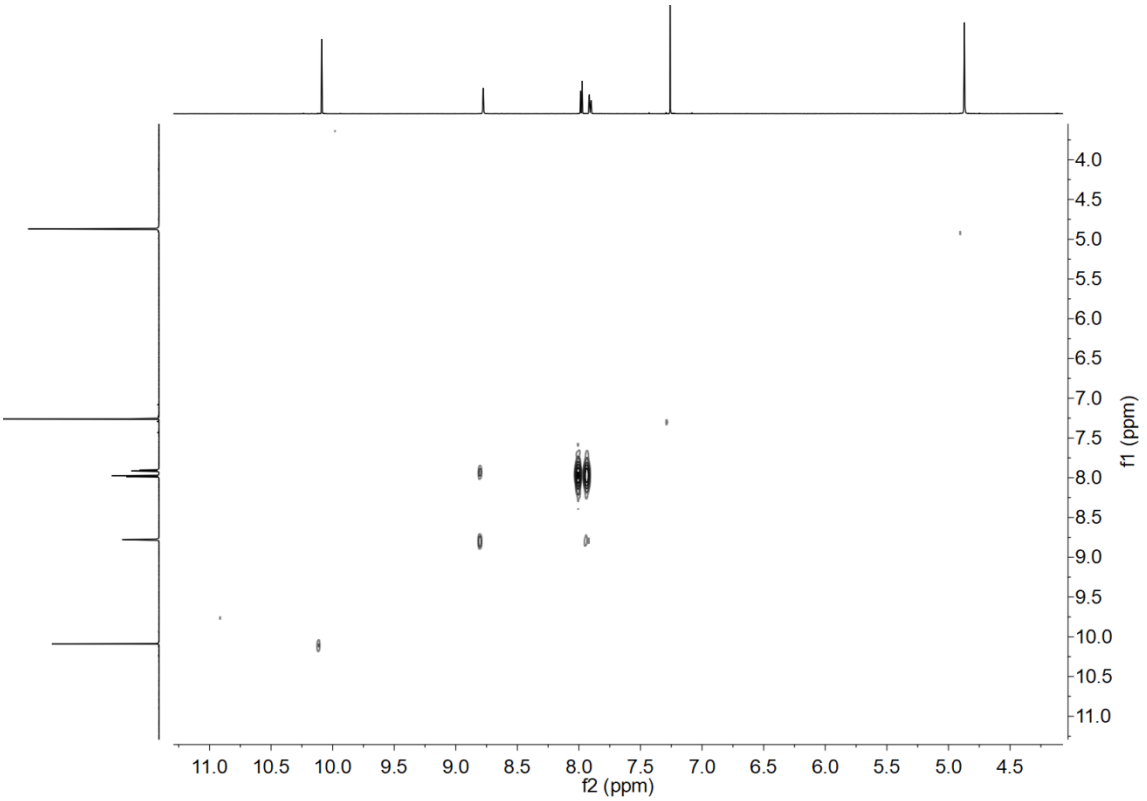

Figure C-11. ^{1}H-^{1}H COSY spectrum of 2-formyl-5-hydroxymethylpyridine (**3a**).

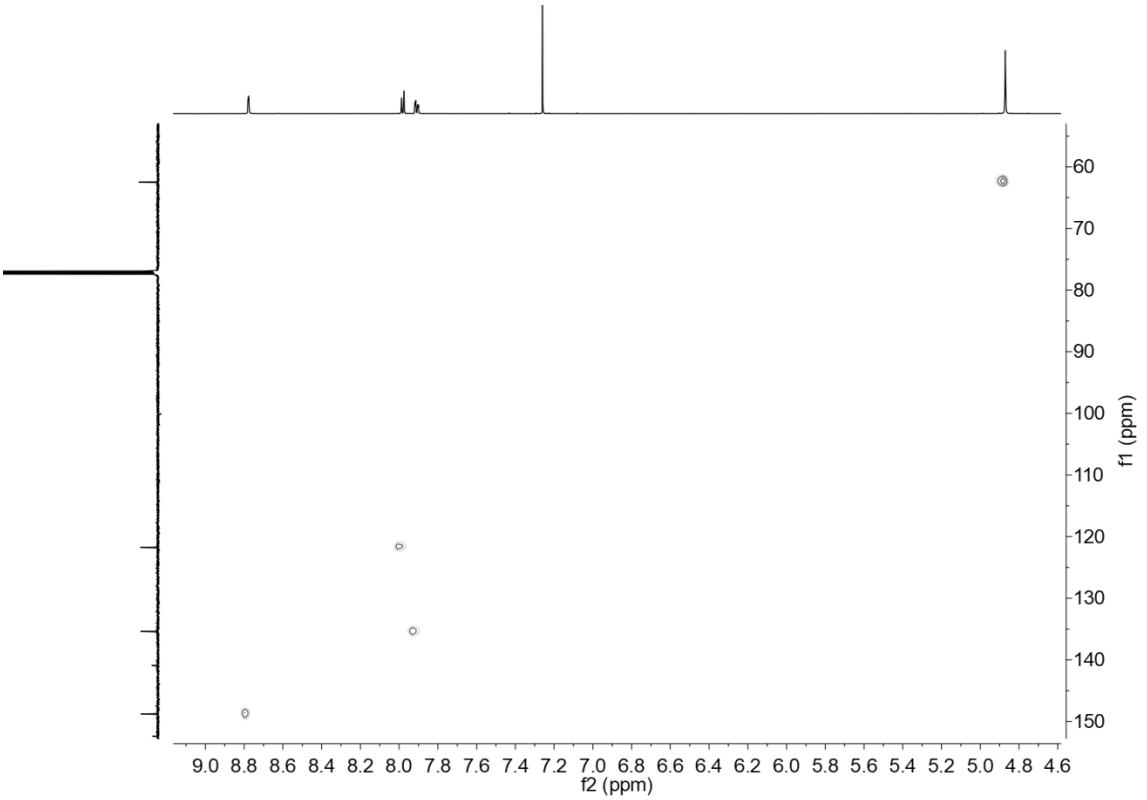

Figure C-12. ^{1}H-^{13}C HSQC spectrum of 2-formyl-5-hydroxymethylpyridine (**3a**).

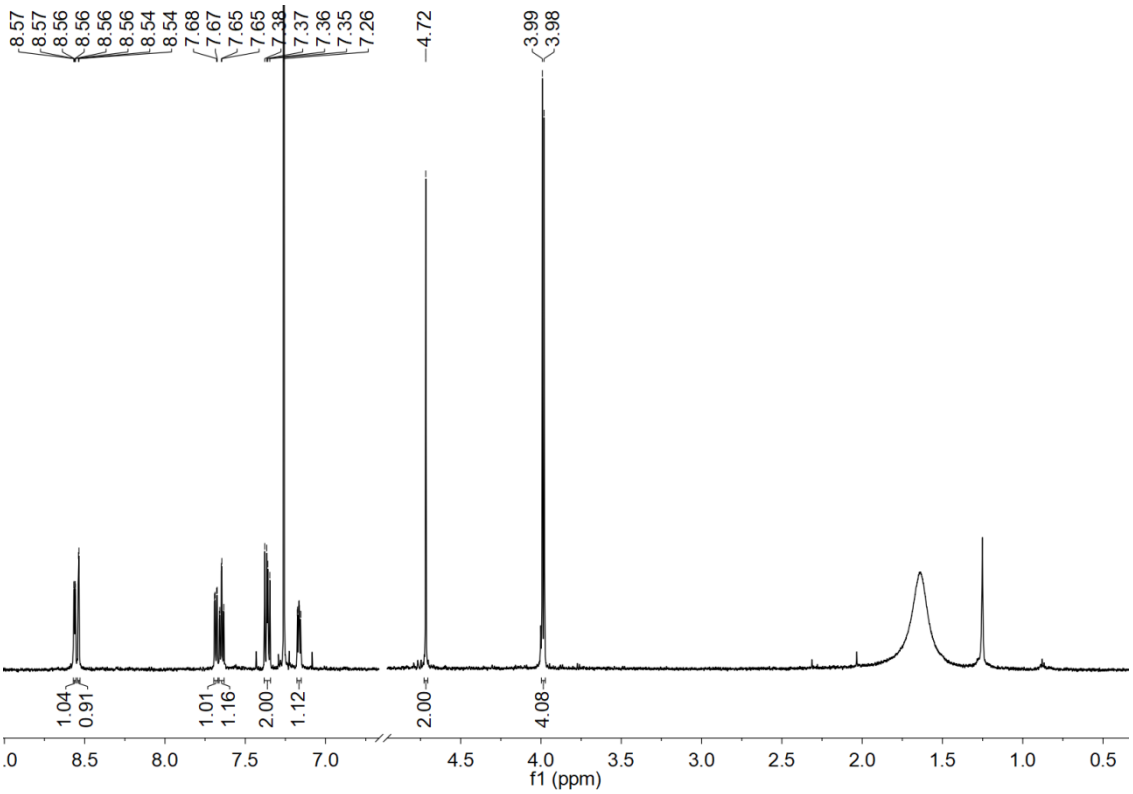

Figure C-13. [1]H-NMR spectrum of 5-hydroxomethyl-*di*-(2-pycolyl)amine (**4a**).

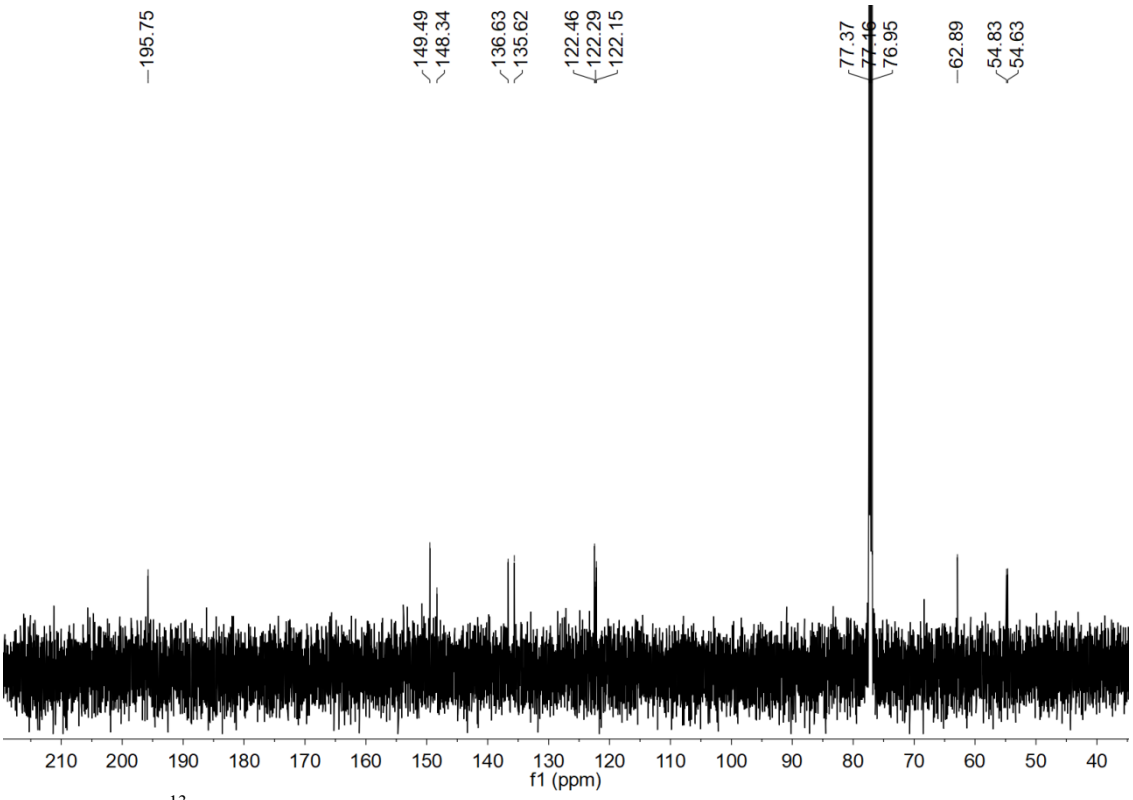

Figure C-14. [13]C-NMR spectrum of 5-hydroxomethyl-*di*-(2-pycolyl)amine (**4a**).

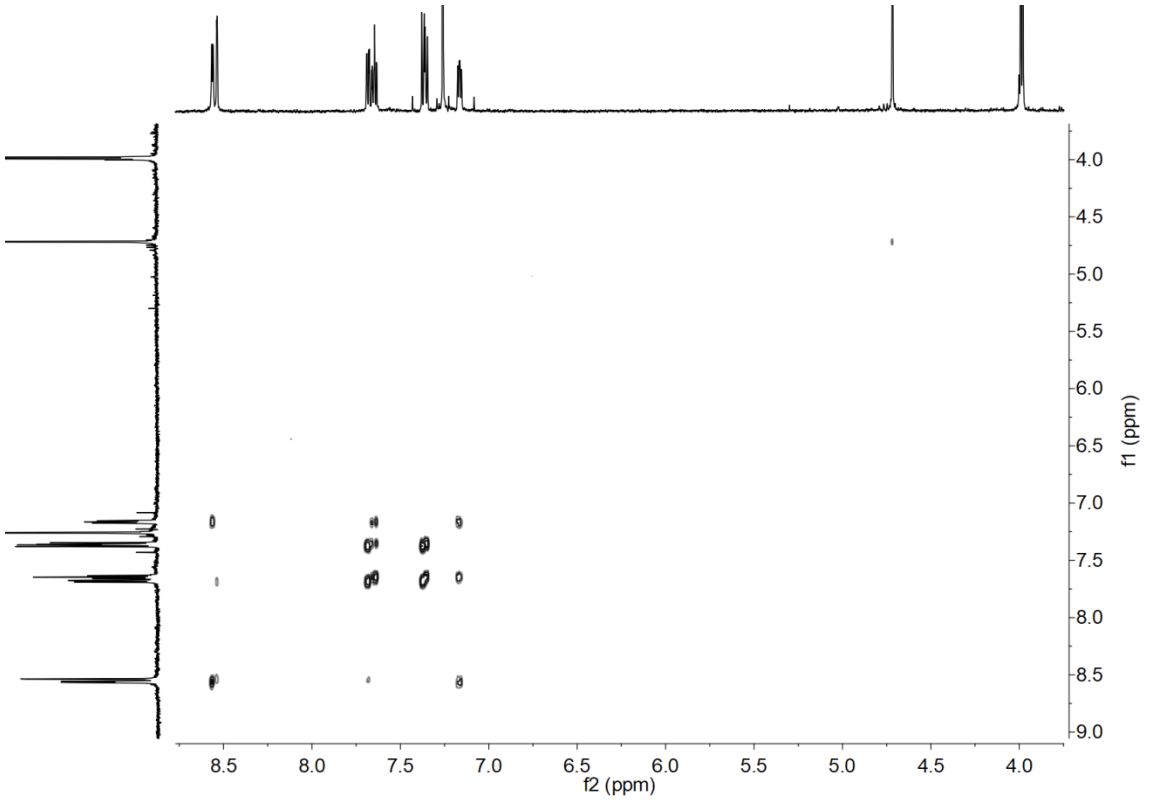

Figure C-15. ^{1}H-^{1}H COSY spectrum of 5-hydroxomethyl-*di*-(2-pycolyl)amine (**4a**).

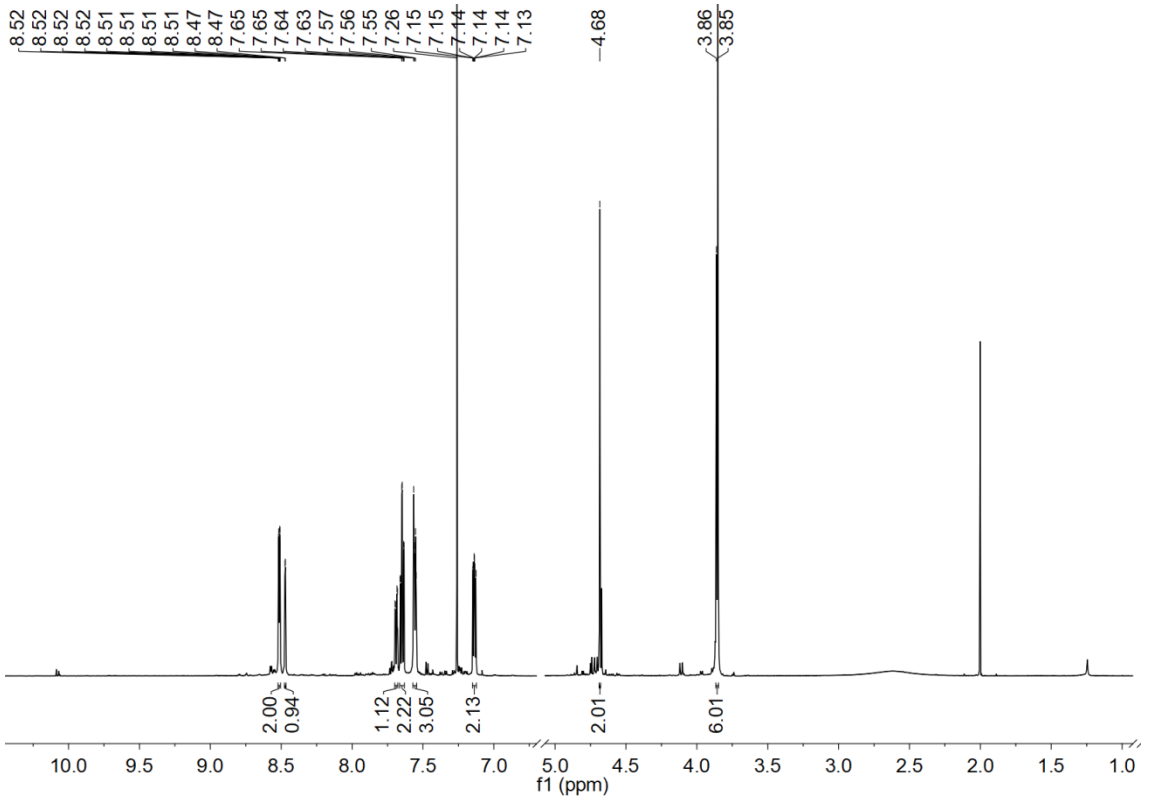

Figure C-16. ^{1}H-NMR spectrum of 5-hydroxomethyl-tris-(2-pycolyl)amine (**5a**).

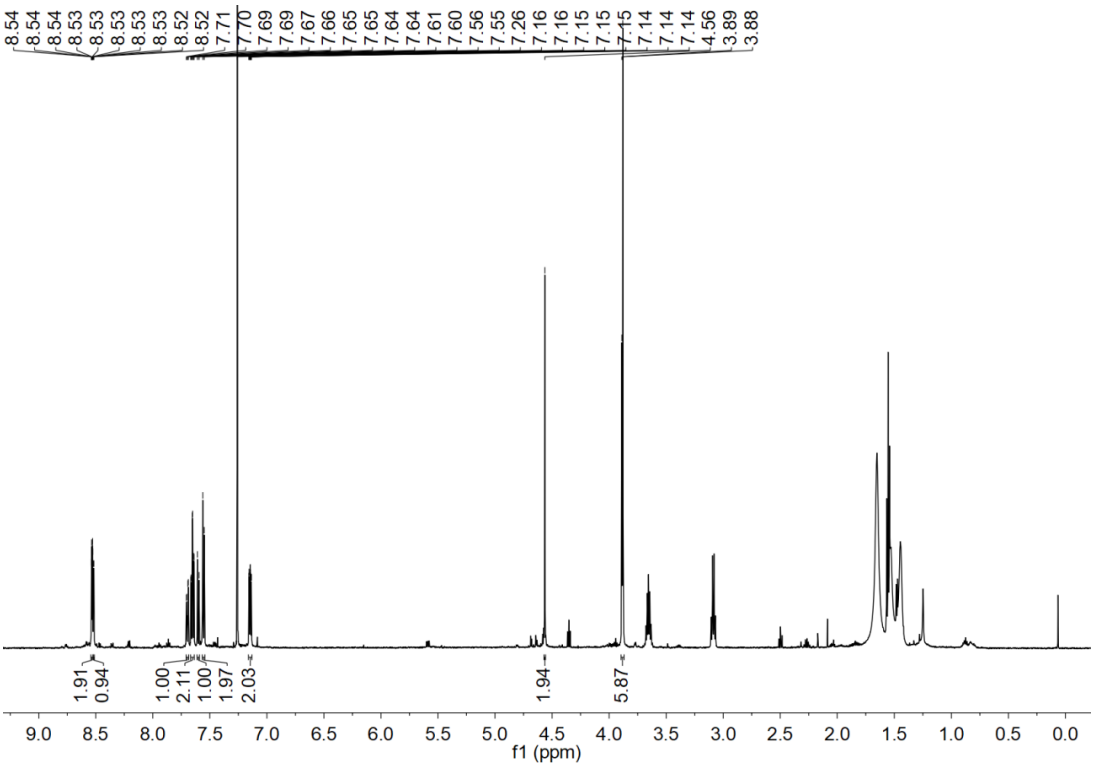

Figure C-17. ^{1}H-NMR spectrum of 5-chloromethyl-tris-(2-pycolyl)amine (**6a**).

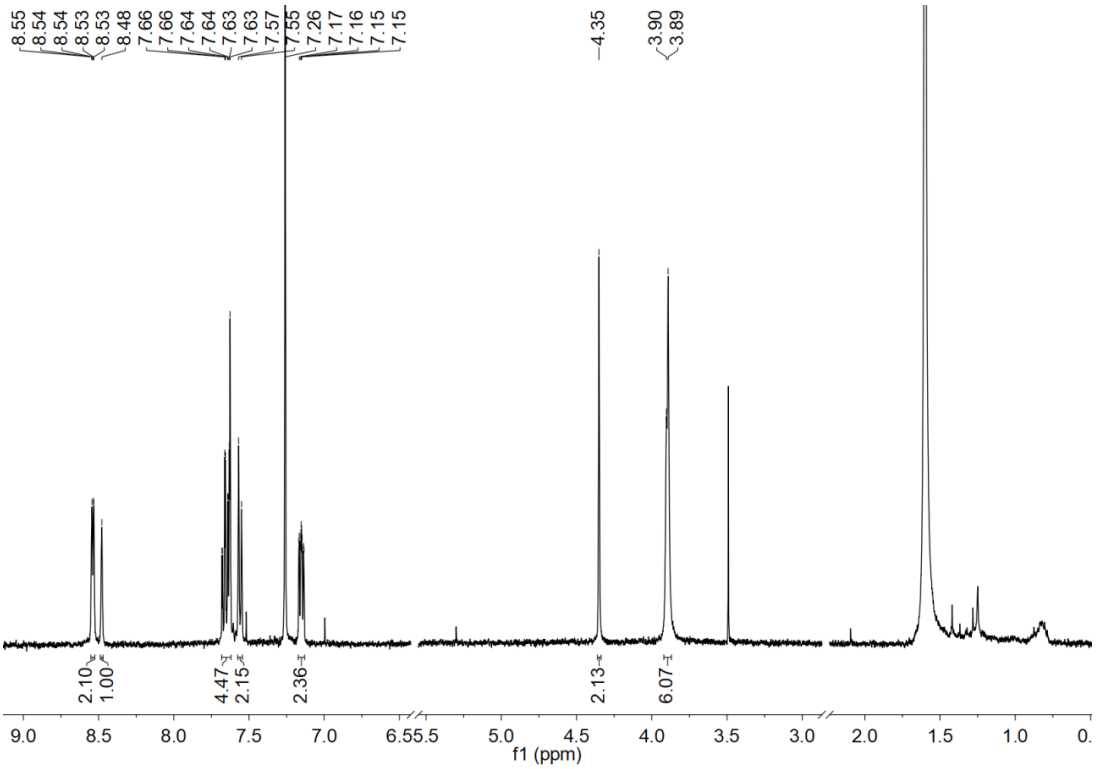

Figure C-18. ^{1}H-NMR spectrum of 5-azidomethyl-*tris*-(2-pycolyl)amine (**7a**).

Route B: Synthesis of *N*-6-(azidomethyl)pyridine-*N*-*di*-(2-picolyl)amine (6N$_3$-TPMA)

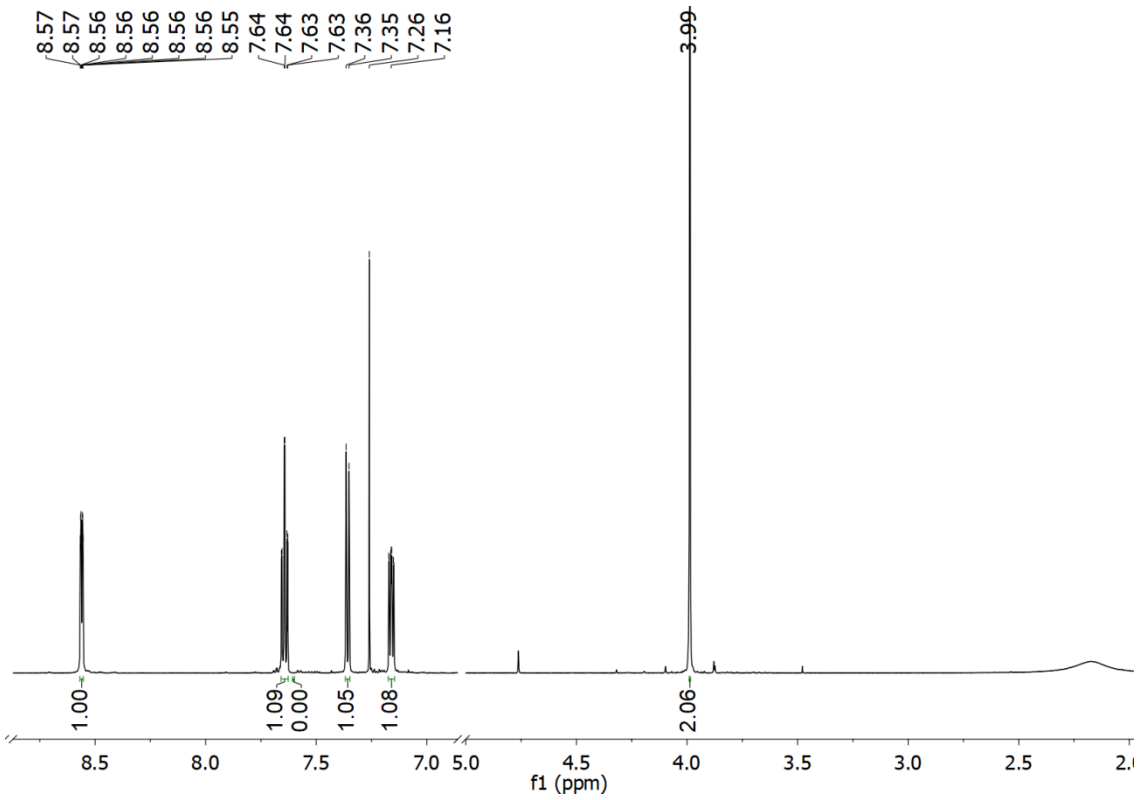

Figure C-19. [1]H-NMR spectrum of *di*-(2-picolyl)amine (**DPA**).

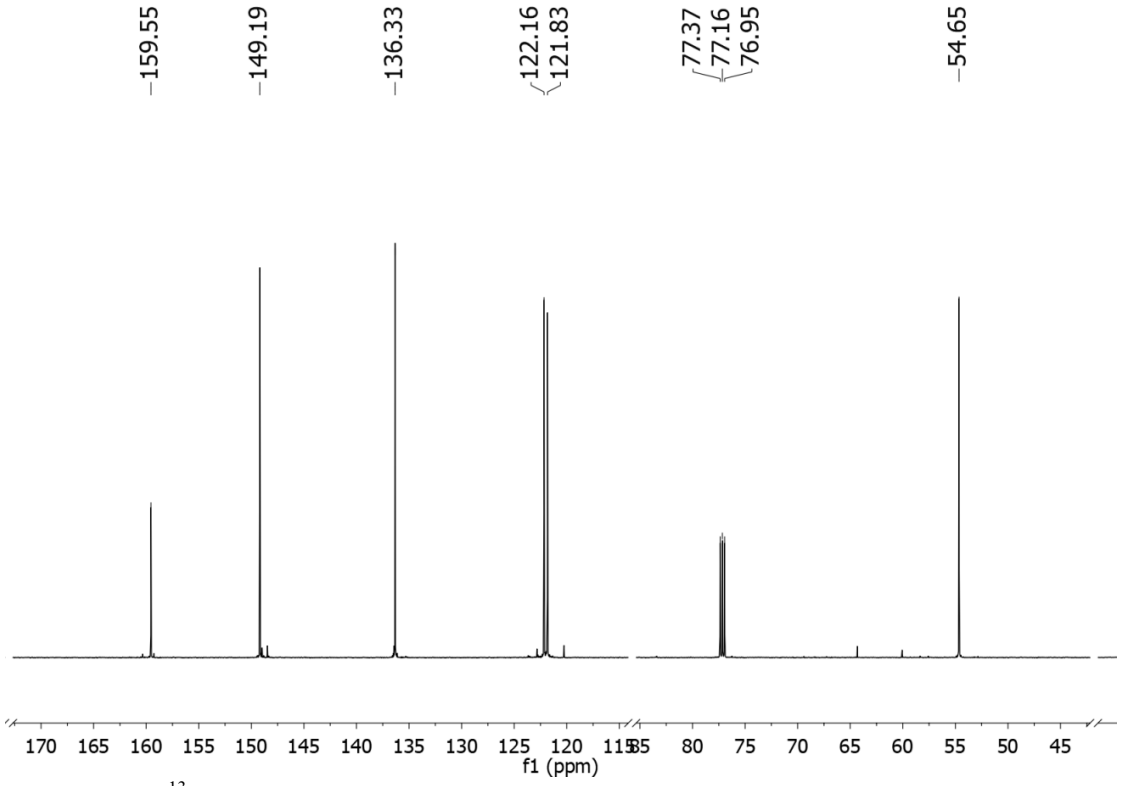

Figure C-20. [13]C-NMR spectrum of *di*-(2-picolyl)amine (**DPA**).

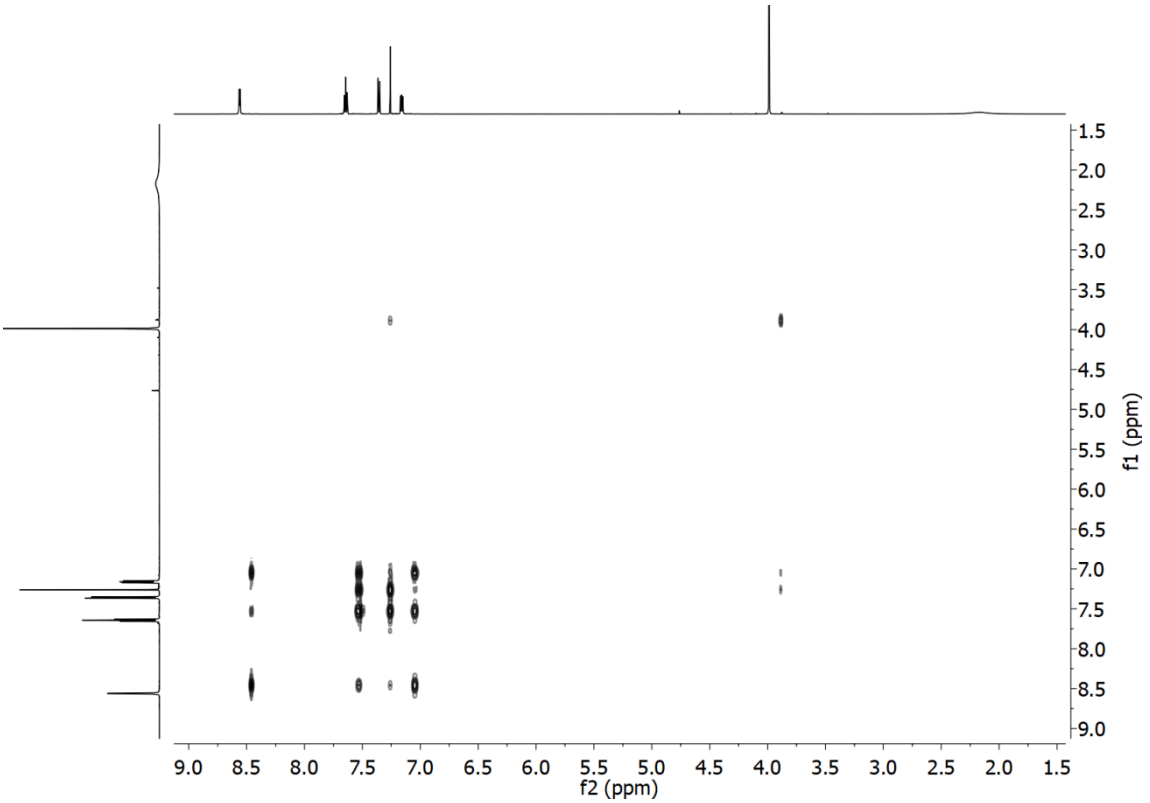

Figure C-21. ^{1}H-^{1}H COSY spectrum of *di*-(2-picolyl)amine (**DPA**).

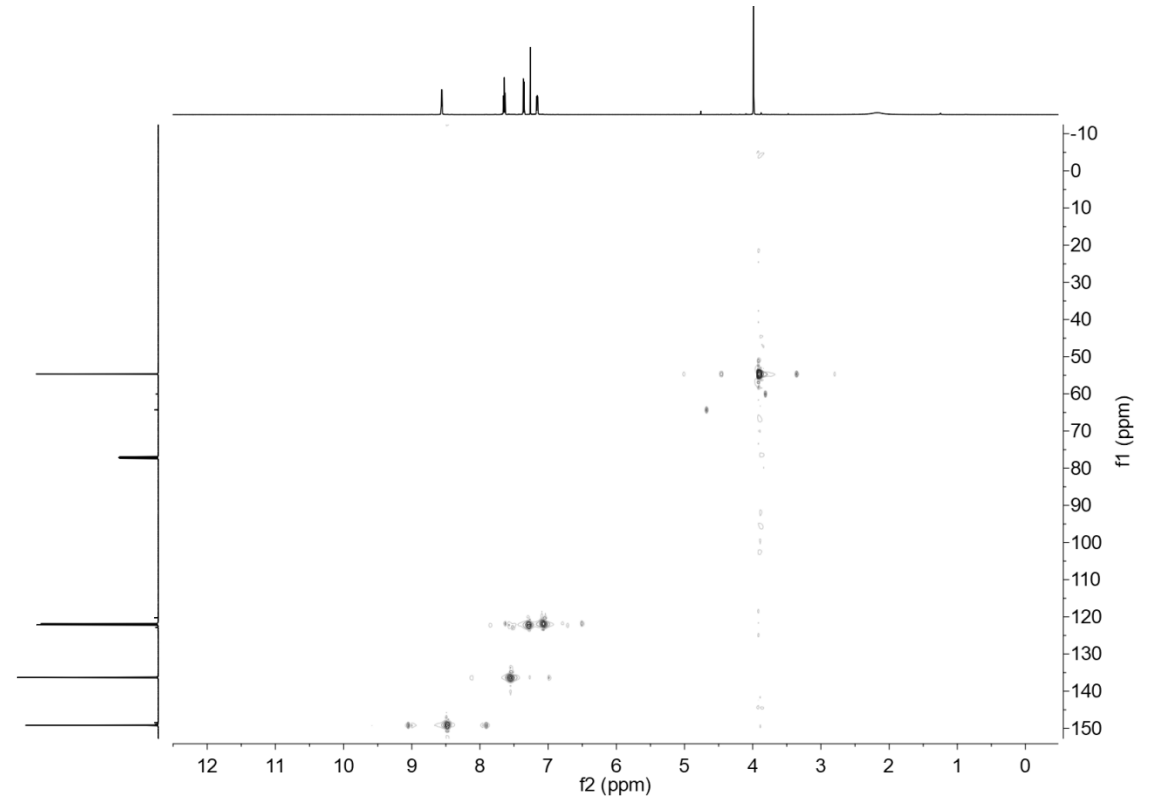

Figure C-22. ^{1}H-^{13}C HSQC spectrum of *di*-(2-picolyl)amine (**DPA**).

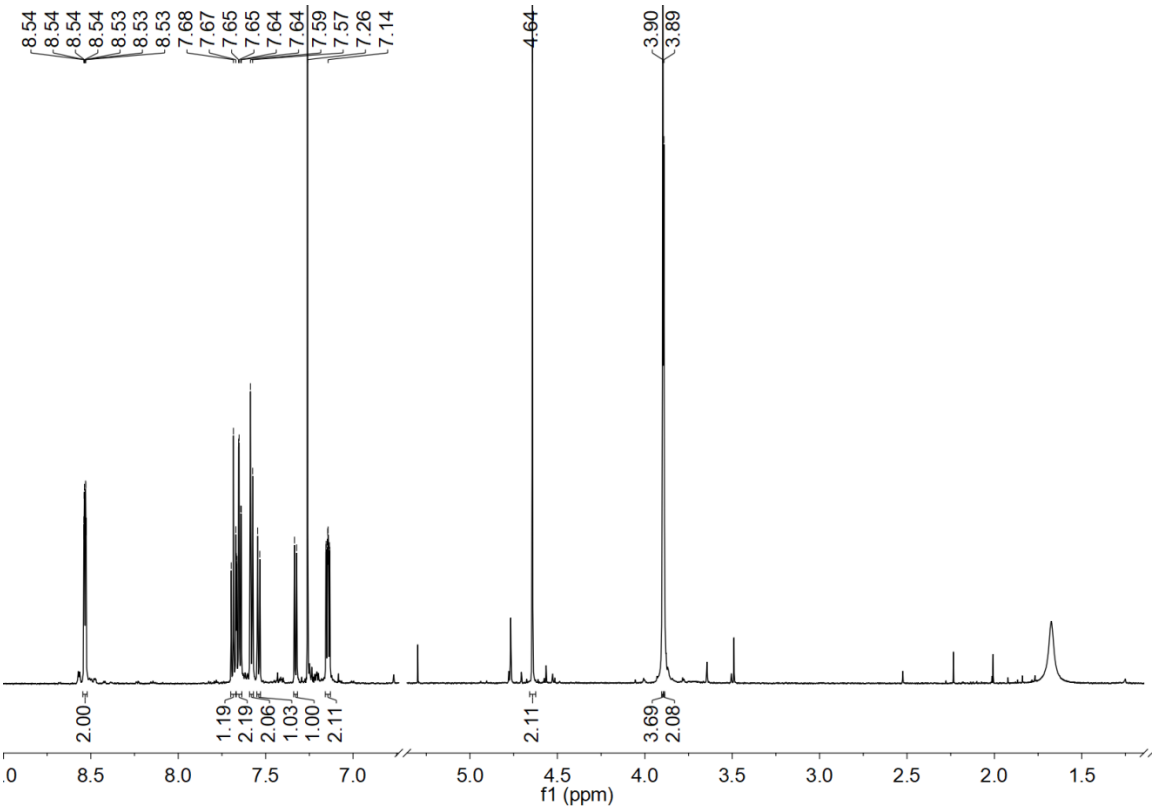

Figure C-23. [1]H-NMR spectrum of *N*-6-(chloromethyl)pyridine-*N*-*di*-(2-picolyl)amine (**1b**).

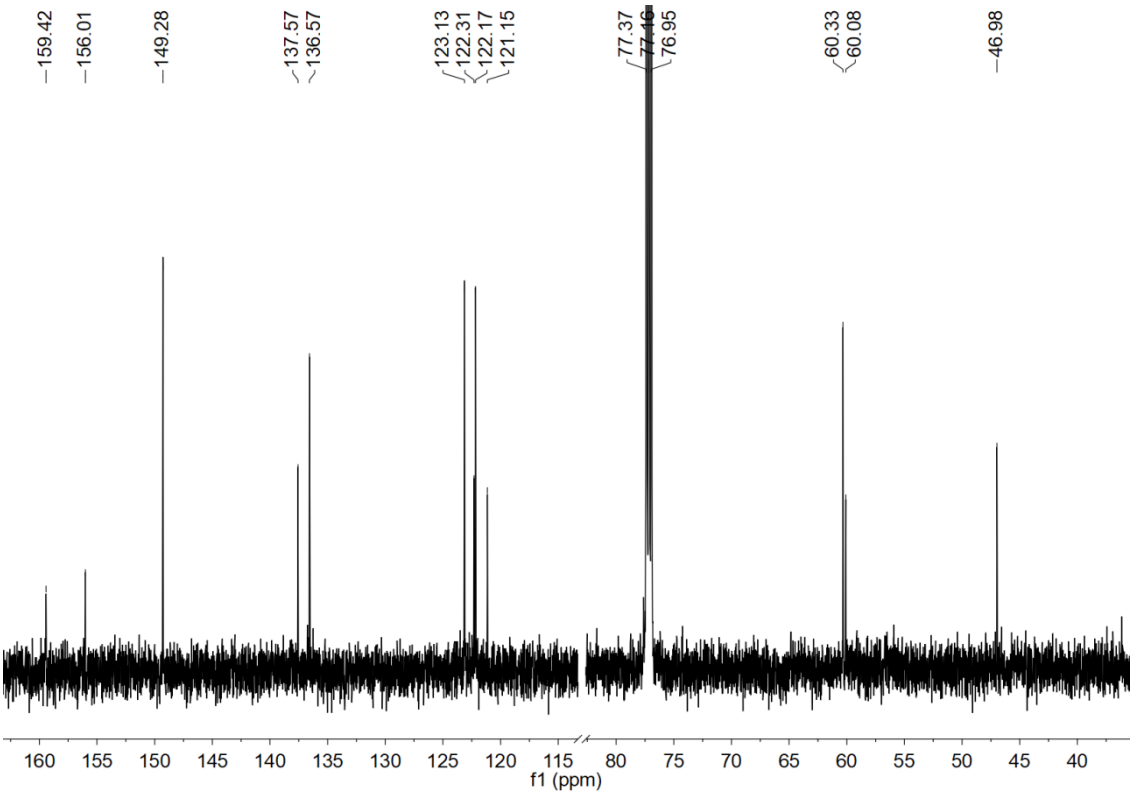

Figure C-24. [13]C-NMR spectrum of *N*-6-(chloromethyl)pyridine-*N*-*di*-(2-picolyl)amine (**1b**).

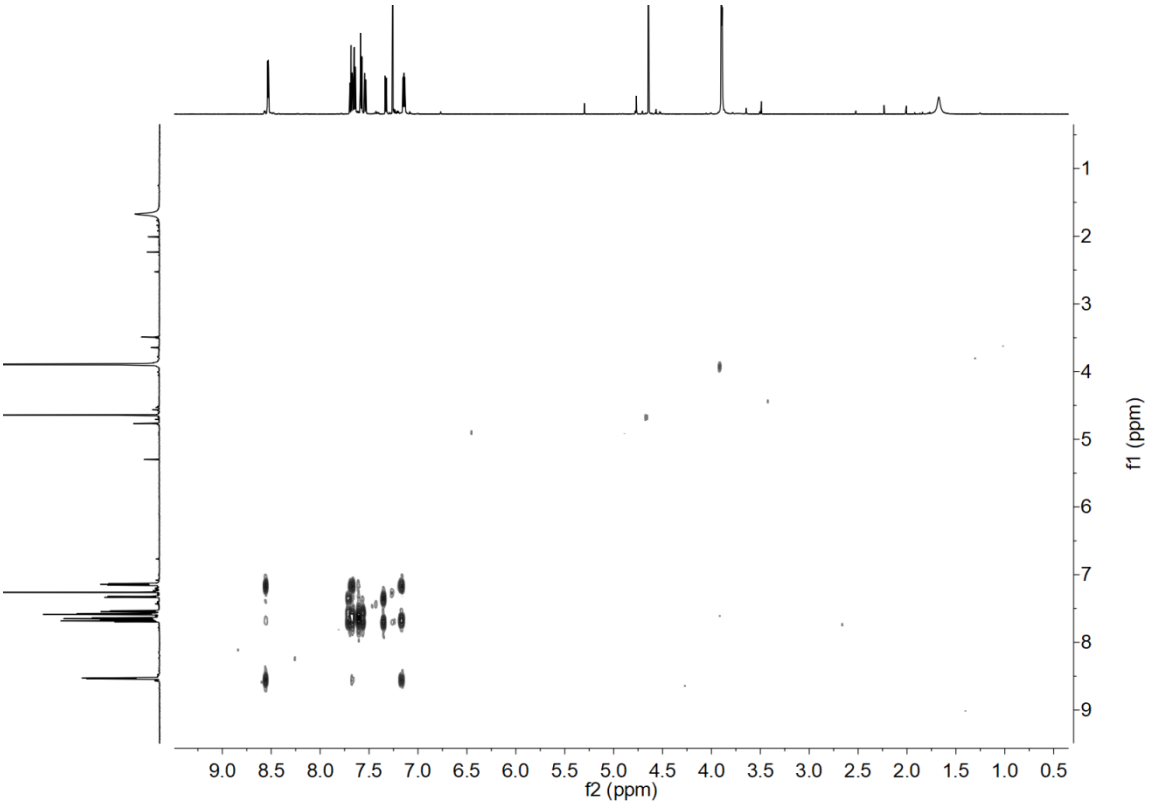

Figure C-25. ^{1}H-^{1}H COSY spectrum of *N*-6-(chloromethyl)pyridine-*N*-*di*-(2-picolyl)amine (**1b**).

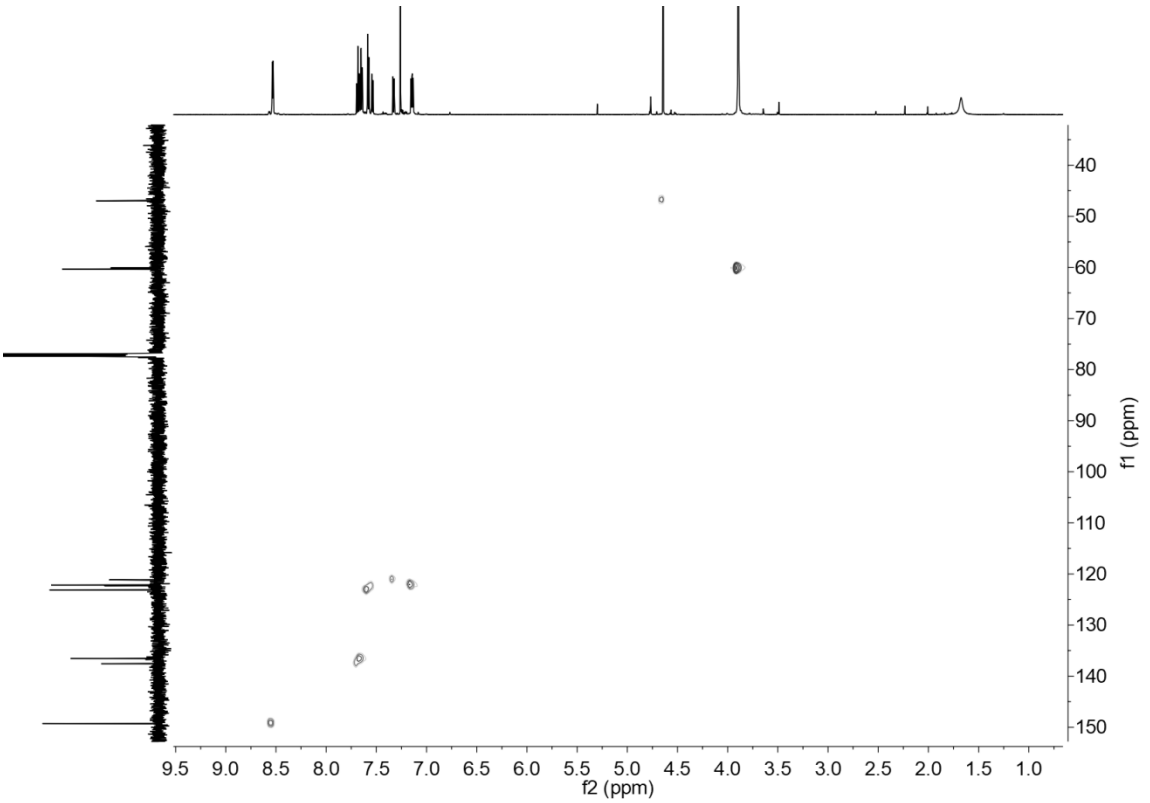

Figure C-26. ^{1}H-^{13}C HSQC spectrum of *N*-6-(chloromethyl)pyridine-*N*-*di*-(2-picolyl)amine (**1b**).

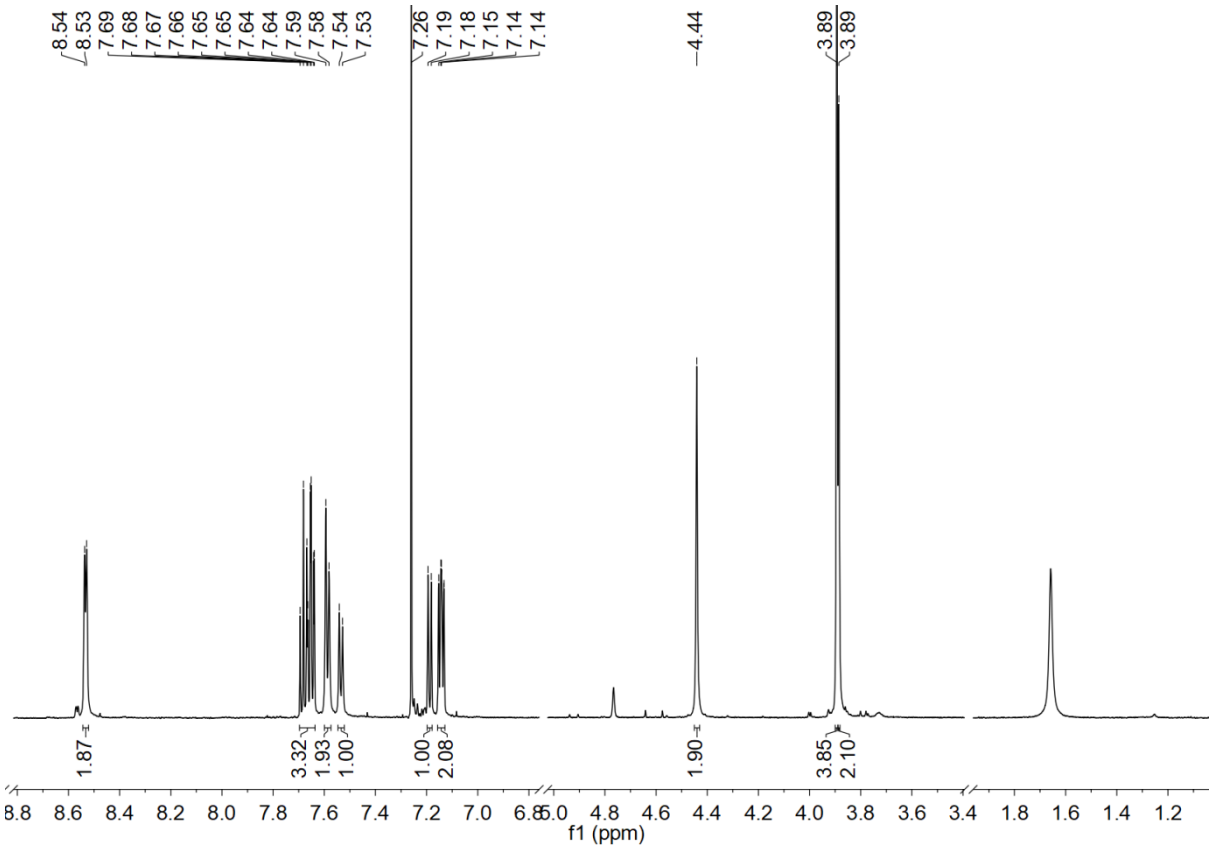

Figure C-27. [1]H-NMR spectrum of *N*-6-(azidomethyl)pyridine-*N*-*di*-(2-picolyl)amine (**2b**).

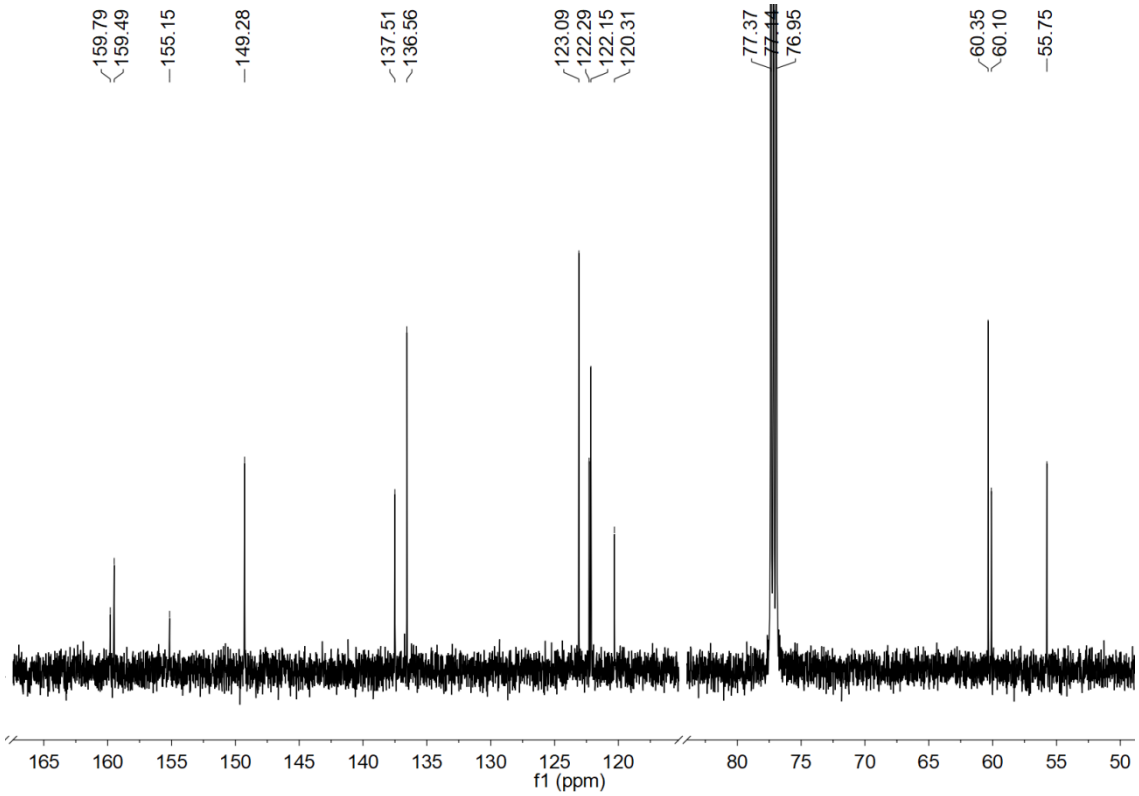

Figure C-28. [13]C-NMR spectrum of *N*-6-(azidomethyl)pyridine-*N*-*di*-(2-picolyl)amine (**2b**).

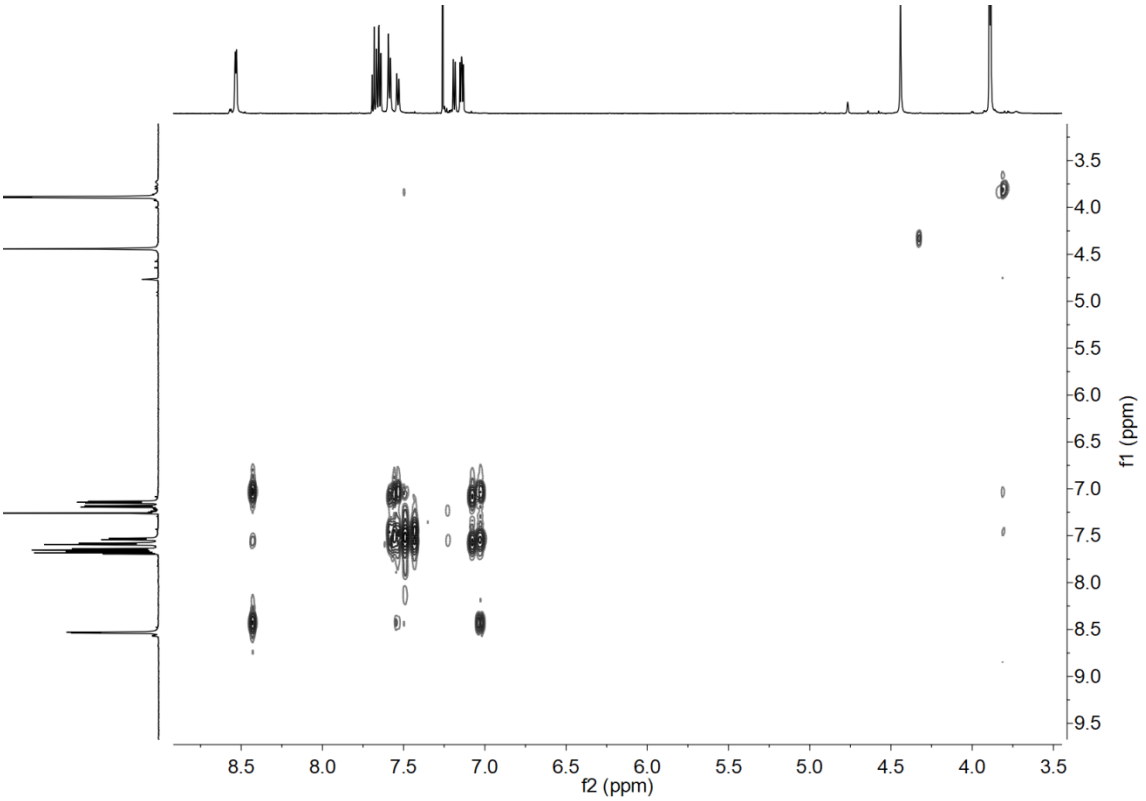

Figure C-29. ^{1}H-^{1}H COSY spectrum of *N*-6-(azidomethyl)pyridine-*N*-*di*-(2-picolyl)amine (**2b**).

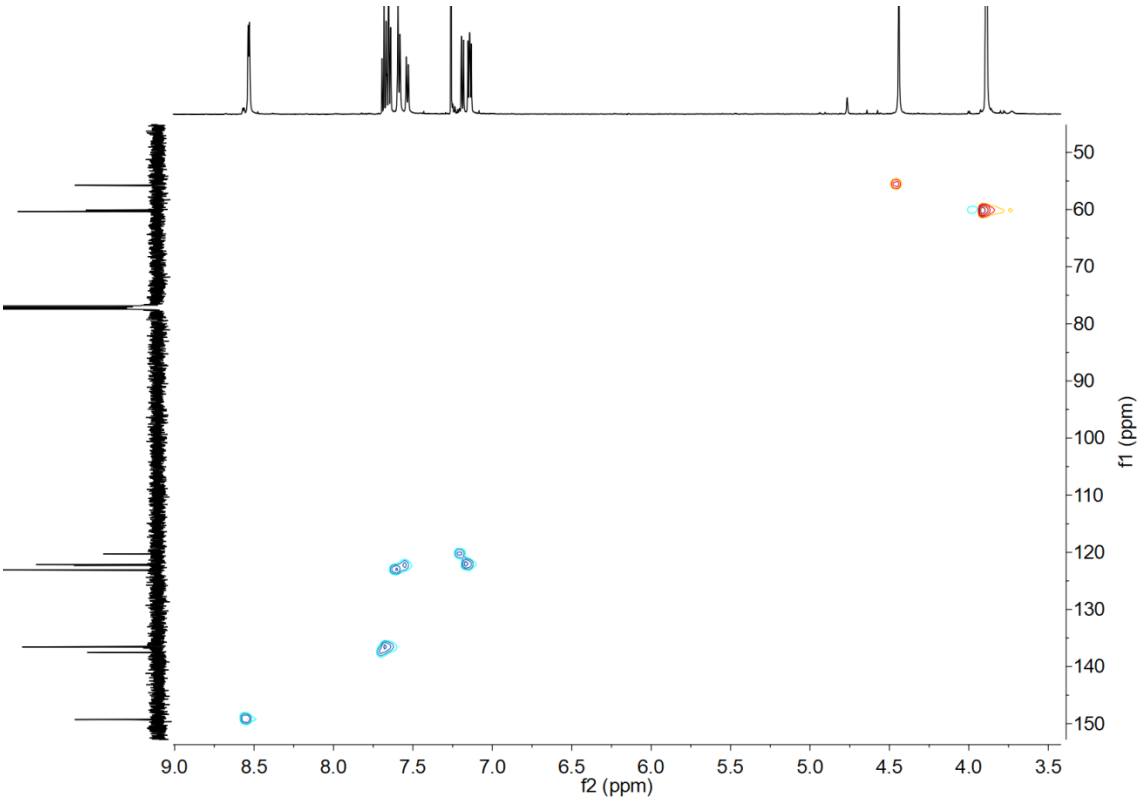

Figure C-30. ^{1}H-^{13}C HSQC spectrum of *N*-6-(azidomethyl)pyridine-*N*-*di*-(2-picolyl)amine (**2b**).

Route C: Synthesis of *N*-4-azidobenzyl-*N*-*di*-(2-picolyl)amine (4N_3-Benzyl-DPA)

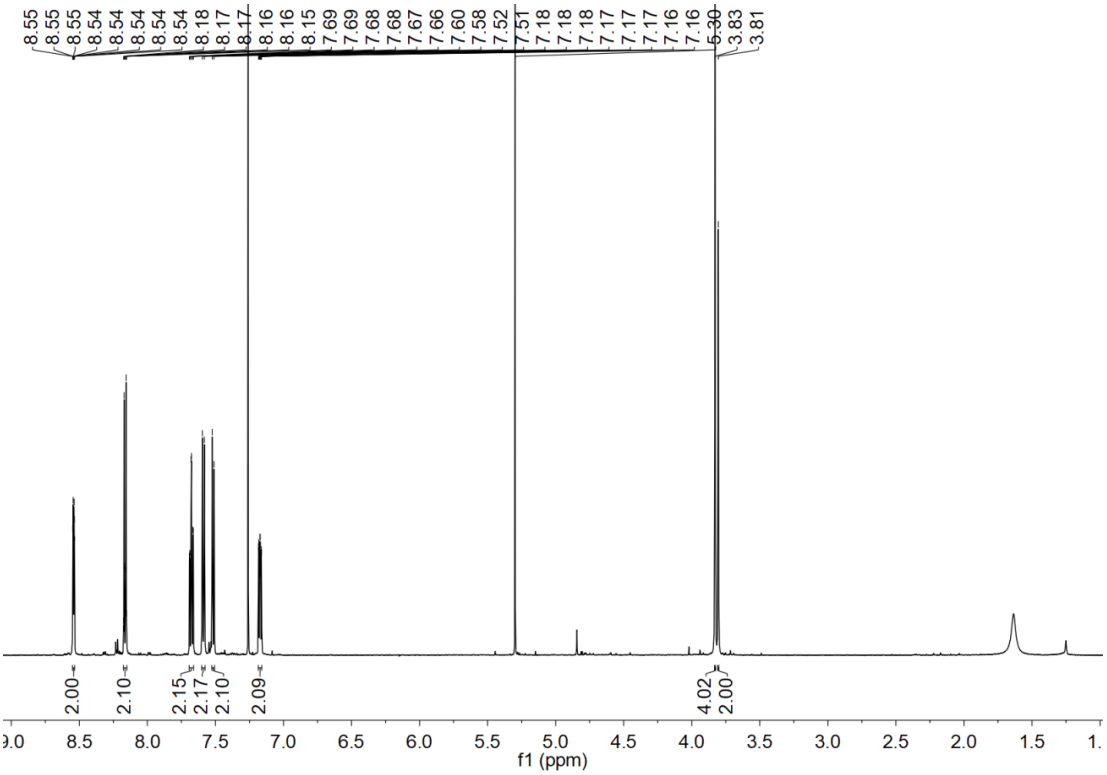

Figure C-31. [1]H-NMR spectrum of *N*-4-nitrobenzyl-*N*-*di*-(2-picolyl)amine (**1c**).

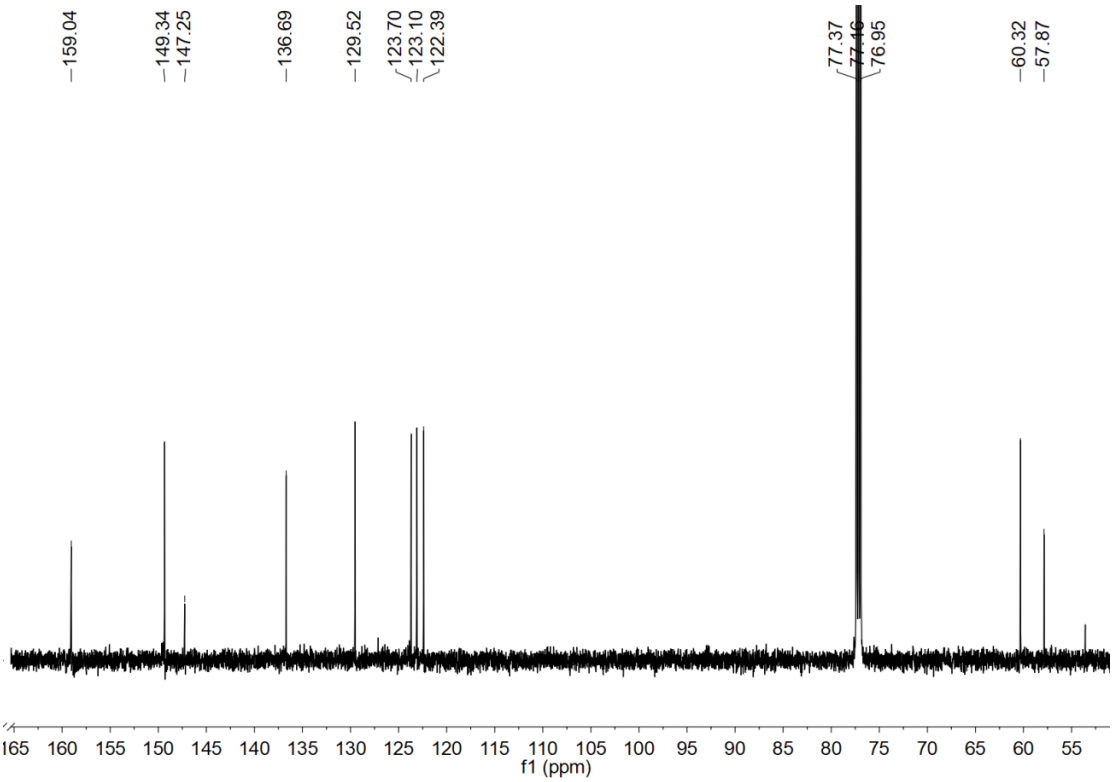

Figure C-32. [13]C-NMR spectrum of *N*-4-nitrobenzyl-*N*-*di*-(2-picolyl)amine (**1c**).

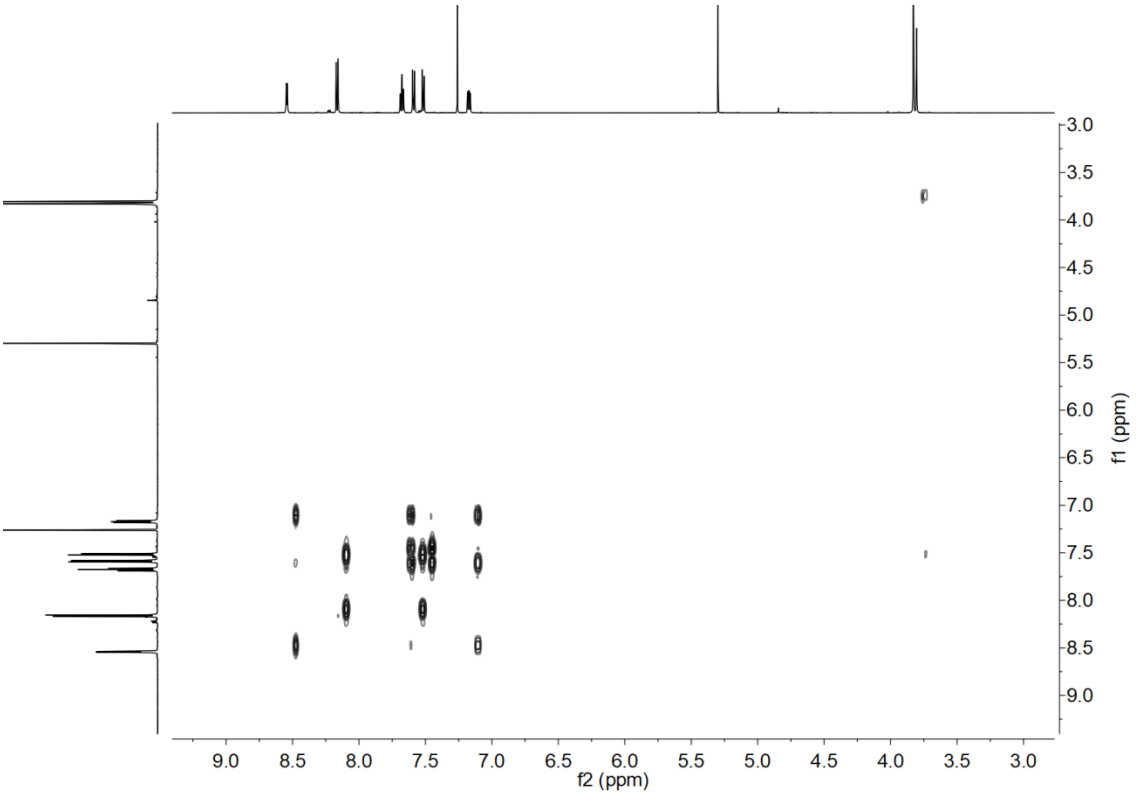

Figure C-33. ^{1}H-^{1}H COSY spectrum of *N*-4-nitrobenzyl-*N*-*di*-(2-picolyl)amine (**1c**).

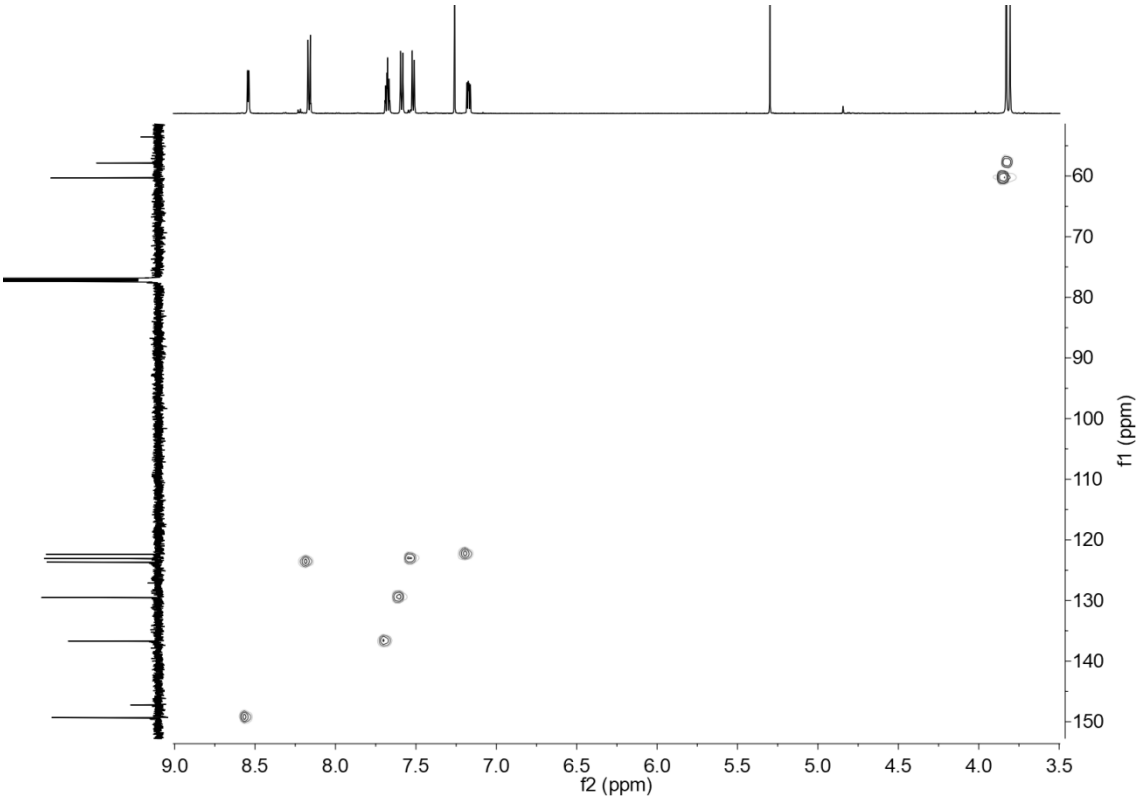

Figure C-34. ^{1}H-^{13}C HSQC spectrum of *N*-4-nitrobenzyl-*N*-*di*-(2-picolyl)amine (**1c**).

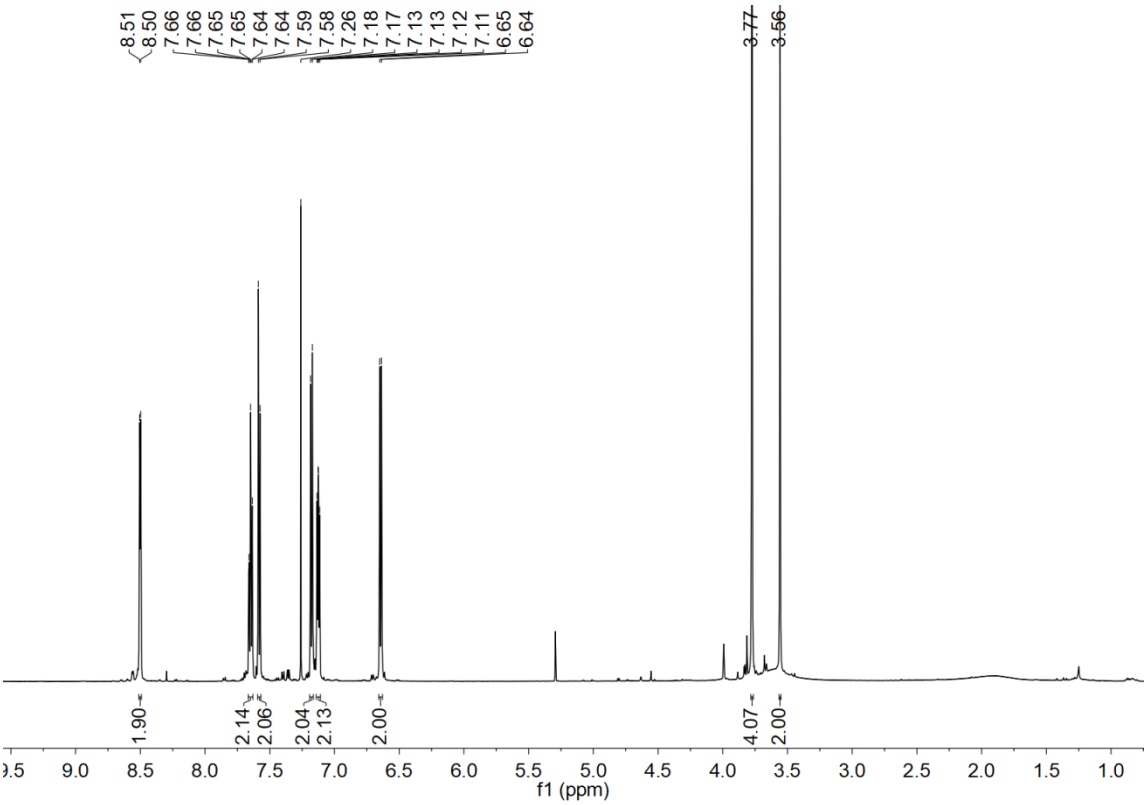

Figure C-35. [1]H-NMR spectrum of *N*-4-amminobenzyl-*N*-*di*-(2-picolyl)amine (**2c**).

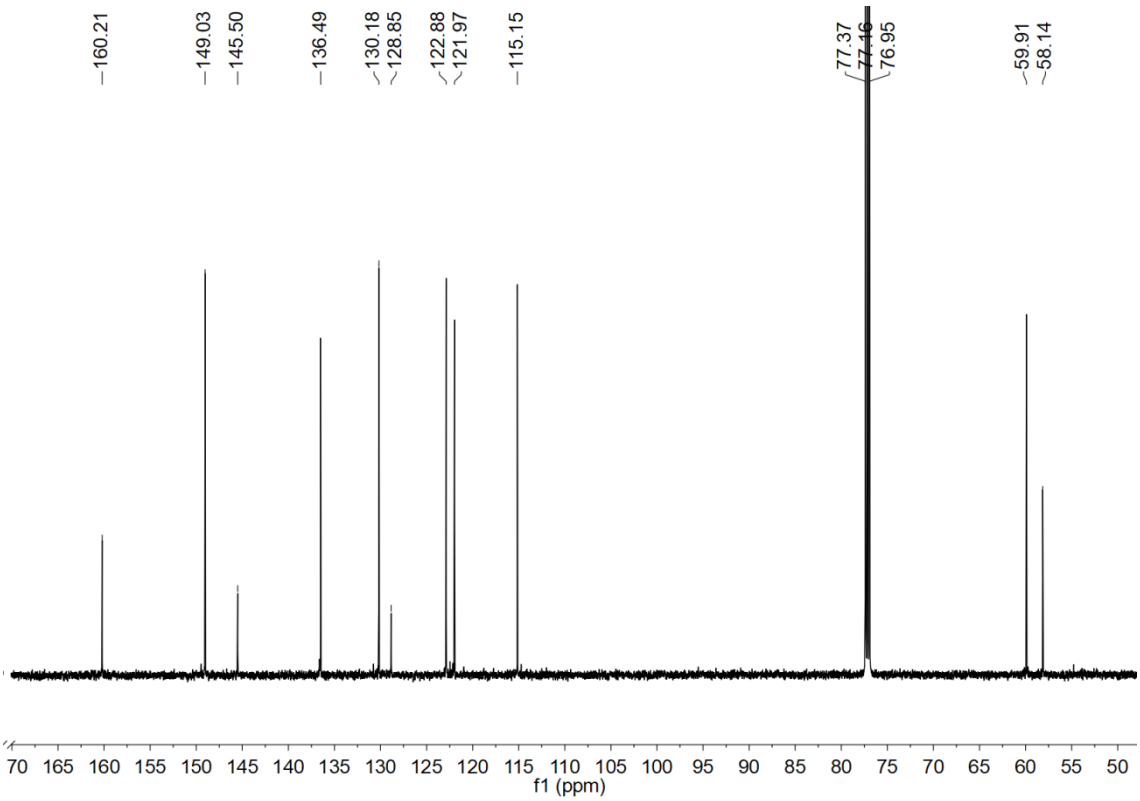

Figure C-36. [13]C-NMR spectrum of *N*-4-amminobenzyl-*N*-*di*-(2-picolyl)amine (2c).

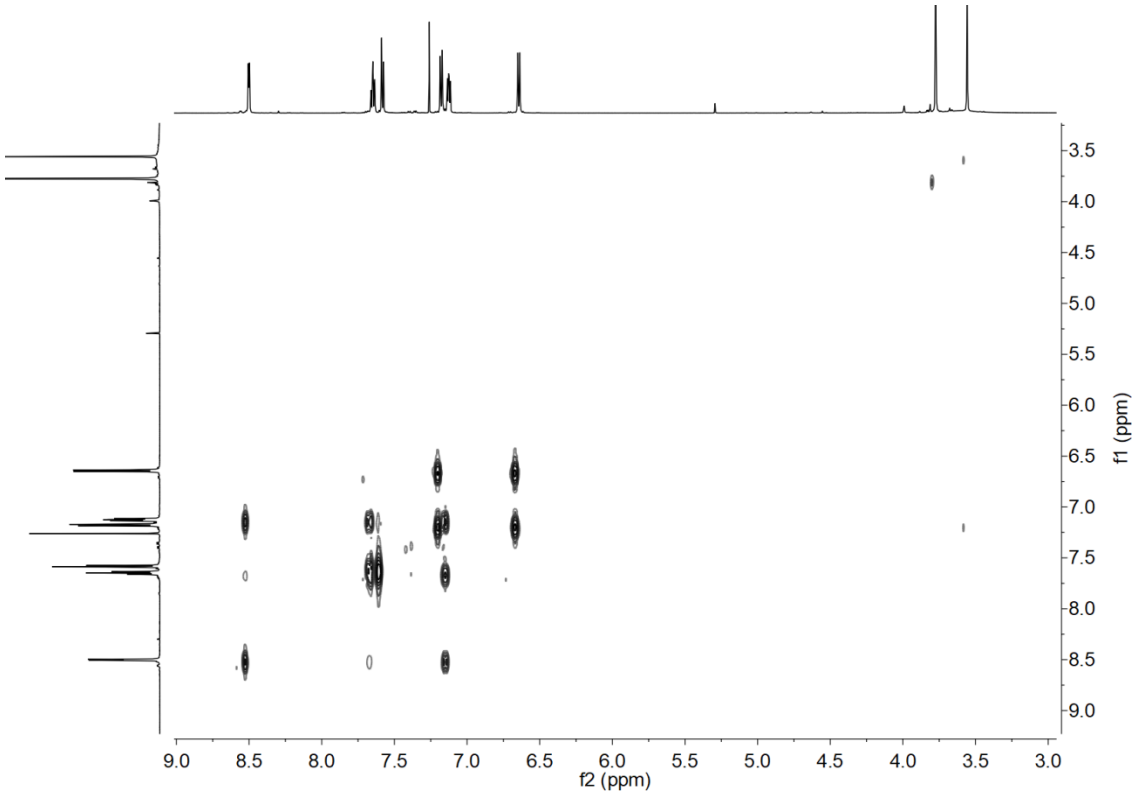

Figure C-37. ^{1}H-^{1}H COSY spectrum of *N*-4-amminobenzyl-*N*-*di*-(2-picolyl)amine (**2c**).

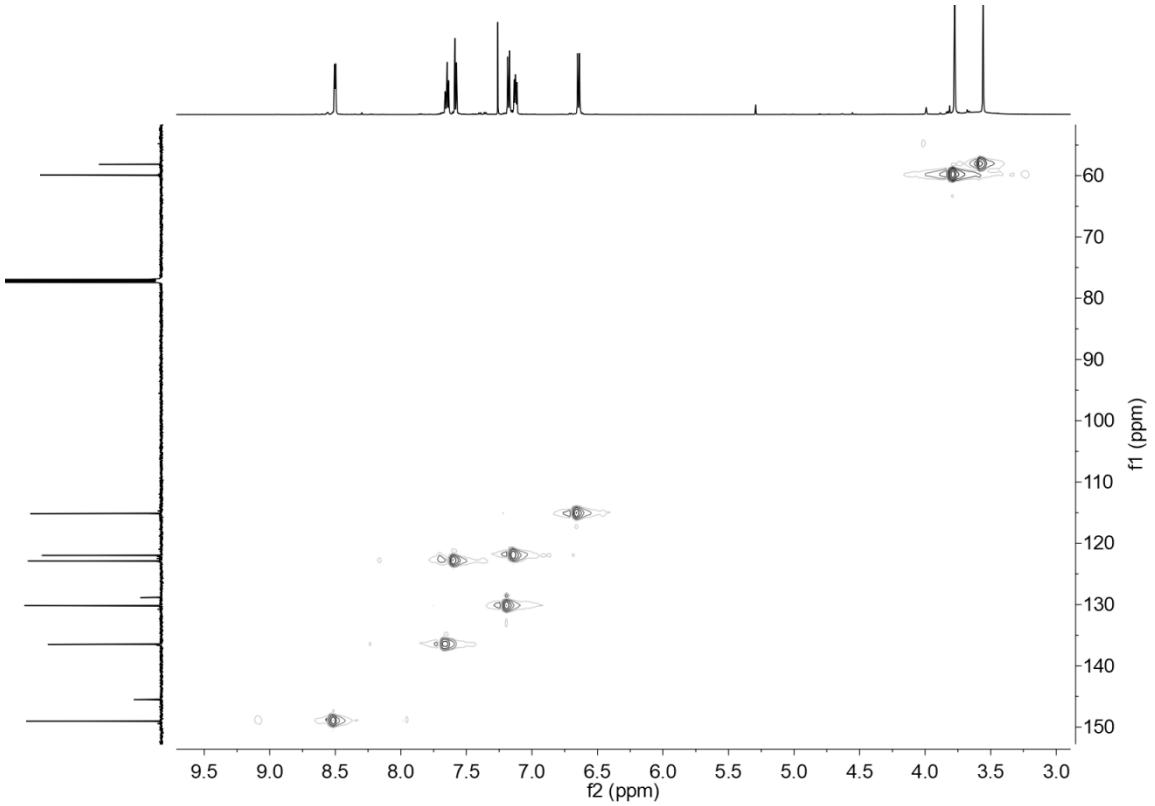

Figure C-38. ^{1}H-^{13}C HSQC spectrum of *N*-4-amminobenzyl-*N*-*di*-(2-picolyl)amine (**2c**).

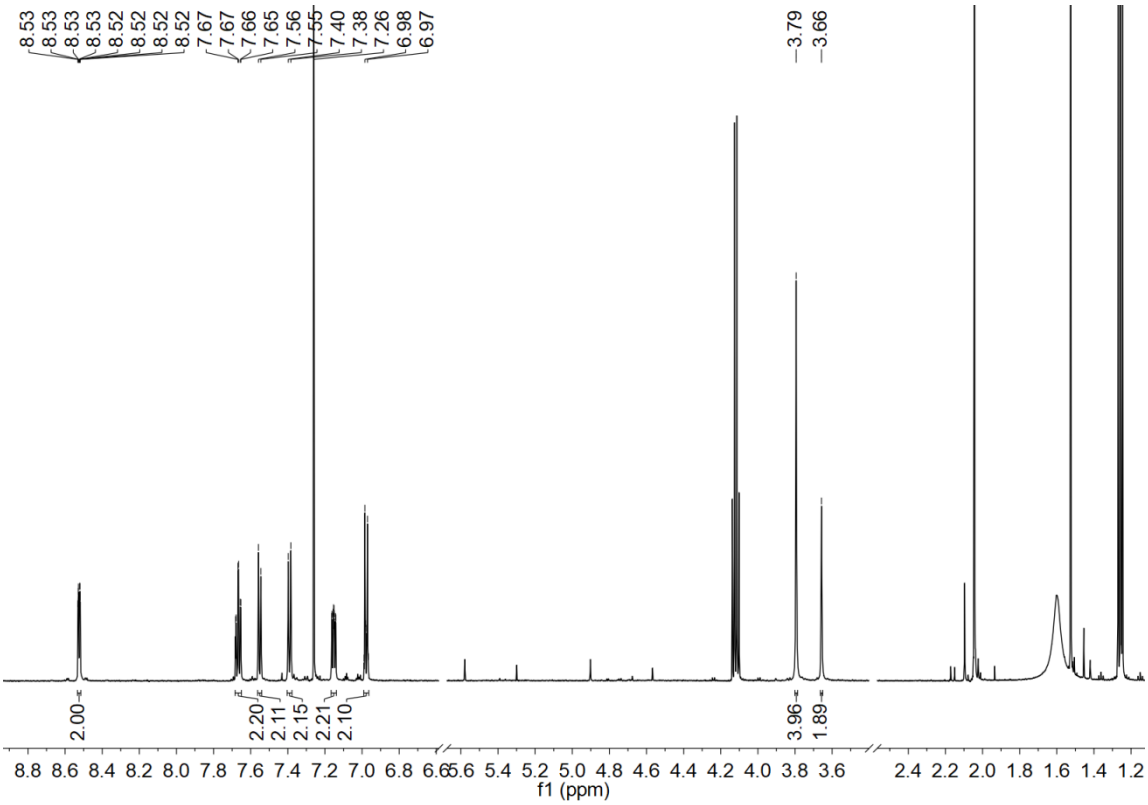

Figure C-39. [1]H-NMR spectrum of *N*-4-azidobenzyl-*N*-*di*-(2-picolyl)amine (**3c**).

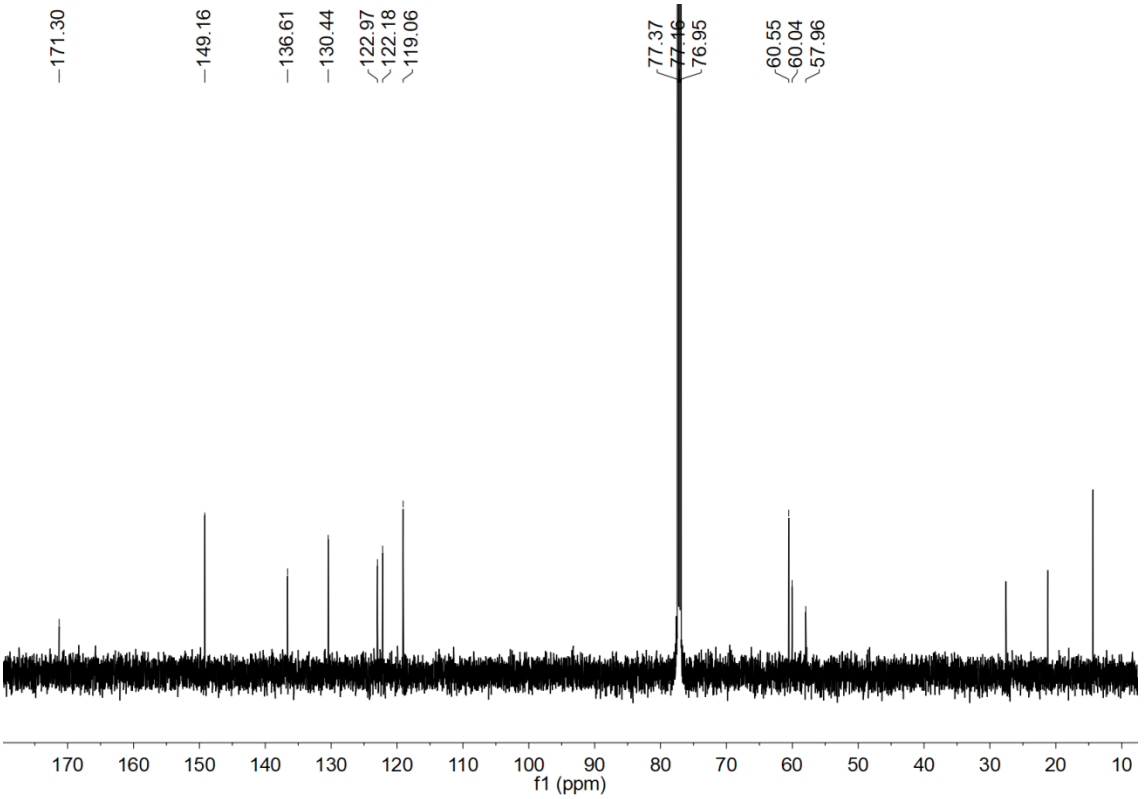

Figure C-40. [13]C-NMR spectrum of *N*-4-azidobenzyl-*N*-*di*-(2-picolyl)amine (**3c**).

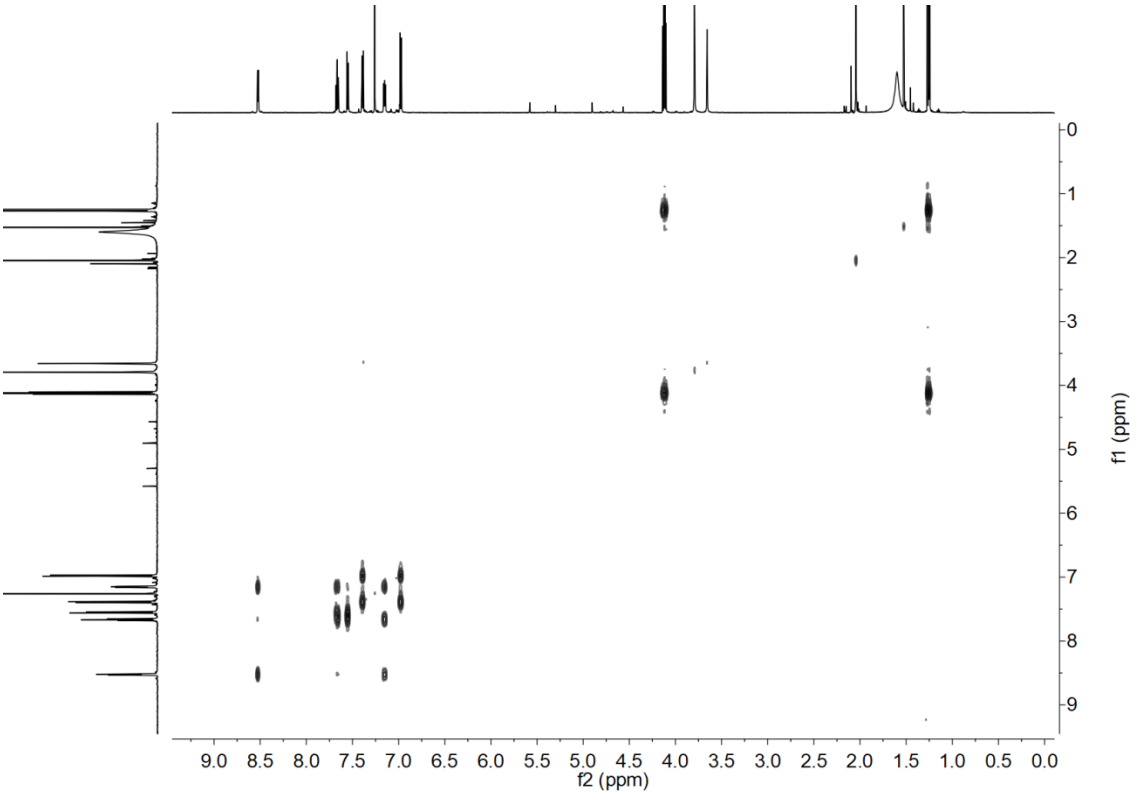

Figure C-41. ^{1}H-^{1}H COSY spectrum of *N*-4-azidobenzyl-*N*-*di*-(2-picolyl)amine (**3c**).

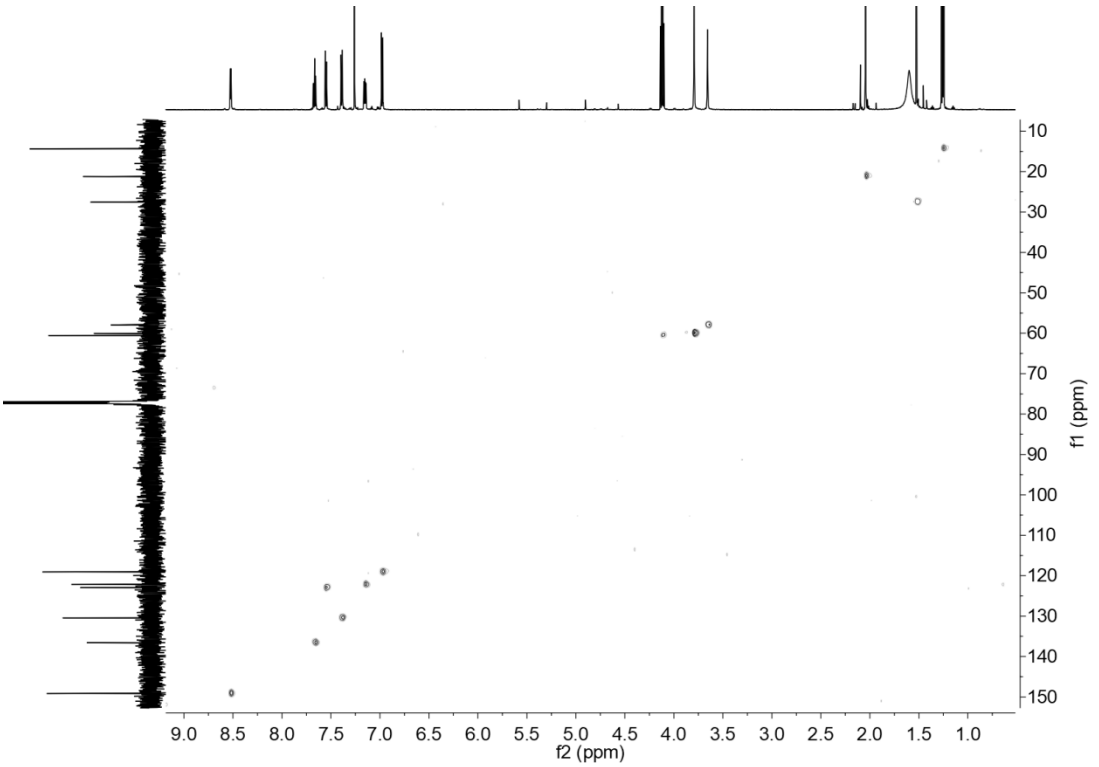

Figure C-42. ^{1}H-^{13}C HSQC spectrum of *N*-4-azidobenzyl-*N*-*di*-(2-picolyl)amine (**3c**).

C-2 X-RAY CRYSTALLOGRAPHY

[Cu(6N$_3$-TPMA)(Phen)](NO$_3$)$_2$

[Cu(Phen)(NO$_3$)](NO$_3$) was prepared according to the procedure reported by Molphy et al.[1] A solution of 6N$_3$-TPMA (0.016g, 0.05 mmol) in EtOH (5 mL) was added dropwise at room temperature to [Cu(Phen)(NO$_3$)](NO$_3$) (0.017g, 0.05mmol) also dissolved in EtOH (5 mL). The mixture was heated at 50 °C for 30 minutes. The volume of the solvent was reduced in vacuo and the product precipitated as a blue powder upon addition of diethyl ether (0.016 g, yield = 47.9%). The powder was dried and crystallized by slow diffusion of Et$_2$O into CH$_3$CN.

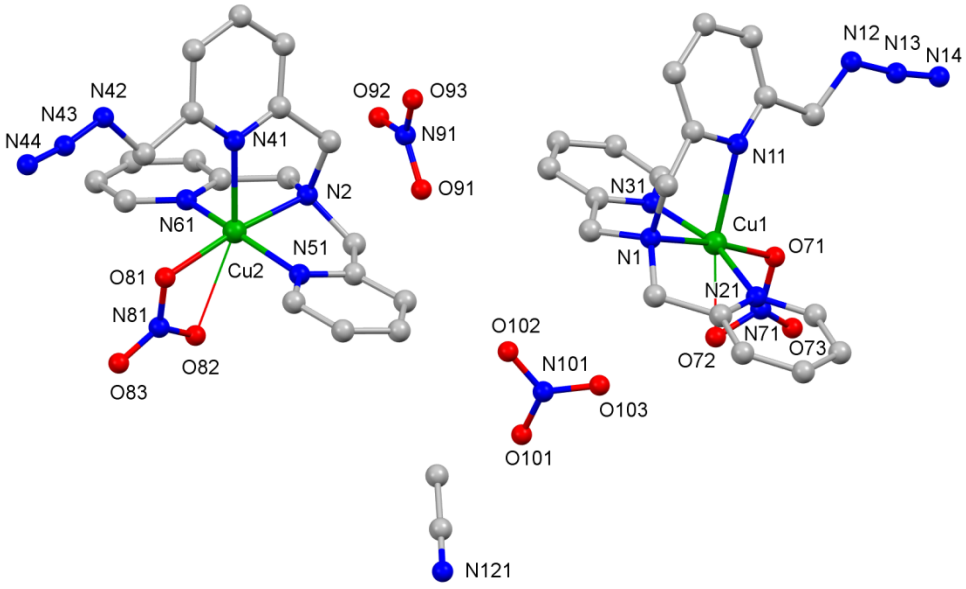

Figure C-43. Asymmetric unit of [Cu(6N$_3$-TPMA)(NO$_3$)](NO$_3$)·½CH$_3$CN

The asymmetric unit (Figure C-43) contains two independent [Cu(6N$_3$-TPMA)(NO$_3$)]$^+$ cations, two uncoordinated nitrate anions, and one molecule of acetonitrile solvent. The copper ions are quite similar (Figure C-44) and are probably best described as approximately square pyramidal with long apical bonds to the pyridines carrying the azide groups (2.3327(16) and 2.2409(12) Å at Cu1 and Cu2, respectively). The remaining donors, an amine, two pyridyl donors and the coordinated nitrite anion make up the basal plane. There is an additional very long bond to a second oxygen donor of the coordinated nitrates (2.5998(15) and 2.5765 (15) Å at Cu1 and Cu2, respectively) which could be considered a (very) asymmetric bidentate ligand (see Table C-2).

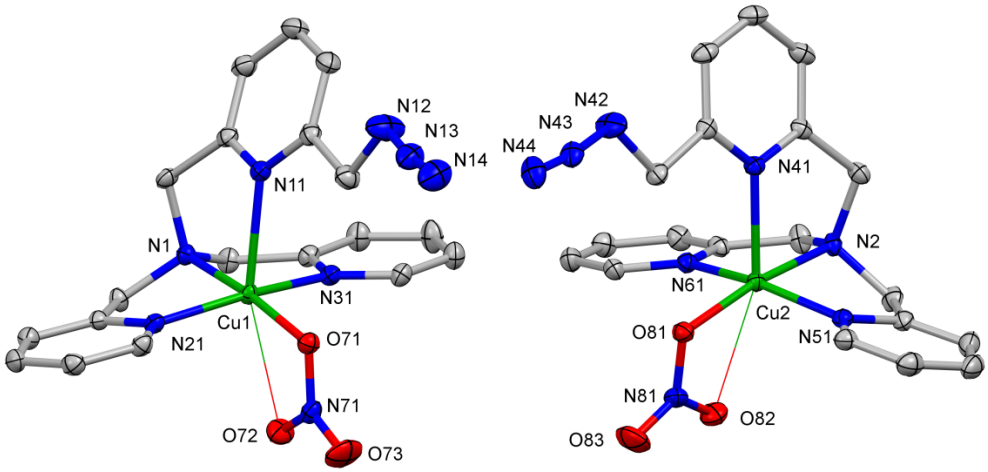

Figure C-44. The structures of the cations, shown with 50% probability ellipsoids. H atoms are omitted and the long axial bond is shown as a thin line.

The coordination geometry of the $6N_3$-TPMA ligand is similar to that observed for the unsubstituted analog.[2] Comparison with the structure of $[Cu(TPMA)(phen)]^{2+}$ (Figure C-45) suggests the methylene carbon on $6N_3$-TPMA prevents coordination of a phenanthrene ligand (or, at least, that the apical pyridine and the phen cannot both bind) due to interaction of the methylene hydrogen atoms with those of the phenanthrene.

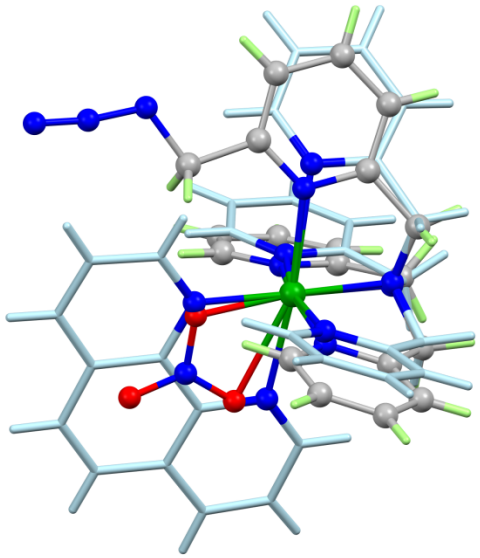

Figure C-45. Overlay of $[Cu(6N_3\text{-TPMA})(NO_3)]^+$ and $[Cu(TPMA)(phen)]^{2+}$ (pale blue).

There is some face-to-face stacking linking the cations and possibly also between the azide group in the cation based on Cu2 with a pyridine of a symmetry-related cation (Figure C-46). There are some weak C-H···O bonds linking the uncoordinated nitrate anions into the structure but these do not appear to be particularly significant.

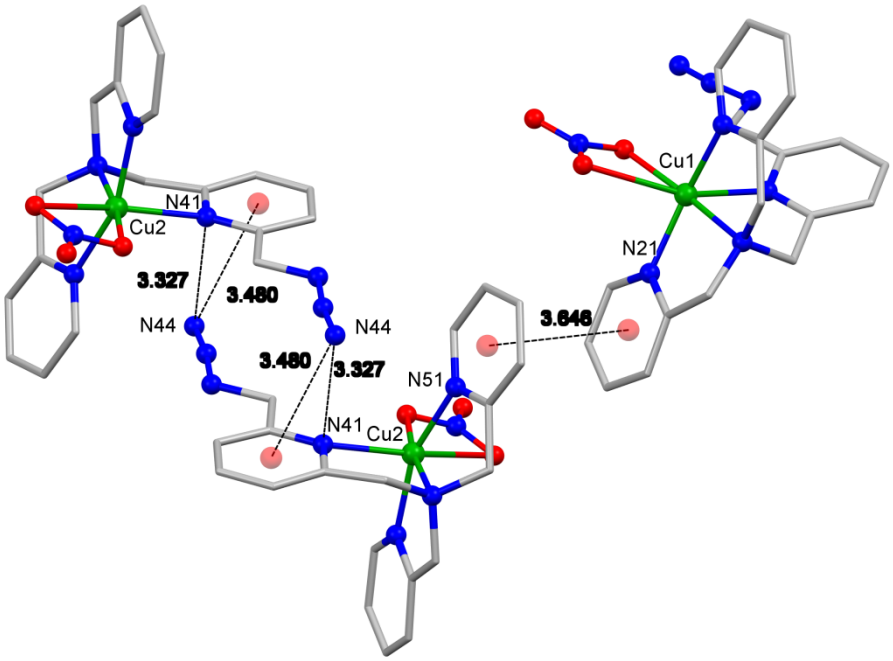

Figure C-46. Interactions between cations. Distances in Å. Red spheres indicate ring centroids.

Experimental

The data were collected at 100(2)K on a Synergy, Dualflex, AtlasS2 diffractometer using CuKα radiation (λ = 1.54184 Å) and the *CrysAlis PRO* 1.171.38.43 suite[3]. Using ShelXle[4] the structure was solved by dual space methods (SHELXT[5]) and refined on F^2 using all the reflections (SHELXL-2018[6]). All the non-hydrogen atoms were refined using anisotropic atomic displacement parameters and hydrogen atoms were inserted at calculated positions using a riding model. There is a little disorder near each non-coordinated nitrate anion this has not been modelled and is responsible for two residual peaks > 1 eÅ[5]. Parameters for data collection and refinement are summarised in Table C-1. CCDC 1939154 contains the supplementary crystallographic data for this paper. These data can be obtained free of charge from The Cambridge Crystallographic Data Centre via www.ccdc.cam.ac.uk/data_request/cif.

Table C-1. Crystal data for $[Cu(6N_3\text{-TPMA})(NO_3)](NO_3)\cdot\frac{1}{2}CH_3CN$

$C_{19}H_{19}CuN_8O_3\cdot NO_3\cdot 0.5(C_2H_3N)$	$Z = 4$
$M_r = 553.50$	$F(000) = 1136$
Triclinic, $P\bar{1}$	$D_x = 1.586$ Mg m^{-3}
$a = 10.6029$ (2) Å	Cu $K\alpha$ radiation, $\lambda = 1.54184$ Å
$b = 14.9442$ (4) Å	Cell parameters from 11083 reflections
$c = 15.8857$ (4) Å	$\theta = 4.2$–$76.7°$
$\alpha = 68.947$ (2)°	$\mu = 1.86$ mm^{-1}
$\beta = 82.439$ (2)°	$T = 100$ K
$\gamma = 82.246$ (2)°	Block, dark blue
$V = 2318.19$ (11) Å^3	0.13 × 0.10 × 0.03 mm

Data collection

XtaLAB Synergy, Dualflex, AtlasS2 diffractometer	9502 independent reflections
Radiation source: micro-focus sealed X-ray tube, PhotonJet (Cu) X-ray Source	8432 reflections with $I > 2\sigma(I)$
Mirror monochromator	$R_{int} = 0.027$
Detector resolution: 5.2923 pixels mm^{-1}	$\theta_{max} = 76.7°$, $\theta_{min} = 4.2°$
ω scans	$h = -13\rightarrow12$
Absorption correction: gaussian *CrysAlis PRO* 1.171.40.29a (Rigaku Oxford Diffraction, 2018) Numerical absorption correction based on gaussian integration over a multifaceted crystal model Empirical absorption correction using spherical harmonics, implemented in SCALE3 ABSPACK scaling algorithm.	$k = -17\rightarrow18$
$T_{min} = 0.937$, $T_{max} = 1.000$	$l = -16\rightarrow19$
21435 measured reflections	

Refinement

Refinement on F^2	Primary atom site location: dual
Least-squares matrix: full	Hydrogen site location: inferred from neighbouring sites
$R[F^2 > 2\sigma(F^2)] = 0.035$	H-atom parameters constrained
$wR(F^2) = 0.091$	$w = 1/[\sigma^2(F_o^2) + (0.0403P)^2 + 1.8547P]$ where $P = (F_o^2 + 2F_c^2)/3$
$S = 1.03$	$(\Delta/\sigma)_{max} = 0.001$
9502 reflections	$\Delta>_{max} = 1.19$ e Å^{-3}
659 parameters	$\Delta>_{min} = -0.87$ e Å^{-3}
18 restraints	

Data collection: *CrysAlis PRO* 1.171.40.29a (Rigaku OD, 2018); cell refinement: *CrysAlis PRO* 1.171.40.29a (Rigaku OD, 2018); data reduction: *CrysAlis PRO* 1.171.38.43 (Rigaku OD, 2015); program(s) used to solve structure: SHELXT[5]; program(s) used to refine structure: *SHELXL2018*/3[6] (Sheldrick, 2015a); molecular graphics: *Mercury*[7]; software used to prepare material for publication: Olex2[8], *publCIF*[9].

Table C-2. Geometric parameters (Å, º) for [Cu(6N_3-TPMA)(NO_3)](NO_3)·½CH_3CN.

Cu1—N1	2.0316 (15)	Cu2—O81	2.0008 (13)
Cu1—N11	2.3327 (16)	Cu2—O82	2.5765 (15)
Cu1—N21	1.9713 (16)	N2—C41	1.488 (2)
Cu1—N31	1.9851 (16)	N2—C51	1.491 (2)
Cu1—O71	1.9936 (13)	N2—C61	1.492 (2)
Cu1—O72	2.5998 (15)	N41—C42	1.343 (2)
N1—C11	1.487 (2)	N41—C46	1.349 (2)
N1—C21	1.489 (2)	N42—N43	1.238 (3)
N1—C31	1.485 (2)	N42—C47	1.472 (2)
N11—C12	1.351 (2)	N43—N44	1.127 (3)
N11—C16	1.342 (2)	N51—C52	1.350 (2)
N12—N13	1.238 (3)	N51—C56	1.341 (3)
N12—C17	1.463 (3)	N61—C62	1.340 (2)
N13—N14	1.129 (3)	N61—C67	1.347 (2)
N21—C22	1.349 (2)	C41—C42	1.507 (3)
N21—C26	1.348 (2)	C42—C43	1.391 (3)
N31—C32	1.349 (2)	C43—C44	1.384 (3)
N31—C36	1.341 (2)	C44—C45	1.388 (3)
C11—C12	1.509 (3)	C45—C46	1.389 (3)
C12—C13	1.386 (3)	C46—C47	1.508 (3)
C13—C14	1.384 (3)	C51—C52	1.508 (3)
C14—C15	1.380 (3)	C52—C53	1.386 (3)
C15—C16	1.389 (3)	C53—C54	1.392 (3)
C16—C17	1.509 (3)	C54—C55	1.384 (3)
C21—C22	1.507 (3)	C55—C56	1.385 (3)
C22—C23	1.384 (3)	C61—C62	1.507 (3)
C23—C24	1.390 (3)	C62—C63	1.384 (3)
C24—C25	1.389 (3)	C63—C64	1.386 (3)
C25—C26	1.376 (3)	C64—C65	1.390 (3)
C31—C32	1.507 (3)	C65—C67	1.382 (3)
C32—C33	1.381 (3)	N81—O81	1.302 (2)

C33—C34	1.386 (3)	N81—O82	1.245 (2)
C34—C35	1.389 (3)	N81—O83	1.219 (2)
C35—C36	1.381 (3)	O91—N91	1.253 (3)
N71—O71	1.304 (2)	O92—N91	1.236 (3)
N71—O72	1.245 (2)	O93—N91	1.233 (2)
N71—O73	1.220 (2)	O101—N101	1.243 (2)
Cu2—N2	2.0377 (15)	O102—N101	1.240 (3)
Cu2—N41	2.2409 (15)	O103—N101	1.247 (2)
Cu2—N51	1.9837 (16)	N121—C122	1.141 (3)
Cu2—N61	1.9876 (16)	C122—C123	1.455 (3)
N1—Cu1—N11	83.15 (6)	N51—Cu2—N41	100.78 (6)
N1—Cu1—O72	118.84 (5)	N51—Cu2—N61	160.00 (6)
N11—Cu1—O72	157.00 (5)	N51—Cu2—O81	95.56 (6)
N21—Cu1—N1	83.17 (6)	N51—Cu2—O82	88.86 (6)
N21—Cu1—N11	105.04 (6)	N61—Cu2—N2	84.62 (6)
N21—Cu1—N31	162.84 (7)	N61—Cu2—N41	92.89 (6)
N21—Cu1—O71	95.18 (6)	N61—Cu2—O81	94.91 (6)
N21—Cu1—O72	85.51 (6)	N61—Cu2—O82	83.21 (6)
N31—Cu1—N1	84.16 (6)	O81—Cu2—N2	171.80 (6)
N31—Cu1—N11	84.85 (6)	O81—Cu2—N41	105.00 (5)
N31—Cu1—O71	96.16 (6)	O81—Cu2—O82	55.14 (5)
N31—Cu1—O72	90.52 (6)	C41—N2—Cu2	107.90 (10)
O71—Cu1—N1	173.70 (6)	C41—N2—C51	109.93 (14)
O71—Cu1—N11	103.15 (5)	C41—N2—C61	112.08 (15)
O71—Cu1—O72	54.90 (5)	C51—N2—Cu2	104.69 (11)
C11—N1—Cu1	107.61 (11)	C51—N2—C61	112.56 (14)
C11—N1—C21	109.74 (14)	C61—N2—Cu2	109.32 (11)
C21—N1—Cu1	106.49 (11)	C42—N41—Cu2	107.20 (11)
C31—N1—Cu1	107.78 (11)	C42—N41—C46	119.01 (16)
C31—N1—C11	112.47 (14)	C46—N41—Cu2	131.79 (13)
C31—N1—C21	112.43 (14)	N43—N42—C47	116.43 (18)
C12—N11—Cu1	103.44 (12)	N44—N43—N42	171.5 (2)
C16—N11—Cu1	132.49 (12)	C52—N51—Cu2	113.44 (13)
C16—N11—C12	118.12 (16)	C56—N51—Cu2	126.97 (13)
N13—N12—C17	115.03 (19)	C56—N51—C52	119.58 (17)
N14—N13—N12	172.6 (2)	C62—N61—Cu2	114.20 (12)
C22—N21—Cu1	114.20 (12)	C62—N61—C67	119.05 (16)
C26—N21—Cu1	126.46 (13)	C67—N61—Cu2	126.60 (13)
C26—N21—C22	119.34 (16)	N2—C41—C42	113.82 (15)

C32—N31—Cu1	113.98 (12)	N41—C42—C41	116.82 (16)
C36—N31—Cu1	126.23 (13)	N41—C42—C43	122.39 (17)
C36—N31—C32	119.58 (16)	C43—C42—C41	120.56 (17)
N1—C11—C12	113.97 (14)	C44—C43—C42	118.31 (18)
N11—C12—C11	116.29 (16)	C43—C44—C45	119.72 (18)
N11—C12—C13	122.51 (18)	C44—C45—C46	118.75 (18)
C13—C12—C11	121.09 (17)	N41—C46—C45	121.81 (17)
C14—C13—C12	118.56 (18)	N41—C46—C47	115.12 (16)
C15—C14—C13	119.48 (19)	C45—C46—C47	123.06 (17)
C14—C15—C16	118.70 (19)	N42—C47—C46	108.28 (16)
N11—C16—C15	122.55 (18)	N2—C51—C52	108.59 (14)
N11—C16—C17	114.98 (16)	N51—C52—C51	114.96 (16)
C15—C16—C17	122.46 (18)	N51—C52—C53	121.50 (19)
N12—C17—C16	109.85 (17)	C53—C52—C51	123.49 (18)
N1—C21—C22	109.33 (14)	C52—C53—C54	118.81 (19)
N21—C22—C21	115.40 (16)	C55—C54—C53	119.29 (19)
N21—C22—C23	121.62 (17)	C54—C55—C56	119.0 (2)
C23—C22—C21	122.89 (16)	N51—C56—C55	121.82 (18)
C22—C23—C24	118.83 (17)	N2—C61—C62	112.55 (15)
C25—C24—C23	119.34 (18)	N61—C62—C61	117.66 (16)
C26—C25—C24	118.89 (18)	N61—C62—C63	122.01 (17)
N21—C26—C25	121.99 (17)	C63—C62—C61	120.33 (17)
N1—C31—C32	110.99 (15)	C62—C63—C64	119.05 (18)
N31—C32—C31	115.98 (16)	C63—C64—C65	118.95 (18)
N31—C32—C33	121.39 (17)	C67—C65—C64	118.81 (18)
C33—C32—C31	122.56 (17)	N61—C67—C65	122.07 (17)
C32—C33—C34	118.83 (18)	O82—N81—O81	117.63 (16)
C33—C34—C35	119.86 (19)	O83—N81—O81	119.27 (17)
C36—C35—C34	118.08 (18)	O83—N81—O82	123.10 (18)
N31—C36—C35	122.25 (17)	N81—O81—Cu2	106.38 (10)
O72—N71—O71	117.99 (15)	N81—O82—Cu2	80.84 (10)
O73—N71—O71	118.80 (17)	O92—N91—O91	121.5 (2)
O73—N71—O72	123.21 (18)	O93—N91—O91	118.8 (2)
N71—O71—Cu1	107.00 (10)	O93—N91—O92	119.4 (2)
N71—O72—Cu1	80.10 (10)	O101—N101—O103	121.35 (17)
N2—Cu2—N41	83.20 (6)	O102—N101—O101	118.45 (19)
N2—Cu2—O82	116.73 (5)	O102—N101—O103	119.84 (19)
N41—Cu2—O82	159.04 (5)	N121—C122—C123	178.7 (3)
N51—Cu2—N2	82.60 (6)		

C-3 Mass Spectrometry Data for the Oligonucleotides

Table C-3. Oligonucleotide sequences, modifications and dC content. Calculated and found m/z; (a) = + 63 m/z caused by the ligand scavenging Cu(II) from the UPLC column in the analysis; (b) = co-eluting starting material. **TGT** = target polypurine strand; **CMP** = complementary polypyrimidine strand; **5′-dC^{H}** = 5′-hexynyl-deoxycytidine; **5′-dC^{O}** = 5′-octadiynyl-deoxycytidine; **int-dU^{O}** = internal-octadiynyl-deoxyuridine; **5′-dT^{H}** = 5′-hexynyl-deoxythymidine; **5′-dC^{BCN}** = 5′-BCN(CEP II)-deoxycytidine**;** **pdU** = 5-(1-propargylamino)-deoxyuridine; **pdU-TO** = pdU with thiazole orange attached; **6N$_3$-TPMA** = *N*-6-(azidomethyl)pyridine-*N*-*di*-(2-picolyl)amine; **5N$_3$-TPMA** = *N*-5-(azidomethyl)pyridine-*N*-*di*-(2-picolyl)amine; **4N$_3$-DPA** = *N*-4-azidobenzyl-*N*-*di*-(2-picolyl)amine.

Oligo name	Sequence	Modification (X)(Y)	dC content (%)	Calcd. Mass	Found Mass
TFO1A	**5′ – X**CC GTT TCC TCT TCT T **– 3′**	5′-dC^{H}	43.8	4884	4884.8
TFO1AI	**5′ – X**CC GTT TCC TCT TCT T **– 3′**	5′-dC^{H}-6N$_3$-TPMA	43.8	5229.4	5291.8[b]
TFO1AII	**5′ – X**CC GTT TCC TCT TCT T **– 3′**	5′-dC^{H}-5N$_3$-TPMA	43.8	5229.4	5291.9[a]
TFO1AIII	**5′ – X**CC GTT TCC TCT TCT T **– 3′**	5′-dC^{H}-4N$_3$-DPA	43.8	5214.4	5341.8[a]
TFO1B	**5′ – X**CC GTT TCC TCT TCT T **– 3′**	5′-dC^{O}	43.8	4829	4828.8
TFO1BI	**5′ – X**CC GTT TCC TCT TCT T **– 3′**	5′-dC^{O}-6N$_3$-TPMA	43.8	5174.4	5236.0[a,b]
TFO1BIII	**5′ – X**CC GTT TCC TCT TCT T **– 3′**	5′-dC^{O}-4N$_3$-DPA	43.8	5159.4	5159.0
TFO1C	**5′ –** CCC GTT TCC **X**CT TCT T **– 3′**	int-dU^{O}	43.8	4815	4814.8
TFO1CI	**5′ –** CCC GTT TCC **X**CT TCT T **– 3′**	int-dU^{O}-6N$_3$-TPMA	43.8	5412.4	5413.2
TFO1CII	**5′ –** CCC GTT TCC **X**CT TCT T **– 3′**	int-dU^{O}-5N$_3$-TPMA	43.8	5412.4	5475.1
TFO1CIII	**5′ –** CCC GTT TCC **X**CT TCT T **– 3′**	int-dU^{O}-4N$_3$-DPA	43.8	5397.4	5398.4
TFO1D	**5′ – X**CC GTT TCC TCT TCT T **– 3′**	5′-dC^{BCN}	43.8	5067	5067.8
TFO1DI	**5′ – X**CC GTT TCC TCT TCT T **– 3′**	5′-dC^{BCN}-6N$_3$-TPMA	43.8	5412.6	5413.2, 5475.2[a]
TFO1DII	**5′ – X**CC GTT TCC TCT TCT T **– 3′**	5′-dC^{BCN}-5N$_3$-TPMA	43.8	5412.6	5475.1[a]
TFO1DIII	**5′ – X**CC GTT TCC TCT TCT T **– 3′**	5′-dC^{BCN}-4N$_3$-DPA	43.8	5397.4	5398.4
TGT1	**5′ –** TCG CCA CCA TGG GTA AAG GAG AAG AAC TTT TCA CTG **– 3′**	-	22.2	11093	11093.1
CMP1	**5′ –** CAG TGA AAA GTT CTT CTC CTT TAC CCA TGG TGG CGA **– 3′**	-	25	11026	11026.0

TFO2A	**5′ – X**CT CTC CCG CTT CCG CT **– 3′**	5′-dC^{H}	58.8	5168	5169.1
TFO2AI	**5′ – X**CT CTC CCG CTT CCG CT **– 3′**	5′-dC^{H}-6N$_3$-TPMA	58.8	5513.4	5576.0[a]
TFO2AII	**5′ – X**CT CTC CCG CTT CCG CT **– 3′**	5′-dC^{H}-5N$_3$-TPMA	58.8	5513.4	5575.9[a]
TFO2AIII	**5′ – X**CT CTC CCG CTT CCG CT **– 3′**	5′-dC^{H}-4N$_3$-DPA	58.8	5498.4	5561.0[a]
TGT2	**5′ –** TTC TGT CAG TGG AGA GGG TGA AGG TGA TGC AAC ATA C **– 3′**	-	13.5	11533	11533.2
CMP2	**5′ –** GTA TGT TGC ATC ACC TTC ACC CTC TCC ACT GAC AGA A **– 3′**	-	35.1	11204	11204.1
TFO3A	**5′ – X**CTC TTT CCT TCC CTT CTT TC **– 3′**	5′-dC^{H}	45.0	6046	6046.3
TFO3AI	**5′ – X**TC TTT CCT TCC CTT CTT TC **– 3′**	5′-dC^{H}-6N$_3$-TPMA	45.0	6391.4	6453.0[a]
TFO3AII	**5′ – X**TC TTT CCT TCC CTT CTT TC **– 3′**	5′-dC^{H}-5N$_3$-TPMA	45.0	6391.4	6453.0[a]
TFO3AIII	**5′ – X**TC TTT CCT TCC CTT CTT TC **– 3′**	5′-dC^{H}-4N$_3$-DPA	45.0	6376.4	6376.1
TFO4A	**5′ – X**CCG CTC TTT CCT TCC CTT CTT TCG CTT TCC TC **– 3′**	5′-dC^{H}	46.9	9656	9656.9
TFO4AI	**5′ – X**CG CTC TTT CCT TCC CTT CTT TCG CTT TCC TC **– 3′**	5′-dC^{H}-6N$_3$-TPMA	46.9	10001.4	10063.7[a]
TFO4AII	**5′ – X**CG CTC TTT CCT TCC CTT CTT TCG CTT TCC TC **– 3′**	5′-dC^{H}-5N$_3$-TPMA	46.9	10001.4	10006.9, 10062.8[a]
TFO4B	**5′ – X**CG CTC TTT CCT TCC CTT CTT TCG CTT TCC TC **– 3′**	5′-dC^{O}	46.9	9601	9600.6
TFO4BI	**5′ – X**CG CTC TTT CCT TCC CTT CTT TCG CTT TCC TC **– 3′**	5′-dC^{O}-6N$_3$-TPMA	46.9	9946.4	10007.0[a]
TFO4BII	**5′ – X**CG CTC TTT CCT TCC CTT CTT TCG CTT TCC TC **– 3′**	5′-dC^{O}-5N$_3$-TPMA	46.9	9946.4	-

TFO4BIII	**5′ – X**CG CTC TTT CCT TCC CTT CTT TCG CTT TCC TC **– 3′**	5′-dC^{O}-4N$_3$-DPA	46.9	9931.4	9993.5[a]
TFO4C	**5′ –** CGC TCT TTC CTT CCC **X**TC TTT CGC TTT CCT C **– 3′**	int-dU^{O}	45.2	9298	9297.7
TFO4CI	**5′ –** CGC TCT TTC CTT CCC **X**TC TTT CGC TTT CCT C **– 3′**	int-dU^{O}-6N$_3$-TPMA	45.2	9643.4	9704.8[a,b]
TFO4CII	**5′ –** CGC TCT TTC CTT CCC **X**TC TTT CGC TTT CCT C **– 3′**	int-dU^{O}-5N$_3$-TPMA	45.2	9643.4	9705.8[a]
TFO4CIII	**5′ –** CGC TCT TTC CTT CCC **X**TC TTT CGC TTT CCT C **– 3′**	int-dU^{O}-4N$_3$-DPA	45.2	9628.4	9689.8[a]
TFO4D	**5′ – X**CG CTC TTT CCT TCC CTT CTT TCG CTT TCC TC **– 3′**	5′-dC^{BCN}	46.9	9838	-
TFO4DI	**5′ – X**CG CTC TTT CCT TCC CTT CTT TCG CTT TCC TC **– 3′**	5′-dC^{BCN}-6N$_3$-TPMA	46.9	10183.6	-
TFO4DII	**5′ – X**CG CTC TTT CCT TCC CTT CTT TCG CTT TCC TC **– 3′**	5′-dC^{BCN}-5N$_3$-TPMA	46.9	10183.6	-
iTFO4D	**5′ – X** CG CTC TTT CCT TCC C**Y**T CTT TCG CTT TCC TC **– 3′**	5′-dC^{BCN}, pdU	46.9	9879	9879
tTFO4D	**5′ – X** CG CTC TTT CCT TCC CTT CTT TCG CTT **Y**CC TC **– 3′**	5′-dC^{BCN}, pdU	46.9	9879	9880
iTOTFO4D	**5′ – X** CG CTC TTT CCT TCC C**Y**T CTT TCG CTT TCC TC **– 3′**	5′-dC^{BCN}, pdU-TO	46.9	10266	10267, 10328[a]
tTOTFO4D	**5′ – X** CG CTC TTT CCT TCC CTT CTT TCG CTT **Y**CC TC **– 3′**	5′-dC^{BCN}, pdU-TO	46.9	10266	10267, 10328[a]
iTOTFO4D_I	**5′ – X** CG CTC TTT CCT TCC C**Y**T CTT TCG CTT TCC TC **– 3′**	5′-dC^{BCN}-6N$_3$-TPMA, pdU-TO	46.9	10612	10674[a]
iTOTFO4D_II	**5′ – X** CG CTC TTT CCT TCC C**Y**T CTT TCG CTT TCC TC **– 3′**	5′-dC^{BCN}-5N$_3$-TPMA, pdU-TO	46.9	10612	10675[a]

tTOTFO4D_I	5′ – X CG CTC TTT CCT TCC CTT CTT TCG CTT YCC TC – 3′	5′-dC^{BCN}-6N$_3$-TPMA, pdU-TO	46.9	10612	10674[a]
tTOTFO4D_II	5′ – X CG CTC TTT CCT TCC CTT CTT TCG CTT YCC TC – 3′	5′-dC^{BCN}-5N$_3$-TPMA, pdU-TO	46.9	10612	10675[a]
TGT3,4	5′ – CGG CGA ACG TGG CGA GAA AGG AAG GGA AGA AAG CGA AAG GAG CGG GCG CTA G – 3′	-	15.4	16398	16397.7
CMP3,4	5′ – CTA GCG CCC GCT CCT TTC GCT TTC TTC CCT TCC TTT CTC GCC ACG TTC GCC G – 3′	-	46.2	15614	15613.7
TFO5A	5′ – XTCT TCG TCG CTC CTC C – 3′	5′-dT^{H}	50.0	4894	4895.0
TFO5AI	5′ – XCT TCG TCG CTC CTC C – 3′	5′-dT^{H}-6N$_3$-TPMA	50.0	5239.4	5301.8[a]
TFO5AII	5′ – XCT TCG TCG CTC CTC C – 3′	5′-dT^{H}-5N$_3$-TPMA	50.0	5239.4	5301.8[a]
TFO5AIII	5′ – XCT TCG TCG CTC CTC C – 3′	5′-dT^{H}-4N$_3$-DPA	50.0	5224.4	-
TGT5	5′ – GAG CTA TTC CAG AAG TAG TGA GGA GGC TTT TTT GGA – 3′	-	11.1	11210	11210.0
CMP5	5′ – TCC AAA AAA GCC TCC TCA CTA CTT CTG GAA TAG CTC – 3′	-	33.3	10908	10908.1

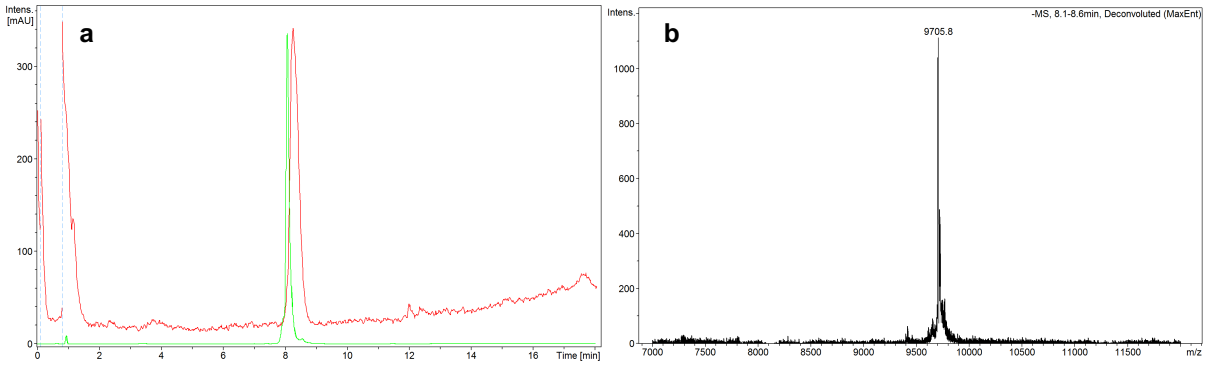

Figure C-47. A UPLC-MS chromatograms of pure TFO4CII. AMN-TFOs were produced in yields according to **Table C-2** and mass was confirmed according to **Table C-3** UPLC x-axis = time (min) and y-axis = UV absorbance at 260nm. **B** Deconvoluted (MaxEnt) mass spectrum of TFO4CII.

C-4 'Click' Reaction Yields

Table C-4. Experimental yields of AMN-TFO hybrids after 'click' reaction, desalting and HPLC purification; **5′-dC^{O}** = 5′-octadiynyl-deoxycytidine; **int-dU^{O}** = internal-octadiynyl-deoxyuridine; **5′-dT^{H}** = 5′-hexynyl-deoxythymidine; **5′-dC^{BCN}** = 5′-BCN(CEP II)-deoxycytidine**; pdU** = 5-(1-propargylamino)-deoxyuridine; **pdU-TO** = pdU with thiazole orange attached; **6N$_3$-TPMA** = *N*-6-(azidomethyl)pyridine-*N*-*di*-(2-picolyl)amine; **5N$_3$-TPMA** = *N*-5-(azidomethyl)pyridine-*N*-*di*-(2-picolyl)amine; **4N$_3$-DPA** = *N*-4-azidobenzyl-*N*-*di*-(2-picolyl)amine.

BCN rxn: Azide = 10 eq, Rxn = 40 °C for 24 hrs. Conversion Yield = 99% (no starting material in MS). Loss of yield due impurities from TO decomposition.

Oligo name	Sequence	Modification (X)(Y)	Yield (%)
TFO1AI	**5′ – X**CC GTT TCC TCT TCT T **– 3′**	5′-dC^{H}-6N$_3$-TPMA	31.9
TFO1AII	**5′ – X**CC GTT TCC TCT TCT T **– 3′**	5′-dC^{H}-5N$_3$-TPMA	19.1
TFO1AIII	**5′ – X**CC GTT TCC TCT TCT T **– 3′**	5′-dC^{H}-4N$_3$-DPA	6.01
TFO1BI	**5′ – X**CC GTT TCC TCT TCT T **– 3′**	5′-dC^{O}-6N$_3$-TPMA	16.3
TFO1BIII	**5′ – X**CC GTT TCC TCT TCT T **– 3′**	5′-dC^{O}-4N$_3$-DPA	1.57
TFO1CI	**5′ –** CCC GTT TCC **X**CT TCT T **– 3′**	int-dU^{O}-6N$_3$-TPMA	49.0
TFO1CII	**5′ –** CCC GTT TCC **X**CT TCT T **– 3′**	int-dU^{O}-5N$_3$-TPMA	40.7
TFO1CIII	**5′ –** CCC GTT TCC **X**CT TCT T **– 3′**	int-dU^{O}-4N$_3$-DPA	8.55
TFO1DI	**5′ – X**CC GTT TCC TCT TCT T **– 3′**	5′-dC^{BCN}-6N$_3$-TPMA	38.6
TFO1DII	**5′ – X**CC GTT TCC TCT TCT T **– 3′**	5′-dC^{BCN}-5N$_3$-TPMA	12.4
TFO1DIII	**5′ – X**CC GTT TCC TCT TCT T **– 3′**	5′-dC^{BCN}-4N$_3$-DPA	50.1
TFO2AI	**5′ – X**CT CTC CCG CTT CCG CT **– 3′**	5′-dC^{H}-6N$_3$-TPMA	35.4
TFO2AII	**5′ – X**CT CTC CCG CTT CCG CT **– 3′**	5′-dC^{H}-5N$_3$-TPMA	22.5
TFO2AIII	**5′ – X**CT CTC CCG CTT CCG CT **– 3′**	5′-dC^{H}-4N$_3$-DPA	4.07
TFO3AI	**5′ – X**TC TTT CCT TCC CTT CTT TC **– 3′**	5′-dC^{H}-6N$_3$-TPMA	35.8
TFO3AII	**5′ – X**TC TTT CCT TCC CTT CTT TC **– 3′**	5′-dC^{H}-5N$_3$-TPMA	24.8
TFO3AIII	**5′ – X**TC TTT CCT TCC CTT CTT TC **– 3′**	5′-dC^{H}-4N$_3$-DPA	23.1
TFO4AI	**5′ – X**CG CTC TTT CCT TCC CTT CTT TCG CTT TCC TC **– 3′**	5′-dC^{H}-6N$_3$-TPMA	54.5
TFO4AII	**5′ – X**CG CTC TTT CCT TCC CTT CTT TCG CTT TCC TC **– 3′**	5′-dC^{H}-5N$_3$-TPMA	25.6

TFO4BI	**5′ – X**CG CTC TTT CCT TCC CTT CTT TCG CTT TCC TC **– 3′**	5′-dC^{O}-6N$_3$-TPMA	64.0
TFO4BII	**5′ – X**CG CTC TTT CCT TCC CTT CTT TCG CTT TCC TC **– 3′**	5′-dC^{O}-5N$_3$-TPMA	31.0
TFO4BIII	**5′ – X**CG CTC TTT CCT TCC CTT CTT TCG CTT TCC TC **– 3′**	5′-dC^{O}-4N$_3$-DPA	17.5
TFO4CI	**5′ –** CGC TCT TTC CTT CCC **X**TC TTT CGC TTT CCT C **– 3′**	int-dU^{O}-6N$_3$-TPMA	50.2
TFO4CII	**5′ –** CGC TCT TTC CTT CCC **X**TC TTT CGC TTT CCT C **– 3′**	int-dU^{O}-5N$_3$-TPMA	52.5
TFO4CIII	**5′ –** CGC TCT TTC CTT CCC **X**TC TTT CGC TTT CCT C **– 3′**	int-dU^{O}-4N$_3$-DPA	21.1
TFO4DI	**5′ – X**CG CTC TTT CCT TCC CTT CTT TCG CTT TCC TC **– 3′**	5′-dC^{BCN}-6N$_3$-TPMA	36.0
TFO4DII	**5′ – X**CG CTC TTT CCT TCC CTT CTT TCG CTT TCC TC **– 3′**	5′-dC^{BCN}-5N$_3$-TPMA	32.1
iTOTFO4D_I	**5′ – X** CG CTC TTT CCT TCC C**Y**T CTT TCG CTT TCC TC **– 3′**	5′-dC^{BCN}-6N$_3$-TPMA, pdU-TO	66.5
iTOTFO4D_II	**5′ – X** CG CTC TTT CCT TCC C**Y**T CTT TCG CTT TCC TC **– 3′**	5′-dC^{BCN}-5N$_3$-TPMA, pdU-TO	67.7
tTOTFO4D_I	**5′ – X** CG CTC TTT CCT TCC CTT CTT TCG CTT **Y**CC TC **– 3′**	5′-dC^{BCN}-6N$_3$-TPMA, pdU-TO	79.0
tTOTFO4D_II	**5′ – X** CG CTC TTT CCT TCC CTT CTT TCG CTT **Y**CC TC **– 3′**	5′-dC^{BCN}-5N$_3$-TPMA, pdU-TO	80.3
TFO5AI	**5′ – X**CT TCG TCG CTC CTC C **– 3′**	5′-dT^{H}-6N$_3$-TPMA	36.7
TFO5AII	**5′ – X**CT TCG TCG CTC CTC C **– 3′**	5′-dT^{H}-5N$_3$-TPMA	13.4
TFO5AIII	**5′ – X**CT TCG TCG CTC CTC C **– 3′**	5′-dT^{H}-4N$_3$-DPA	14.3

C-5 Thermal melting data

Table C-5. T_M were recorded in 10 mM PO_4^{3-}, 150 mM NaCl, 2 mM $MgCl_2$, pH ~ 6 buffer in absence and presence of 1 eq of Cu(II) to the TFO. T_M temperatures were calculated by the first derivative of the sigmoidal regression fit for the triplex melting curves on GraphPad Prism® 6.0 software. Final T_M values are an average of 3 melting curves. **n.d.** = not determined because T_M < 12 °C. **5′-dC^O** = 5′-octadiynyl-deoxycytidine; **int-dU^O** = internal-octadiynyl-deoxyuridine; **5′-dT^H** = 5′-hexynyl-deoxythymidine; **5′-dC^{BCN}** = 5′-BCN(CEP II)-deoxycytidine**;** **pdU** = 5-(1-propargylamino)-deoxyuridine; **pdU-TO** = pdU with thiazole orange attached; **6N$_3$-TPMA** = *N*-6-(azidomethyl)pyridine-*N*-*di*-(2-picolyl)amine; **5N$_3$-TPMA** = *N*-5-(azidomethyl)pyridine-*N*-*di*-(2-picolyl)amine; **4N$_3$-DPA** = *N*-4-azidobenzyl-*N*-*di*-(2-picolyl)amine.

Oligo name	Modification	T_M (°C) - Cu(II)	T_M (°C) + Cu(II)	ΔT_M
TFO1A	5′-dC^H	22.3 ± 0.2	22.0 ± 0.2	-0.3
TFO1AI	5′-dC^H-6N$_3$-TPMA	21.7 ± 0.1	25.1 ± 0.3	3.4
TFO1AII	5′-dC^H-5N$_3$-TPMA	20.3 ± 0.2	22.1 ± 0.9	1.8
TFO1AIII	5′-dC^H-4N$_3$-DPA	22.5 ± 0.3	22.6 ± 0.3	0.1
TFO1B	5′-dC^O	19.3 ± 0.1	n.d.	-
TFO1BI	5′-dC^O-6N$_3$-TPMA	18.9 ± 0.1	19.6 ± 0.2	0.7
TFO1BIII	5′-dC^O-4N$_3$-DPA	21.4 ± 0.2	22.2 ± 0.7	0.8
TFO1C	int-dU^O	24.6 ± 0.0	24.0 ± 0.7	-0.6
TFO1CI	int-dU^O-6N$_3$-TPMA	22.5 ± 0.0	23.1 ± 0.3	0.6
TFO1CII	int-dU^O-5N$_3$-TPMA	21.4 ± 0.1	21.6 ± 0.5	0.2
TFO1CIII	int-dU^O-dU-4N$_3$-DPA	17.7 ± 0.2	18.7 ± 0.7	1.0
TFO1D	5′-dC^{BCN}	29.9 ± 0.5	30.3 ± 0.2	0.4
TFO1DI	5′-dC^{BCN}-6N$_3$-TPMA	18.0 ± 0.2	19.5 ± 0.8	1.5
TFO1DII	5′-dC^{BCN}-5N$_3$-TPMA	17.9 ± 0.1	18.4 ± 0.2	0.5
TFO1DIII	5′-dC^{BCN}-4N$_3$-DPA	18.9 ± 0.1	21.0 ± 0.5	2.1
TFO2A	5′-dC^H	n.d.	-	-
TFO2AI	5′-dC^H-6N$_3$-TPMA	-	-	-
TFO2AII	5′-dC^H-5N$_3$-TPMA	-	-	-
TFO2AIII	5′-dC^H-4N$_3$-DPA	-	-	-
TFO3A	5′-dC^H	43.1 ± 0.0	43.0 ± 0.9	-0.1
TFO3AI	5′-dC^H-6N$_3$-TPMA	41.6 ± 0.2	42.2 ± 0.9	0.6
TFO3AII	5′-dC^H-5N$_3$-TPMA	41.4 ± 0.1	42.2 ± 0.8	0.8
TFO3AIII	5′-dC^H-4N$_3$-DPA	42.6 ± 0.1	49.0 ± 0.5	6.4
TFO4A	5′-dC^H	47.3 ± 0.4	47.3 ± 0.6	0.0
TFO4AI	5′-dC^H-6N$_3$-TPMA	45.8 ± 0.4	47.8 ± 0.6	2.0
TFO4AII	5′-dC^H-5N$_3$-TPMA	45.8 ± 0.2	48.1 ± 0.3	2.3

TFO4AIII	5′-dC^{H}-4N$_3$-DPA	44.5 ± 0.0	47.1 ± 0.8	2.6
TFO4B	5′-dC^{O}	45.2 ± 0.1	44.6 ± 0.8	-0.6
TFO4BI	5′-dC^{O}-6N$_3$-TPMA	46.4 ± 0.4	50.6 ± 0.3	4.2
TFO4BII	5′-dC^{O}-5N$_3$-TPMA	46.4 ± 0.3	46.5 ± 0.7	0.1
TFO4BIII	5′-dC^{O}-4N$_3$-DPA	46.1 ± 0.1	46.5 ± 0.7	0.4
TFO4C	int-dU^{O}	45.1 ± 0.2	46.2 ± 0.6	1.1
TFO4CI	int-dU^{O}-6N$_3$-TPMA	40.8 ± 0.3	42.2 ± 1.0	1.4
TFO4CII	int-dU^{O}-5N$_3$-TPMA	40.1 ± 0.2	45.5 ± 1.0	5.4
TFO4CIII	int-dU^{O}-4N$_3$-DPA	40.6 ± 0.1	42.9 ± 0.4	2.3
TFO4D	5′-dC^{BCN}	42.6 ± 0.3	43.6 ± 0.9	1.0
TFO4DI	5′-dC^{BCN}-6N$_3$-TPMA	43.4 ± 0.1	46.4 ± 0.5	3.0
TFO4DII	5′-dC^{BCN}-5N$_3$-TPMA	45.5 ± 0.1	46.2 ± 0.3	0.7
iTOTFO4D	5′-dC^{BCN} , pdU-TO	60.9 ± 0.1	-	-
tTOTFO4D	5′-dC^{BCN} , pdU-TO	61.0 ± 0.2	-	-
iTOTFO4D_I	5′-dC^{BCN}-6N$_3$-TPMA, pdU-TO	61.7 ± 0.2	-	-
iTOTFO4D_II	5′-dC^{BCN}-5N$_3$-TPMA, pdU-TO	61.6 ± 0.2	-	-
tTOTFO4D_I	5′-dC^{BCN}-6N$_3$-TPMA, pdU-TO	59.9 ± 0.2	-	-
tTOTFO4D_II	5′-dC^{BCN}-5N$_3$-TPMA, pdU-TO	59.8 ± 0.1	-	-
TFO5A	5′-dT^{H}	n.d.	-	-
TFO5AI	5′-dT^{H}-6N$_3$-TPMA	-	-	-
TFO5AII	5′-dT^{H}-5N$_3$-TPMA	-	-	-
TFO5AIII	5′-dT^{H}-4N$_3$-DPA	-	-	-

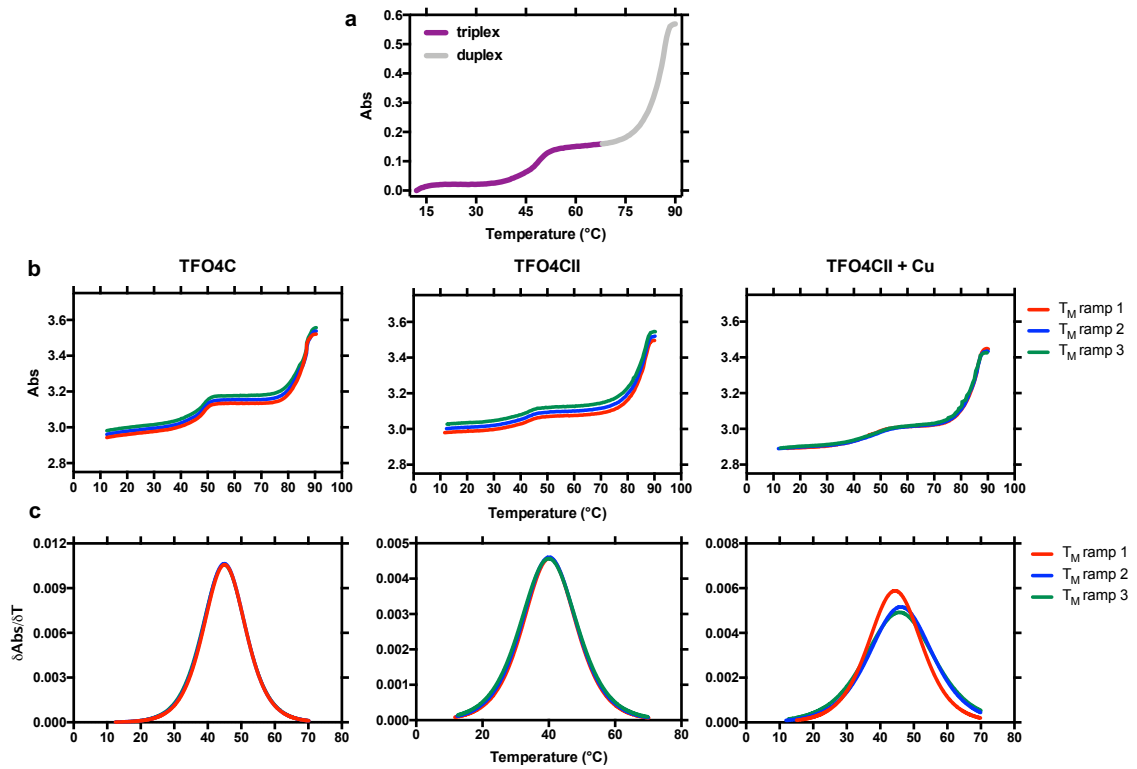

Figure C-48. **A** Plot of UV melting of a triplex, the first transition is indicative of triplex denaturation (purple) while the second is indicative of duplex denaturation (grey). **B** UV melting curves of TFO4C, TFO4CII and TFO4CII with 1 eq of Cu(II) recorded as a function of temperature (12–95 ˚C) in the given buffers. **C** Smoothed first derivative of triplex thermal denaturation curves.

C-6 DNA Damage

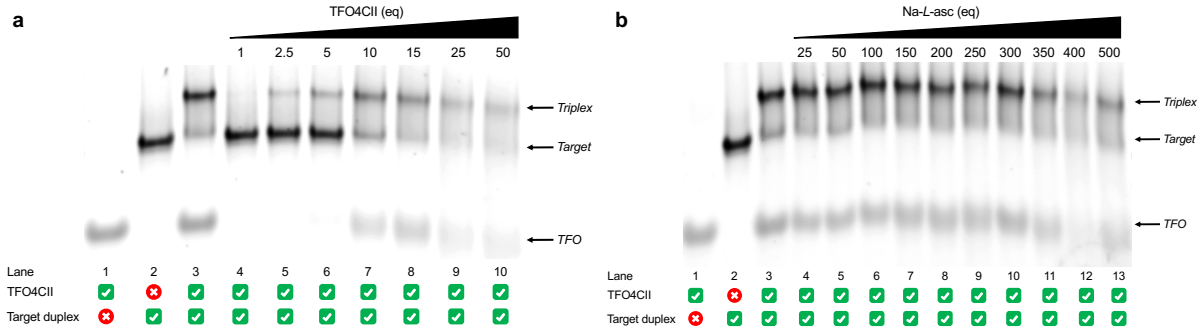

Figure C-49. A Nuclease activity of TFO4CII; duplex GFP target (52 bp, 1.25 pmol) treated with increasing concentrations of TFO4CII (1-50 eq to the duplex, lane 4-10) in the presence of Na-*L*-asc (3.125 mM). **B** Catalytic nuclease activity of TFO4CII; duplex GFP target (52 bp, 1.25 pmol) treated with 25 eq of TFO4CII in the presence of increasing concentrations of Na-*L*-asc (25-500 eq to TFO4CII, lanes 4-13).

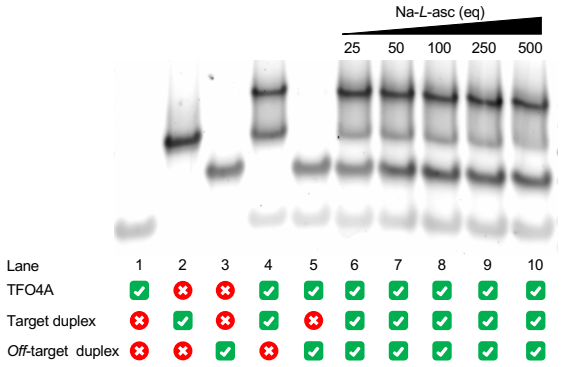

Figure C-50. Control cleavage of 'non-clicked' TFO4A in presence of Cu(II) and Na-*L*-asc; duplex GFP target (52 bp, 1.25 pmol) treated with 25 eq of TFO4A in the presence of 1 eq of Cu(II) and increasing concentrations of Na-*L*-asc (25-500 eq to TFO4CII, lanes 4-13).

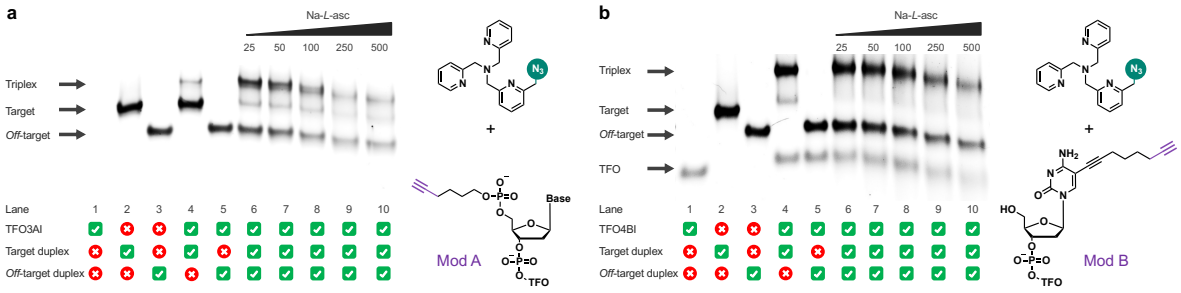

Figure C-51. 25 eq. of Cu(II) bound hybrids TFO3AI (**A**) and TFOBI (**B**) were exposed to the GFP target and an *off*-target duplex (1.25 pmol) in the presence of increasing concentrations of Na-*L*-asc (25-500 eq).

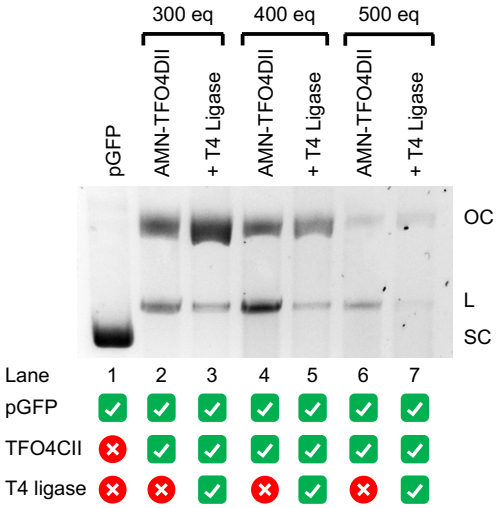

Figure C-52. T4 DNA re-ligation optimization of pGFP cleaved by TFO4CII (lanes 2-7). (SC = supercoiled; L = linear; OC = open circular).

C-7 References

[1] Z. Molphy, A. Prisecaru, C. Slator, N. Barron, M. McCann, J. Colleran, D. Chandran, N. Gathergood, A. Kellett, *Inorg. Chem.* **2014**, *53*, 5392–5404.

[2] N. Zuin Fantoni, Z. Molphy, C. Slator, G. Menounou, G. Toniolo, G. Mitrikas, V. McKee, C. Chatgilialoglu, A. Kellett, *Chem. Eur. J.* **2019**, *25*, 221–237.

[3] *CrysAlis PRO 1.171.38.43*, Rigaku Oxford Diffraction, **2015**.

[4] C. B. Hübschle, G. M. Sheldrick, B. Dittrich, *J. Appl. Crystallogr.* **2011**, *44*, 1281–1284.

[5] G. M. Sheldrick, *Acta Crystallography* **2015**, *A71*, 3–8.

[6] G. M. Sheldrick, *Acta Crystallography* **2015**, *C71*, 3–8.

[7] C. F. Macrae, I. J. Bruno, J. A. Chisholm, P. R. Edgington, P. McCabe, E. Pidcock, L. Rodriguez-Monge, R. Taylor, J. van de Streek, P. A. Wood, *J Appl Cryst* **2008**, *41*, 466–470.

[8] O. V. Dolomanov, L. J. Bourhis, R. J. Gildea, J. a. K. Howard, H. Puschmann, *J Appl Cryst* **2009**, *42*, 339–341.

[9] S. P. Westrip, *J. Appl. Crystallogr.* **2010**, *43*, 920–925.